ABSTRACT

Title of dissertation: COMBINATORIAL EXPLORATION OF PHASE TRANSFORMATION IN NiTi-BASED THIN FILM LIBRARIES FOR SHAPE MEMORY ALLOY APPLICATIONS

Naila M. Al Hasan
Doctor of Philosophy, 2020

Dissertation directed by: Professor Ichiro Takeuchi
Department of Materials Science and Engineering

Ni-Ti based shape memory alloys (SMAs) have found widespread use in the last 70 years but improving their functional stability remains a key quest for more robust and advanced applications. Named for their ability to retain their shape via a reversible martensitic phase transformation (PT), they are sensitive to compositional variations. Tuning the SMA lattice parameters, transformation temperature and thermal hysteresis (ΔT) by alloying with ternary and quaternary elements, therefore, is a challenging materials exploration effort. Combinatorial materials science streamlines synthesis, characterization and data management processes from multiple high-throughput techniques. In this dissertation, composition spreads of Ni-Ti-X (X = Co, Hf, Pd, V) and Ni-Ti-Cu-Y (where Y = Co, Fe, Pd, V) thin film libraries were synthesized by magnetron co-sputtering to probe a substantial composition space with different stoichiometries under identical conditions. Composition-dependent PT temperature, microstructure and thermal conductivity

were investigated using high-throughput wavelength dispersive spectroscopy (WDS), temperature-dependent resistance *R(T)*, synchrotron x-ray diffraction (XRD) and scanning hot probe (SHP) microscopy measurements.

Through case studies of ternary Ni-Ti-Co and quaternary Ni-Ti-Cu-V systems, I discuss phase determination and how functional properties correlate with composition and local microstructure using composition-structure-property maps. In the Ni-Ti-Co library, a new, expanded composition space having PT with small thermal hysteresis and c(Co) >10 at.% was identified. Of the 177 compositions, 31 had stable PT with near-zero ΔT in four. Elemental range for SMA compositions was 25.8 at.% < c(Ni) < 70.5 at.%, 21.4 at.% < c(Ti) < 64.3 at.%, and 5.5 at.% < c(Co) < 26.4 at.%. Crystallographic evidence points to a cubic Pm3m structure present as single or mixed with hexagonal or orthorhombic structures for all these compositions.

In the Ni-Ti-Cu-V library, PT was observed in 32 compositions (21.3 at.% < c(Ni) < 30.9 at.%, 49.4 at.% < c(Ti) < 57.5 at.%, 13.8 at.% < c(Cu) < 21.6 at.% and 4.1 at.% < c(V) < 6.2 at.%), predominantly in the Ti-rich region, with zero or near-zero ΔT in five. Increasing V up to 6 at.% stabilized the mixture of transforming cubic and tetragonal phases. These newly identified composition regions provide flexibility in and expand the operating temperature window for their application in different technologies.

Lastly, a novel application of SMAs as phase change materials is briefly investigated through high-throughput determination of their thermal conductivity using

scanning hot probe microscopy. Binary, ternary and quaternary thin film libraries of Ni-Ti, Ni-Ti-V and Ni-Ti-Cu-V were evaluated as a benchmarking exercise.

COMBINATORIAL EXPLORATION OF PHASE TRANSFORMATION IN NiTi-BASED THIN FILM LIBRARIES FOR SHAPE MEMORY ALLOY APPLICATIONS

by

Naila M. Al Hasan

Dissertation submitted to the Faculty of the Graduate School of the
University of Maryland, College Park in partial fulfillment
of the requirements for the degree of
Doctor of Philosophy
2020

Advisory Committee:
Professor Ichiro Takeuchi, *Chair/Advisor*
Associate Professor Isabel Lloyd
Professor Lourdes Salamanca-Riba
Professor Manfred Wuttig
Professor Reinhard Radermacher, *Dean's Representative*

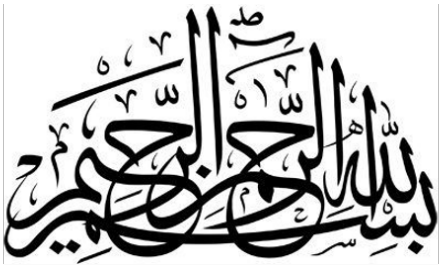

In the name of God, the Compassionate, the Merciful

Dedication

For my grandmothers, Ashraf Unisa and Kaneeze Zehra, and my grandfathers, Mohib Ul-Haq and Syed Vasif Ali, whose legacies of learning live on.

And to refugees, immigrants, migrants, and third-culture kids everywhere.

Acknowledgments

Prophet Muhammad, peace be upon him, famously said, "one who does not thank people, does not thank God."

No one gets a degree alone. Indeed, it takes a village.

I, for one, have three communities in three states along with friends all over the world who have loved and supported me unconditionally through my time in graduate school. Thank you for all the energy.

I especially dedicate this work to the Piscataway and Nacotchtank tribes, who were forcibly removed by European colonizers from the land on which University of Maryland, College Park stands today. Thereafter, to Mummy & Daddy, "The Gang" – Nabila, Aala, Saad, Emad, Pasha, Nida, and Muna, my nieces - Noora and Asiya, and my beloved husband and prank-partner for life Nathan, for their unwavering support and love.

My immense gratitude to the companionship of fellow doctoral students, Christopher Klingshirn and Zoey Warecki; I could not have asked for a better set of graduate school friends with a moral compass and strength of character than them.

Thank you to my advisor, Prof. Dr. Ichiro Takeuchi, for giving me the freedom to be creative in the lab but also "tough" guidance in interpreting data. Thank you to all my group members for fruitful discussions, food delivery, pranks, office sleepovers, and help in preparing presentations every step of the way.

A special thanks to my committee members for their service; I am especially happy and incredibly proud to have two women professors. Dr. Isabel Lloyd for

being a role model, her refreshing humor, valuable feedback and guidance in asking critical questions; Dr. Manfred Wuttig for big picture perspectives and fun hypothetical scenarios, nurturing my intellectual curiosity and way of presenting technical information; Dr. Lourdes Salamanca-Riba for her challenging yet thought-provoking defects course as well as being a badass role-model, and last but not least, Dr. Reinhard Radermacher for his insightful mentorship of students in navigating graduate school and radically straightforward leadership - I wish more advisors would dedicate time to teaching life-management strategies and clarifying their expectations of fresh graduate students.

In no particular order, I'd like to also thank mentors from my undergraduate education at Houston Baptist University: Dr. Taiya Fabre, Dr. Robert Towery, Dr. Gardo Blado, Dr. James Claycomb, Dr. Rachel Hopp; from Pacific Northwest National Lab: Karen Wieda, Dr. Julia Laskin, Dr. Grant Johnson, Dr. Don Gunaratne, Brandi Heath, Dr. Jun Cui; from University of Maryland, College Park: Kathleen Hart, Dr. Eric Marksz, Drew Stasak, Stephen Barbagallo, Dr. Phillip Piccoli, Dr. Yangang Liang, Dr. Xiaohang Zhang, Dr. Seunghun Lee, Dr. Heshan Yu, Dr. Yunlong Geng, Dr. Jason Hattrick-Simpers, Dr. Gilad Kusne, Alan Santos, Dr. Sean Fackler, Dr. Miriam Hiebert, Medina Alogba, Dr. Elif Tan, Dr. Darryl Pines, Dr. Linda Macri at the Graduate Writing Center with Dr. Cara Snyder, Jenna Bishop, Olivia Noble, Kay Morris, Michael McNicholas, Joy Chao, Dr. Jarred Young, Dr. Elizabeth Lathrop, Dr. Iftekhar Jaim; from Ruhr University, Bochum in Germany: Dr. Alan Savan, Dr. Sigurd Thienhaus, Dr. Alfred Ludwig, Dr. Peer Decker, Timo Allermann, and Dr. Tobias Oellers;

from my extended family: Abdul Raoof Uncle, Qadeer Raoof Aunty, the Nesbitt family, the many friends I cannot list here and everyone from my schooling years at International Indian School, Jeddah. Last but certainly not least, my gratitude to all my co-workers from HW6 Sugar Land Chase Bank and Missouri City Wal-Mart who supported my educational pursuits during and beyond my time there.

Finally, I'd like to acknowledge the generous funding support for this work provided by U.S. Department of Education's Graduate Assistance in Areas of National Need (GAANN) Fellowship, U.S. Army Research Laboratory and the National Science Foundation Graduate Research Fellowship Program (NSF-GRFP) under Grants DGE 1322106 and DGE 1840340.

Completed on 19th of October 2020, day 222 of the novel coronavirus (COVID-19) outbreak, declared a global pandemic by The World Health Organization on 11th March 2020.

Table of Contents

List of Tables

List of Figures

List of Abbreviations

A_f	[°C]	austenite finish temperature
A_s	[°C]	austenite start temperature
AFM	[-]	atomic force microscope
at.%	[-]	atomic percent
B2	[-]	cubic austenite phase
B19	[-]	orthorhombic martensite phase
B19'	[-]	monoclinic marteniste phase
COP	[-]	coefficient of performance
DC	[A]	direct current
eCE	[-]	elastocaloric effect
EC	[-]	elastocaloric cooling
GHG	[-]	greenhouse gases
HCA	[-]	hierarchical cluster analysis
HTE	[-]	high-throughput experimentation
DSC	[-]	differential scanning calorimetry
LN_2	[-]	liquid nitrogen
M_f	[°C]	martensite finish temperature (B19')
M_s	[°C]	martensite start temperature (B19')
NMF	[-]	non-negative matrix factorization
PCC	[-]	pearson correlation coefficient
PCM	[-]	phase change material
RF	[Hz]	radio frequency
RT	[-]	room temperature
R(T)	[-]	temperature-dependent resistance
SE	[-]	superelastic effect
SI	[-]	supplementary information
SHP	[-]	scanning hot probe
SMA	[-]	shape memory alloy
SME	[-]	shape memory effect
SThM	[-]	scanning thermal microscope
ΔT	[°C]	thermal hysteresis
T	[°C]	temperature
TEM	[-]	transmission electron microscope
TT	[-]	transformation temperature
WDS	[-]	wavelength dispersive spectroscopy
XPS	[-]	X-ray photoelectron spectroscopy
XRD	[-]	X-ray diffraction

Chapter 1: Introduction

New and more efficient cooling technologies are needed to reduce building energy consumption and environmental impact. Residential and commercial buildings currently account for 70% of the nation's electricity use and 40% of our CO_2 emissions each year, 5% of which comes directly from air conditioning [14,15]. Moreover, typical refrigerants used in cooling devices are potent greenhouse gases (GHGs) that have 1000 to 9000 times the capacity to warm the atmosphere than CO_2, thereby contributing to global climate change; their replacement is akin to taking 629 million cars off the road [16]. Due to the essential nature of refrigeration and cooling in modern civilization, research into the development of new cooling technologies based on caloric materials has risen significantly. A recent report by the US Department of Energy has recognized elastocaloric cooling (EC), also known as thermoelastic cooling, as a promising alternative to state-of-the-art vapor compression cooling system – it has a high temperature change that can be achieved over a wide working temperature range, and an excellent coefficient of performance (COP, 6.0 vs 3.2 for baseline vapor-compression systems) [17].

1.1 Introduction to Shape Memory Alloys (SMAs)

Solid materials can exhibit caloric effects when a change in the entropy and/or temperature of a material occurs when subjected to a sudden change in an external field [18, 19]. The EC is an application of the shape memory effect (SME) – also known as superelastic effect (SE) – and elastocaloric effect (eCE) present in shape memory alloys (SMAs). The earliest SMA was discovered in 1932 by Arne Olander while the term, "shape memory" was described by the Vernon brothers in 1941 for their polymeric dental material [20,21]. SMAs are named as such due to their ability to return to their original shape after being subjected to an external field. They are produced by a process of memorization between two phases that are magnetic field-, electric field-, temperature-, pressure- or mechanical deformation-dependent and can withstand large transformation stresses and strains [18, 19]. The SME and eCE are a result of a reversible, solid to solid, first order, diffusion-less martensitic phase transformation (PT) between two phases having three crystal structures – a high temperature, high symmetry cubic phase called austenite or B2 and low temperature, low symmetry martensitic phase present as twinned or detwinned variants called B19' [22]. Shape memory effect is associated with a temperature induced transformation whereas the superelastic effect only needs to overcome a critical stress threshold to be induced [18]. The associated crystallographic shearing deformation, discussed in Sec. 1.2, has a latent heat associated with it that can be harnessed for heating and cooling applications [1].

SMAs offer several advantages – the force and displacement per unit volume of thin film (actuation output) is greater than other microactuation mechanisms, rapid actuation, a narrow temperature hysteresis which translates to greater transformation efficiency, corrosion resistance, bio-compatibility, and a cleaner alternative to GHGs [23, 24]. While thermal effects in copper (Cu)-based SMAs were reported as early as 1980 [25, 26], elastocaloric cooling using CuZnAl shape memory alloy was first proposed by Bonnot in 2008 [27, 28]. However, one of the most commercially relevant SMAs is nitinol – an equiatomic alloy of nickel (Ni) and titanium (Ti). It was first discovered at the Naval Ordinance Laboratory (NOL) in 1962 by William Buehler and Frederick Wang who named it NiTiNOL [1,29,30]. With a temperature change of ΔT = 20-40 K, nitinol has the largest eCE of all SMAs and is used as a benchmark material with the following characteristics: high latent heat (20 J/g), average transitional stress (700 MPa), long fatigue life (>360,000 cycles), and low hysteresis (1 J/g) for an efficient transformation process to reduce loss [22,31,32]. As a result, in addition to the development of novel solid-state refrigerants and cooling systems based on EC [27, 33], NiTi based SMAs have found applications in a wide range of fields – from aerospace [34, 35] and automotive [36] to biomedical therapy in orthodontics and stents [37–47] to even clothing [48].

Efforts are, thus, underway to develop materials having greater property specificity including reducing the high cost of commercial NiTi [18]. Overall performance of SMAs is defined by operating temperature, mechanical work, material/operational life (structural/functional fatigue) and energy efficiency/dissipation [49]. Two properties of interest and importance in SMAs as related to this thesis work are transfor-

mation temperature and thermal hysteresis, both of which are expanded on in the following sections. The thermodynamic parameters and characteristic transformation temperatures can be altered by variation in both the elements and their proportion in the composition of the alloy [50, 51]. Common metallic SMAs are based on Cu, Fe, and NiTi, of which NiTi-based SMAs were chosen due to commercial availability, easy synthesis, and relatively low cost of production. Ternary Ni-Ti-X (X = Co, Hf, Pd, V) and quaternary Ni-Ti-Cu-Y (Y = Co, Fe, Pd, V) were produced by magnetron co-sputtering and characterized using high throughput techniques. The third and fourth elements were chosen to reduce the transformation temperature of the alloy to around room temperature whereas copper (Cu) was used in quaternary alloys to reduce the critical stress needed to induce transformation [1, 52]. More details to follow.

1.2 Phase Transformation of NiTi SMAs

The two phases an SMA transforms between are essentially made up of three different crystal structures: high temperature and high symmetry austenite (B2), low temperature and low symmetry martensite (B19') in twinned and detwinned forms, thus giving rise to six possible transformations [1, 53]. For the NiTi system, the following Figure 1.1 illustrates possible crystallographic transformation pathways [1, 54]:

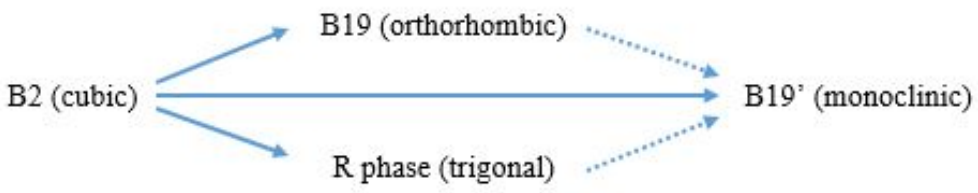

.

Figure 1.1: Crystallographic transformation pathways in NiTi shape memory alloy. Adapted from [1]

The dotted arrows in Figure 1.1 indicate a possible stopping point at the intermediate structure. Rhombohedral structure is not listed here but also possible. The two-step transformation through an intermediate phase can be brought on by thermo-mechanical processing and/or doping with a ternary element [55]. The transformation is classified as a first order one due to the presence of the hysteresis [1]. In a typical elastocaloric cooling cycle, assuming a SMA is in the austenite phase, the exothermic austenite to martensite transformation causes a temperature increase in the material when an applied external stress is beyond a critical transformation stress (Figures 1.2 and 1.3) [2, 3]. Critical temperature parameters associated with this step are martensitic transformation start temperature M_s and martensite transformation finish temperature M_f (Figure 1.3) [3]. This transformative deformation occurs via migration of twin boundaries such that there is growth of some and shrinking of others. A reverse martensite to austenite transformation process results in a temperature decrease and shape retention upon removing the stress, going through austenitic start and finish temperatures, A_s and A_f, respectively [1, 56]. This deformation-transformation cycle can be repeated reliably for SMAs if material degradation does not occur. An example of a stress-strain curve for an SMA during

an elastocaloric cooling cycle is given in Figure 1.3. Shape is set by heating to above A_f temperature so that transformation to austenite is complete. Deformation is also semi-permanent as deformed material is recovered upon heat treatment.

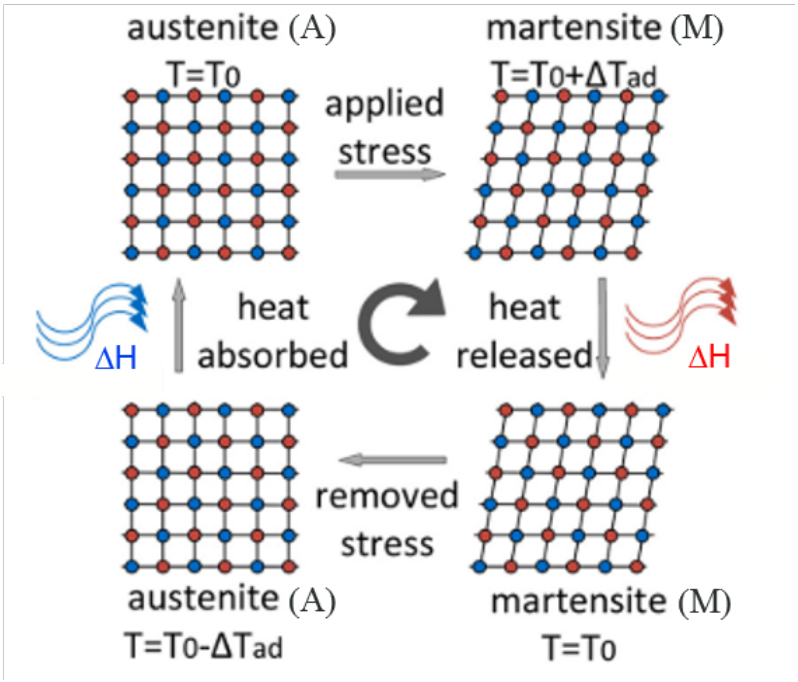

Figure 1.2: Crystallographic rearrangement during an elastocaloric cooling cycle. Adapted from [2].

As the shear deformation during transformation is induced by increasing temperature or applying stress, the Clausius–Clapeyron equation is used to describe the relationship between influence of temperature and stress on the SMA as follows:

$$\frac{d\sigma}{dT} = -\frac{\Delta S}{\epsilon} = -\frac{\Delta H^*}{\epsilon T} \tag{1.1}$$

where σ is the applied uniaxial stress, ΔH^* is transformation enthalpy, ΔS is entropy change between the parent phase and martensite per unit volume, ϵ is the

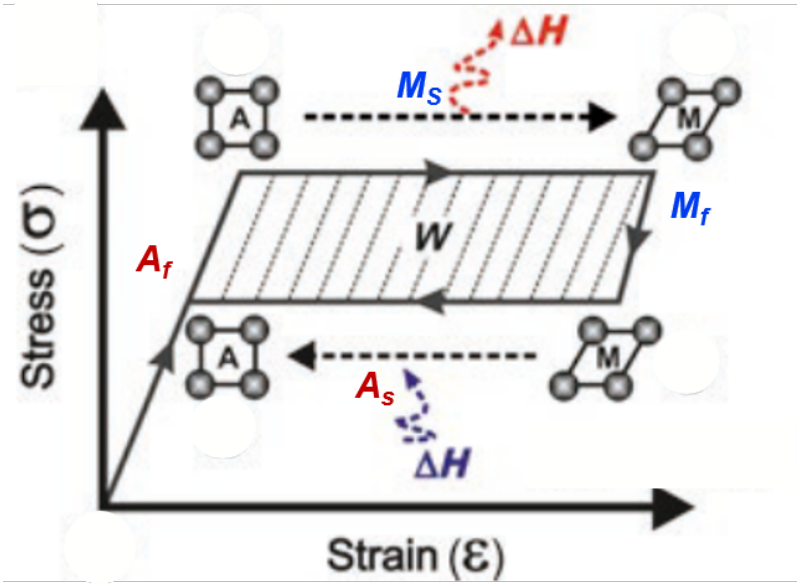

Figure 1.3: Stress-strain behavior of an SMA during an elastocaloric cooling cycle. Adapted from [3].

transformation strain, and T is temperature [1, 57–59]. From Figure 1.3, coefficient of performance (COP) is defined as:

$$COP = \frac{\Delta H}{W} \tag{1.2}$$

where W is the mechanical work input and ΔH is the cooling energy output [3]. The inverse relationship requires a reduced work input or an increased cooling output capacity to increase COP.

Transformation and shape memory characteristics of NiTi depend on metallurgical factors of alloying composition, annealing temperature, aging temperature and time [60]. For example, addition of Cu substituting Ni retains the SME up to 25 at.% such that a 10 at.% substitution results in a two-step martensitic transformation pathway of cubic (B2) → orthorhombic (B19) → monoclinic (B19') [61]. In

contrast, only 1.5 at.% of Fe is needed for a two-step transformation, albeit through a different intermediate phase of rhombohedral structure: cubic (B2) → rhombohedral (R) → monoclinic (B19') [61]. Variation of Ni content can be used to tune the transformation temperature and shape memory behavior (Figure 1.4) [1].

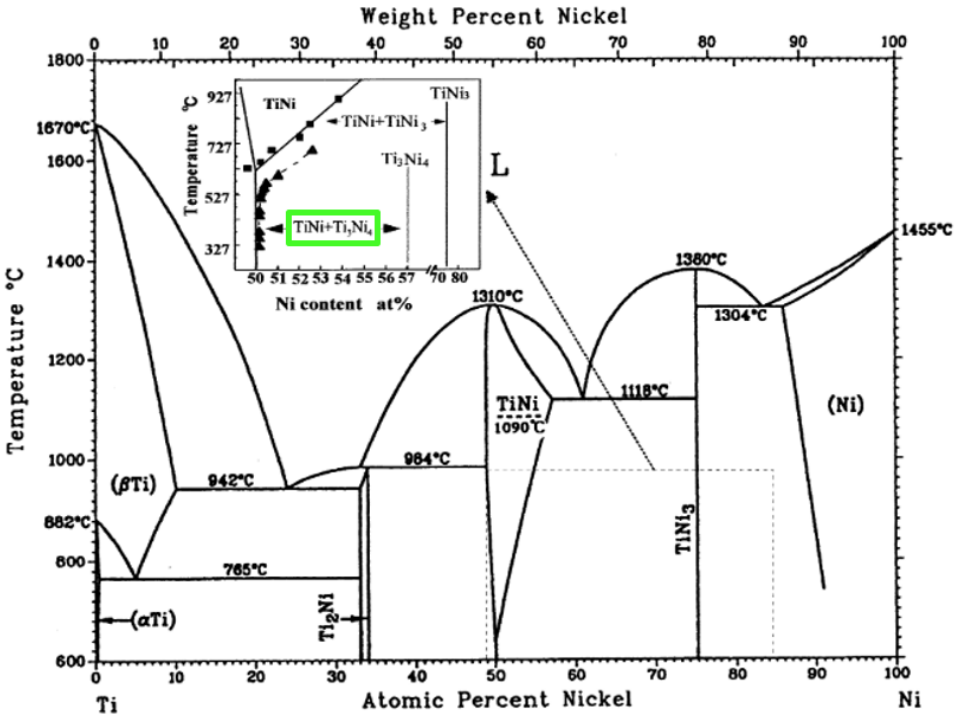

Figure 1.4: Phase diagram of NiTi as adapted from [1]. A metastable phase of TiNi and Ti_3Ni_4 is highlighted in green which has an important role in improving shape memory characteristics and tuning transformation temperature.

For Ti-rich compositions, aging treatments can be used to achieve constant and high transformation temperatures. This is due to the formation of Ti-rich plate precipitates several atomic layers thick on 100 planes that are the origin of stable shape memory behavior. Figure 1.4 is a phase diagram for the NiTi system which provides guidance on the crystallographic phases present at various conditions; some important phases are as follows: NiTi's B2 phase in CsCl type ordered structure

of $Pm3m$ space group, cubic $NiTi_2$ and Ti_4Ni_2O in $Fd3m$ space group, Ni_3Ti in DO_24, Ni_3Ti_2 in two phases as a function of temperature – tetragonal $I4/mmm$ at high temperature and orthorhombic $Bbmm$ at low temperature, and Ti_3Ni_4 in the $R3$ space group [1]. These established reports are used to evaluate crystallographic studies carried out in this dissertation and discussed in chapters 3, 4 and 5.

1.3 Thermal hysteresis

As mentioned previously, the transformation is as a first order transition due to the hysteresis [1]. Understanding the underlying mechanism of reversibility of the martensitic phase transformation in SMAs is critical to their practical application. The area integrated under a stress-strain curve of an SMA is it's mechanical work such that lower transformation stresses and/or strains increase its performance [49]. In absence of a mechanical load, however, thermal hysteresis is defined as the energy dissipated during forward and reverse phase transformation and measured as a difference in heating and cooling transition temperatures, $\Delta T = (A_f - M_s)$ [62,63]. A small hysteresis indicates highly reversible and efficient transformation, low amounts of damage and low irreversible plastic deformation during the PT process and can change over many cyclical loadings, thereby, affecting fatigue life [62]. Thermoelastic martensitic transformation is typically characterized by a hysteresis for energy dissipated in the form of frictional work or elastic strain energy during phase transformation that negatively impacts SMA efficiency and can be directly measured [64,65].

Therefore, it remains an important consideration when selecting SMAs for targeted applications – fast actuation necessitates small hysteresis preference where as a large hysteresis is sought in applications of pipe joining where retaining a predefined shape within a large temperature range is needed [66]. They can range between ≈0 K to >70 K [3, 12, 51].

Normally a consequence of nucleation, thermal hysteresis in SMAs arise as a result of domain-wall pining that occurs due to long range elastic strain accumulating from defects and thermal activation of phase transitions [62, 67–70]. These domain walls are the site of fully developed austenite/martensite interfaces and an elastic transition layer that stores interfacial energy. Transformation hysteresis, hence, is the energy barrier that needs to be overcome during the forward and reverse transformation.

The size of hysteresis increases with decreasing compatibility between the austenitic and martensitic interfaces [49, 51, 62, 71, 72]. It is described by the geometric non-linear theory of martensite (GNLTM) which provides direction in manipulating and fine tuning the size of the hysteresis by targeting the martensite and austenite crystallographic compatibility [12, 73–76]. Briefly, ΔT is governed by the transformation stretch matrix U such that $\det\mathbf{U} = 1$ signifies a no volume change condition. The transformation matrix is further defined by the ordered eigenvalues λ_1, λ_2, and λ_3, where λ_2 when equal to 1 signifies presence of a perfectly coherent interface between austenite and martensite. As an example, for a transformation between cubic austenite of sides a to a martensitic orthorhombic crystal structure

of sides a, b, and c, λ_2 can be defined as [77]:

$$\lambda_2 = \frac{b_{B19}}{\sqrt{2}a_{B2}} = \frac{d(010)_{B19}}{d(110)_{B2}} \tag{1.3}$$

At this interface, the interfacial energy is eliminated reducing the thermal hysteresis.

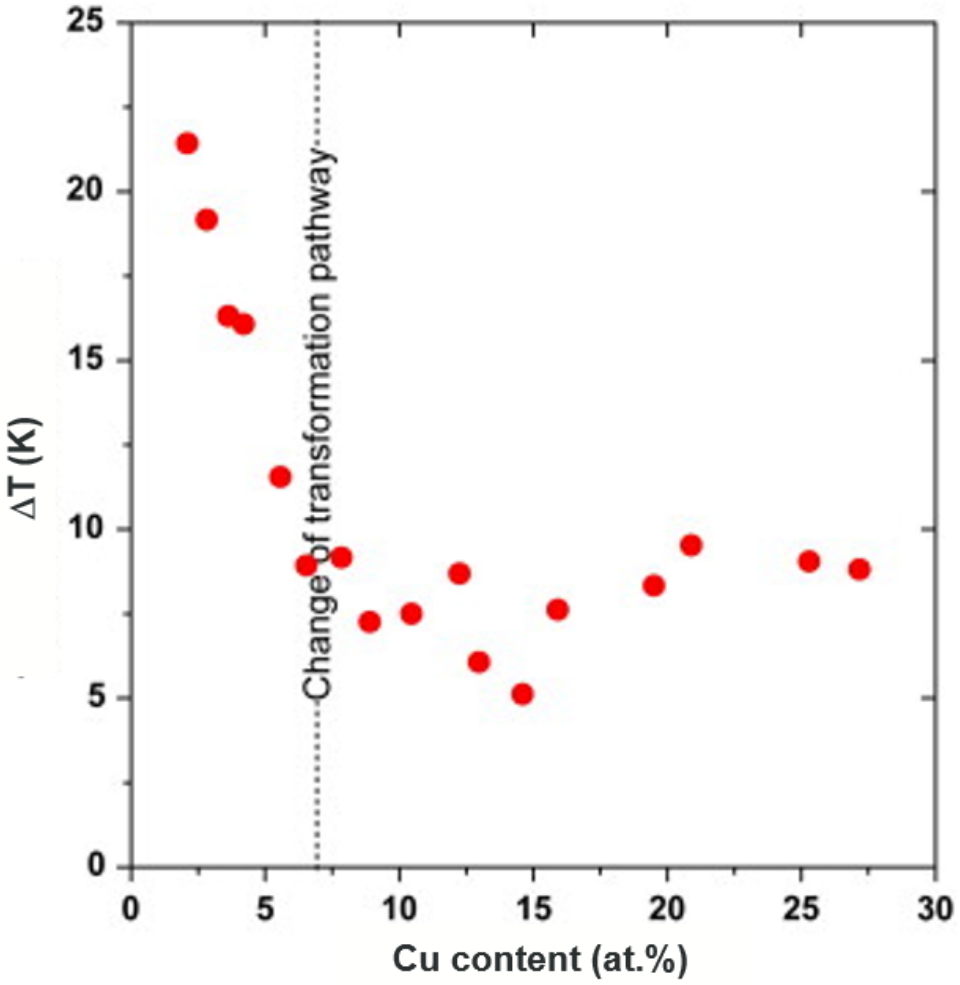

Figure 1.5: Influence of Cu content on thermal hysteresis of $Ni_{49-x}Ti_{59}Cu_x$. Adapted from [4, 5].

Zarnetta et al show how the thermal hysteresis of NiTi can depend on the amount of Cu added to it (Figure 1.5) [4, 5, 78]. Hysteresis as a function of composition

and lattice parameter for ternary alloys using Cu, Pd, Zr and Hf are reported by Bucsek et al: Ni-Ti-Cu alloys of compositions $Ni_{34}Ti_{54}Cu_{12}$ and $Ni_{36}Ti_{51}Cu_{13}$ have low hysteresis overall. Unaged alloys of Ni-Ti-Pd have lowest hysteresis when λ_2 = 1 and through the formation of P-phase precipitates when aged. For Ni-Ti-Hf, unaged alloys follow theoretical predictions of low hysteresis but not when aged despite similar λ_2 values ((0.9337 for unaged, 0.9394 for aged). They are also lower than Ni-Ti-Zr alloys [49]. For quaternary alloys of Ni-Ti-Cu-Pd, thermal hysteresis decreased for compositions with $\lambda_2 = 1$, such that the greater preference of Pd than Cu to occupy Ni sites regardless of concentration increases the sensitivity of ΔT to Pd by an order of magnitude [12]. Lastly, small thermal hysteresis and large latent heat are difficult to obtain as a combined set of desired properties due to a proportional relationship between them [3, 51, 79].

1.4 Effect of alloying with third and fourth elements on transformation temperatures

Efforts have been undertaken recently to improve NiTi SMAs based on specific applications, to control transformation temperatures for enhancing their reliability and applicability [1,32,58,80–82]. Ternary and quaternary elements have been added to NiTi to improve structural stability and functional fatigue life for application in cooling and heat pumping devices through intermetallic precipitates [49, 83]. Addition of a third and fourth element to Ni-Ti alloy has also been shown to affect

both the transformation temperatures and thermal hysteresis of NiTi. For example, adding a third element to manipulate the temperature regime within which this transformation occurs have been carried out using Zr [84], Pd [51], Pt [85, 86], Ag [87], Hf [88, 89] and Au [90] to develop high temperature SMAs [1, 71, 89]. Reduction of transformation temperature was achieved using Fe, Cr, V, Mn and Co as ternary alloys [89]. Addition of Pd and Hf has also been shown to decrease and reduce temperature hysteresis, respectively [12, 91]. Addition of Cu has also been shown to reduce the thermal hysteresis but without decreasing transformation temperature relative to the binary NiTi, thereby leading to enhanced fatigue properties [92–97]. Addition of both Cu and Co has been shown to reduce the martensitic and austenitic start temperatures in combination with Ni's composition as well as improve the fatigue properties [3]. Intermediate phases of B19 and R form as they require less strain energy, influencing the energetics of B2 phase when elastic constants change in c_{44} and c' directions [1, 98]. Resistance of B2 against transformation is affected by the change in matrix valence electron concentration such that the variation in M_s is dictated by precipitation in NiTi-based SMAs. A decrease in M_s is correlated with an increase in matrix valence electron concentration and vice versa; hence, elastic constants of the phase transforming matrix are important, which are furthermore related to crystal electron concentration [98]. A summary of the dependence of M_s on the concentration of a ternary element added to NiTi is shown in Figure 1.6 [1]. Certain elements like Zr and Hf increase the M_s while others reduce it. I used this as a guide to select Co, Fe, Pd, and V for my work. It is important to note that the line fits are between few data points meaning

single compositions were investigated one by one, which is a slow process making it difficult to accurately determine correlations.

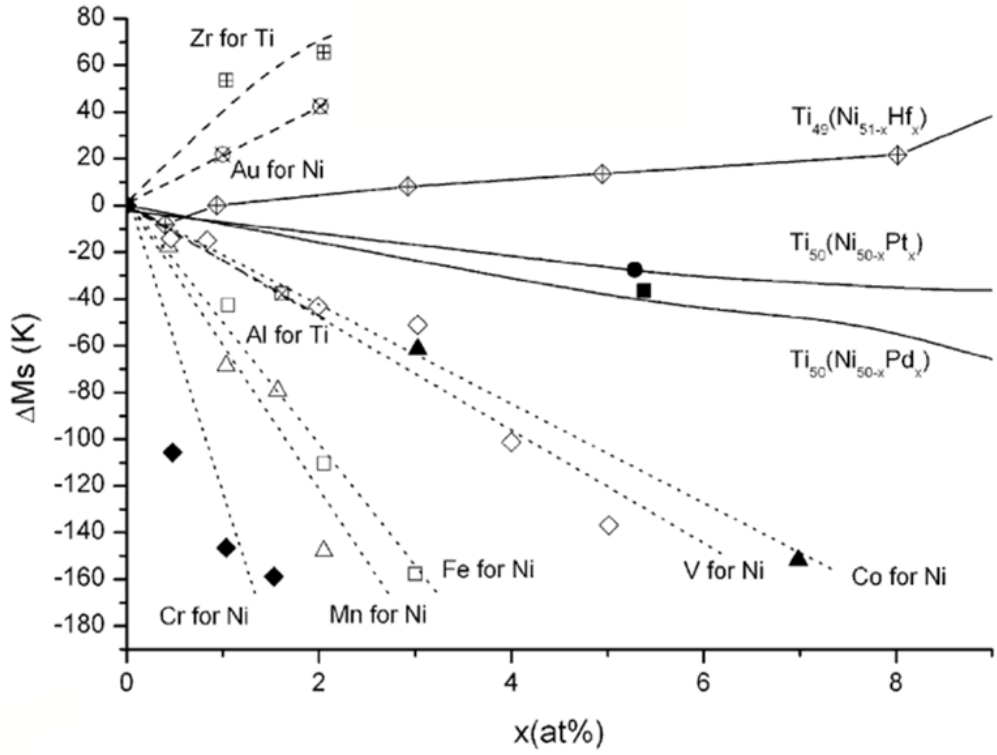

Figure 1.6: Change in martensitic start temperature with change in concentration of a ternary element to NiTi. Adapted from [1].

Fewer studies report on the addition of a fourth element to NiTi SMA with a varying third element. Following is a summary of some of the quaternary SMA systems prepared in bulk form found in literature. For Ni-Ti-Fe-Ta and Ni-Ti-Fe-Nb, the role of Nb and Ta on grain morphology was evaluated. The authors report an increased yield strength, decreased plasticity, decreased transformation temperatures, one- and two-step cooling and heating phase transformations, respectively [99]. Influence of Co on Ni-Ti-Nb was investigated to have a reduction in transformation temperature and lattice parameter, increase in yield strength,

and a recoverable strain of 7.8% [23]. Thermomechanical processing was employed to improve super-elasticity in Cu-Al-Mn-Ni [100]. For Ti-Nb-Mo-Sn, tensile and thermal cycling show stable SME at room temperature with a martensite transformation temperature at 261 K and a recoverable strain of 4.8% [101]. Impact of Al addition was studied on the corrosion and electrochemical behavior of Co-Ni-Ga magnetic SMA [102]. Another Co-Ni-Ga system was studied for the addition of Cr and reported to increase the phase transformation temperature [103]. In Cu-Al-Mn-Ti, Cu_2AlTi precipitates were shown to stabilize stress induced martensite from Cu_2AlMn parent structure [104]. Improved fatigue properties were demonstrated for the bulk quaternary Ni-Ti-Cu-Co alloy when it was cycled through 10 million stress-strain cycles [3, 52]. Quaternary alloys of Ni-Ti-Cu with Cr, Fe, and V were evaluated for crystallographic compatibility by Jaeger et al who showed correlation between thermal and mechanical hysteresis with crystallographic fit as well as the generation of irreversible strains in SMAs [79]. Zarnetta et al optimize synthesis conditions for near-zero thermal hysteresis in Ni-Ti-Cu-Pd [12]. Finally, superelastic stability of Ni-Ti-Cu-V at low transformation temperatures was tested in a custom built elastocaloric cooling device [105–107]. This is also a rare instance of obtaining a large latent heat with small thermal hysteresis for a combined set of improved properties.

In order to explore a wider range of compositions for shape memory effect and improved functional properties as well as stability, thin film SMAs are produced as composition spreads using combinatorial magnetron sputtering. Some systems re-

ported in literature include the high-throughput characterization and visualization of large XRD datasets using a novel software which was first demonstrated using Si-Sn-Co-C [108]. For the Ti-Ni-Cu-Pd system, high-throughput characterization was used to screen compositions having zero thermal hysteresis and scaled up for subsequent bulk testing [12,51]). Two crystallographic compatible Ni-Ti-Cu-Co thin films of specific compositions were studied for stability when subjected to thermal and superelastic cycling. A small grain size was reported to be critical for limiting defect generation in addition to crystallographic stability [77]. Another study reports on the decrease in both the M_s and latent heat in Ni-Ti-Cu-Co [51].

Despite all these studies, however, there remains a gap in the systematic investigation of material properties based on composition, especially as very limited compositions have been investigated. This work seeks to synthesize, characterize, and systematically investigate the phase transformation behavior in ternary and quaternary SMA materials libraries for solid state cooling, thermal energy storage, and shape memory applications.

1.5 Shape memory alloys as phase change materials (PCMs)

NiTi-based SMAs were recently demonstrated as solid state, ultrahigh performance metallic PCMs by harnessing their reversible martensitic transformation [109]. Latent heat associated with this solid to solid transformation is indicative of the thermal storage capacity with the figure of merit (FOM) for developing SMA

materials suitable for thermal energy storage (TES) applications described by Lu as:

$$FOM = \rho \times L \times \kappa_{HT} \tag{1.4}$$

where ρ is density, L is latent heat of transformation and κ_{HT} is the high-temperature-phase thermal conductivity [110]. I use this information to evaluate the thermal conductivity of the SMAs I synthesized and thus, their potential for deployment as thermal energy storage systems in the form of phase change materials.

1.6 Combinatorial materials science for materials discovery and development

Thin film libraries allow access to greater composition spreads, which, when combined with high-throughput analysis techniques, provide the ability to rapidly screen materials for specific applications [111]. Termed as combinatorial materials science, it offers a powerful, accelerated approach to discovering new materials by further coupling with machine learning techniques (Figure 1.7). We can understand the correlation between physical properties and composition as a systematic evaluation of parameters of interest which can then be manipulated to fine-tune the functionalities of materials through concurrent sample synthesis and high-throughput experimentation (HTE) [4]. Over the last few decades, it has led to an efficient exploration and design of functional alloys with targeted properties [112]. Some

advantages of applying combinatorial studies to thin films in particular instead of bulk alloys are:

1. Composition spreads spanning entire composition spaces are possible
2. Facilitates easy screening via high-throughput characterization, reducing the time between alloy discovery and development and eventual deployment
3. Many parameter spaces can also be rapidly explored
4. Thin films offer the advantage of amorphization of alloys, which leads to smaller grain sizes that are in turn useful for mechanical properties [1]
5. Promising compositions can then be scaled up for bulk studies.

Materials libraries employed in this work consist of hundreds of compositions within a 3-inch (76.2 mm) silicon (Si) wafer having a concentration and thickness gradient from concurrent sputter deposition of a given number of elements. Fundamental properties of composition and structure are sequentially characterized using wavelength dispersive spectroscopy (WDS) and synchrotron X-ray diffraction (XRD), respectively. Automation of property measurement is central to the high-throughput experimentation methodology along with data analysis and visualization capabilities. Machine learning techniques of clustering and rapid basis pattern deconvolution process of non-negative matrix factorization (NMF) were employed to simplify classification of materials from the large data sets to map and determine

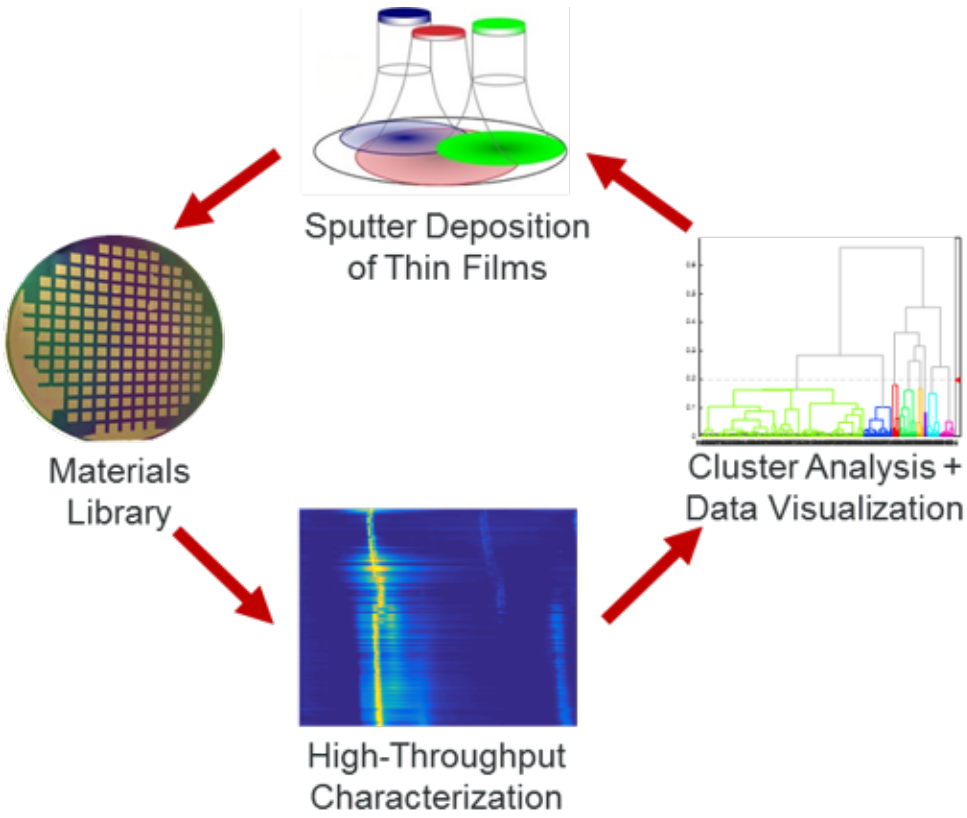

Figure 1.7: Combinatorial materials science uses high-throughput experimentation for the discovery and development of new materials. Magnetron co-sputter technique was used to synthesize thin film libraries on 3-inch substrates which are characterized rapidly using XRD, XPS, and *R(T)*. The large data sets from these are analyzed using machine learning which allows the determination of a phase map.

composition-structure-property relationships [113–115]. These are elaborated upon in chapters 2, 3, 4, and 5.

1.7 Research objectives

The overall goal of this project was to investigate the impact of addition of a third and fourth element on transformation properties of Ni-Ti and Ni-Ti-Cu- based alloys towards the design and development of elastocaloric cooling and thermal

energy management materials. This goal can be divided into the following main efforts:

1. Fabrication of thin film libraries:

   Combinatorial synthesis of high purity ternary and quaternary thin film libraries covering a large compositional space using magnetron co-sputtering system. Libraries of Ni-Ti-X (where X = Co, Hf, Pd, V) and Ni-Ti-Cu-Y (where Y = Co, Fe, Pd, V) were fabricated.

2. Employ high-throughput characterization techniques to determine:

   (a) Chemical composition

   (b) Structure

   (c) Shape memory effect $\rightarrow$ determine phase transformation temperatures

   (d) Thermal conductivity and latent heat

3. Map composition-structure-property relationships:

   To create composition-structure-property maps from the large high-throughput datasets using machine learning. These will be used to determine relationships between each category to aid in the adaptive design and development of materials with targeted properties.

4. Create experimental databases:

   Compile and classify the large datasets into an easy-to-access reference database.

1.8 Dissertation outline

This dissertation explores phase transformation in different shape memory alloys in thin film form using combinatorial materials science. It began with an introduction of shape memory alloys in this chapter, a description of the methods used to synthesize and investigate them in chapter 2, followed by focused descriptions of findings from specific alloys systems as case studies in chapters 3, 4, and 5. I conclude with a summary of the highlights and recommendations for future studies.

Chapter 2: Experimental approach

Experiments were carried out at facilities at the University of Maryland, College Park and collaborator institutions of SLAC Stanford National Accelerator Laboratory, Ruhr University Bochum in Germany (RUB), and industry partner, Kratos Analytical, Inc. Wafer orientation in all experiments was such that the long flat edge was positioned at the bottom with the first set of 5 sample pads labeled 1 to 5 situated parallel to the edge from left to right (Figure 2.1). This eased and streamlined data management.

2.1 Thin film synthesis with sputter deposition

Quaternary thin film composition spreads between 150 and 250 nm thick were deposited on 3-inch (76.2 mm) thermally oxidized (2 μm SiO_2) Si wafers (thickness 400 μm, IWS) in vacuum (base pressure: 5×10^{-7} Torr, 6.6×10^{-5} Pa) magnetron sputtering system at room temperature. Sputtering rates and deposition time were controlled to achieve a targeted composition range. High purity (99.98 %) elemental targets of 1.5-inch (38.1 mm) diameter were sputtered using DC (Seren IPS), RF

(Advance Energy) power sources and ultrahigh purity argon (Ar, 99.9997%, Airgas) deposition pressure of 5 $\times$ 10^{-3} Torr (0.67 Pa) (Figure 2.1a, 2.1b). Each wafer was covered with a patterned Si mask to delineate 177 individual compositions evenly across the wafer at a Δx, Δy of 4.5 mm; an index number map for the compositions in a library is shown in Figure 2.1c. Substrate was water cooled to avoid crystallization during sputter deposition and to maintain low temperatures. Figure 2.2 depicts the different components in a sputtering chamber with the water lines, target and substrate positions [6]. The resulting films were annealed in vacuum without atmospheric exposure at two conditions: 500 °C for 1 hr and 700 °C for 15 min with a heating rate of 60 °C/min and ±4 °C, as determined to be appropriate for crystallization of binary NiTi thin films [116]. Deposition rates were determined for each element used in this work under a given power source for a preset time and are listed in Appendix Table M.1. Thickness from step height was measured using atomic force microscopy (AFM, Digital Instruments Dimension 3100 AFM system) as shown in Figure 2.3. Based on the calibrated deposition rates listed in Appendix Table M.1 and the density of each element, the required power ratio to achieve a desired composition was determined and listed in Appendix Tables N.1 – N.4. Total time for synthesis and annealing a thin film library is 2 hours before it is ready for characterization.

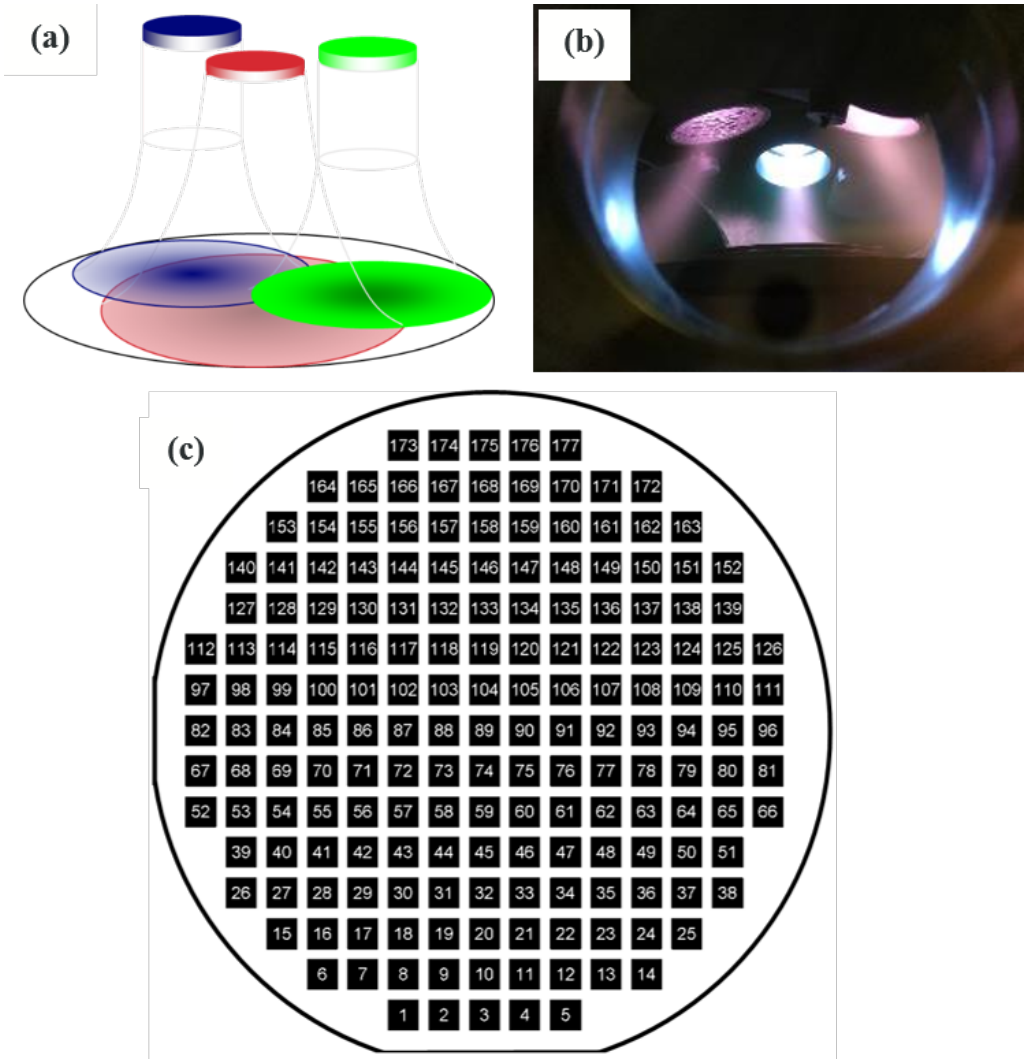

Figure 2.1: (a) Schematic courtesy of Dr. T. Gao showing multi-target co-sputtering, (b) image of sputter deposition in progress, and (c) index number map of thin film library on a 3-inch wafer with long flat edge at the bottom.

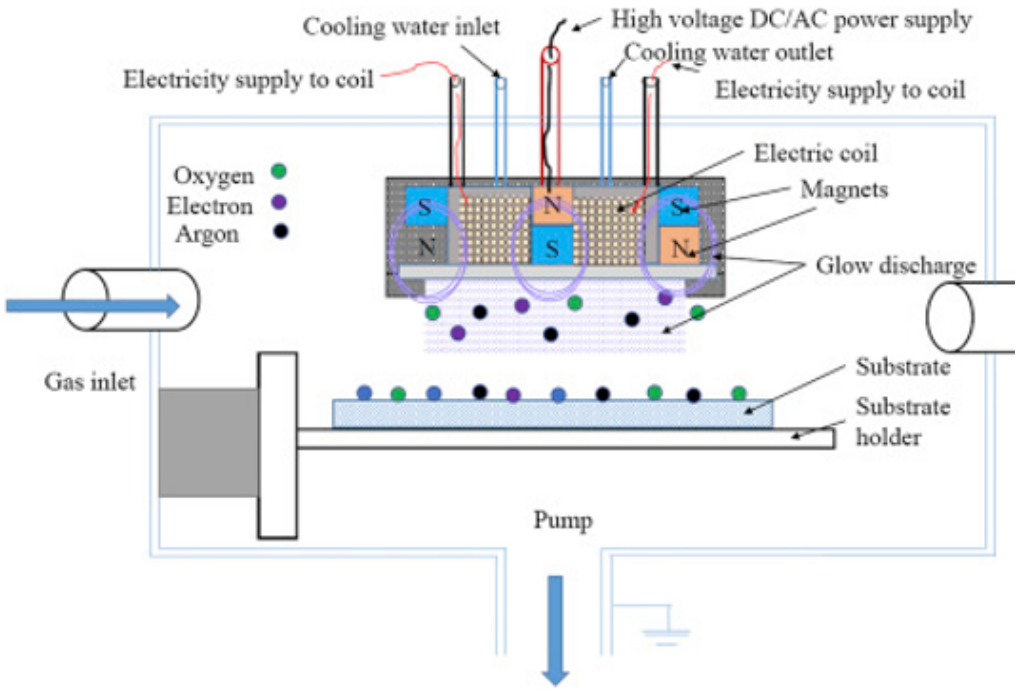

Figure 2.2: Schematic adapted from [6] showing basic chamber components for magnetron sputtering.

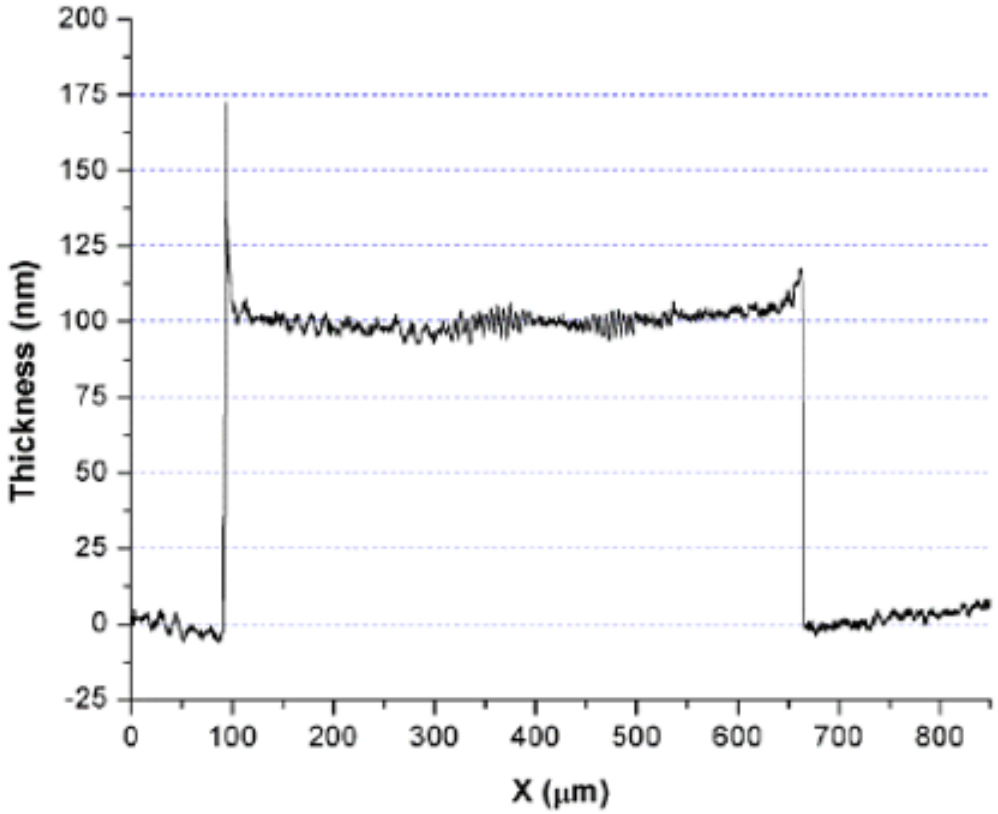

Figure 2.3: Film thickness measured by a profilometer or atomic force microscope.

2.2 High-throughput measurements

Combinatorial materials science is facilitated by the development of rapid and accurate measurement techniques to characterize large numbers of samples in parallel. Automation of these measurements sidesteps the otherwise labor-intensive and time-consuming task of performing investigations in a serial and manual manner. The following subsections elucidate the experimental details of characterization techniques used to measure composition, structure and phase transformation properties with wavelength dispersive spectroscopy, X-ray diffraction, 4-point probe and scanning hot probe microscopy. High-throughput X-ray photoelectron spectroscopy (XPS) measurements were performed by Jonathan Counsell at Kratos Analytical Inc. in the United Kingdom and provide insights on local chemical bonding behavior in the Ni-Ti-Co library. These are presented extensively in Appendix G.

2.3 Chemical composition from wavelength dispersive spectroscopy (WDS)

Composition variation in the thin film libraries as well as bulk samples were determined using wavelength dispersive X-ray spectroscopy (WDS) analysis in an electron probe microanalyzer (EPMA) JXA 8900R Microprobe, with an acceleration voltage of 15 kV. Standardization of references was carried out with pure metal references and compositions were determined to be within an experimental error of <0.3 at.%. WDS was selected over energy dispersive spectroscopy (EDS) due to its higher accuracy and precision in quantifying elemental content via better energy resolution from peak/background ratio [117].

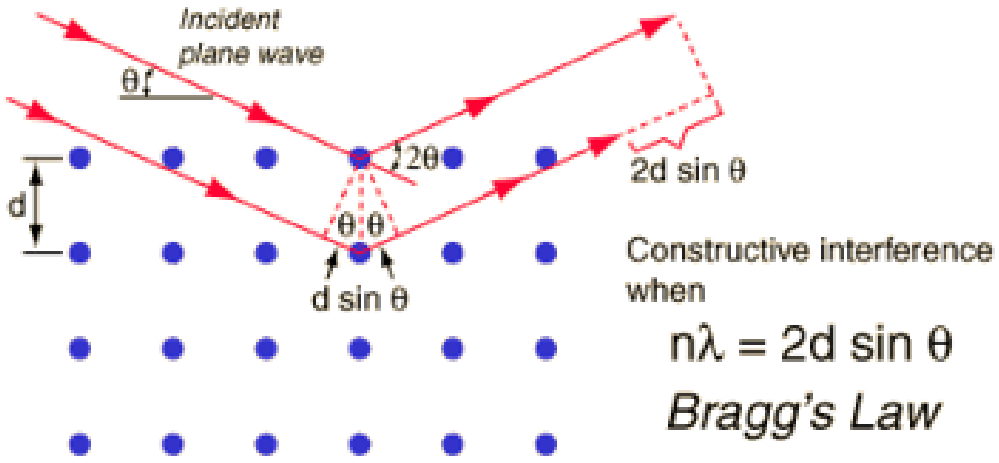

Figure 2.4: Bragg's law adapted from [7].

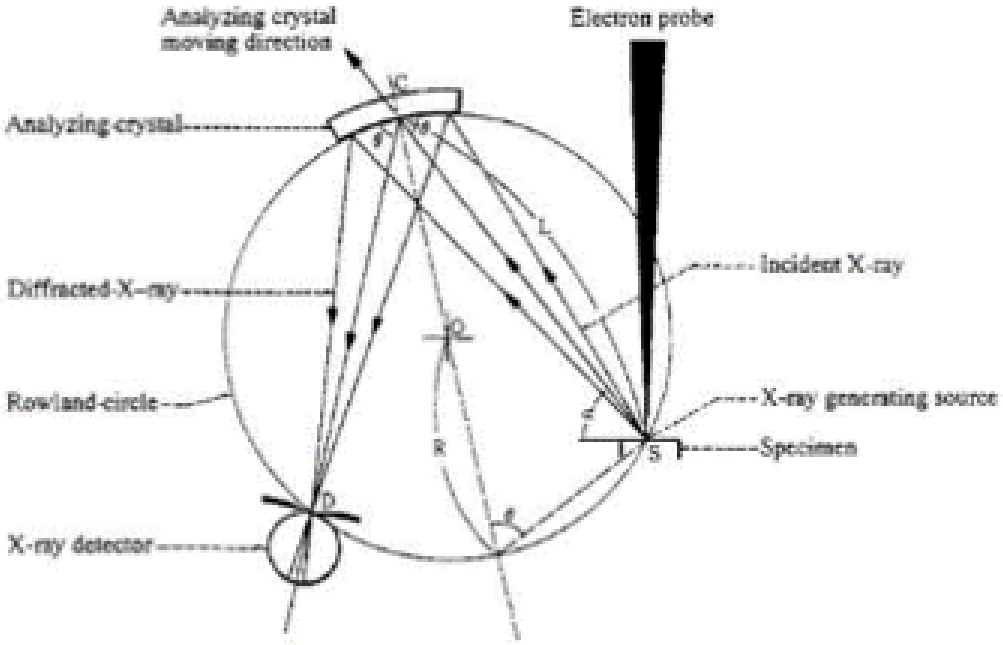

Figure 2.5: Rowland Circle from [8].

When a filament (thin coiled wire) of tungsten (W) is heated to ∼2500 K, some electrons acquire enough thermal energy to overcome the attractive forces in the material, resulting in ejection of electrons in the form of a current flowing away from the material. In an EPMA, these electrons form into a beam, hit the sample, excite electrons from various energy shells in the sample and form characteristic x-rays that can be used to distinguish the elements present in a sample. Characteristic x-rays produced at the sample reach the analyzing crystals which have a well-defined d-spacing. X-rays that fulfill Bragg's Law (shown in Figure 2.4) diffract off the crystal [7, 118]. The sample, analyzing crystal, and detector (gas flow proportional counter) must all lie on a geometrical construction called the Rowland Circle (Figure 2.5). One can alter the diffracted wavelength by moving the analyzing crystal and detector along the Rowland Circle [8, 9].

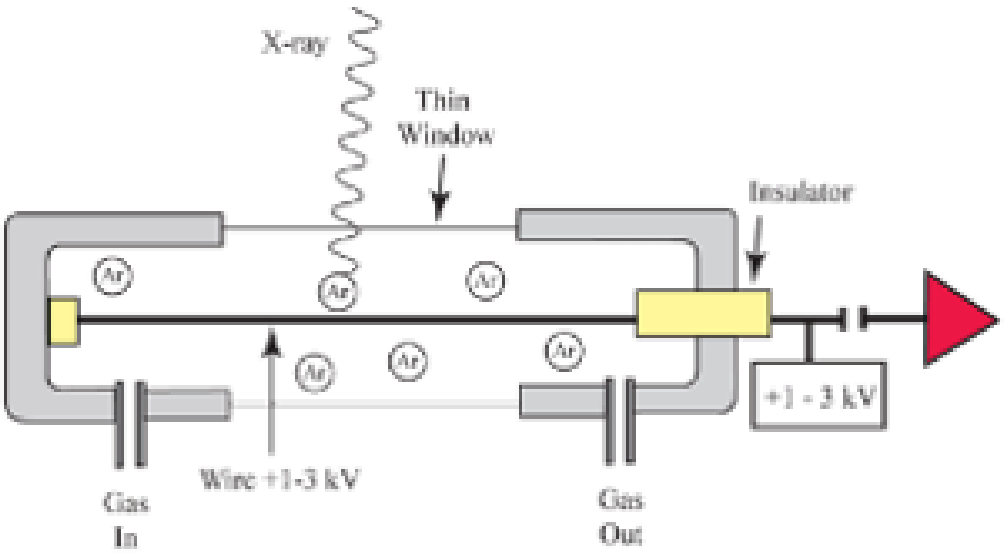

Figure 2.6: Gas flow proportional counter from [9].

After characteristic x-rays are produced at the sample and diffract off the analyzing crystal, they penetrate through a thin window into a gas flow proportional counter (Figure 2.6). The x-rays ionize gas atoms inside the proportional counter. The wire inside the gas flow proportional counter is positively biased (electrically), while the walls of the gas flow proportional counter are negatively biased (electrically). Therefore, the positive ions are accelerated towards the wall and the produced electrons hit the wire, and the current is measured. This current can be used to determine the counts of each element present [9, 119].

2.4 Crystal structure analysis with synchrotron X-ray diffraction (XRD)

Structural information was obtained at room temperature by collecting two-dimensional XRD patterns on the combinatorial library at beamline 1-5 at Stanford Synchrotron Radiation Lightsource (SSRL). The experiment was performed with

14.99 keV energy collimated to ∼0.3 mm × 0.3 mm beam size and a wavelength of 0.82657 Å (0.82657×10^{-10}m). MarCCD detector (Rayonix) was used to collect the data at an exposure rate of 30 s. Thus, a library of 177 samples could be completely measured within 2 hours. To minimize influence of diffraction from the silicon substrate, the library was scanned with a small grazing incidence angle of 1-2°. The grazing incidence geometry resulted in an approximate 3-mm probe footprint on the library. An automated algorithm was used to measure the entire library with a step size of 4.5 mm. For data analysis, the geometric parameters of 2D detector such as the direct beam position, tilting, rotation and sample to detector distance were extracted from measuring standard LaB_6 powder pattern. These parameters were used to transform initial raw images that were acquired as a function of Q and χ in diffraction coordinate into one-dimensional (1D) diffraction patterns by integrating and normalizing over the χ angle. Bragg angle (2θ) is related to scattering vector (Q) by the relationship:

$$Q = 4 \times \pi \times \frac{sin\theta}{\lambda} \tag{2.1}$$

with wavelength (λ), helping to generate a more traditional 1 dimensional spectrum of intensity vs. 2θ.

2.5 Cluster analysis of high-throughput XRD data

An unsupervised machine learning algorithm was used as an exploratory data analysis tool as well as a phase mapping tool. Hierarchical cluster analysis (HCA)

was performed using Pearson Correlation Coefficient (PCC) clustering model with criteria for similarity and dissimilarity between input data, such that data grouped into a cluster share similar characteristics in comparison with data in other clusters [120]. An example of a HCA solution in the form of a dendogram is shown in Figure 2.7.

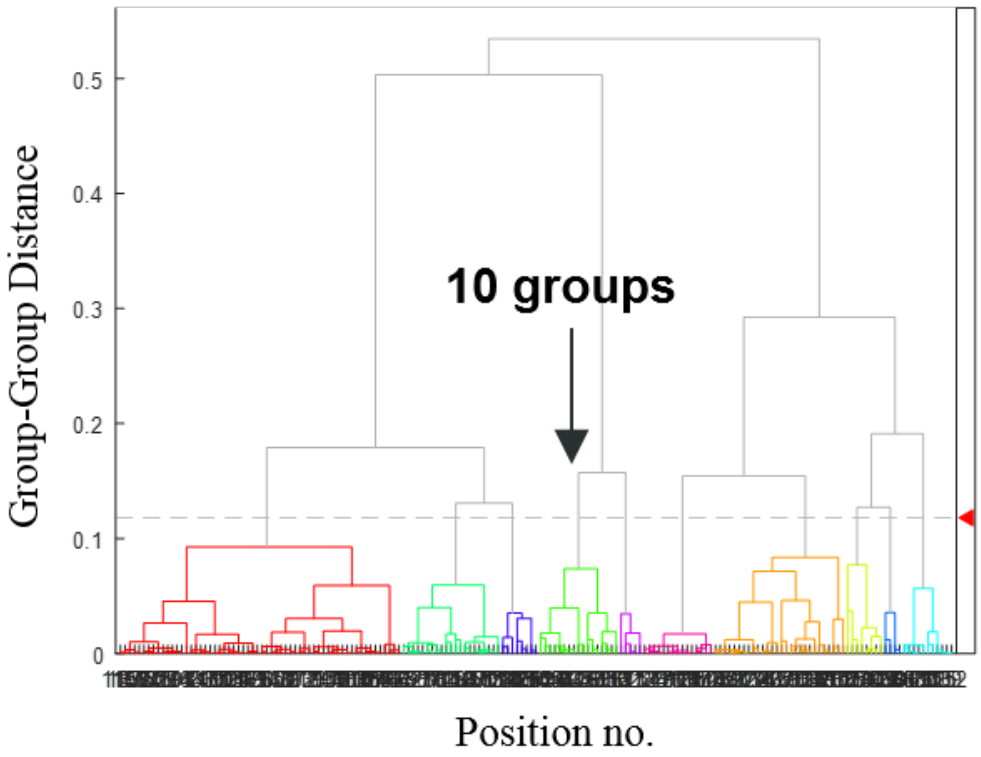

Figure 2.7: HCA groups patterns based on similarities such that each vertical line in a dendogram solution represents a cluster of patterns.

For two spectra x and y having means $\overline{x}$ and $\overline{y}$, the distance metric for similarity is given by $D = \frac{1}{2}$ (1 - C_{xy}) where C_{xy} is the Pearson correlation coefficient clustering model defined as [113]:

$$C_{xy} = \frac{\sum_{i=1}^{n}(x_i - \overline{x})(y_i - \overline{y})}{[\sum_{i=1}^{n}(x_i - \overline{x})^2 \sum_{i=1}^{n}(y_i - \overline{y})^2]^{\frac{1}{2}}} \tag{2.2}$$

Different groupings based on the D values are shown in Figure 2.8. It was applied to the diffraction patterns using CombiView which is a MATLAB-supported data visualization platform developed by the Takeuchi group [121].

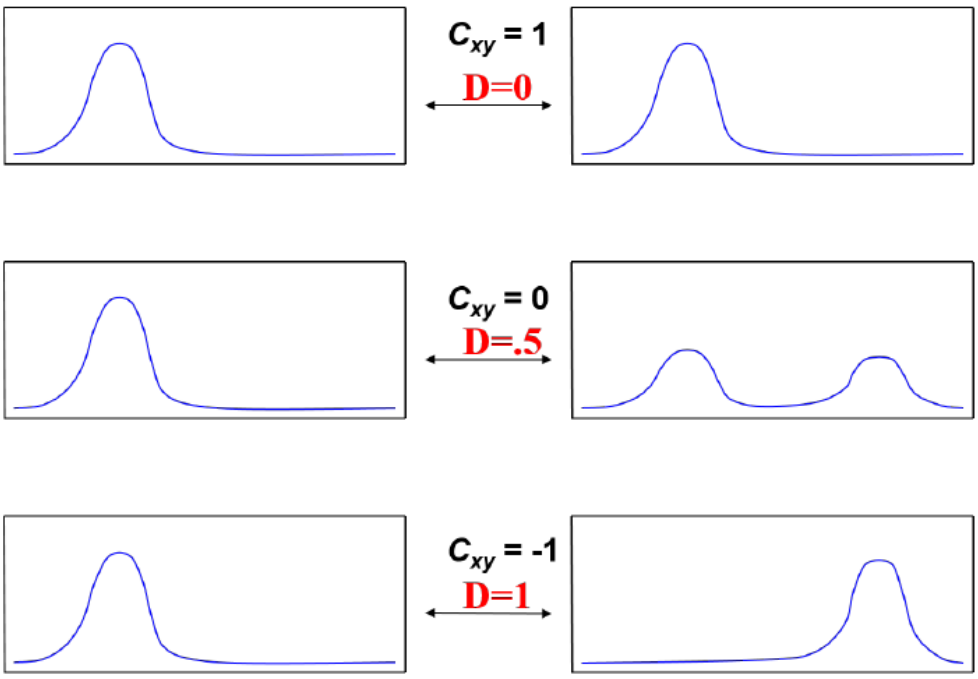

Figure 2.8: Distance metric values and corresponding grouping of XRD patterns from the Pearson Correlation Coefficient [10].

Representative diffraction patterns from the clusters were then analyzed for peak assignment using Bruker's DIFFRAC.EVA software versions 3.1, 4.0 and 5.2

to match peaks from powder diffraction file (pdf) reference patterns from the International Centre for Diffraction Data (ICDD) database [122].

2.6 XRD pattern analysis for phase identification

Patterns down selected from unsupervised machine learning were evaluated using Bruker's DIFFRAC.EVA versions 3.1, 4.0 and 5.2 software for phase identification from peak analysis, in conjunction with the International Center for Diffraction Data's (ICDD) data mining software, PDF-2 (Powder Diffraction File) database [122, 123]. The procedure is as follows: a text file is created from the 1D XRD data for each sample position within a library. The text file is uploaded into EVA v4, the background is accounted for by adjusting the curvature between 0.020 and 0.048 with a threshold of 0.005 and then selecting only the relevant elements to narrow the search within the database.

2.7 High-throughput X-ray photoelectron spectroscopy (XPS)

XPS analyses were carried out with a Kratos Axis NOVA spectrometer using a monochromatic Al K-α source (30 mA, 15 kV). XPS can detect all elements except hydrogen (H) and helium (He). It probes the surface of the sample to a depth of 5-7 nm and has detection limits ranging from 0.001 to 0.5 at.% depending on the element/matrix. The instrument work function was calibrated to give a binding

energy (BE) of 83.96 eV for the Au 4f7/2 line for metallic gold and the spectrometer dispersion was adjusted to give a BE of 932.62 eV for the Cu 2p3/2 line of metallic copper. Elemental binding energies are listed in Table 2.1. The Kratos charge neutralizer system was used on all specimens. Survey scan analyses were carried out with an analysis area of 300 $\times$ 700 μm and a pass energy of 160 eV. High resolution analyses were carried out with an analysis area of 300 $\times$ 700 μm and a pass energy of 20 eV. Spectra have been charge-corrected to the main line of the carbon 1s spectrum (adventitious carbon) set to 285.0 eV (operating conditions: base pressure 4 $\times$ 10^{-10} Torr or 5.3 $\times$ 10^{-8} Pa; operating pressure during depth profiles 2 $\times$ 10^{-8} Torr or 2.6 $\times$ 10^{-6} Pa).

Photoelectron Peak	**Binding Energy (eV)**
Ni 2p	853
Co 2p	778
O 1s	530
Ti 2p	455
C 1s	285

Table 2.1: XPS species and associated binding energies.

For quantification, Shirley background subtraction removed the contribution of inelastically scattered electrons. For chemical state analysis, peaks were fitted with symmetric Gaussian-Lorentzian components using the ESCApe data system and were quantified using modified Wagner relative sensitivity factors. Spatial distribution plots were performed using the ESCApe data system whereby a series of analysis points can be created either freehand or as a grid. The spectra were analyzed as grouped data post quantification. A Delaunay triangulation is fitted onto the acquisition locations [124]. A linearly interpolated color scheme is then applied

to each triangle based on the vertex values, each of which represents an acquired atomic concentration value.

Depth profiling was performed using 4 kV monatomic Ar^+ ions; ion-beam flux ~5.8 μA with a crater raster area of 2 mm × 2 mm. Selected area spectroscopy (110 μm) was employed to limit the possibility of crater edge effects and ion beam inhomogeneities. Typical acquisition times for survey and high-resolution spectra are 1 minute each with 2 hours for depth profiles. Chemical composition determination from WDS, in contrast, takes 6 hours total.

2.8 Non-negative matrix factorization (NMF) of XPS and XRD data

Non-negative Matrix Factorization (NMF) method was used to automate the analysis of XRD data. NMF results in basis components which often directly represent the diffraction spectra of the different crystal structures, while the corresponding weights reflect the abundance of each structural phase at a given composition [125]. The goal of NMF is to obtain a factorization of the observational data matrix X combining all measured diffraction spectra as:

$$X = WH + \epsilon \tag{2.3}$$

Each of the measured spectra is formed by a linear mixing of K unique but unknown basis components forming the matrix W (Figure 2.9) [11]. The values of H

correspond to the contribution of each basis component to the spectrum measured at a given point in composition space. Since both factor matrices W and H are unknown, and even their size K (i.e., the number of basis components) is unknown, the problem is under-determined. Nevertheless, NMF can be obtained by minimizing the Frobenius norm $\frac{1}{2}||X - W \times H||_F^2$ or the Kullback–Leibler (KL) divergence $D(X||W \times H)$ [114, 126, 127]. Extending NMF to XPS datasets is straightforward, and all the properties that make it an attractive XRD decomposition tool transfer to XPS data analysis, confirming experimental analysis.

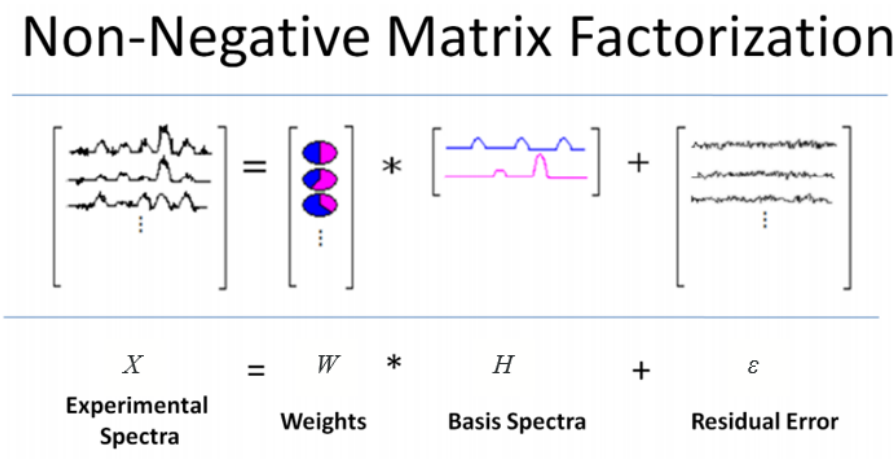

Figure 2.9: Pattern deconvolution using NMF to find basis spectra. Adapted from [11].

2.9 Four-point probe resistance-temperature *R(T)* measurements

Film resistance as a function of temperature $R(T)$ was measured to determine transformation temperature parameters of A_s, A_f, M_s, M_f, and ΔT (A_f – M_s) as crystal structure changes correspond with measurable electrical changes. Sheet resistance is independent of sample geometry and was measured using a four-point probe method described by van der Pauw in a customized high-throughput test stand (Figure 2.10) with an automated platform of 5 sets of 4-point probes [128–130]. Spacing between probe tips is 500 μm and test stand is enclosed in a box purged with nitrogen (N_2) gas (Figure 2.11). Measurements were performed between -40 °C and 120 °C with a heating/cooling rate of 5 °C/min and 50 mA source current.

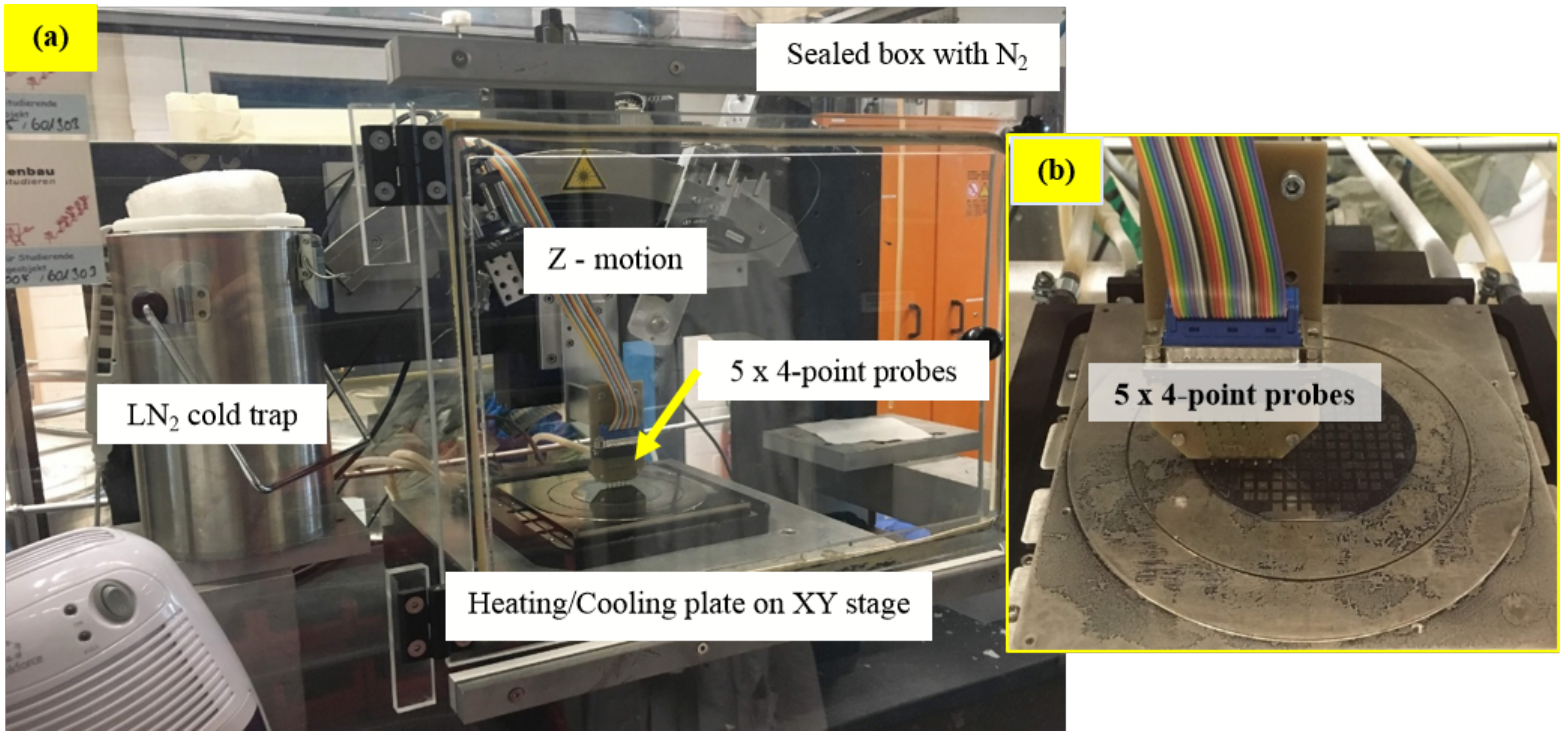

Figure 2.10: (a) High-throughput automated test stand on a passive damping table to measure temperature- dependent resistance, enclosed in a box purged with nitrogen. (b) Image showing detail of probe head with 5 sets of 4 probes.

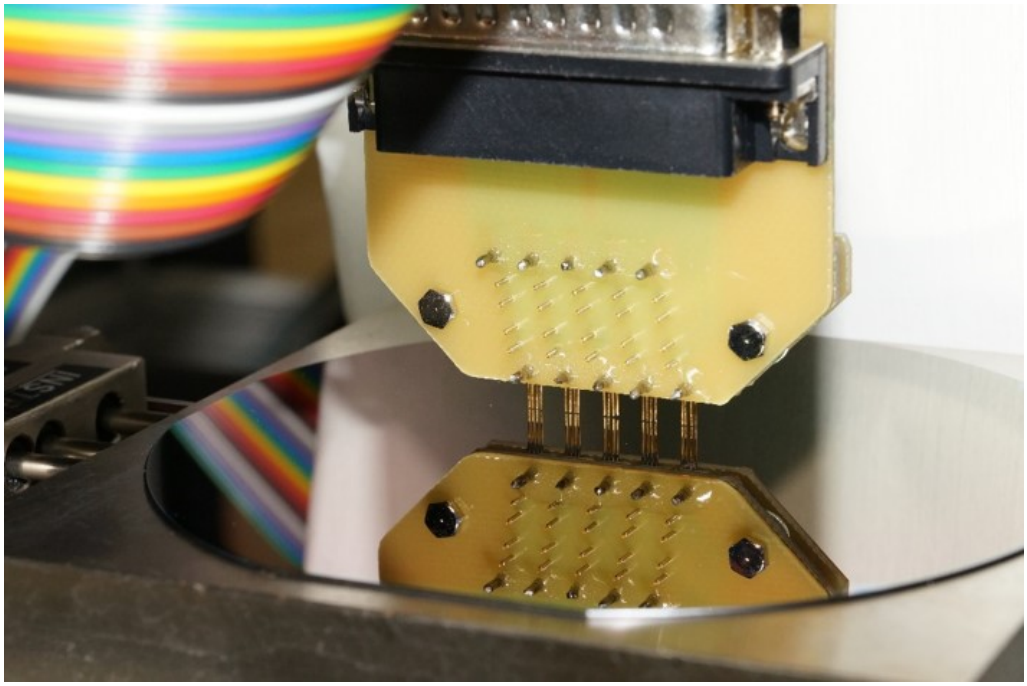

Figure 2.11: Image showing detail of probe head with 5 sets of 4-point probes.

The tangent method is used on an $R(T)$ curve to determine A_s, A_f, M_s, M_f, and ΔT (A_f – M_s) as shown in Figure 2.12 [12]:

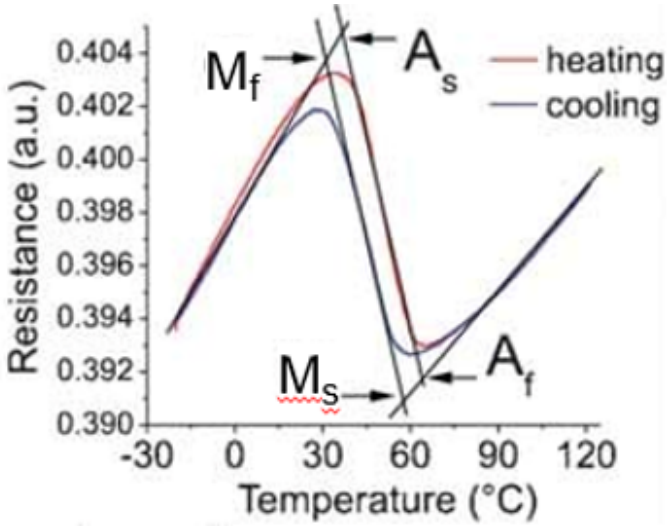

Figure 2.12: A typical $R(T)$ curve for an alloy with reversible phase transformation. The tangent method is shown which is used to determine the temperatures indicating phase transformation. Adapted from [12].

2.10 Thermal conductivity measurements using scanning hot probe (SHP)

In this work, I use scanning hot probe (SHP) as an extension of scanning thermal microscopy (SThM) fitted on the tip of a modified atomic force microscope probe (Figure 2.13) to characterize thermal conductivity of combinatorial thin films on a Si substrate [131, 132] . It is based on Joule heating of a small filament to localized heating to a nano- or microscale region. The probe tip used in this work is comprised of a thin palladium (Pd) filament on a silicon nitride (Si_3N_4) cantilever

that is Joule-heated, and its electrical resistance is monitored such that the probe acts both as a heat source as well as a temperature sensor [131–134]. When the probe is heated far away from a sample, the electrical resistance of the probe changes with the filament's temperature coefficient of resistance [13, 132]. The probe temperature decreases when in contact with a sample which can be used to determine the thermal properties of the sample once the probe tip is properly calibrated. A representative schematic of the system used for characterization in this work is shown in Figure 2.13.

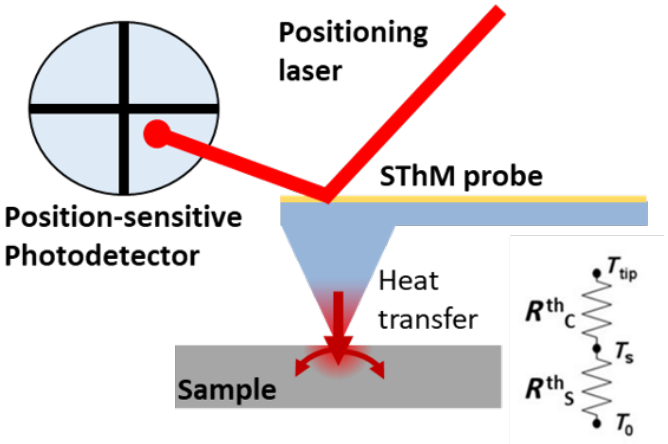

Figure 2.13: Schematic of a scanning hot probe. Image courtesy of A. Wilson, ARL.

To accurately characterize thermal conductivity of materials, the scanning hot probe must be appropriately calibrated. Figure 2.14 depicts the heat transfer mechanisms away from the probe, which must be accounted for.

To account for probe-to-ambient heat loss (including convective and radiative losses as well as heat loss to the contacts), a Wheatstone bridge circuit configuration is utilized with two reference resistors in one leg and the probe and a varistor in the other leg. The bridge is balanced (such that resistance and current across both

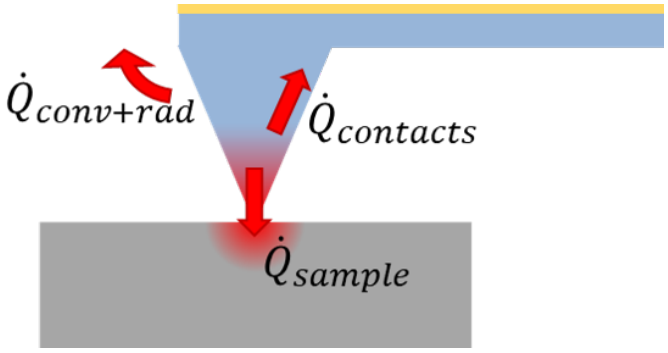

Figure 2.14: Schematic depicting heat flow from the probe. Image courtesy of A. Wilson, ARL.

legs are equal) with the probe far from the sample, which effectively sets the "no heat transferred to sample" resistance at the applied power to the circuit. When the probe is brought into contact with the sample, some of the heat being generated by the probe is absorbed by the sample, which reduces the probe's resistance and changes the measured voltage difference across the reference and sample legs of the circuit. Since the difference was zero when the probe was far from the sample, the change in resistance may be attributable to heat transfer to the sample. Rebalancing the bridge before each measurement ensured consistent treatment of the data in our measurements.

The SHP method was carried out using Bruker GLA1 probes with an Anasys SThM system attached to a Veeco NanoMan atomic force microscope (AFM) with radiation shielding (Figure 2.15). Environmental conditions of room temperature (RT) and humidity are recorded at the beginning of experiments. After all equipment was powered on and connected, a small (0.25V) output voltage was applied to the probe (such that negligible heat was generated by the probe) for a time ahead of measurement to allow capacitive effects of the power supplies and electrical

connections to settle. Room temperature and humidity were recorded within the radiation shield of the AFM, near the sample, and changes in room temperature were accounted for in the probe's resistance via the manufacturer's specified value of thermal coefficient of resistance (TCR) of 0.003 1/°C [134, 135]. When ready for measurement, the output voltage to the probe was changed to 1.25V (corresponding to ∼1 mA) and with no sample mounted (or the probe lifted far from the sample where there was no heat transfer to the sample), the Wheatstone bridge circuit was balanced as described before. Then the probe was brought into contact with the sample in an area free of dust and debris, and after an initial 500 nm scan size, on a relatively flat area, the scan size was set to zero, and the probe voltage was recorded. The probe was then lifted and moved to another spot on the sample and this process was repeated for two to three data points per sample. This procedure was used for both the reference samples as well as the combinatorial film samples. Additional details can be found in Chapter 5.

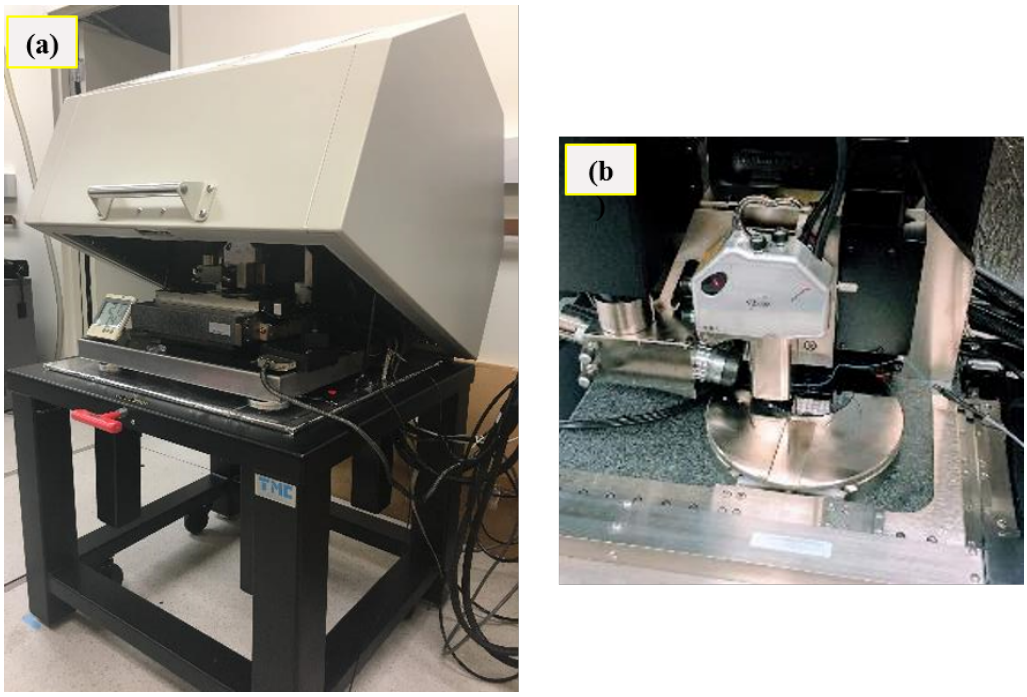

Figure 2.15: (a) AFM set up with a radiation shield and scanning hot probe mounted; (b) x-y movable stage has a 3 inch wafer loaded for measurement.

A summary of the alloy systems and high-throughput characterization techniques used in this study is shown in Figure 2.16 along with the measured properties.

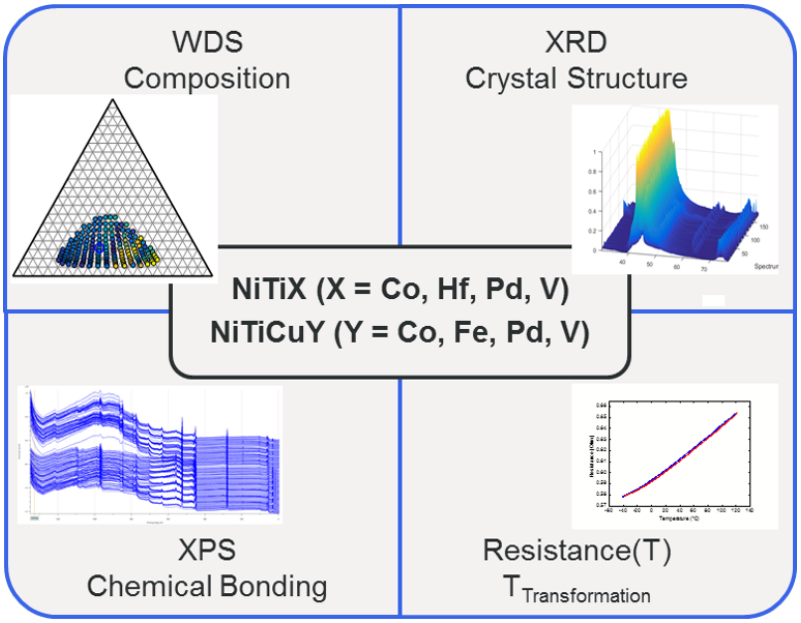

Figure 2.16: A summary of SMAs and high-throughput characterization techniques used in this study along with the measured properties.

Chapter 3: Phase transformation in Ni-Ti-Co thin film library

Combinatorial synthesis and high-throughput characterization of a Ni-Ti-Co thin film materials library is reported for exploration of reversible martensitic transformation. The library was prepared by magnetron co-sputtering, annealed in vacuum at 500 °C without atmospheric exposure and evaluated for shape memory behavior as an indicator of transformation. A new, expanded composition space having phase transformation with low thermal hysteresis and Co >10 at.% is found. Through cluster analysis of XRD data, I identified and mapped the constituent structural phases. Composition-structure-property maps for the ternary system are made to correlate the functional properties to the local microstructure and composition of the Ni-Ti-Co thin film library. These findings were recently published in *ACS Combinatorial Science* [136].

3.1 Introduction

A co-sputtered Ni-Ti-Co thin film library is investigated for SME through the evaluation of the phase transformation. First reported in 1975 [137], the Ni-Ti-

Co alloy has since found wide applications: as a component of permanent magnets [138–140], high-entropy alloys [141, 142], shape memory alloys [24], and superalloys [143, 144] along with substantive use in biomedical applications [37–47]. The addition of Co to NiTi has been shown to reduce the M_s and A_s temperatures in combination with the Ni content; it has also been shown to increase yield strength [145, 146]. These improvements are sought out in elastocaloric cooling technology where ambient transition temperatures and small thermal hysteresis are desired [92]. Until now, investigations on the structural phases, mechanical properties, elastic properties, and phase transformation behavior that have been reported for Ni-Ti-Co involved one-by-one bulk preparation that covered a limited composition space, with addition of Co investigated only up to 10 at.% [47, 147–156]. A more comprehensive study of the ternary system by Zhou et al, to determine the liquidus surface projection at 1373 K also involved one-by-one bulk preparation of 35 alloys. They evaluate the microstructure and different crystallographic phases present but do not report on the mechanical or transformation properties of Ni-Ti-Co [157]. To the best of my knowledge, no systematic investigations of phase transformation in Ni-Ti-Co alloys, both in bulk and thin-film form that probe a greater composition space, have been reported thus far. Hence, this study aims to fill this information gap in identifying composition regions having martensitic phase transformation, with a focus on small thermal hysteresis.

To quickly identify the compositions that transform in the ambient temperature range, a Ni-Ti-Co composition spread was synthesized using magnetron co-

sputtering and its composition-structure-property was mapped with high-throughput characterization. Unsupervised machine learning methods were used to both manage the large data sets acquired and analyze them efficiently [113, 114]. The composition was determined using wavelength dispersive spectroscopy (WDS). I also evaluated the use of X-ray photoelectron spectroscopy (XPS) as a high-throughput chemical characterization technique; an automated, typical WDS measurement of a 177-sample library takes about 6 hours whereas total acquisition time for XPS survey scans for the same sample library requires only half the time. Although surface effects and corrosion behavior of NiTi-based bulk as well as thin-film systems have been previously studied with XPS [37, 148, 158–160], I report on systematic high-throughput XPS characterization and an indexed spectral database for Ni-Ti-Co. Using synchrotron X-ray diffraction (XRD) and high-throughput four-point probe temperature-dependent resistance *R(T)* measurements, I report on the microstructure, phase diagram, and martensitic transformation behavior of Ni-Ti-Co alloys. I also report on phase transformation in compositions beyond $Ni_{50-x}Ti_{50}Co_x$ (x = 0 to 10 at.%). Furthermore, I identified a composition space with small thermal hysteresis (ΔT) that is promising for higher transformation efficiency and long-term stability.

3.2 Experimental results

Figure 3.1 shows a ternary elemental plot of the compositional range covered in this study. With an x-y scanning table and characterization tools, the library was spatially analyzed, which offers another way to visualize data. An image of the materials library and corresponding labeled wafer positions are shown in section 3.5 of the chapter supplementary information (SI) Figure S3.4a and S3.4b, respectively. Throughout the paper, I will use both methods to facilitate understanding of the different insights; experimental details are provided at the end.

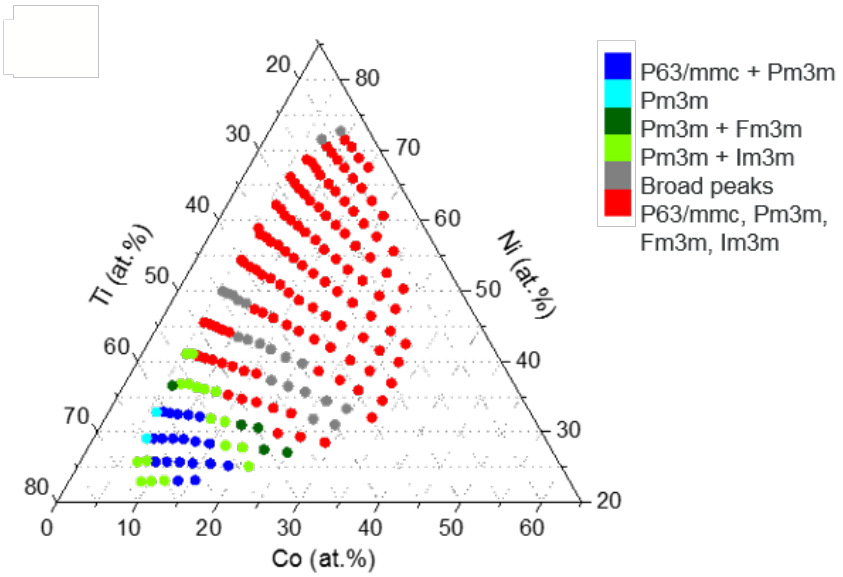

Figure 3.1: Ternary plot of Ni, Ti, and Co determined from high-throughput WDS. Compositions are grouped by color based on results from the Pearson Correlation Coefficient (PCC) hierarchical clustering model. Compositions grouped inside gray ellipses were determined to transform through an intermediate structure.

3.2.1 Characterization of chemical composition

Chemical composition determined from WDS shows elemental concentrations of 22.8 at.% < c(Ni) < 72.8 at.%, 17.6 at.% < c(Ti) < 68.2 at.%, and 5.4 at.% < c(Co) < 33.2 at.%. Distribution of the elements by wafer position is shown in SI Figure S3.2a-c; these match the configuration of the targets inside the deposition chamber. The center of this library on the wafer has a composition of $Ni_{46.2}Ti_{40.1}Co_{13.7}$. Compositions with the highest and lowest Ni content are $Ni_{72.6}Ti_{18.6}Co_{8.8}$ and $Ni_{23}Ti_{68}Co_9$, highest and lowest Ti are $Ni_{23}Ti_{68}Co_9$ and $Ni_{67.5}Ti_{17.7}Co_{14.8}$, and highest and lowest Co are $Ni_{34.4}Ti_{32.5}Co_{33.1}$ and $Ni_{45.5}Ti_{49}Co_{5.5}$, respectively. Additionally, I obtained crystallographic evidence for carbide and oxide phases of Ti. Chemical composition data from WDS and XPS agree qualitatively for Ni and Ti distributions shown in Figures S3.5a, b and S3.5d, e. Slight difference observed in the spatial distribution of Co (Figures S3.5c and S3.5f) may be associated to a surface energy effect as XPS captures chemical activity present in the top 10 nm. In addition to differences in sampling depths, the variation in Co distribution may also be due to local surface aggregation of Co for a particular alloy blend. Despite the reduction in measurement time from XPS, I use WDS compositions going forward due to its higher accuracy and precision in quantifying elemental content. I do, however, use oxidation state mapping from XPS to understand crystallographic trends in the following sections.

3.2.2 Transformation temperature from 4-point probe measurements

Compositions in the library were screened for phase transformation using a high-throughput four-point probe measurement system as measurable electrical changes accompany crystal structural changes during phase transformation [129, 161]. I successfully identified compositions with phase transformation and narrow ΔT in the ambient temperature range. Film sheet resistance as a function of temperature, $R(T)$, was measured between -40 °C to 120 °C. Austenitic start (A_s), austenitic finish (A_f), martensitic start (M_s) and martensitic finish (M_f) temperatures were determined by applying the tangent method to the $R(T)$ curves, as demonstrated in the inset of Figure 3.2a. The first-order martensitic transformation is associated with a thermal hysteresis (ΔT) that reduces the reversibility of the transformation. This hysteresis is a result of energy dissipation due to frictional work and plastic accommodation during lattice distortions [54, 67, 68, 162]. The hysteresis width determines the energy loss and inefficiency of the transformation such that a narrow width favors sustained reversibility [62]. Thermal hysteresis is determined by the difference between austenitic finish (A_f) and martensitic start (M_s) temperatures.

The $R(T)$ curves obtained can be divided into three categories – (1) linear, non-transforming curves with increasing slopes, (2) non-linear, transforming curves (Figure 3.2a) and (3) linear, non-transforming curves with decreasing slopes (examples are highlighted with a black box in SI Figure S3.6). Linear $R(T)$ curves with

increasing slopes showing no transformation were obtained for most of the library. Of the 177 compositions measured, 31 were observed to have reversible transformation behavior and hence, shape memory effect; these are listed by ascending Ni content in Table 3.1. Composition regions with SME at Co content greater than 10 at.% were identified for the first time. SME was observed in an elemental range for Ni from 25.8 to 70.5 at.%, Ti from 21.4 to 64.3 at.%, and Co from 5.5 to 26.4 at.%, respectively. Temperature ranges observed for martensite start, austenite finish and thermal hysteresis were -25.2 °C $< M_s <$ 106.5 °C, -23.2 °C $< A_f <$ 140.4 °C, and 0.7 °C $< \Delta$T $<$ 131.2 °C, respectively. Distribution of thermal hysteresis is shown in Figure 3.2b. Four compositions with 5.9 at.% $<$ c(Co) $<$ 18.3 at.% were observed to have ΔT between 0.5 and 2.1 °C with the higher Co composition transforming at higher temperatures (M_s = 106.5 °C, A_f = 107.9 °C). Average A_f and M_s temperatures are around 79.6 °C and 14.4 °C, respectively, which are essential for SMA use in ambient temperatures. Some transformation pathways were incomplete in the evaluated range as seen from the missing Ms values in Table 3.1.

These results are important as SME has been reported in bulk compositions of $Ti_{50}Ni_{50-x}Co_x$ (x = 2, 4, 6, and 8) but not observed for $Ti_{50}Ni_{40}Co_{10}$ measured at liquid nitrogen temperature [40, 151]. Addition of Co preferentially substitutes Ni up to 14 at.% which has been shown to reduce the M_s. Although only a slight reduction in M_s is observed, our observations are overall in agreement with previous reports demonstrating addition of Co to reduce A_s and M_s through substitution of Ni [146]. Seven compositions were determined to have phase transformation through

an intermediate structure (dotted, Figure 3.1). These are not listed in the table as additional nano-characterization measurements and temperature-dependent XRD are needed to verify these observations. Nonetheless, a two-step transformation has been previously reported for bulk Ni-Ti-Co and is also well known to occur in NiTi as well as ternary systems such as TiNiCu, TiNiFe and TiNiMo [61, 147, 163–166].

Ni	**Ti**	**Co**	M_s	A_f	$A_f - M_s = \Delta$**T**
[at. %]			**[°C]**		
25.8	63.5	10.7	-10.3	73.1	83.5
29.1	64.3	6.6	-25.2	-23.2	2.0
29.1	63.5	7.4	-	-8.3	8.3
29.8	47.7	22.5	-	83.9	83.9
32.8	61.3	5.9	-4.9	-2.8	2.1
32.9	60.4	6.7	-15.0	-14.3	0.7
35.2	51.2	13.6	58.0	95.8	37.9
35.7	52.4	11.9	-	79.6	79.6
37.3	36.3	26.4	0.8	61.1	60.3
38.6	38.3	23.1	15.5	79.4	64.0
39.7	39.7	20.6	10.6	109.9	99.3
42.5	43.6	13.9	-	72.9	72.9
45.3	48.4	6.3	-8.8	95.9	104.7
46.4	27.9	25.7	2.0	81.9	79.9
49.6	44.0	6.4	40.4	116.8	76.4
51.4	26.4	22.2	1.3	78.6	77.2
53.0	27.5	19.5	-12.8	78.5	91.3
54.0	39.8	6.2	22.8	109.7	86.9
54.4	40.0	5.7	24.8	94.2	69.4
58.9	35.6	5.5	29.7	140.4	110.6
59.3	25.8	14.9	0.7	95.8	95.0
59.5	22.2	18.3	106.5	107.9	1.5
60.0	31.0	9.0	19.3	99.0	79.7
60.7	26.4	13.0	-2.4	104.8	107.2
60.7	31.4	7.9	3.3	105.3	102.0
61.8	26.6	11.5	-6.3	104.3	110.6
65.3	27.9	6.8	73.5	111.0	37.5
67.4	24.2	8.4	16.1	104.0	87.8
68.2	24.3	7.5	5.2	107.7	102.6
68.6	24.7	6.6	-24.9	106.2	131.2
70.5	21.4	8.2	19.6	69.5	49.9

Table 3.1: Composition, martensitic start (M_s), austenitic finish (A_f), and thermal hysteresis (ΔT) determined from $R(T)$ for ternary Ni-Ti-Co SMA library by ascending Ni content.

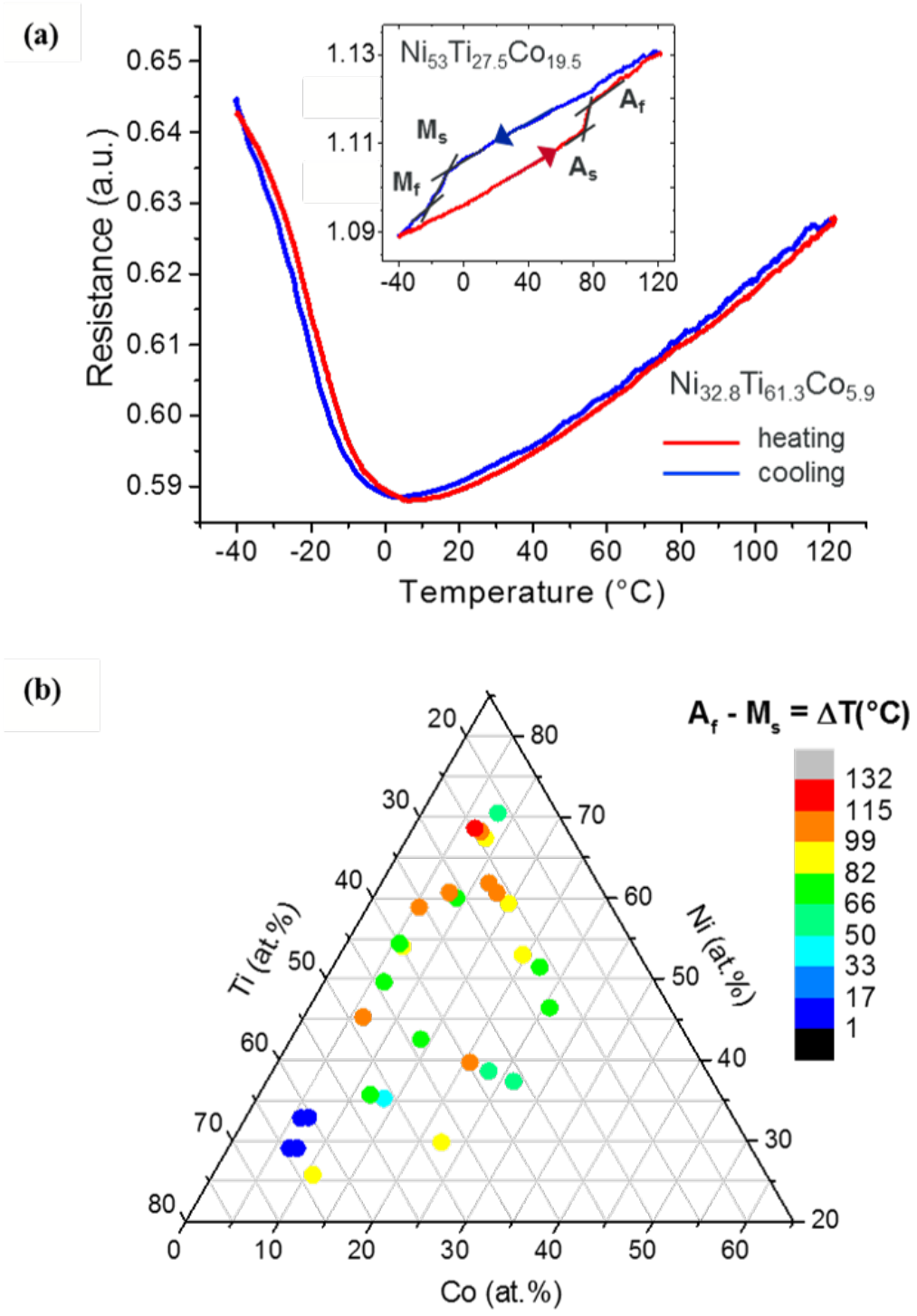

Figure 3.2: (a) $R(T)$ curve for $Ni_{32.8}Ti_{61.3}Co_{5.9}$ showing near-zero thermal hysteresis. Inset shows the tangent method to determine phase transformation temperatures A_s, A_f, M_s, and M_f from $R(T)$ curve for $Ni_{53}Ti_{27.5}Co_{19.5}$ alloy showing reversible phase transformation with large thermal hysteresis. (b) Distribution of thermal hysteresis $\Delta T = A_f - M_s$ in °C as a function of composition. Color scale bar from blue to red indicates small to large temperature widths.

3.2.3 Crystal structure and phase determination through cluster analysis

MATLAB based data visualization platform CombiView allows linking of sample composition with its XRD and XPS spectral patterns (SI Figure S3.7) and was used to perform the hierarchical cluster analysis on the XRD data (SI Figure S3.8) [121]. An initial cluster analysis resulted in 32 groups. Upon refining and combining cluster groups based on number of low intensity peaks, six groups were determined consisting of 16 phases (see space group in Table 3.2). Representative XRD patterns were analyzed using EVA4 XRD software from Bruker and matched against the International Centre for Diffraction Data (ICDD) database [122]. Results of the cluster analysis and phase distribution in a ternary composition plot are shown in SI Figure S3.8b-c and Figure 3.1, respectively. Selected diffraction patterns representing phases present in the six groups defined by PCC are shown in Figure 3.3. Crystal structures identified in this alloy library are listed in Table 3.2. Depending on where a composition was in the thermal cycle of the transformation, I expected to identify cubic, monoclinic or orthorhombic structures for compositions exhibiting phase transformation. Most common crystal type present was cubic austenite structure $Pm3m$ in the form of NiTi or $Co_{0.15}Ni_{0.85}Ti$ crystal types and present in a single phase in only two compositions, $Ni_{29.1}Ti_{64.3}Co_{6.6}$ and $Ni_{32.8}Ti_{61.3}Co_{5.9}$ (positions 163 and 172, light blue cluster in Figure 3.1) – both of these also had near-zero thermal hysteresis $R(T)$ curves. The $Pm3m$ phase is

present predominantly in a mixture with other cubic phases $Im3m$ and $Fm3m$, shown as dark green, light green and red groups in Figure 3.1. These were observed to have linear, non-transforming $R(T)$ curves (SI Figure S3.6). For compositions in the Ni-rich region, mixed phases of hexagonal (prototype Ni_4In) and cubic (prototypes TiV, Co_2NiGa, $Co_{0.5}Ni_{0.5}Ti$, and $GaTiCo_2$) crystal structures were present, seen in red in Figure 3.1. Rhombohedral Ni_2Ti and Ni_4Ti_3 structures were also identified, and it was noted that NiTi is present in cubic, monoclinic, and hexagonal forms. For compositions with SME discussed in the previous section, both single phase and a mixture of cubic with orthorhombic structures were identified as seen from light and dark blue patterns in Figure 3.3. A mixture of hexagonal NiTi and cubic $(Co_5NiTi_4)_{0.2}$ for wafer position 162 (WDS composition $Ni_{32.9}Ti_{60.4}Co_{6.7}$) also exhibited transformation with near-zero thermal hysteresis. It is important to note that this is a qualitative, not quantitative assignment. Similarly, for wafer position 90 (WDS composition $Ni_{42.5}Ti_{43.6}Co_{13.9}$) where a potential two-step transformation was observed, a mixture of hexagonal $Ti(Co_{1.5}Ni_{1.5})$ and cubic $Pm3m$, $Im3m$ structures of the prototypes $Co_{0.807}Ge_{0.123}W_{0.070}$ and $Cr_{0.875}Ti_{0.125}$ were identified. Since our library explores a composition space not yet reported, these and other prototype structures listed in the table provide an understanding of the type of crystal structures that may be present as I could not match every XRD peak with a listing in the ICDD. Finally, the gray cluster in Figure 3.1 is defined by a non-crystalline phase in which broad peaks were observed in the 2-theta (2θ) range of 40° to 48° (gray pattern in Figure 3.3) that corresponded with linear, non-transforming $R(T)$ curves characterized by decreasing slopes. The cluster forms a phase boundary sepa-

rating NiTi – $NiTi_2$ double phase for compositions rich in Ti (dark blue in SI Figure S3.8c), that follows a distribution of Ti^{4+} peak observed from XPS mapping (SI Figure S3.9). Although no clear relationship could be drawn between variation of Ni or Co content with phase transformation, crystallographic evidence for SME could be established, in agreement with theoretical and experimental observations reported in literature [37–39, 150, 157, 165]. These results also build on the challenging work associated with determining stable intermediate phases [155].

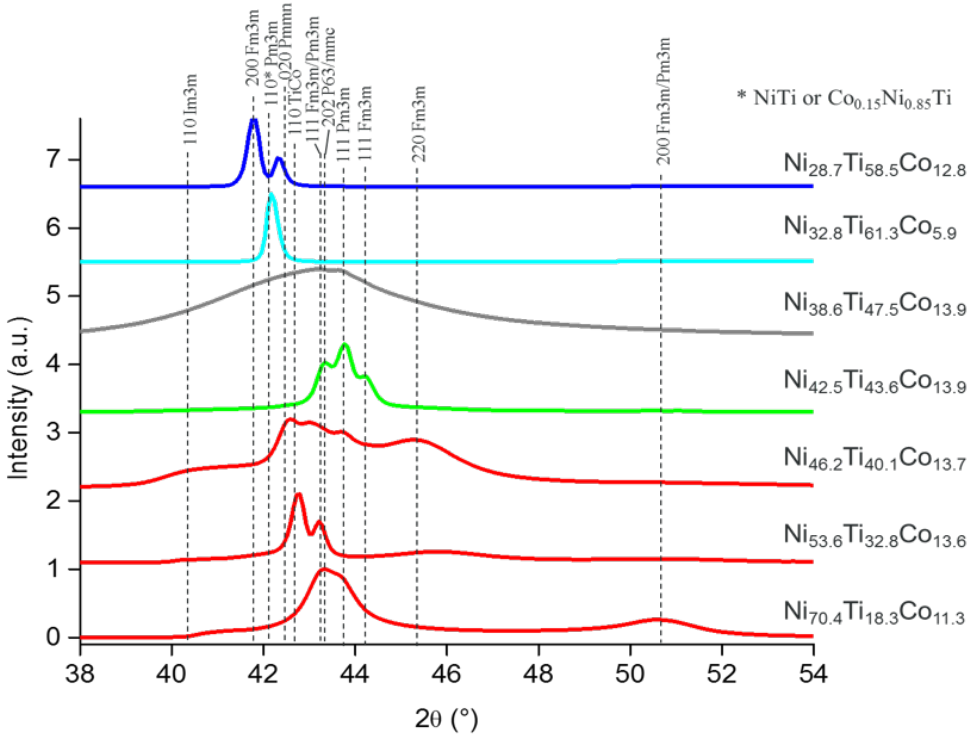

Figure 3.3: Selected X-ray diffraction patterns (wafer positions 94, 172, 91, 90, 89, 87, and 82 from top to bottom) representing phases present in the six clusters identified by PCC arranged in ascending Ni content. Patterns are offset for clarity.

Formula	Space Group	Space Group Number	Prototype
$(CoNi_2)$ Ti	P63/mmc	194	hexagonal
$(Co_{0.15}Ni_{0.85})$ Ti	Pm-3m	221	
$(Co_{0.5}Ni_{0.5})$ Ti	Pm-3m	221	
$(Co_5NiTi_4)_{0.2}$	Pm-3m	221	
$(Ni_{0.875}Co_{0.125})$ Ti	Pm-3m	221	
			tetragonal
	I4/mmm	139	$Al(Cr_{1.818}Ti_{0.182})$
			$Al(Cr_{1.818}Nb_{0.182})$
Co O	Fm-3m	225	
Co Ti	Pm-3m	221	
Co_2 Ge Ti	Fm-3m	225	
			Co2 Ni Ga
Co_2 Ni Ti	Fm-3m	225	Fe Ni
			Mg Ni_2 Sn
Co_2 Ti_4 O	Fd-3m	227	
Co_3 Ti_3 O	Fd-3m	227	
			orthorhombic
	Iba2	45	
			$Cr_{0.9585}$ Ga_2 Sb_2
			Monoclinic
	P1m1	6	
			Fe Ni
Ni Ti	P21/m	11	monoclinic
Ni Ti	P-3	147	hexagonal
Ni Ti	Pm-3m	221	
Ni Ti2	Fd-3m	227	
$Ni_{1.02}$ $Ti_{0.98}$	Pm-3m	221	
Ni_2 Ti	R-3m	166	rhombo.h.axes
Ni_2 Ti_4 O	Fd-3m	227	
Ni_4 Ti_3	R-3	148	rhombohedral
			tetragonal
	I4/m	87	
			Ni_4 W
Ti $(Co_{1.5}$ $Ni_{1.5})$	P63/mmc	194	Co Mn Sn
Ti C	Fm-3m	225	Ti Co Ni Sn
Ti Co	Pm-3m	221	
Ti_4 Ni_2 $O_{0.3}$	Fd-3m	227	
			(Co Ni) Sn_2 Ti_2
	F43m	216	Ti_2 Ni Al
			Ni V
	Im-3m	229	Ti V
			orthorhombic
	Pmam	51	
			Ti $Ni_{0.8}$ $Cu_{0.2}$
			orthorhombic
	Pmmn	59	
			Nb Ni_3

Table 3.2: Crystal structures identified in the Ni-Ti-Co thin film materials library; the default crystal structure type is cubic unless specified otherwise under prototype.

3.3 Discussion

To understand the relationship between composition, structure, and phase transformation, we can now align the data for material properties of the Ni-Ti-Co library across the chemical composition space. Phase transformation was observed in different parts of the composition plot with very little apparent connection to elemental variation. Of all the cubic space groups, transforming compositions are comprised of the $Pm3m$ type in single phase or in mixture with $Fm3m$. While other compositions have similar crystal structures, they do not undergo transformation; this may be due to the presence of other crystal types such as non-transforming cubic and hexagonal phases. It is also difficult to determine exact influence of composition on the presence of a particular crystal type since these are not single phases. Furthermore, the presence of additional phases may demand greater energy for the SME phase to transform, thereby increasing the thermal hysteresis width. This is supported by stable $R(T)$ curves having near zero thermal hysteresis for compositions $Ni_{29.1}Ti_{64.3}Co_{6.6}$ and $Ni_{32.8}Ti_{61.3}Co_{5.9}$ at positions 163 and 172 with a single crystal phase of NiTi or $Co_{0.15}Ni_{0.85}Ti$ types. Fabricating a materials library having smaller concentration gradients and centered around the composition space identified to have narrow hysteresis coupled with temperature-dependent XRD measurements may better elucidate the crystal phase composition of the transforming samples. Additionally, while scale-up of these compositions to verify the narrow thermal hysteresis in bulk is needed, thin films of Ni-Ti-Cu, Ni-Ti-Cu-Co and Ni-Ti-Cu-V have

been successfully scaled up and tested over many cycles [3,12,106]. Abrupt changes in $R(T)$ curves are also observed from one measurement area to the next such that they have linear and/or non-linear curves characterized by decreasing slopes from left to right (Figure S3.6). A cluster of XRD patterns reflects a similar distribution across the wafer and forms a phase boundary separating NiTi – $NiTi_2$ double phase for compositions rich in Ti (SI Figure S3.8c). XPS mapping of the Ti^{4+} peak across the wafer further confirms this observation (SI Figure S3.9). It may be that the annealing time is not long enough to produce large enough crystallites in this area of the materials library. Overall, while it is difficult to draw a definitive relationship between variation of Ni or Co content with phase transformation, I establish crystallographic evidence for SME, in agreement with observations already reported in literature for other Ni-Ti-Co alloys [37–39,150,157,165]. Nonetheless, these results expand on the challenging work of determining stable intermediate phases reported previously [155].

3.4 Summary and conclusions

A combinatorial Ni-Ti-Co thin film materials library covering a large composition space was synthesized using magnetron co-sputtering and annealed at 500 °C for 1 hour in vacuum. Large data sets of composition, transformation temperatures, and crystal structure were obtained from high-throughput WDS and XPS, four-point probe temperature-dependent resistance and synchrotron XRD measure-

ments that enabled rapid materials characterization and screening. Transformation temperatures were probed in the -40 °C to 120 °C range to screen for shape memory alloys that could be used in ambient temperatures applications. By employing combinatorial synthesis and high-throughput experimentation, I demonstrate the effectiveness of the methodology in systematically mapping phase transformation and drawing composition-structure-property relationships. Cross sample position analysis between and within data sets allowed for greater insights and the following observations were drawn:

- Chemical composition space bounded between 22.8 at.% < c(Ni) < 72.8 at.%, 17.6 at.% < c(Ti) < 68.2 at.%, and 5.4 at.% < c(Co) < 33.2 at.% was synthesized
- Phase transformation was observed in compositions beyond the range previously reported as $Ni_{50-x}Ti_{50}Co_x$ (x = 0 to 10 at.%), with Co concentration between 5 – 26 at.%
- A new compositional region having narrow thermal hysteresis (ΔT between 0.5 and 2 °C) centered around 6 at.% Co in Ti-rich regions was identified
- Transforming compositions are composed of mixtures of cubic structures from $Pm3m$ and $Fm3m$ space groups as well as orthorhombic and hexagonal structures
- Non-transforming compositions were characterized by crystalline mixtures of multiple cubic $Pm3m$ phases, $Pm3m$ with $Fm3m$ along with $Im3m$ cubic

phases in addition to non-crystalline phases defined by broad XRD peaks around $2\theta = 40^{\circ}$

- Alloys with distinct XRD patterns for a single cubic phase showed near-zero thermal hysteresis
- Large data sets produced in this work may be used to develop machine learning models for predictive experimentation

In summary, this study highlights a strategy that can be extended to other alloy systems and properties to discover new materials with enhanced functionalities.

3.5 Chapter supplementary information

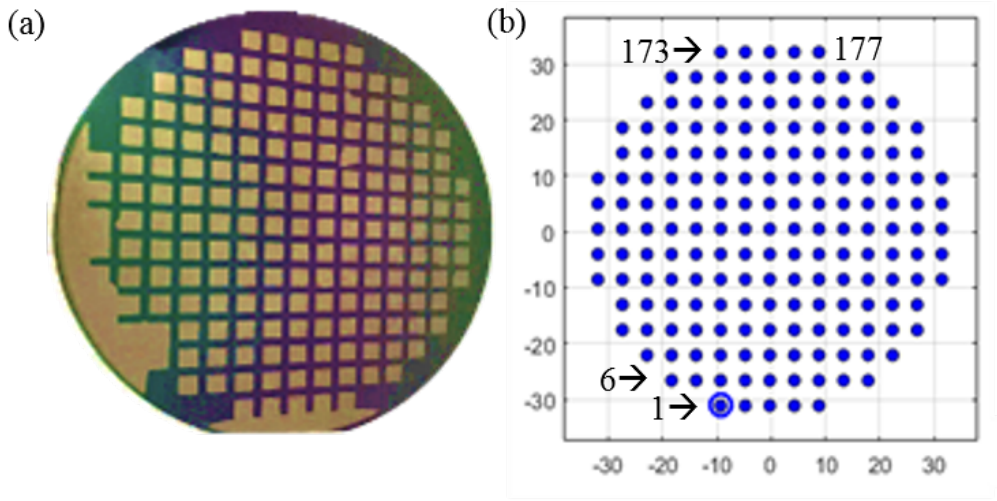

Figure 3.4: (a) Ni-Ti-Co thin film library having 177 samples on a 3-inch SiO_2 wafer, (b) x-y coordinates position map (numbering begins at bottom row 1 – 5, left to right) with the long flat edge of the wafer positioned at bottom.

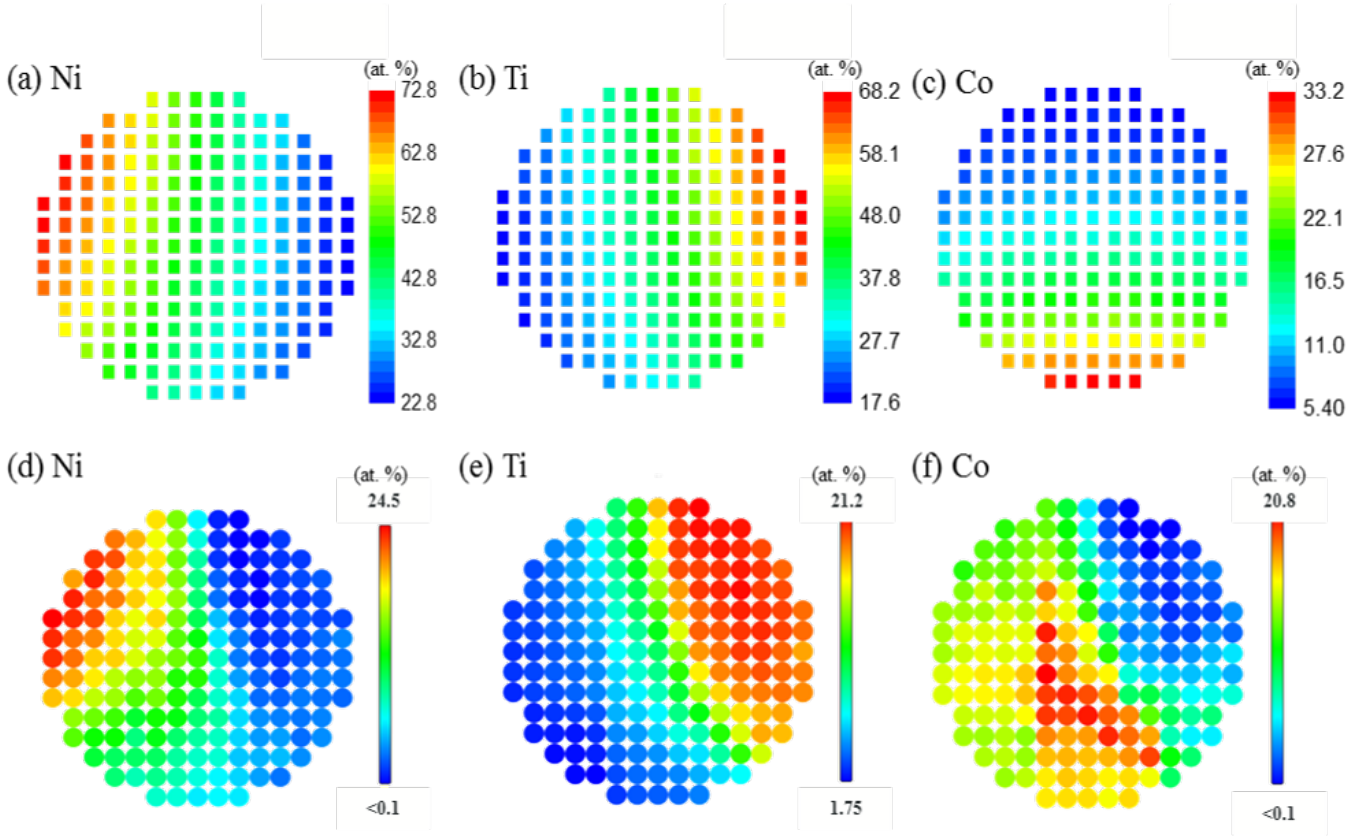

Figure 3.5: Elemental distribution of Ni, Ti, and Co (at.%) determined from high-throughput wavelength dispersive spectroscopy (a, b, c) and X-ray photoelectron spectroscopy (d, e, f) show good qualitative agreement, not quantitative.

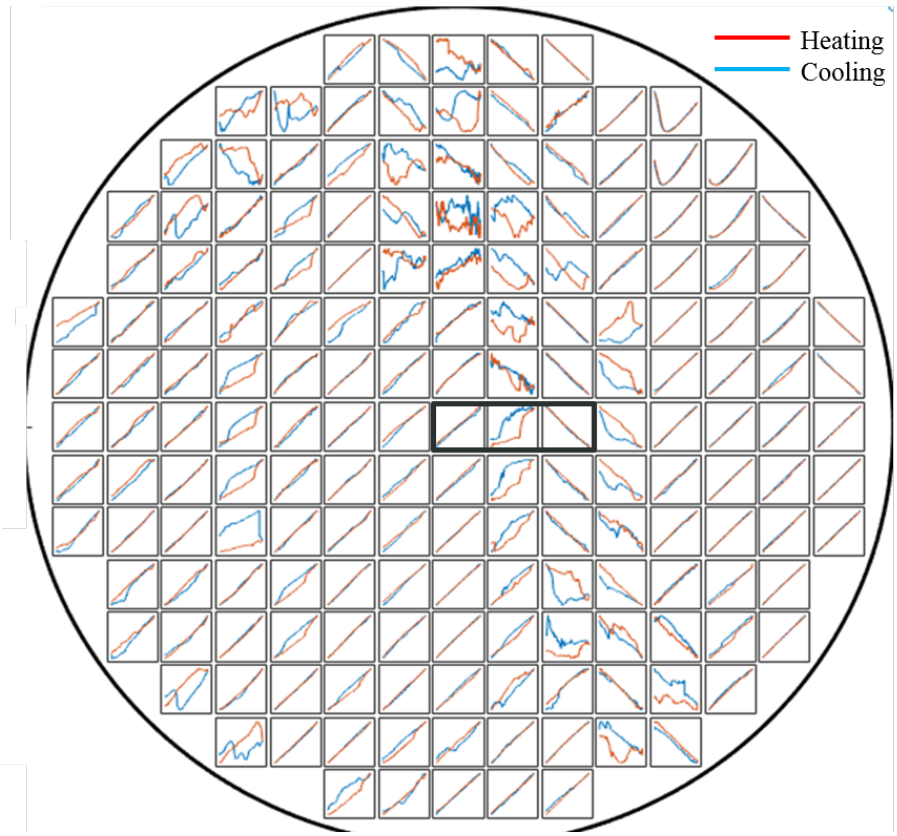

Figure 3.6: Resistance as a function of temperature $R(T)$ curves for the 177 samples by wafer position. Examples of the three types of $R(T)$ curves are highlighted in a black box: (1) linear, non-transforming curves with increasing slopes, (2) non-linear, transforming curves and (3) linear, non-transforming curves with decreasing slopes. Heating and cooling are indicated by red and blue colors, respectively. Long flat edge of wafer is positioned at bottom.

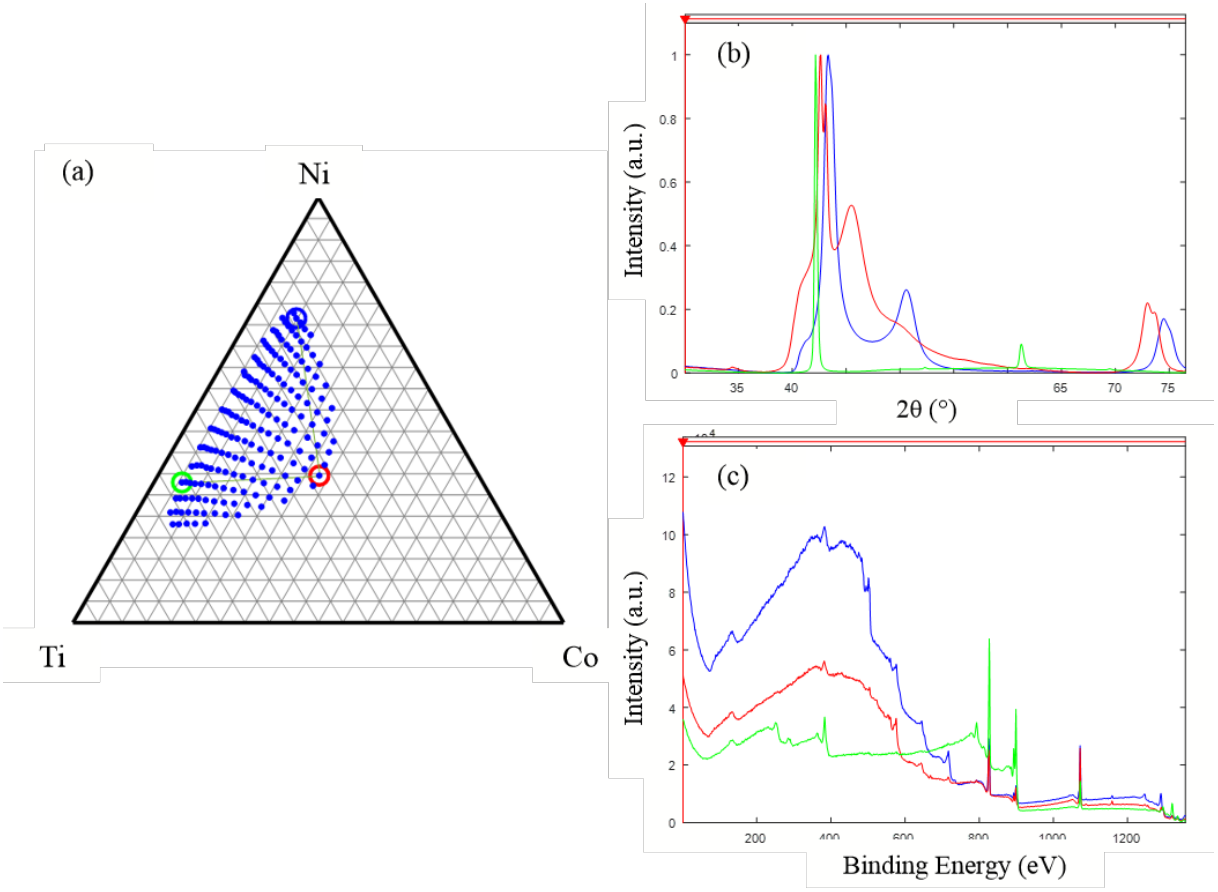

Figure 3.7: MATLAB based data visualization platform CombiView allows linking of sample composition with its spectral pattern. (a) Composition range covered in this study plotted on a ternary map. Three compositions at element-rich points in the map are selected. (b) XRD patterns for these points demonstrate distinct patterns and (c) corresponding XPS spectra also showing distinct variation in signal. Color of the spectra match the composition selection.

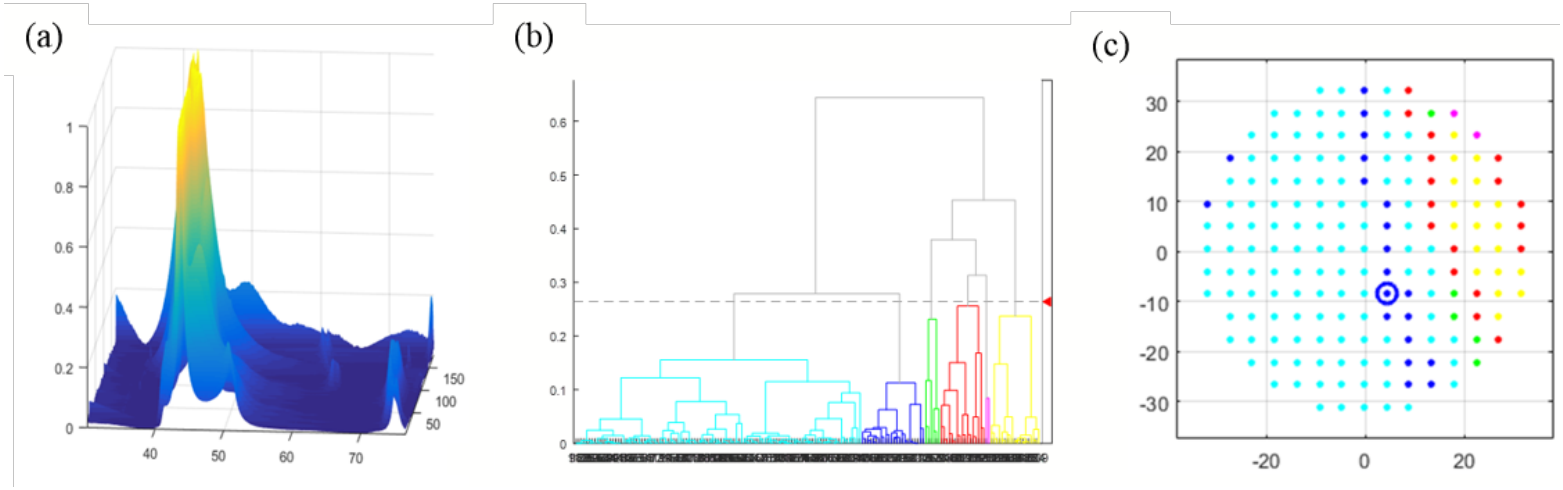

Figure 3.8: CombiView also allows linking of sample composition with its diffraction pattern by wafer position and was used to perform hierarchical cluster analysis to create the structural phase diagram. (a) 3 dimensional depiction of the 177 diffraction patterns from the library by position and with x-axis of 2θ between 30 and 75 degrees (b) Dendogram of results from the PCC hierarchical clustering model showing grouping of XRD patterns based on similarities in peak positions (c) Identification of phase boundaries by wafer position as delineated from hierarchical clustering shown in (b).

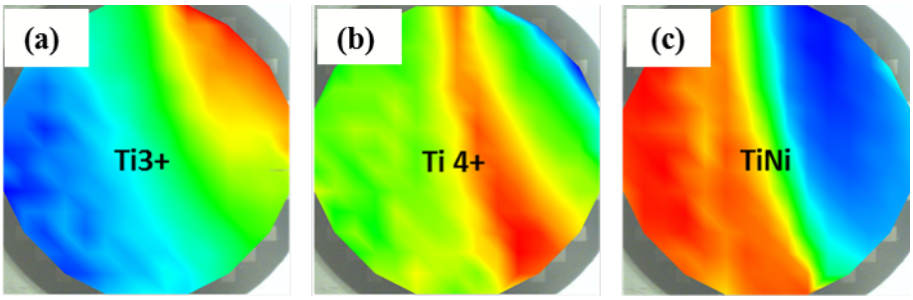

Figure 3.9: Peak fitted distribution of (a) Ti^{3+}, (b) Ti^{4+}, and (c) TiNi across the wafer. High to low distributions are indicated by variation in color from red to blue, respectively; wafer oriented with long flat edge on bottom.

Chapter 4: Phase transformation properties of Ni-Ti-Cu-V

In this chapter, a composition spread of Ni-Ti-Cu-V thin-film library was investigated for phase transformation at ambient temperatures. Of the 177 compositions in the materials library, 32 were observed to have shape memory effect, of which five had zero or near-zero thermal hysteresis. These compositions provide flexibility in the operating temperature regimes that they can be used in. A phase map for the quaternary system and correlations of functional properties are discussed with respect to the local microstructure and composition of the thin-film library.

4.1 Introduction

Shape memory alloys (SMAs) of nickel-titanium (Ni-Ti) are functional materials with thermal (one-way effect, 1-WE) and mechanical (pseudoelasticity, PE) "memory" [58]. This property has been extensively covered in chapter 1 so I will review some concepts briefly. A thermal hysteresis ΔT occurs when there is a difference in the temperature at which 50% of the material is transformed into martensite upon cooling and 50% into austenite upon heating, so that $\Delta T = A_f - M_s$ [167].

Transformation temperatures (A_f) range between 0 °C and 100 °C for commercial NiTi alloys with a hysteresis width of 25 °C to 40 °C [168]. Austenitic and martensitic NiTi structures have cubic B2 and monoclinic B19' crystal lattices, respectively [1, 58, 169]. In addition, intermediate structures such as rhombohedral or trigonal R-phase and B19 facilitate geometric compatibility during transformation. Phases and crystal lattices present in the Ni-Ti system have been extensively studied, but undesirable functional and structural properties including the strong dependence of transformation temperatures on composition and, hence, tight control of synthesis parameters present a significant challenge in their adoption into new technology [22, 51, 170–172]. Nonetheless, Ni-Ti SMAs enjoy widespread applications ranging from actuators, stents, orthodontics, and sensors to eco-friendly refrigeration and even fashion [52, 173–178].

As mentioned previously, the transformation temperature regime is a critical parameter in determining the application of SMAs along with their functional fatigue. The addition of ternary and quaternary alloying elements enables the modification and fine-tuning of the material transformation temperature for specific applications [1, 51, 89]. Using combinatorial materials science, we gain access to many compounds covering a substantial compositional space with different stoichiometries under identical conditions. Hence, it enables the rapid discovery and development of new materials with targeted properties [179].

In this study, I report on new Ni-Ti-Cu-V quaternary thin-film compositions having near-zero thermal hysteresis, as determined by high-throughput resistance

measurements. A systematic workflow was adopted for the rapid determination of composition-structure-property relationships and a composition-phase map for the quaternary alloy was developed through automated data analysis employing hierarchical clustering techniques. This work validates theoretical predictions and builds on experimental efforts in developing new SMAs [12, 62].

4.2 Experimental results

In this work, I investigated the influence of composition on structure and transformation property of quaternary $[Ni_{36}–Ti_{52}–Cu_{12}]_{(100-x)}V_x$ alloys in thin film form. High-throughput characterization of the composition and crystal structure was performed using WDS and synchrotron XRD, respectively. Transformation behavior was characterized using resistance as a function of temperature measurements. Machine learning using a MATLAB-based data visualization platform, CombiView, developed in-house was used to sort compositions by diffraction patterns, and therefore structures, into clusters in order to rapidly identify constituent phases and determine phase boundaries [121].

4.2.1 Compositional Analysis

Automated WDS measurements were carried out on all 177 samples in the materials library. Figure 4.1 shows the composition variation across the wafer with atomic percent ranges for the four elements as follows: Ni from 21.3 to 58.3 at.%, Ti

from 23.3 to 57.5 at.%, Cu from 12.9 to 24.9 at.%, and vanadium (V) from 2.9 to 6.2 at.%. The targeted composition $Ti_{41.8}Ni_{37.5}Cu_{16.0}V_{4.6}$ was obtained in the center. Distribution of the elements corresponded with the elemental target gun positions inside the sputtering chamber.

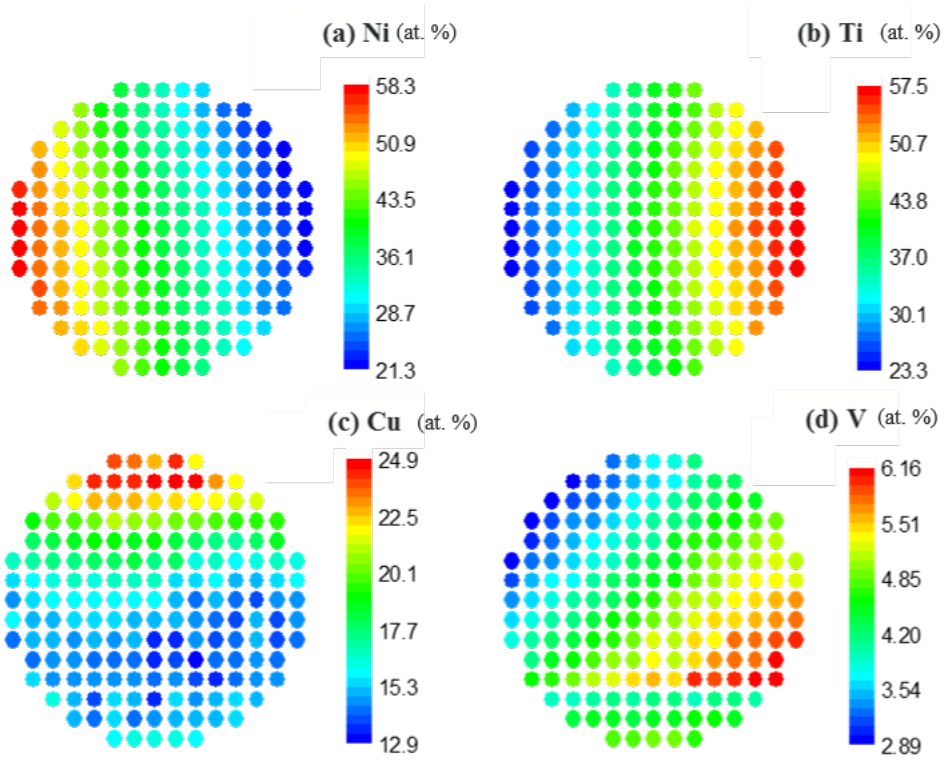

Figure 4.1: Elemental distribution of (a) Ni, (b) Ti, (c) Cu, and (d) V on a 3-inch Si wafer. The color scale for each element indicates composition in atomic % from high to low indicated by the progression from red to blue. The wafer was oriented with the long flat edge at the bottom.

4.2.2 Transformation temperature from $R(T)$ measurements

The property of interest for this library was shape memory effect determined from phase transformation curves. These were obtained by carrying out temperature-dependent resistance measurements. Phase transformation temperatures of austenitic

finish (A_f), and martensitic start (M_s) temperatures were determined using the tangent method [12]. Phase transformation activity for each composition as a function of wafer position in the thin film library is shown in Figure 4.2(a). Regions of transformation indicated by curves shaped as variations of "U" and "2" were observed to be limited to the right side of the wafer. The left-half portion can be divided into two main regions: The first region encompassed many compositions in the center of the wafer with non-transforming, linear behavior; the second region was limited to compositions in the far left showing non-transforming and nonlinear behavior without clear curves. Positions and compositions clustered by SME activity are shown in 4.2(b) and 4.2(c), respectively, where there are reversible phase transformations with non-linear $R(T)$ curves (yellow, teal, pink), non-transforming regions with linear curves in blue, and non-linear curves in green and red. Phase transformation parameters of thermal hysteresis (ΔT = A_f – M_s), austenitic finish (A_f), and martensitic start (M_s) temperatures are shown in Figure 4.3. All compositions with phase transformation behavior are listed in Table 4.1. SME was observed in 32 compositions with five compositions having zero or near-zero thermal hysteresis and one composition with a maximum of ΔT of 17.2 °C. Elemental range for compositions having SME was observed as follows: Ti = 49.4 to 57.5 at.%, Ni = 21.3 to 30.9 at.%, Cu = 13.8 to 21.6 at.% and V = 4.1 to 6.2 at.%. The boundaries of the temperature regime where transformations to austenite occurred were observed to be centered around 13 °C to 29 °C while martensitic start temperature were slightly reduced between 10 °C and 20 °C. Thermal hysteresis of $\leq$4 °C was observed in 19 compositions.

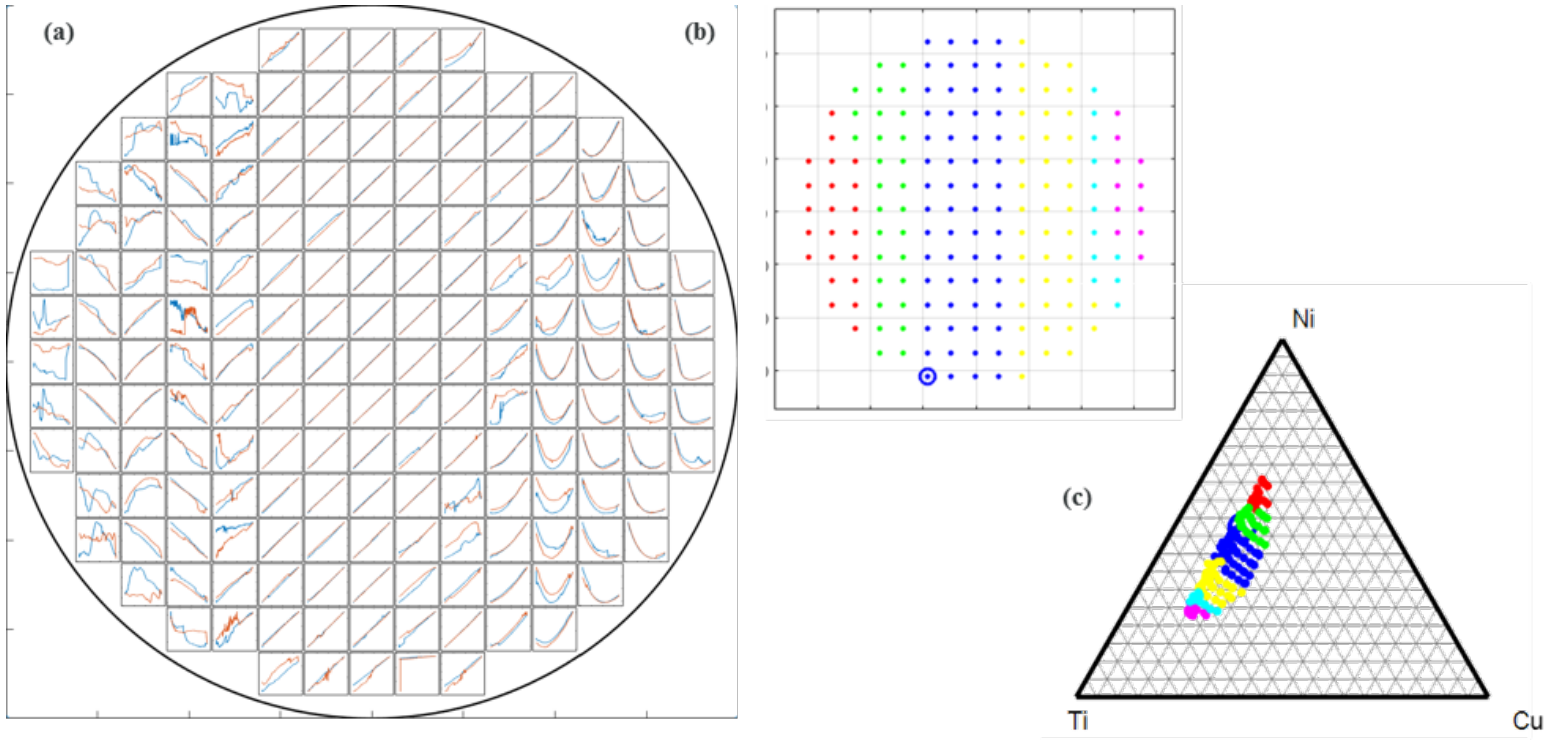

Figure 4.2: (a) Temperature-dependent resistance $R(T)$ curves for $[Ni_{36}–Ti_{52}–Cu_{12}]_{(100-x)}V_x$ showing regions of transformation. Reversible transformation is observed on the right portion of the wafer as indicated by broad "U"- and "2"-shaped curves. Heating and cooling curves are indicated by red and blue colors, respectively. (b) Grouping by SMA activity of wafer positions and (c) compositions projected on a ternary Cu-Ni-Ti plot where V is between 2.9 and 6.2 at.%.

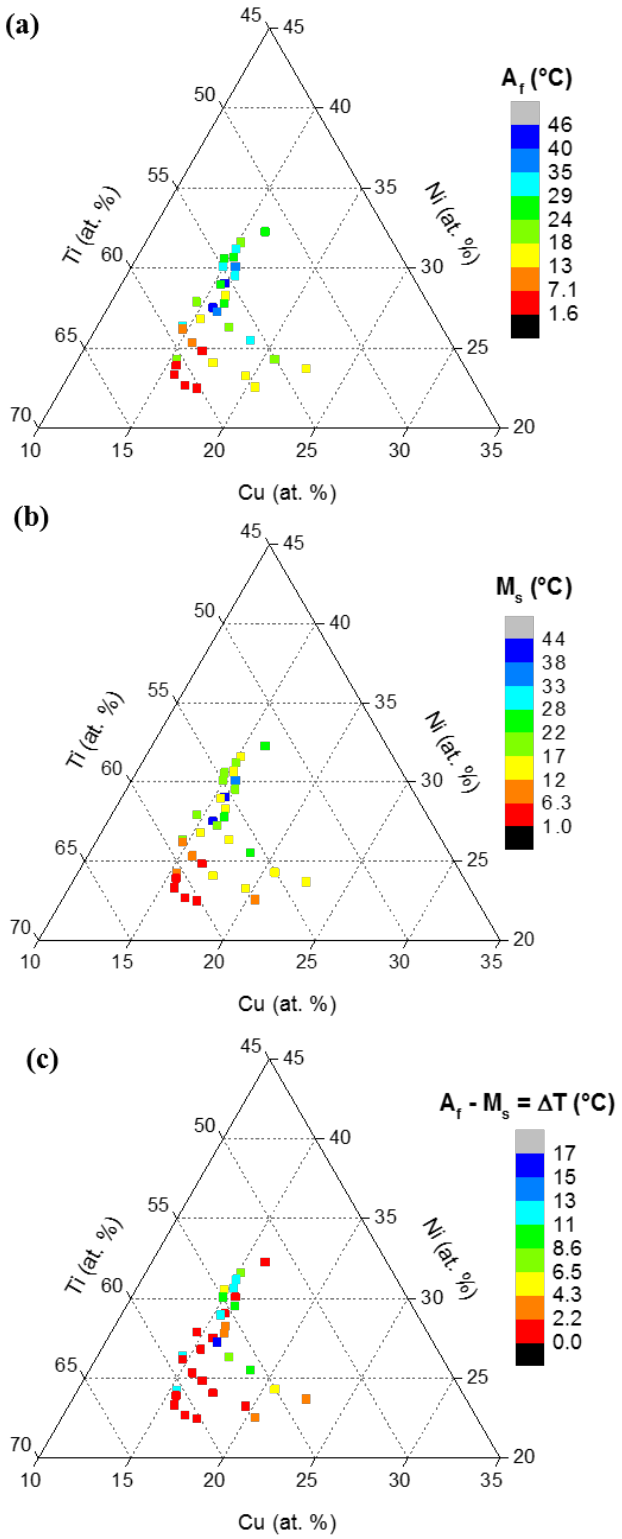

Figure 4.3: Ni-Ti-Cu-V compositions having SME projected onto Cu-Ni-Ti ternary plots with atomic concentration of V held constant between 2.9 and 6.2 at.%. Phase transformation parameters of (a) austenitic finish (A_f) temperature (°C), (b) martensitic start (M_s) temperature (°C) and (c) thermal hysteresis $\Delta T = A_f - M_s$ in °C. Color scale bars from blue to red indicate high to low temperatures.

Ti	**Ni**	**Cu**	**V**	A_f	M_s	A_f - M_s = Δ**T**
	[at. %]					**[°C]**
57.1	21.3	16.5	5.1	6.4	4.8	1.6
54.2	21.5	19.5	4.9	13.6	10.0	3.6
57.5	21.5	15.7	5.3	4.4	2.4	2.0
57.5	22.0	14.8	5.7	6.0	6.0	0.0
54.2	22.1	18.6	5.1	14.8	14.0	0.8
57.1	22.5	14.6	5.8	1.6	1.2	0.4
51.2	22.6	21.6	4.5	14.4	12.0	2.4
56.7	22.8	14.4	6.0	21.2	10.4	10.8
55.5	22.8	16.5	5.2	13.2	12.8	0.4
52.4	23.1	19.7	4.8	21.2	15.2	6.0
55.5	23.5	15.6	5.4	5.2	3.6	1.6
55.7	23.9	14.8	5.6	12.0	10.0	2.0
53.0	24.2	17.8	5.0	34.4	24.8	9.6
55.8	24.7	13.9	5.7	11.6	9.6	2.0
55.5	24.8	13.8	5.9	29.5	17.2	12.3
53.6	25.0	16.3	5.1	21.2	14.4	6.8
54.3	25.2	14.4	6.1	16.0	16.0	0.0
53.7	25.8	15.2	5.3	35.2	18.0	17.2
53.3	25.8	14.7	6.1	42.9	41.9	1.0
52.9	26.3	15.3	5.5	26.8	24.0	2.8
54.3	26.4	13.8	5.5	19.6	17.6	2.0
52.5	26.7	15.1	5.8	18.0	14.0	4.0
52.0	27.3	14.6	6.2	45.6	43.5	2.1
52.5	27.3	14.5	5.7	28.8	16.4	12.4
51.7	28.0	15.1	5.2	30.7	20.4	10.3
52.0	28.5	14.1	5.4	30.6	21.7	8.9
52.1	28.9	15.0	4.1	40.0	38.0	2.0
51.0	28.9	14.4	5.7	26.5	15.2	11.3
51.7	28.9	14.0	5.4	24.0	18.0	6.0
50.6	29.4	14.2	5.8	30.0	17.5	12.5
50.0	29.7	14.3	6.0	22.8	16.0	6.8
49.4	30.9	15.5	4.2	25.0	24.0	1.0

Table 4.1: Thermal hysteresis, austenitic finish and martensitic start temperatures for quaternary-Ni-Ti-Cu-V SMAs by ascending Ni content.

4.2.3 Crystal structure and phase identification

The data visualization platform CombiView allows the linking of sample position on the wafer with its corresponding composition and diffraction pattern [111, 113,121]. The structural phase diagram was determined through a hierarchical cluster analysis of the diffraction patterns, as shown in Figure 4.4. A Pearson Correlation Coefficient cluster analysis resulted in six clusters for the Ni-Ti-Cu-V materials library. Table 4.2 lists the crystal structure and space group of the phases found in the library. For non-transforming compositions, both linear and non-linear $R(T)$ curves were observed, which were attributed to double phase and low symmetry crystal structures. The default structure type is a cubic phase, unless specified otherwise under prototype.

Formula	Space Group	Space Group Number	Prototype
NiTi	Pm3m	221	$(Ti_{0.64}Zr_{0.36})$ Ni
Ti $Ni_{0.8}Cu_{0.2}$	P21/m	11	monoclinic
Cu Ni Ti	I4/mmm	139	tetragonal
$Ni_{0.25}Cu_{0.75}$	Im3m	229	
$Ti_2C_{0.06}$	P63/mmc	194	hexagonal
$(Cu_{0.03}Ni_{0.97})_3$ Ti	P63/mmc	194	
Ti $(Ni_{2.79}$ $Cu_{0.21})$	R-3m	166	rhombo.H.axes
Ti $Ni_{0.8}$ $Cu_{0.2}$	Pmam	51	orthorhombic
Ti $(Cu_{0.053}$ $Ni_{0.947})_3$	P63/mmc	194	
$(Ti_{0.67}$ $V_{0.33})$ Ni_3	P63/mmc	194	
Ti Ni_2 Cu	Pmmn	59	

Table 4.2: Overview of crystal structures identified in the Ni-Ti-Cu-V materials library

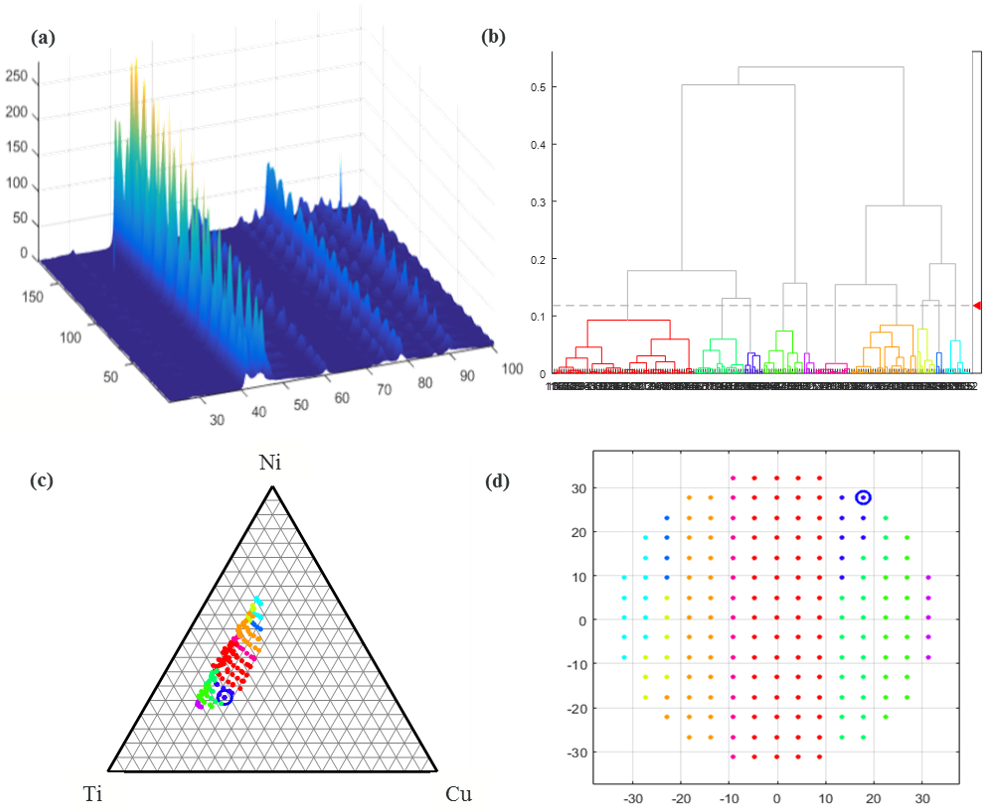

Figure 4.4: Hierarchical cluster analysis of diffraction patterns for a quaternary thin film library covering range $[Ni_{36}–Ti_{52}–Cu_{12}]_{(100-x)}V_x$. MATLAB based data visualization platform CombiView allows linking of sample position on wafer with its composition and diffraction pattern, which is used to perform hierarchical cluster analysis to create a structural phase diagram. (a) 177 diffraction patterns with an x-axis of 2θ between 22 and 100 degrees. (b) Pearson correlation coefficient cluster analysis model showing grouping of XRD patterns based on similarities in peak positions. (c) Composition space covered in this study as projected on a ternary plot of Cu-Ni-Ti with constant V identifying structural phase boundaries as delineated from hierarchical clustering shown in (b), and (d) grouping by position on wafer (long flat edge at bottom).

4.2.4 Assessment of the thin film phase diagram

Results for the transformation properties and phases identified in the present study are listed in Table 4.1 and Table 4.2, respectively. Martensitic phase transformation determined from resistance measurement shows that the shape memory effect is limited to the Ti-rich region. SME variation changes with Ni and V content such that SME is observed to be between 21.3 and 33.4 at.% Ni and between 4.0 and 6.2 at.% V, respectively. This is in agreement with values reported in bulk by Frenzel et al [51, 106].

Clustering diffraction patterns using Pearson correlation coefficient model match the grouping of compositions based on the shape memory behavior. Cubic NiTi with a mixture of cubic $Ni_{0.25}Cu_{0.75}$ and tetragonal CuNiTi phases were found in Ti rich regions with the highest V content. The increased replacement of Ni by V was observed to stabilize the transformable cubic and tetragonal martensite variants (Figure 4.5). A mix of cubic crystal structure having a prototype formula $(Ti_{0.64}Zr_{0.36})Ni$ and hexagonal Ti $(Cu_{0.053}Ni_{0.947})_3$ made up the majority of the composition space covered in this materials library having no transformation. For Ni rich regions, orthorhombic phases of $TiNi_2Cu$/Ti $Ni_{0.8}Cu_{0.2}$ mixed with hexagonal $(Ti_{0.67}V_{0.33})Ni_3$ were identified as Ni content was reduced.

The addition of Cu to binary NiTi such that Cu replaces Ni has been shown to decrease the misfit between austenite and martensitic lattices. This translates to a slight decrease in M_s and reduced width of the thermal hysteresis, which,

when combined, improves fatigue properties. The influence of the addition of V as a ternary element to NiTi was reported by Frenzel et al [51] who demonstrated a reduction in M_s. In addition, the mechanical behavior was stabilized so that a small residual strain was maintained compared with binary NiTi. Addition of V to NiTi was also shown to improve fatigue and efficiency as well as endurance limit [180]. Ni-Ti-Cu-V has been demonstrated for application as an elastocaloric material that is able to fulfill the potential of using $Ni_{45}Ti_{47.25}Cu_5V_{2.75}$ in ribbon form [106,107] and $Ni_{50}Ti_{45.3}V_{4.7}$ in a square prismatic form [180]. The identification of new compositions having reduced thermal hysteresis is a starting point for scale up experiments to determine their long-term robustness through mechanical testing.

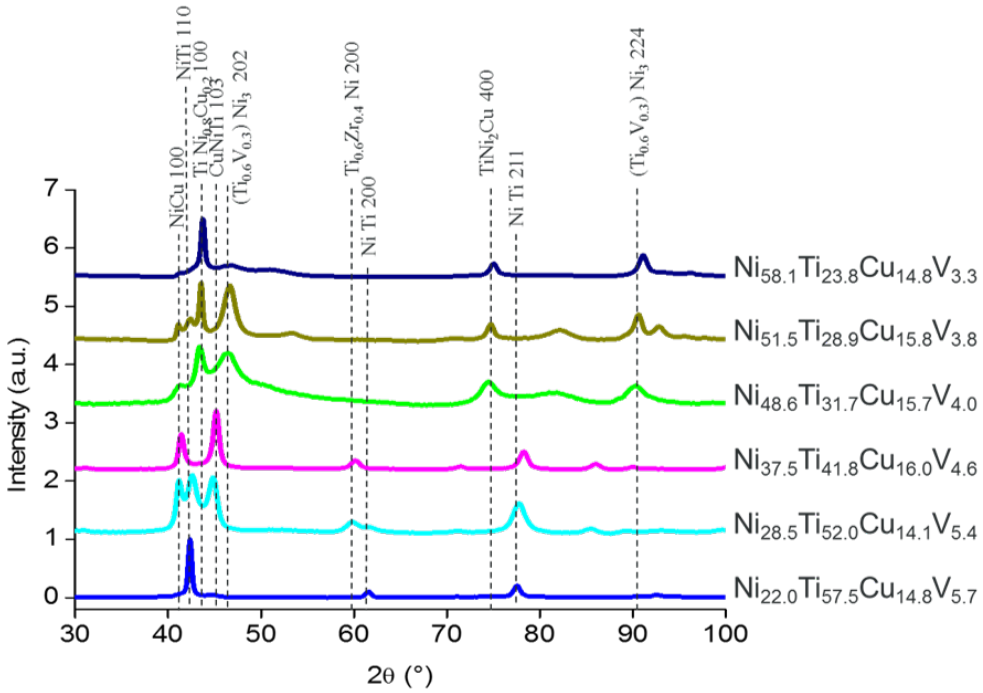

Figure 4.5: Selected diffraction patterns representing the six clusters identified by Pearson correlation coefficient clustering model. Substitution of Ni by V increases with distance from the abscissa, reflecting a shift in the non-transforming orthorhombic and hexagonal phase mixture to transformable cubic and tetragonal crystal structures. Patterns are offset for clarity.

4.2.5 Effect of temperature cycling on film resistance

Thermal stability over many cycles is an important consideration in the optimization of heat transfer and the determination of functional fatigue, specifically, when using SMAs for elastocaloric cooling [92]. Film sheet resistance at room temperature (Figure 4.6a) was measured prior to cycling the library between -40 °C to 120 °C for temperature-dependent resistance measurements. The effect of temperature cycling on film resistance was evaluated since the library was subjected to 84 temperature cycles, and is shown in Figure 4.6b with the difference mapped in Figure 4.6c. While the shape memory effect was stable, as determined from the observation of transformation in Figure 4.2a, an overall reduction in sheet resistance was observed. XRD measurements collected post thermal-cycling show little to no change in diffraction patterns, thereby suggesting good structural stability (data not shown).

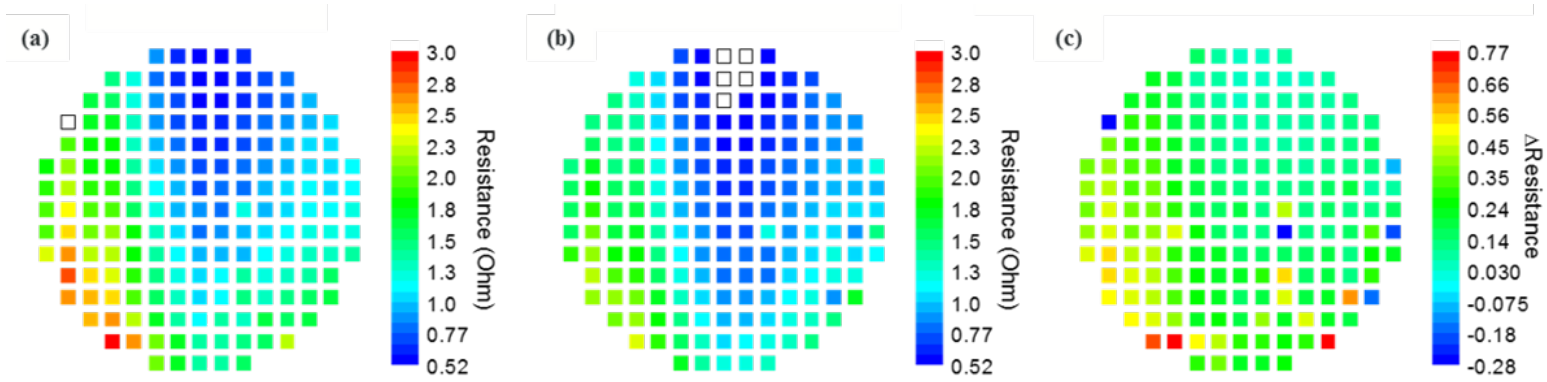

Figure 4.6: Thin film sheet resistance at room temperature (a) before and (b) after 84 temperature cycles between -40 °C and 120 °C. Post cycling resistance was mapped using the same scale as pre-cycling; values outside of this range are indicated by colorless boxes. (c) difference in resistance from a and b. Color scale from red to blue indicates high to low values, respectively. The wafer was oriented with the long flat edge at bottom.

4.3 Conclusions

In this work, I report on the combinatorial thin film synthesis and high-throughput characterization of a quaternary alloy. I provide an overview of the dependence of material properties on composition and structure through composition-structure-property maps. The Ni-Ti-Cu-V materials library I synthesized spans a composition region that has shape memory behavior. A strong correlation can be made between the microstructure and phase transformation property and, hence, composition. SMA effect is prominent in the Ti-rich region with a significant number of compositions having near-zero thermal hysteresis. Increasing addition of V was observed to stabilize the mixture of cubic and tetragonal phases identified in compositions exhibiting SMA behavior. For non-transforming compositions, both linear and non-linear $R(T)$ curves were observed which were attributed to double phase and low symmetry crystal structures. Shape memory effect and thermal hysteresis were stable over close to a hundred cycles. This work explored and validated the use of V as a fourth element in fine tuning the operating temperature of a Ni-Ti-Cu ternary alloy in the ambient temperature regime for elastocaloric cooling applications. Work remains to be undertaken to understand the limits of V addition on the enhancement of efficiency and functional stability of the elastocaloric effect in NiTi alloys.

Chapter 5: Mapping ambient thermal conductivity of SMA thin film libraries

In the previous chapter, compositions in the Ni-Ti-Cu-V materials library having near zero thermal hysteresis were identified. In this chapter, combinatorial thin film systems Ni-Ti, Ni-Ti-V, and Ni-Ti-Cu-V were investigated for thermal energy storage applications using combinatorial materials science. Composition spread thin film libraries were prepared using combinatorial magnetron sputtering. The thermal conductivity, resistance, and thickness were determined using high-throughput characterization techniques. X-ray diffraction results were used to determine phase diagrams for each system and correlations between composition, phase, and functional properties are discussed.

I report on measuring thermal conductivity for evaluating a novel application of SMAs as phase change materials (PCMs) for thermal energy storage and management with minimal temperature increase of the material. Although latent heat is an important parameter to measure for shape memory alloys in using them as refrigerants, it is not a trivial task to obtain for thin films. For compositions

with promising initial parameters, additional analysis can be carried out to evaluate additional properties.

5.1 Introduction

Energy drives societal development through economic and technological advancement [181]. However, the impact of unrelenting use of non-renewable resources over the last century resulted in accelerated global warming has shifted our focus to developing sustainable resources to meet electrical and thermal energy conversion and storage needs. Challenges remain in fully adopting renewable energy sources due to their intermittent nature with reliance on carbon-based fuels as secondary sources for round the clock energy supply. Phase change materials (PCMs) for thermal energy storage (TES) present an opportunity to fill this gap in an expansive technological space ranging from localized thermal management to large scale power systems [182].

NiTi-based SMAs were recently demonstrated as solid-state, ultrahigh performance metallic PCMs by harnessing their martensitic transformation [109]. Phase change materials are substances that absorb or release energy as they undergo a change from one physical state to another. This energy is also known as latent heat and can be used for providing functional heating and cooling [183]. There are different types of PCMs based on the state of matter [182]. Solid-Liquid PCMs have long filled the role of thermal energy storage media to address intermittency typi-

cal of renewable energy resources [184, 185], and remain the most suitable material class for this purpose [182]. The solid to solid phase transformations in SMAs also have an associated latent heat that can be harnessed for PCM applications in absorption of large amounts of heat from electronic devices or in the field for military applications. Metallic solid state PCMs offer the advantage of easy integration and packaging with structural frameworks which are often the challenge to overcome with solid-liquid and even polymer-based solid-solid PCMs that leak or require enhancement of the poor thermal conductivity [182, 186–188]. Heat capacity, melting point, and thermal energy storage density are other important thermophysical properties for the development of efficient PCMs. Thermal conductivity is also a critical property for high-power or high-speed charging and discharging applications using thin-films in microelectromechanical systems (MEMS) such as micro-actuators [189], pressure, electrochemical, and gas sensors [190–192], micropumps [193] etc. where nano-structuring and other size effects contribute to significant differences in thin film properties relative to bulk samples.

5.1.1 Thermal conductivity of NiTi-based bulk materials and thin films

While thermal conductivity measurements have been reported for bulk binary and ternary SMAs in thin-film, cylindrical and wire forms (summarized in Table 5.1), no studies have been found investigating composition spreads in binary, ternary

Material	k (W/mK)	Ref
NiTi	18	[199]
$Ni_{49}Ti_{51}$	11.5 vs 1.47 (0 vs 68% porosity)	[200]
Ni Ti	12.6(±8%)	[201]
Ni Ti (100 °C)	15.6(±10%)	
NiTi:Ga ($T_{ambient}$)	28.9(±5%)	
	8.6-14 28 (Aust) 14 (Mart)	[196], [194]
	15.6–28	[196], [202], [195]
	33-41	[202], [195]
NiTi cylinder 8x8mm^2 (diameter x length)	8-12 13 (Aust) 9 (Mart)	[203]
$Ti_{50}Ni_{50-x}Cu_x$ (x=0–30 at.%)	14	[204]
$Ni_{50}Ti_{50}$ $Ni_{40}Ti_{50}Cu_{10}$ $Ni_{48.5}Ti_{50}Fe_{1.5}$	22 (avg.) 55 (B19 → R) 14.5, 18.5 (B19' → R, B2 → R)	[61]
Thin film NiTi	4.9 → 5.6	[197]

Table 5.1: Summary of NiTi-based SMA materials and their thermal conductivity as reported in literature.

or quaternary SMA systems [109, 194–198]. This report offers the first study of this kind. Furthermore, this report is also the first to cover high-throughput, non-destructive measurement of thermal conductivity of SMAs in thin film form.

5.1.2 Thermal conductivity characterization techniques for thin films

Thermal properties of thin films can be measured by a variety of electrical, reflectance, photoacoustic and optical methods [205–210]. These groups of methods are classified further based on transient or steady state heating. Transient heating methods involve measuring a thermal response of a sample material to sinusoidal

heating due to an alternating current or the time response of the sample material to a heating signal. Time-domain thermoreflectance (TDTR) and frequency-domain thermoreflectance (FDTR) are two types of transient methods [211–214]. FDTR is most widely used and is a contactless, optical measurement technique to characterize thermal conductivity of solids [215, 216]. In steady state heating, temperature is increased by passing a direct current through a metal heater. The corresponding rise in temperature is measured either by a separate sensor or by the heater itself being used as a thermometer. Many reports on thermophysical properties of thin films deposited on substrates have also been investigated using the 3-omega method [214, 217–219].

Scanning thermal microscopy (SThM), in contrast to the other methods of characterizing thermal conductivity of thin films, is non-destructive, requires minimal sample preparation, and boasts the best spatial resolution of temperature mapping techniques [131, 132, 220, 221]. In addition, SThM may offer a fast, quantitative determination of thermal conductivity of thin films if the probe-to-sample thermal exchange is appropriately calibrated [13, 133, 222–226]. SThM may be broken into two main modes: active mode and passive mode. In active mode (a-SThM), the probe is self-heated, typically via Joule heating, and the amount of heat going into the sample is used to determine the sample's thermal properties [132]. This is also known as the scanning hot probe (SHP) method. In passive mode (p-SThM), an external temperature is measured [220]. In both cases, accurate quantitative determination of thermal exchange parameters between probe and sample (which is key

to accurate measurement) is a difficult challenge [223, 224, 227–229]. Recent studies have investigated conditions under which one can expect an accurate measure of thermal conductivity via SHP [13, 133, 225, 230–233], and the method has been used to characterize thermal conductivity of a wide host of thin films and nanostructured materials [13, 132, 135, 222, 225, 234–238]. In this report, I use SHP method described in section 2.10 to characterize thermal conductivity of combinatorial Ni-Ti, Ni-Ti-V and Ni-Ti-V-Cu films on substrate.

5.2 Theory and probe calibration

As previously mentioned in section 2.10, probe-to-sample thermal exchange calibration is crucial for accurate measurement of thermal conductivity via SHP. Several methods have been proposed (which are discussed in detail in a previous study [225]), and it was determined that owing to its simplicity and ease of use, the implicit (curve-fitting) method was the best choice for this study. It was determined that this was an appropriate choice for probe calibration given the expected film thickness range (200-300 nm) and surface roughness range (<5 nm rms roughness on all sample areas measured, which was previously determined to be an appropriately smooth sample for this style of probe [239]). Six smooth (<5 nm rms roughness) samples of known thermal conductivity were used to calibrate the probe. These were used in a previous study comparing calibration strategies [225]. As the probe is brought into contact with the sample, the steady-state change in probe voltage

(with a consistent output voltage of 1.25V, which corresponds to ∼1 mA of current) is recorded for each reference sample the resulting plot is depicted in Figure 5.1. More details about the experimental procedure for performing sample measurements are provided in section 2.10.

The measured probe voltage drop (V_S-V_R) vs thermal conductivity (k_{ref}) is then curve fitted using a Boltzmann distribution (dashed line in Figure 5.1) taking the following form:

$$(V_S - V_R) = A_2 + (A_1 - A_2)/(1 + e^{\frac{K_s - K_0}{dk}}) \tag{5.1}$$

where A_1, A_2, k_0, and dk are fitting constants and k_S is sample thermal conductivity.

Solving for thermal conductivity of unknown samples, we find:

$$k_s = k_0 + dk \times ln(\frac{A_1 - A_2}{(V_S - V_R) - A_2} - 1) \tag{5.2}$$

Checking for self-consistency by using the equation to predict thermal conductivity, we find good agreement with the reference values, as denoted in Table 5.2.

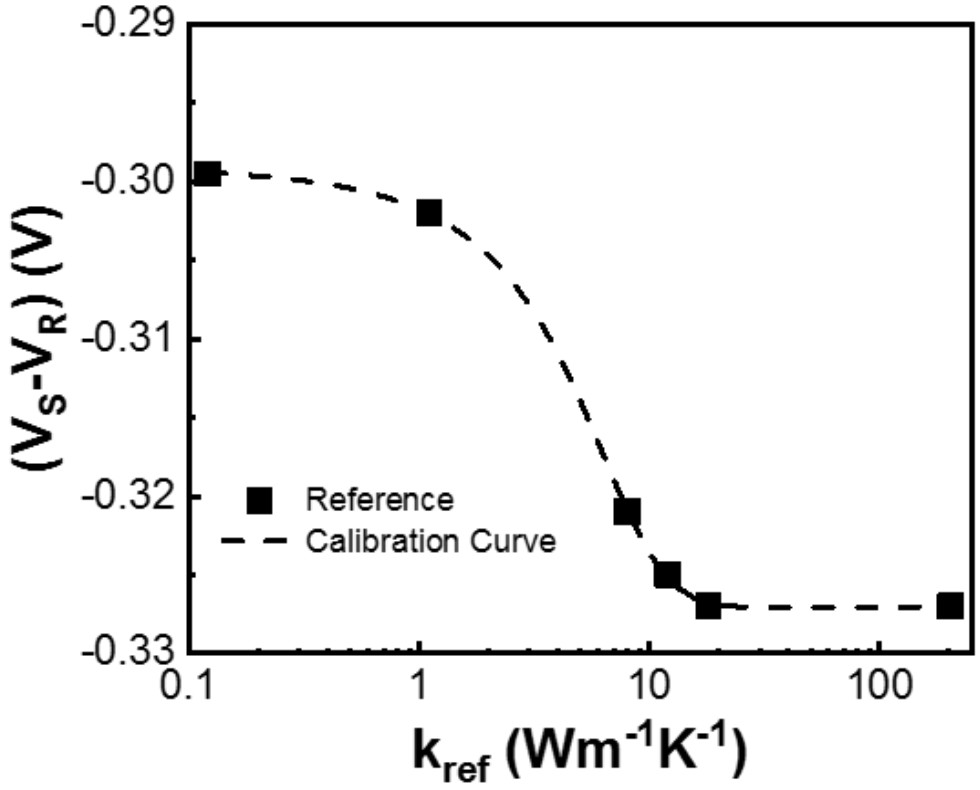

Figure 5.1: Calibration curve to determine probe voltage drop (V_S- V_R) as a function of reference sample thermal conductivity (k_{ref}). [Courtesy of A. Wilson, ARL].

Material	K_{295K} **literature [W/mK]**	K_{295K} **measured [W/mK]**	**Ref**
Polyimide	0.12	0.14	[240]
Quartz	1.1	1.07	[241]
50 nm Al_2O_3 on Si	8	8.06	[225], [242]
10 nm Al_2O_3 on Si	12	11.65	[225], [242]
NiTi A_f 39 °C	18	22.00$^+$	[243]
Si	146	5.18*	[244]
GaN	203	22.00$^+$	[245]

Table 5.2: Reference samples used for probe calibration and predicted values from equation 5.1.
*It was determined that this Si wafer had a 25 nm native oxide layer, which led to a much lower apparent thermal conductivity in the measurement. It was not included in the curve fit.
$^+$Above 22 W/mK, sensitivity to thermal conductivity is significantly reduced due to contact thermal resistance.

5.3 Experimental procedures and results

5.3.1 Synthesis and characterization of combinatorial thin films

Thin films of Ni-Ti, Ni-Ti-V and Ni-Ti-Cu-V were prepared on thermally oxidized 3-inch (76.2 mm) Si wafers as described in section 2.1 of sample synthesis using magnetron co-sputter deposition. Table 5.3 shows the synthesis conditions for the films reported here and the properties that were measured for them. As this work was interrupted by the COVID19 lockdown [246], not all measurements could be made, reflecting the empty or partial indications in the table; technique acronyms are defined at the beginning of the thesis.

Sample ID	**Power [W]**				**Deposition Time**	**Annealing**		**WDS**	**XRD**	**R(T)**	κ
	Ti	**Ni**	**Cu**	**V**	**[min]**	**[°C]**	**[min]**				**[W/ mK]**
NiTi	95	40	-	-	27	500	60	P	-	-	P
NiTiV	100	65	-	20	47			Y	Y	-	P
NiTiCuV	85	27	30	15	30			Y	Y	Y	Y

Table 5.3: Summary of thin film material libraries, their synthesis conditions, and properties measured.
*P = partially measured; Y = yes

5.3.2 Thermal conductivity characterization by scanning hot probe

With the probe appropriately calibrated, the 3-inch wafers with composition gradients (Ni-Ti, Ni-Ti-V, Ni-Ti-Cu-V) were sequentially placed on a movable mechanical stage of the AFM. Each patterned square of the NiTi-based composition wafers was measured sequentially. Equation 5.2 was used to determine thermal conductivity. Figure 5.2 depicts several representative data points determined via the calibrated curve fit.

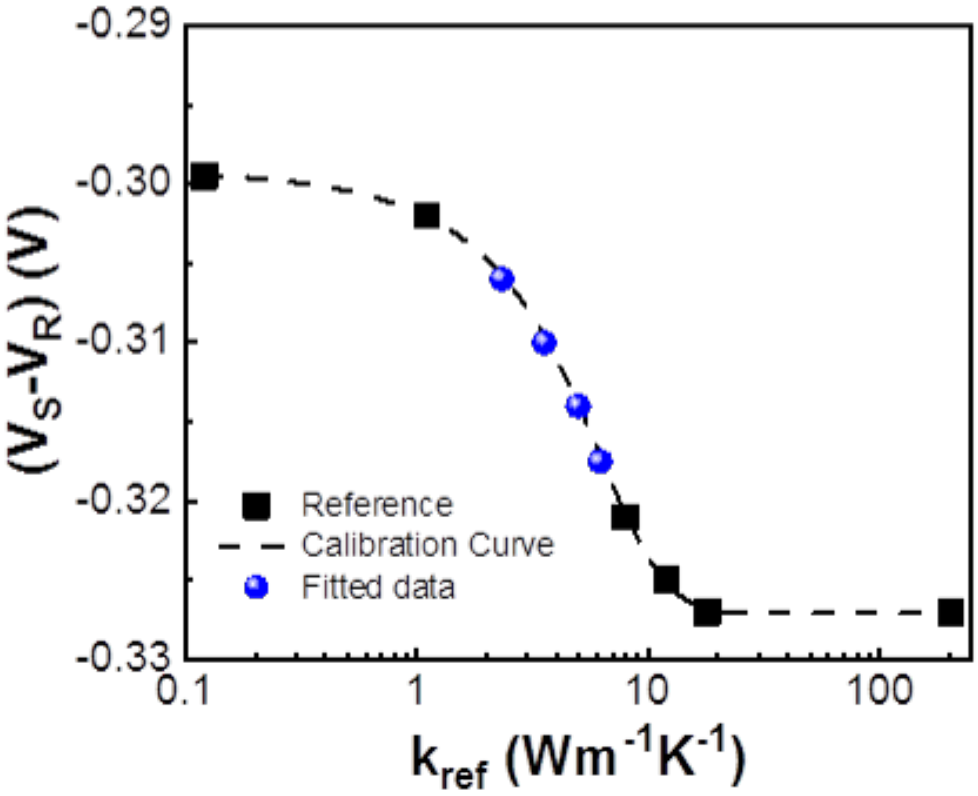

Figure 5.2: Measured data (blue dots) fitted via calibrated curve (dashed black line), obtained by measurement on reference samples (black squares). [Courtesy of A. Wilson, ARL].

5.3.3 Ni-Ti composition spread library

The binary Ni-Ti thin film materials library covered a composition range with Ni between 19.7 at.% to 68.9 at.% and Ti between 80.3 at.% to 31.1 at.%. Thermal conductivity was measured for 17 wafer positions shown in Figure 5.3(a), which ranged between 4.2 to 13.2 W/mK. Figures 5.3(b) and 5.3(c) show the thermal conductivity κ by Ni and Ti concentrations where the increasing Ni content reflects in an increase in κ. This follows our expectations of measurements performed at room temperature where the highest κ corresponds with the material in austenitic phase at RT. These values are comparable (albeit slightly lower) to bulk κ of binary NiTi measured via Xenon flash where the martensite was $\sim$7-10 W/mK and austenite was around 13-18 W/mK across the temperature range explored (data not shown). Thus, the κ values for binary Ni-Ti composition spread thin film are consistent with recent bulk measurements.

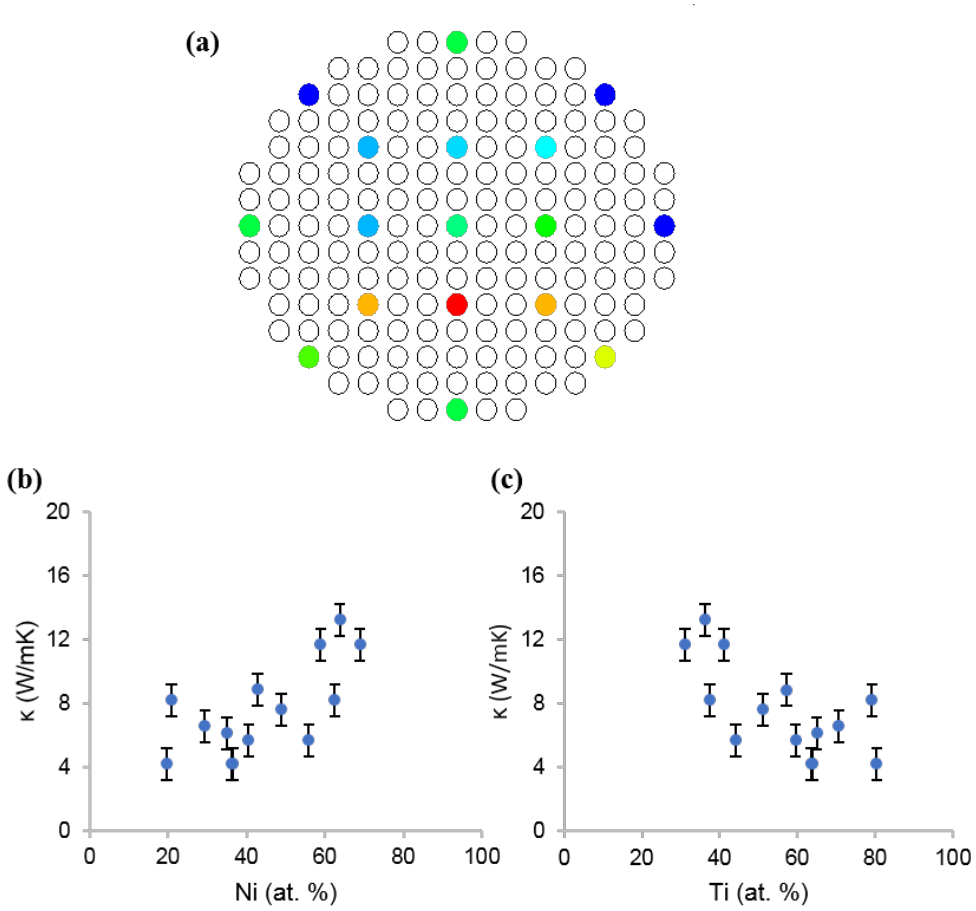

Figure 5.3: Thermal conductivity of binary materials library Ni-Ti plotted by (a) wafer position. Shown for elemental concentrations of (b) Ni and (c) Ti.

5.3.4 Ni-Ti-V composition spread library

Chemical composition for the ternary Ni-Ti-V thin film library covered a composition range with 31.6 at.% < c(Ni) < 80.5 at.%, 15.5 at.% < c(Ti) < 63.8 at.% and 1.8 at.% < c(V) < 11.0 at.% (Figure 5.4(a)). 16 wafer positions were evaluated for thermal conductivity, which ranged from 4.5 to 15.9 W/mK, as shown in Figure 5.4(b). From 5.4(b), a wide range of κ values are observed at higher Ni content without any discernable trend. Thermal conductivity as a function of elemental concentration of Ni, Ti, and V for the sample is shown in Figure 5.5. A high κ around V = 5-6 at.% followed by a decrease with increasing V is observed (Figure 5.5(c)) while no clear trend could be visually identified for Ni and Ti. This change in κ at V = 5-6 at.% raises the question of whether phase transformation or other material properties are also affected in the same range. Since $R(T)$ measurements had not yet been performed on this library for an understanding of phase transition by composition, XRD patterns were evaluated for structural phases as an indirect investigation of change in phase and transition temperature.

Using PCC hierarchical cluster analysis described previously, the structural phases present in the library were determined (Figure S5.12). Four main clusters of patterns were identified, represented in Figure 5.6, consisting of five phases and an oxide (see space group in Table 5.4). The predominant structure was found to be cubic of the $Pm3m$, $Fm3m$ and $Im3m$ space groups, present in single and mixed phases. Hexagonal phases of Ni_3Ti and $(Ti_{0.67}V_{0.33})Ni_3$ were also identified.

Table 5.4 lists all the crystal structures identified in the Ni-Ti-V materials library. Broad peaks in the 2θ range of 38° to 51° (yellow XRD pattern in Figure 5.6) for a non-crystalline phase were also observed. It is important to note that these are a qualitative assignment of phases and not quantified over the library. Since $R(T)$ data was not available on this system, transforming compositions and parameters could not be identified. However, it is expected that compositions having single phase Pm3m or mixed with tetragonal or orthorhombic crystal structures are transformable.

Lattice parameters of crystal structures determined for the four XRD patterns in Figure 5.6 were used to discern the relationship between thermal conductivity and crystal lattice and is shown in Figure 5.7. As all of the phases are cubic, the lattice parameter used was the a value from the structures. No clear trend could be identified.

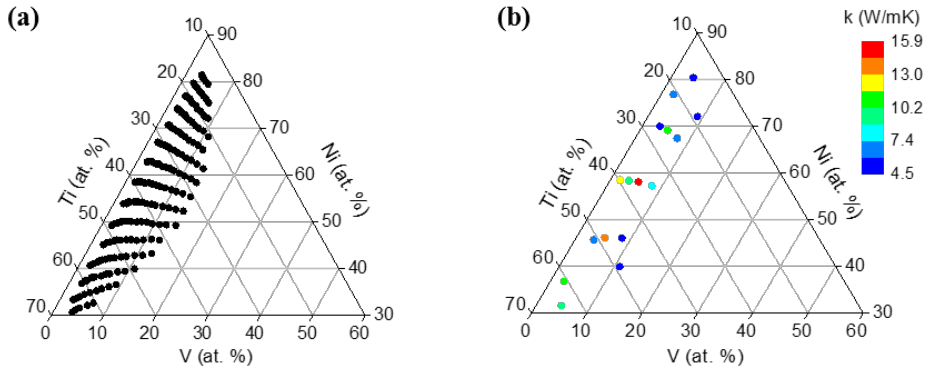

Figure 5.4: (a) Composition range and (b) thermal conductivity as a function of sample composition for Ni-Ti-V materials library.

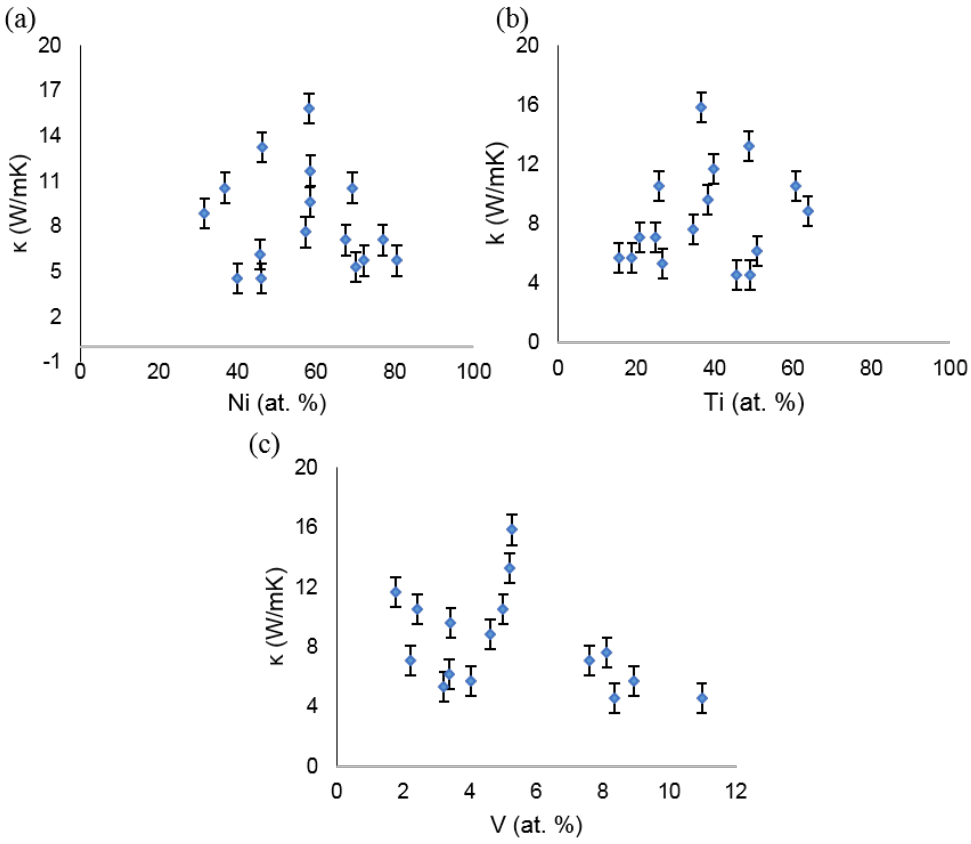

Figure 5.5: Thermal conductivity for the Ni-Ti-V materials library by elemental concentrations of (a) Ni, (b) Ti, and (c) V.

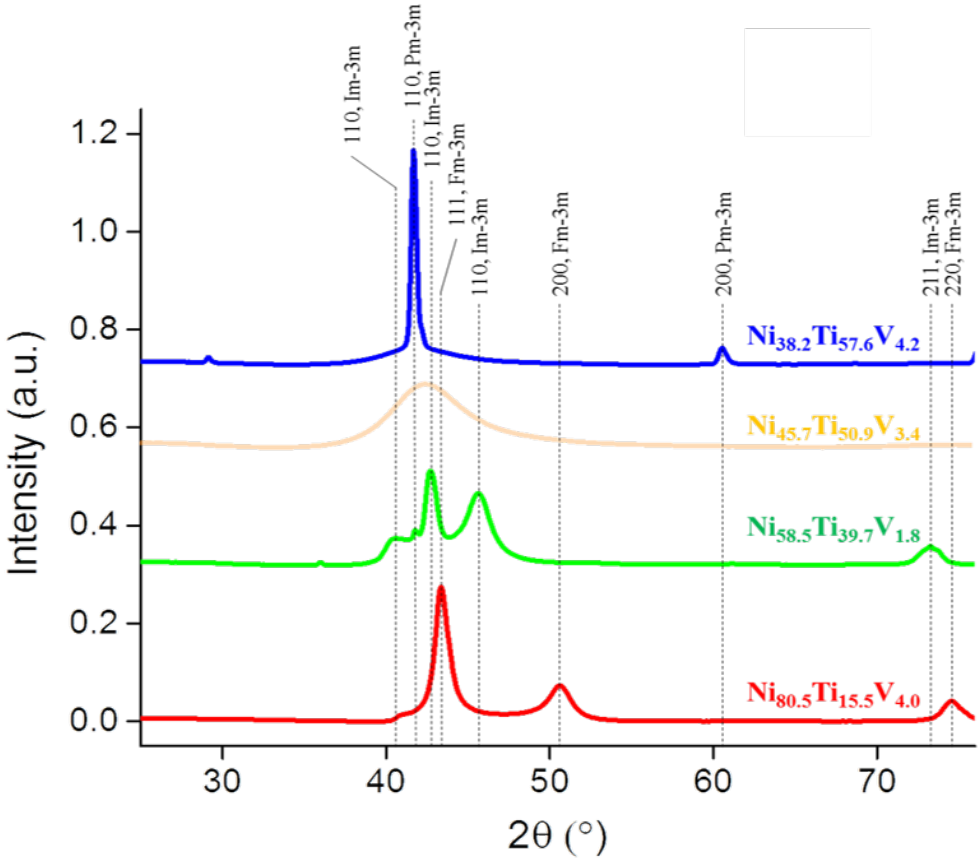

Figure 5.6: Representative XRD patterns (wafer positions 109, 136, 175, and 82 top to bottom) from the Ni-Ti-V library arranged in decreasing order of Ni from the abscissa, reflecting a shift from singly $Fm3m$ phase to a mixture of $Im3m$ with $Pm3m$ and single phase again of $Pm3m$. Patterns are offset for clarity.

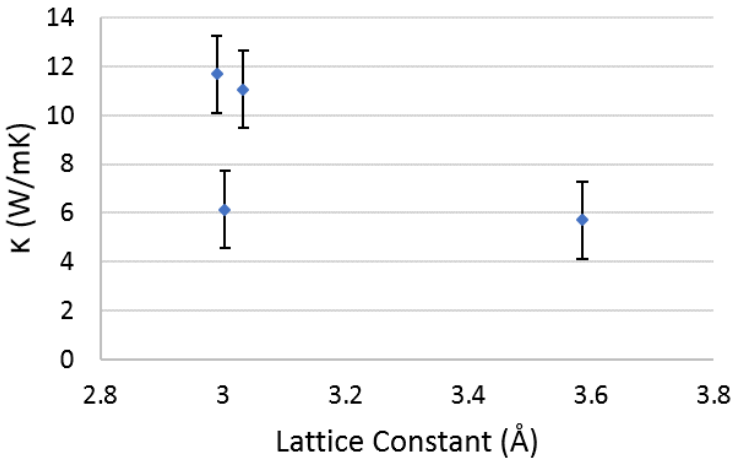

Figure 5.7: Thermal conductivity as a function of lattice constant a for the representative Ni-Ti-V XRD patterns in Fig. 5.6.

Formula	Space Group	Space Group Number	Prototype
$(Ti\ V_{99})_{0.02}$	Im3m	229	
C_8	Im3m	204	
$(Ni_{82}\ Ti_{18})_{0.04}$	Fm3m	225	
$(Ti_{0.67}\ V_{0.33})\ Ni_3$	P63/mmc	194	hexagonal
$Cu\ Ni\ Ti_2$	Pm3m	221	
Ni	Im3m	229	
Ni Ti	Pm3m	221	
$Ni_{0.15}\ V_{0.85}$	Im3m	229	
$Ni_{0.6}\ V_{0.4}$	Fm3m	225	
$Ni_{1.02}\ Ti_{0.98}$	Pm3m	221	
$Ni_3\ Ti$	P63/mmc	194	hexagonal
$Ni_3\ V$	Fm3m	225	
Ti V	Im3m	229	
$Ti_{0.05}\ V_{0.95}$	Pm3m	229	
$V_{16}\ O_3$	I4/mmm	139	tetragonal
V	Im3m	229	

Table 5.4: Overview of crystal structures identified in the Ni-Ti-V materials library. Default crystal type under prototype is cubic unless specified otherwise.

5.3.5 Ni-Ti-Cu-V composition spread library

The composition covered in the library was shown in the previous chapter as varying across the wafer with atomic percent ranges for the four elements as follows: Ni from 21.3 to 58.3 at.%, Ti from 23.3 to 57.5 at.%, Cu from 12.9 to 24.9 at.%, and V from 2.9 to 6.2 at.%. Figure 5.8(a) shows the library as a ternary plot with vanadium held normal to the page as the 4th axis of a 3-dimensional pyramid. Thermal conductivity was measured for the entire library and it ranged from 0.5 to 18.1 W/mK. κ as a function of composition is shown in Figure 5.8(b) also as a ternary plot holding V on axis normal to the page and in Figure 5.9 as a function of elemental concentration. A reduction in κ with addition of copper was observed as seen in Figure 5.9(c). Overall, compositional change does not reflect in a significant κ change.

The crystallographic characterization for the library is extensively covered in the previous chapter. Like the Ni-Ti-V library in the previous section, representative XRD patterns (Figure 4.5, repeated as 5.10 for convenience) for the Ni-Ti-Cu-V library were used to obtain lattice parameters and evaluate against thermal conductivity for any correlations. The phases here were cubic, hexagonal and orthorhombic but only lattice parameter a from the structures was used to plot against κ in Figure 5.11. No clear trend could be identified.

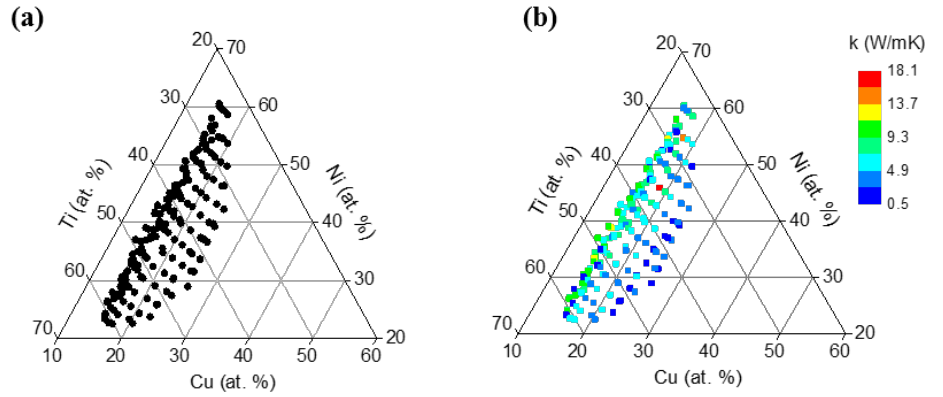

Figure 5.8: (a) Composition range and (b) thermal conductivity as a function of sample composition for Ni-Ti-Cu-V materials library projected on a ternary plot with V content held between 2.9 and 6.1 at.%.

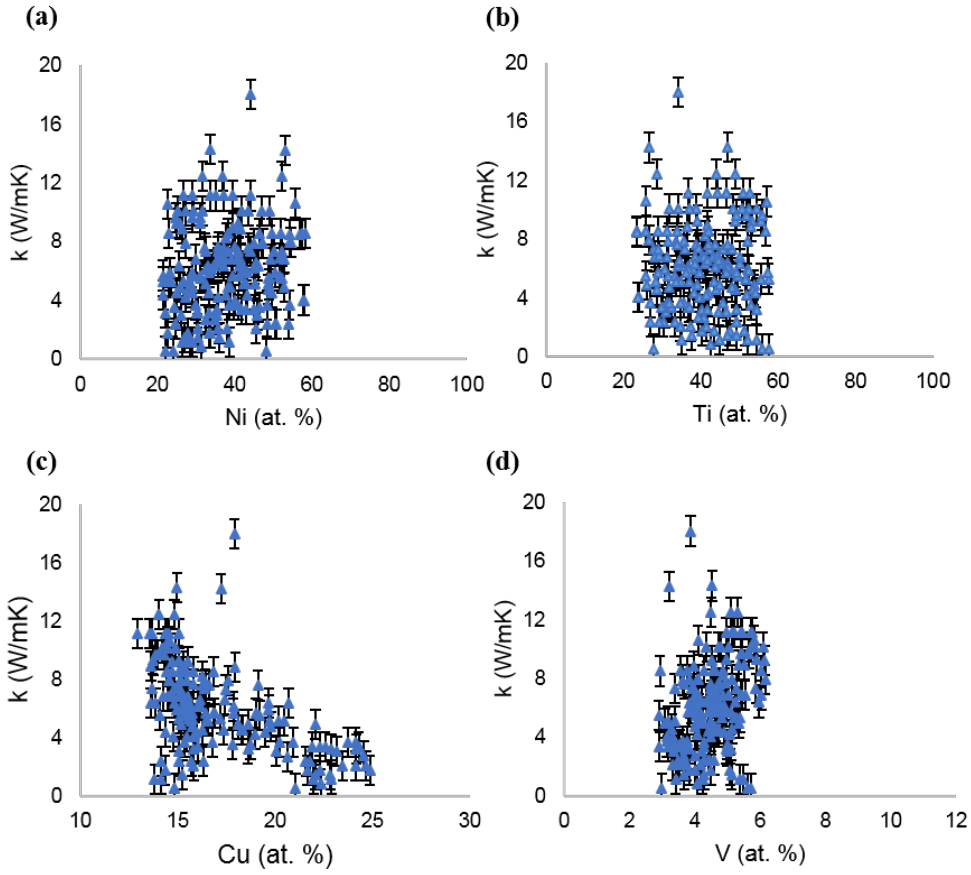

Figure 5.9: Thermal conductivity for the Ni-Ti-Cu-V materials library by elemental concentrations (a) Ni, (b) Ti, (c) Cu and (d) V.

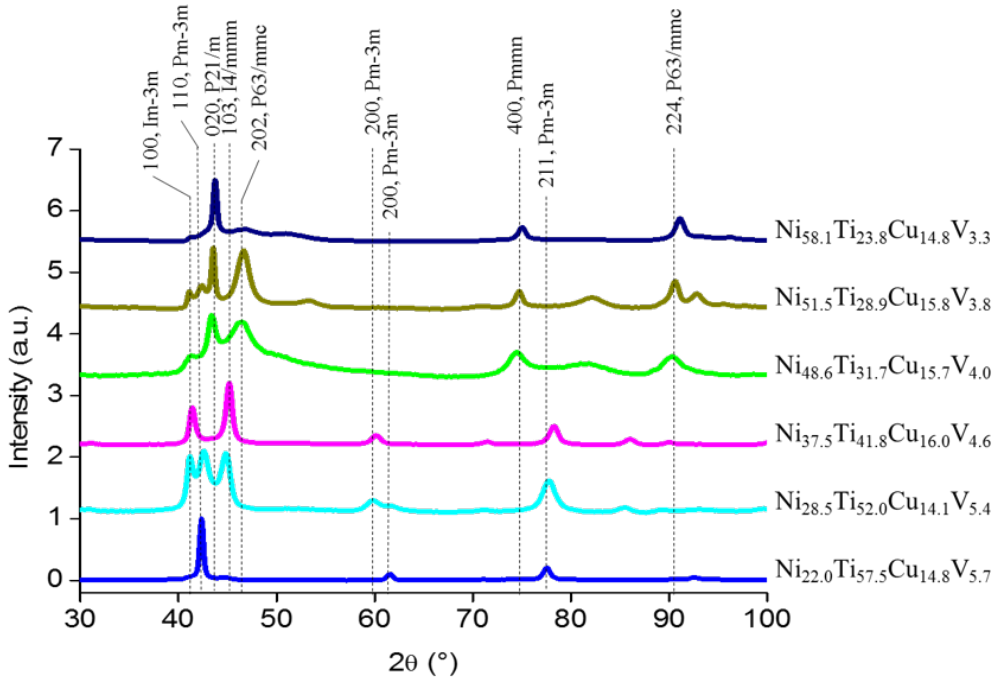

Figure 5.10: Selected diffraction patterns representing the six clusters identified by the Pearson correlation coefficient clustering model. Substitution of Ni by V increases with distance from the abscissa, reflecting a shift in the non-transforming orthorhombic

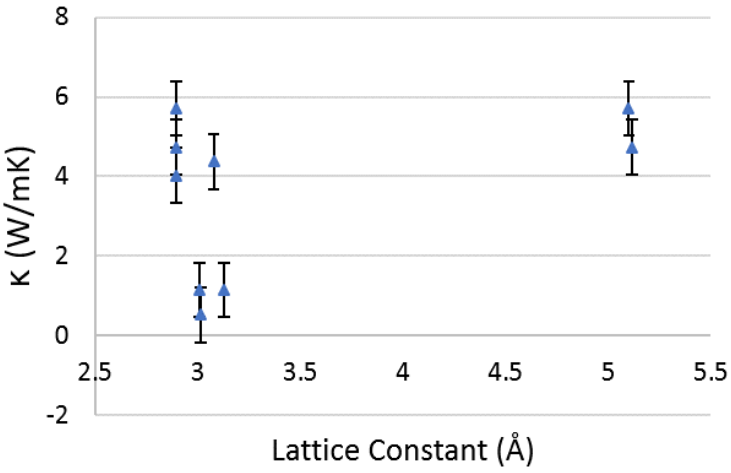

Figure 5.11: Thermal conductivity as a function of lattice constant for the representative Ni-Ti-Cu-V XRD patterns in Fig. 5.10.

5.4 Discussion

The binary Ni-Ti composition space as well as the impact of addition of ternary and quaternary elements to NiTi's thermal properties have not been extensively studied, especially as thin films. Generally, thermal conductivity of a metal is given by the sum of the electronic κ_e and lattice κ_L terms:

$$\kappa = \kappa_e + \kappa_L \tag{5.3}$$

where the electronic term is further defined by Wiedemann-Franz law of:

$$\frac{\kappa_e \rho}{T} = L_0 \tag{5.4}$$

where T is temperature, ρ is dc electrical resistivity, and L_0 is the Lorentz number with a value of $L_0 = 2.45 \times 10^{-8}$ WΩK^{-2} [61]. Furthermore, the effective thermal conductivity κ_{eff} of a thin film is comparable to bulk when its thickness t_f is greater than 50 nm [225], from the correlation of thickness to sample thermal resistance R_S by:

$$R_s = \frac{1}{4\kappa_{eff} b} \tag{5.5}$$

where b is the thermal exchange radius [225]. It increases when t_f <50 as a result of the increasing influence of the substrate at low thicknesses (where Si substrate $\kappa_{bulk} = 150$ W/mK) [225,233]. Grain size also plays an important role in influencing

thermal conductivity such that scattering by the grain boundaries reduces κ [247]. In other words, the smaller the grain size, the greater the control it has in determining κ. Hence, thermal conductivity is highly influenced by not only temperature but also thickness and grain size.

For all the combinatorial films investigated in this chapter, the film thickness ranged from an average of 147 nm ($\pm$5 nm) for Ni-Ti library to an average of 264 nm ($\pm$5 nm) for Ni-Ti-Cu-V (Figure S5.13). It is hypothesized that the grain size in this size range is likely to be the same or less than the film thickness, thereby, having significant influence on κ. This makes it imperative to have control over grain size which is, in turn, dependent on processing conditions in addition to composition.

From Figure 5.3 for the Ni-Ti system, the increasing Ni content reflects an increase in κ. As increasing Ni content stabilizes austenite through the Ti_3Ni_4 precipitate, it follows our expectations of a high κ for a material in austenitic phase at RT. When bulk binary NiTi was measured with Xenon flash, the martensite registered at $\sim$7-10 W/mK whereas the austenite was between 13-18 W/mK across the temperature range explored (data not shown); these values are comparable (albeit slightly lower) to the bulk κ. Therefore, the binary NiTi thin film κ values are consistent with recent bulk measurements.

For the case of Ni-Ti-V, a wide range of κ values are observed at higher Ni content without a clear trend. A high κ around V = 5-6 at.% followed by a decrease is observed (Figure 5.5(c)) while no clear trend could be visually identified for Ni

and Ti. This change in κ at V = 5-6 at.% raises the question of whether phase transformation or other material properties are also affected in the same range. M_s temperature has been reported to decrease with increasing V concentration up to 6 at.% [51] whereas no change in M_s occurs due to formation of (Ti,V)Ni + V_9(Ti,Ni) [98, 248]. Measuring resistance as a function of temperature to evaluate phase transformation in this library, therefore, is an effort to be undertaken in the near future.

For the Ni-Ti-Cu-V system, an overall relationship between composition and κ is unclear. However, elemental influence on κ from Cu is observed (Figure 5.9(c)). Composition-dependent thermal conductivity of NiTi was reported to reach a maximum at stoichiometry (15 W/mK at room temperature) and decrease with deviation from stoichiometry [194, 195]. This library was shown to have the transforming phases of austenite and martensite present. Cu substitution for Ni as size factor is favorable but TiCu is tetragonal instead of cubic [194]. Larger discrepancy in thermal conductivity was found at elevated temperatures (for austenite) than for martensite (κ_M) [196]. Ingale et al show that the specific heat capacity of $Ni_{40}Ti_{50}Cu_{10}$ and $Ni_{48.5}Ti_{50}Fe_{1.5}$ is reduced by two orders of magnitude, despite an increase in the thermal conductivity by 1.5 factors [61]. The single vs two step transformation are characterized by change in thermal conductivity due to change in the lattice term κ_L instead of the electronic term κ_e [61, 249]. When investigating dependence of κ on the lattice parameters of this library, a correlation was difficult to observe but may be visualized differently. Furthermore, for binary AB compounds, the general rule

proposed has been that a monotonical reduction in thermal conductivity occurs in constituent A from constituent B with increasing horizontal distance in the period table such that κ[CoTi] $>$ κ[NiTi] [202]. Thermal conductivities obtained from webelements.com (Anon n.d.) for elements relevant to this chapters are listed in Table 5.5. In principle, κ[VTi] $<$ κ[NiTi]; however, more careful studies are required to verify this claim in the shape memory thin film systems.

Element	κ_{295K} **[W/mK]**
Ti	21.9
V	30.7
Ni	91.0
Cu	400
Si	150

Table 5.5: Thermal conductivities of pure metals

Indeed, repeatability is a significant limitation of SHP for determining thermal conductivity and is a result of changes in contact thermal resistance and thermal exchange area [132, 250]. These changes are a result of a physical alteration of the tip, change in probe geometry, probe-to-sample distance, pressure between sample and probe, changes in ambient temperature, humidity or even sample thermal conductivity [13, 132] (SI Figure S5.14).

Efforts planned for the near future to answer important questions that have come up in the undertaking of this reported work are as follows:understand phase transformation trends in Ni-Ti-V from $R(T)$ curves by performing resistance vs temperature studies using a four-point probe; perform molecular dynamics simulations to determine the effect of addition of ternary and quaternary elements

on transition temperature, latent heat, and thermal conductivity of NiTi; verify increase in κ with temperature by mapping thermal conductivity and its evolution over temperature from higher accuracy frequency domain thermoreflectance (FDTR(T)); investigate grain structure of Ni-Ti-Cu-V from TEM; investigate grain structure evolution in Ni-Ti-Cu-V from temperature-dependent transmission electron microscopy (TEM(T)); and investigate microstructure evolution in Ni-Ti-Cu-V from temperature-dependent X-ray diffraction (XRD(T))

5.5 Conclusions

Binary, ternary and quaternary thin film libraries of Ni-Ti, Ni-Ti-V, and Ni-Ti-Cu-V were evaluated for thermal conductivity using scanning hot probe as a benchmarking exercise. The probe was calibrated using an implicit method where reference materials were fitted to an equation used later to determine thermal conductivity of the unknown samples. Although SHP is not a high-throughput measurement technique, it was used to spatially map the entire quaternary Ni-Ti-Cu-V library. Thermal conductivity was mapped as a function of composition as well as elemental concentration to determine correlations. Work remains to be done in accurately determining the thermal conductivity of NiTi-based alloys in thin film form using high-throughput characterization techniques.

5.6 Chapter Supplementary Information

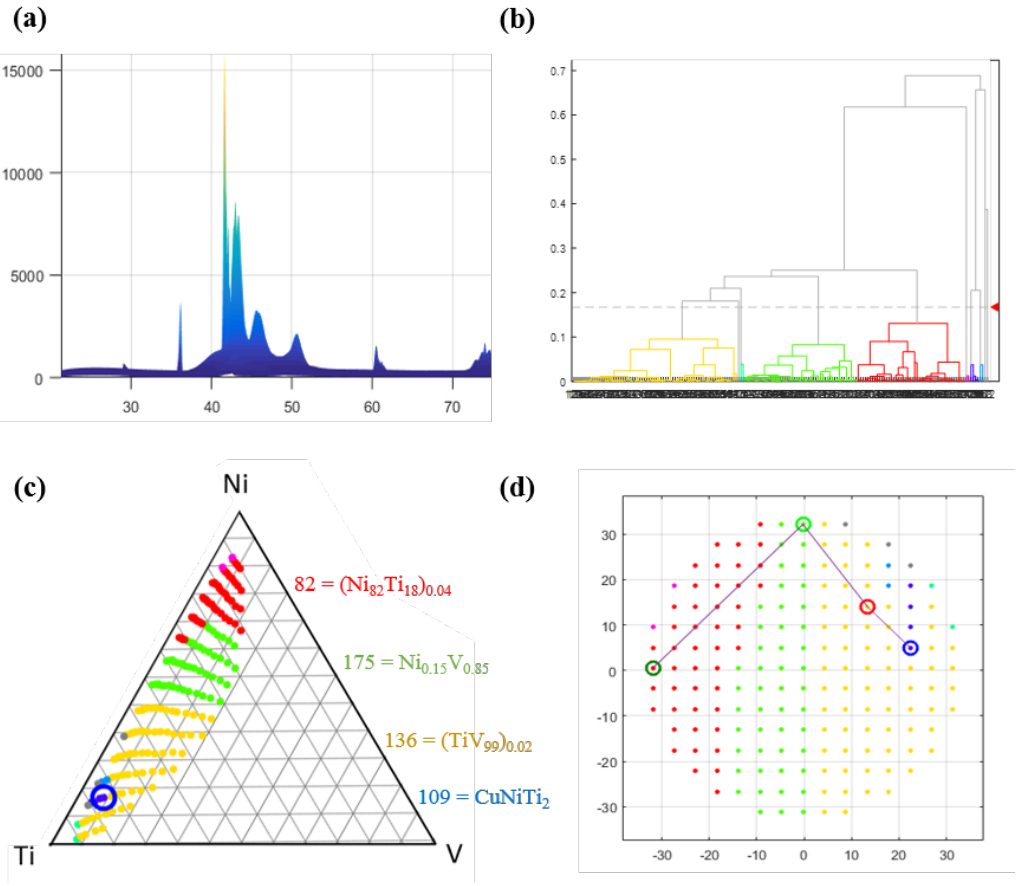

Figure 5.12: Hierarchical cluster analysis of diffraction patterns for the ternary Ni-Ti-V thin film library. (a) 177 diffraction patterns with an x-axis of 2θ between 22 and 75 degrees. (b) Pearson Correlation Coefficient solution showing of grouping of XRD patterns based on similarities in peak positions. (c) Composition space covered in the thin film library grouped by the PCC solution and (d) grouping by position on wafer (long flat edge on bottom) with representative compositions selected and major phase identified for it.

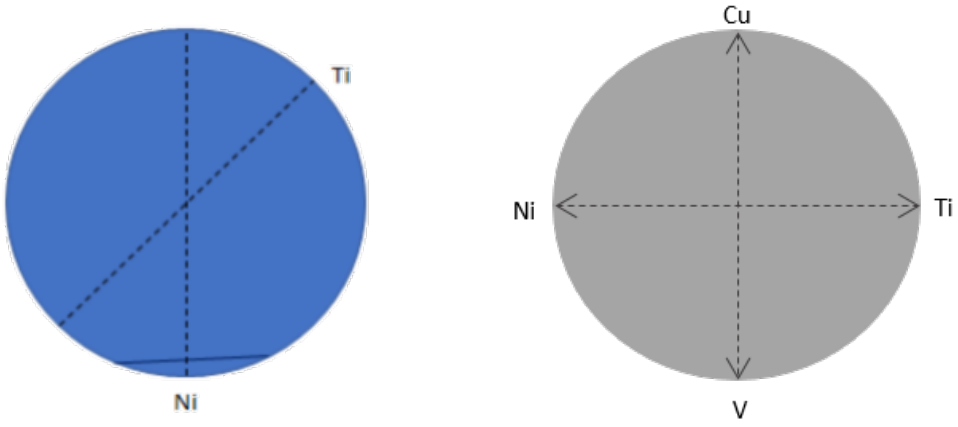

Figure 5.13: Line profiles on wafer along which thickness measurements were performed. Arrows on the quaternary show direction of increasing elemental concentration.

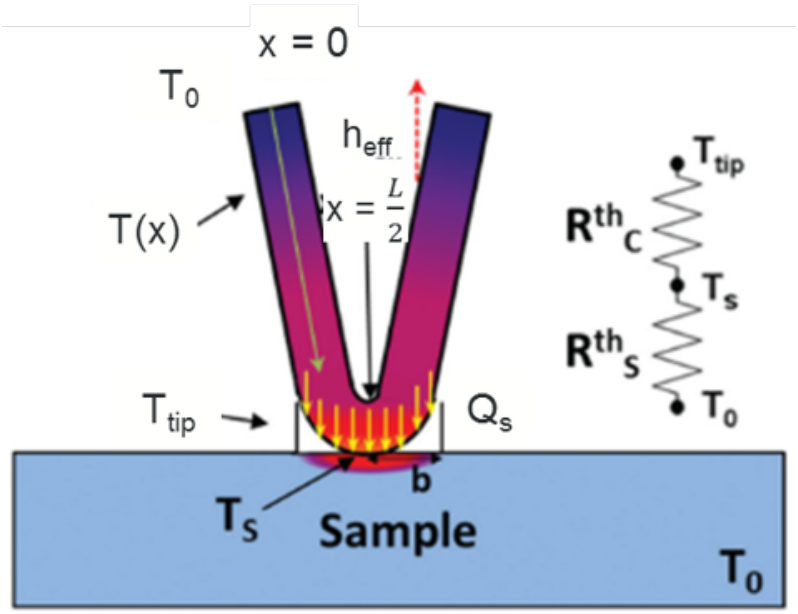

Figure 5.14: Probe and sample thermal interaction showing thermal exchange radius, b, and thermal contact resistance R_C^{th} as adapted from [13].

The change in sample properties can be approximated with the following equation where a large change in temperature may induce microstructural changes:

$$\Delta T \approx \frac{I^2 R t}{\frac{2}{3}\pi r^3 \rho c} \tag{5.6}$$

where R is thermal contact resistance or R_c^{th}, t is time, ρ is film density, and c is specific heat of NiTi film. Taking values of R = 312.9 Ω, t = 10 s, I = 0.004 A, ρ = 6450 kg/m^3 [251] and c = 840 J/kgK [251], we get an approximate value of 1.2 $\times$ 10^7 K.

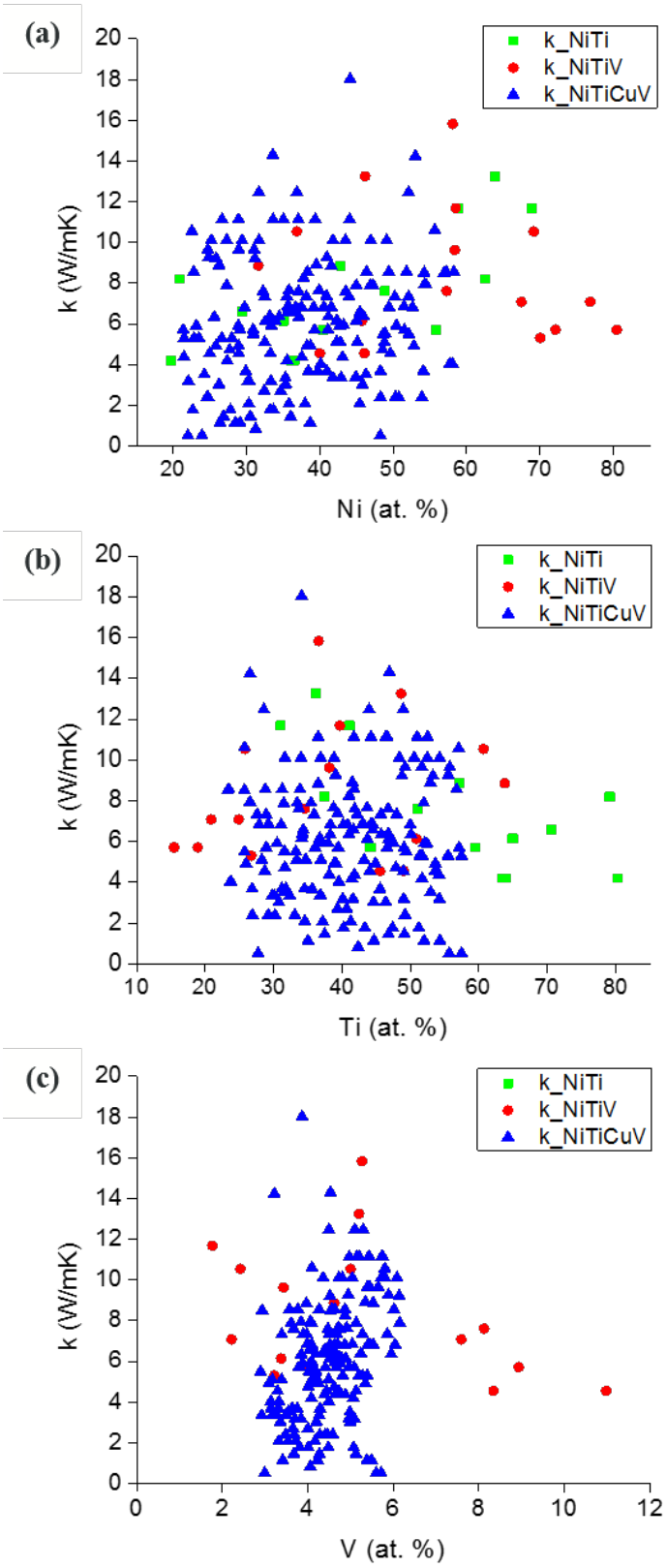

Figure 5.15: Thermal conductivity as a function of elemental content (a) Ni, (b) Ti, (c) V in Ni-Ti, Ni-Ti-V, and Ni-Ti-Cu-V thin film libraries.

Chapter 6: Conclusions and Outlook

The unique properties of shape memory alloys compared to regular metals make them highly attractive candidates for many applications. The economic impact of their deployment is immense, evidenced by the number of patents proposed and awarded, amounting to over 15,700 as of this writing [63, 252]. For the intended application in elastocaloric cooling, replacing gas refrigerants having GHG leak potential with solid-state refrigerants based on NiTi shape memory alloys offers a sustainable and clean alternative. In the present work, NiTi-based ternary and quaternary shape memory alloys were investigated using combinatorial materials science. Composition spreads covering previously unexplored composition spaces were prepared with magnetron co-sputtering of pure targets. These were then characterized for different properties using automated high-throughput techniques, thereby, providing large datasets for high resolution analysis and machine learning. New shape memory alloy compositions were discovered in the Ni-Ti-Co system, having small thermal hysteresis. Nonetheless, a new compositional region having narrow thermal hysteresis (ΔT between 0.5 and 2 °C) centered around 6 at.% Co in Ti-rich regions was identified. XRD patterns for these compositions had signatures

for single phases having cubic crystal structures, thus, confirming the theoretical and experimental studies reported in literature for phase transforming Ni-Ti alloys. However, no systematic dependence of transformation temperatures on chemical composition with Co content could be identified.

Similarly, investigation of the the Ni-Ti-Cu-V thin film library showed a new composition space having near-zero thermal hysteresis, stable over at least 100 temperature cycles. Increasing addition of V was observed to stabilize compositions exhibiting SMA behavior through the identified mixture of cubic and tetragonal phases. Martensite start temperature was indeed reduced overall in the library but it is unclear what the dependency is in a quaternary alloy with elemental concentration of V. In both the above systems, crystallography was crucial to understanding and predicting the observance of shape memory effects in a materials library.

Recommendations for future work on NiTi-based SMAs arise from new questions identified during this dissertation work. It is clear that the compositions having optimized thermal hysteresis and phase transformation characteristics need to be scaled up and evaluated for performance at the system level. It is also clear that only a small composition space for both the ternary Ni-Ti-Co and quaternary Ni-Ti-Cu-V was covered, which limits straightforward correlation of properties with chemical composition. As such, an expanded composition space needs to be evaluated for better predictions and modeling as well as greater collaboration between theory and experimentation. Furthermore, only a limited number of processing conditions were investigated, and additional microstructural studies could provide greater insights

into material properties. For example, temperature dependent X-ray diffraction and microscopy may elucidate the two-step transformation processes by following the evolution of grains and microstructure over a temperature range. Strengthening NiTi alloys with nanoprecipitates of supercooled austenite in a stiff matrix has been shown useful to prepare self-healing metallic alloys [253, 254]. Studying influence of size of the particle, matrix composition, temperature and strain of the system on the martensitic phase transformation of the nanoparticles [253] may also provide critical additional insights. For thermal conductivity measurements, work remains to be done in automating characterization with SHP as well as frequency-domain thermoreflectance.

All together, these efforts should bridge the gap between fundamental studies of thin films with practical applications of scaled up alloys. Ultimately, combinatorial materials science has its own limitations based on the large parameter space we can explore and if our goal is to accelerate the discovery and development and deployment of materials, an effort in that direction is employing predictive experimentation by applying machine learning methods to the large datasets and automate trend discovery. This would allow us to predict fruitful experiments, focusing time and resources on systematic rather than random efforts, hoping for serendipitous discoveries. Finally, the combinatorial methodology applied in this work could be extended to material systems and applications beyond shape memory alloys and applications.

Appendix A: XRD analysis of Ni-Ti-Hf thin film materials library

Increase in M_s in Ni-rich Ni-Ti-Hf due to precipitation of Ni_4Ti_3 [255] but decrease due to formation of (Ti, Hf)$_2$Ni [256]. Transformation temperature and superelasticity at >100 °C with SME under high stress 500 MPa, therefore, high temperature SMA. Low ductility, high slope in stress-induced martensite transformation region. Microstructural engineering via aging, alloying, and processing [257]. Replacement of Ti with Hf up to 30 at.% Hf linearly increases transformation temperature up to 525 °C [257–259]. Ni lean Ni-Ti-Hf have the following disadvantages: Ni-lean Ni-Ti-Hf alloys have large hysteresis (>50 °C), poor ductility at room temperature, lack of cyclic stability due to the high stress for the reorientation of martensite and de-twinning, low strength for slip, poor formability, and low workability. In equal concentrations, influence of Hf is greater than Au and Pd on the transformation temperatures (TTs) [260–262]. Some common methods to improve the mechanical and shape memory properties of Ni-Ti-Hf alloys include thermomechanical processing, grain refinement in polycrystalline alloys, solid-solution hardening, and precipitate hardening [256–259, 262–264].

In this appendix, the influence of deposition time is evaluated for Ni-Ti-Hf thin film materials library using high-throughput synchrotron-XRD and WDS studies.

A.1 Chemical composition

Two libraries were prepared at deposition times of 20 and 45 minutes (Table A.1). The elemental variation for the two libraries are shown in Figure A.1 and Table A.2. The wafer center of the 20 min and 45 min libraries were $Ni_{36.1}Ti_{50.6}Hf_{13.4}$ and $Ni_{38.0}Ti_{49.1}Hf_{12.9}$, respectively. Influence of deposition time on composition was minimal as can be observed from the chemical composition of the center pads (Table A.1) and Table A.2.

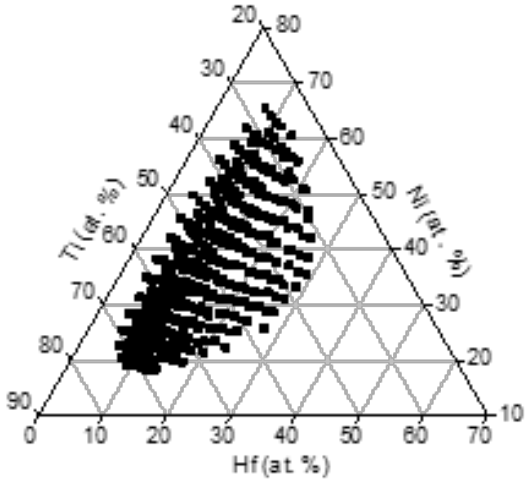

Figure A.1: Composition space covered by the Ni-Ti-Hf thin film materials libraries deposited at two different times of 20 and 45 minutes; showing 354 data points.

ID #	Sample ID	Power [W]			Deposition Time	Annealing		Measured Center Pad Composition
		Ti	Ni	Hf	[min]	[°C]	[min]	Ni-Ti-Hf [at. %]
1	Ni-Ti-Hf_20min	100	31	25	20	500	60	36.1 – 50.6 – 13.4
2	Ni-Ti-Hf_45min				45			38.0 – 49.1 – 12.9

Table A.1: Synthesis conditions for Ni-Ti-Hf thin film libraries at two deposition times.

Element	Min [at. %]	Max [at. %]	Range [at. %]
Ni-Ti-Hf_20min			
Ni	18.2	60.9	42.7
Ti	27.2	71.7	44.5
Hf	6.4	28.8	22.5
Ni-Ti-Hf_45min			
Ni	19.7	65.6	45.9
Ti	25.4	72.0	46.6
Hf	4.3	27.6	23.4

Table A.2: Elemental variation within the Ni-Ti-Hf thin film libraries.

A.2 Crystal structure and phase identification

Influence of deposition time on crystal structure is also minimal. All 354 compositions could be clustered into four main groups, most of which had broad amorphous peaks shifted by a few degrees (Figure A.2). Crystal phases identified in both the libraries are listed in Table A.3. Representative XRD patterns with peaks identified for crystal phases are plotted in Figure A.3.

Trivial Name	**Space Group**	**Space Group Number**	**Prototype**
$HfNi_2$	Fd3m	227	cubic
$HfNi_3$	R-3m	166	rhombo.h.axes
HfTi	P63/mmc	194	hexagonal
$NiHf_2$	I4/mcm	140	tetragonal
NiTi	Pmcm	51	orthorhombic
NiTi	Pm3m	221	cubic
NiTi	P-3	147	hexagonal
Ti	P63/mmc	194	hexagonal
Ti_2Ni	Fd3m	227	cubic
TiC_2	Pm3m	221	cubic
$TiO_{1.25}$	I4/m	87	tetragonal

Table A.3: Overview of crystal structures identified in the Ni-Ti-Hf materials libraries deposited at two different times.

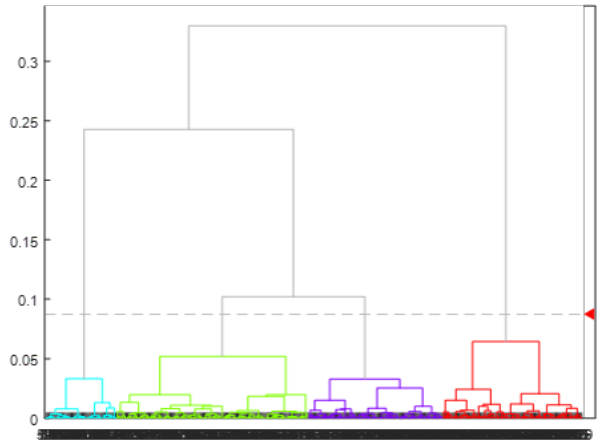

(a)

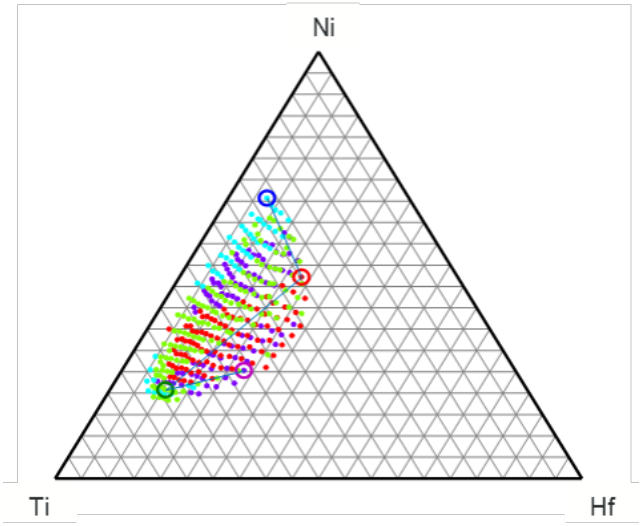

(b)

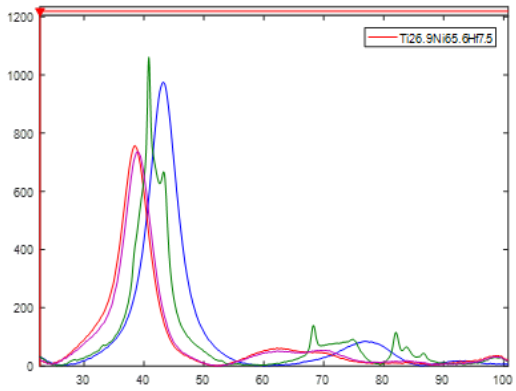

(c)

Figure A.2: (a) Dendogram showing hierarchical clustering of XRD patterns for the Ni-Ti-Hf materials library (b) grouped by compositions with (c) representative positions selected.

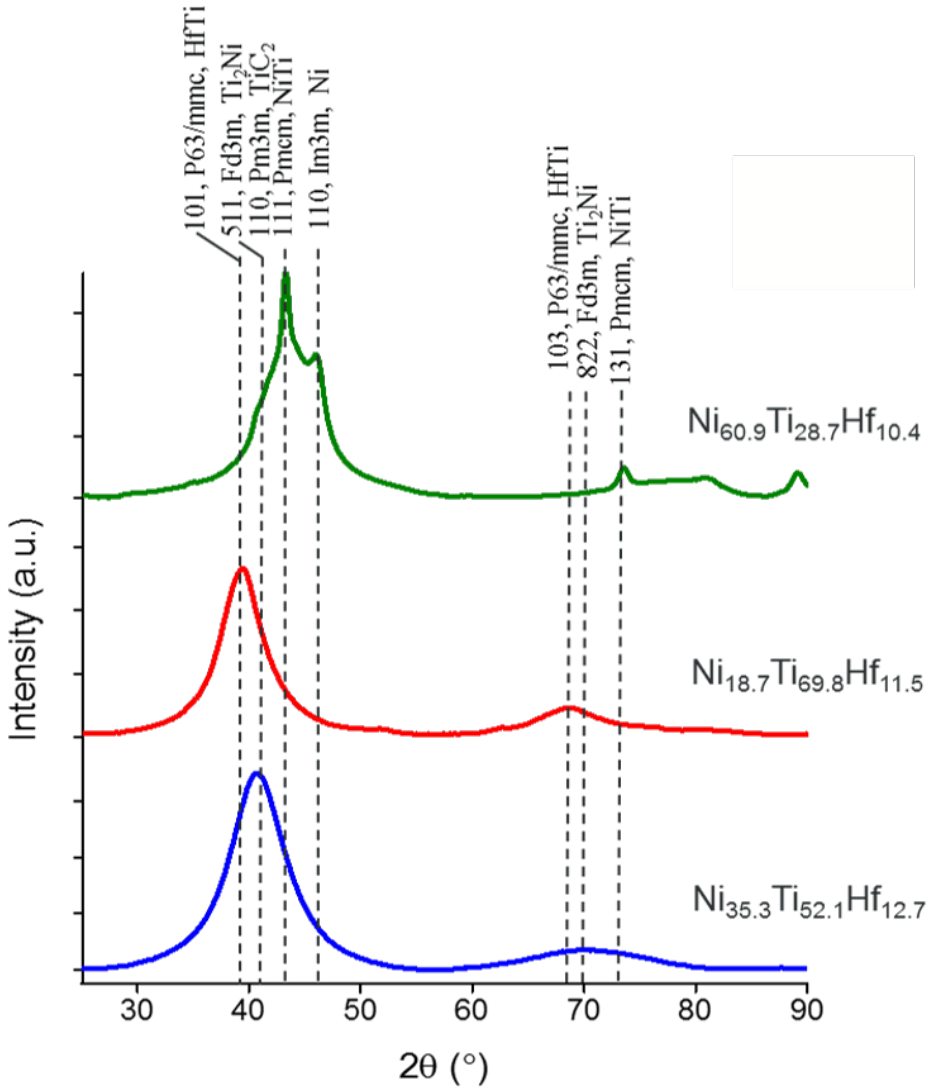

Figure A.3: Selected X-ray diffraction patterns identified from PCC representing phases present in the Ni-Ti-Hf materials libraries deposited at 20 and 45 minutes. Patterns are arranged by ascending Hf content and offset for clarity.

Appendix B: XRD analysis of Ni-Ti-Pd thin film materials library

B.1 Chemical composition

Chemical composition was evaluated for two of the four libraries prepared for the ternary Ni-Ti-Pd. Table B.1 lists the conditions under which these were prepared. Table B.2 lists the elemental variation in the films deposited for 40 and 65 minutes.

ID #	Sample ID	Power [W]			Deposition Time	Annealing		Measured Center Pad Composition
		Ti	Ni	Pd	[min]	[°C]	[min]	Ni-Ti-Pd [at. %]
3	Ni-Ti-Pd_15min	100	30	20	15	500	60	
6	Ni-Ti-Pd_30min				30	-	-	
4	Ni-Ti-Pd_40min				40	500	60	34.1 – 36.5 – 29.3
5	Ni-Ti-Pd_65min				65			31.5 – 46.4 – 22.1

Table B.1: Synthesis conditions for Ni-Ti-Pd thin film libraries at four deposition times.

Element	**Min** [**at. %**]	**Max** [**at. %**]	**Range** [**at. %**]
Ni-Ti-Pd_40min			
Ni	18.1	56.2	38.1
Ti	17.3	59.0	41.7
Pd	14.9	51.8	36.9
Ni-Ti-Pd_65 min			
Ni	15.5	54.6	39.1
Ti	23.7	68.3	44.6
Pd	10.8	42.3	31.5

Table B.2: Elemental variation in the Ni-Ti-Pd thin film material library.

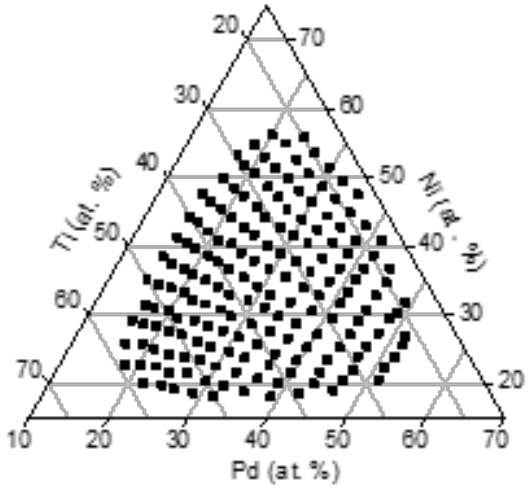

Figure B.1: Composition range of Ni-Ti-Pd materials library deposited for 40 min.

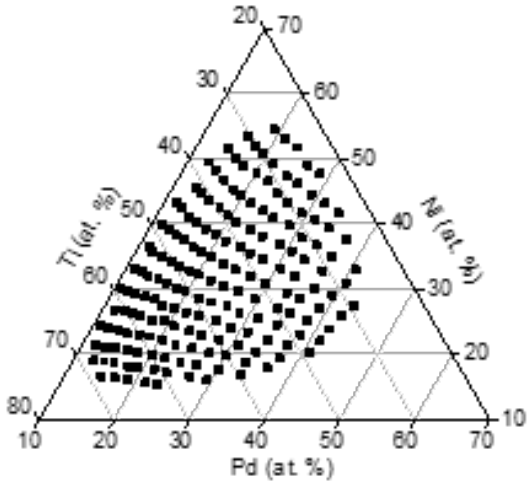

Figure B.2: Composition range of Ni-Ti-Pd materials library deposited for 65 min.

B.2 Crystal structure and phase identification

Tables B.3 and B.4 list the crystal structures present in the 30 min un-annealed library and those deposited at different deposition times but annealed at 500 °C for 1 hr. For the library that was not annealed, only cubic $Fm3m$ structures were found.

Trivial Name	Space Group	Space Group Number	Prototype
$Ni_{0.92}Pd_{0.08}$	Fm3m	225	cubic
$(Ni_{23}Ti_2)_{0.16}$	Fm3m	225	
$(Ni_{82}Ti_{18})_{0.04}$	Fm3m	225	
$(Ni_9Ti)_{0.4}$	Fm3m	225	
Ni	Fm3m	225	

Table B.3: Overview of crystal structures identified in the as-is Ni-Ti-Pd materials library (without heat treatment).

Trivial Name	Space Group	Space Group Number	Prototype
$Ni_{0.92}Pd_{0.08}$	Fm3m	225	
$(Ni_{82}Ti_{18})_{0.04}$	Fm3m	225	
$Pd_{0.2}Ti_{0.8}$	Im3m	229	
$Pd_{0.9}Ni_{0.1}$	Fm3m	225	
Ni	Im3m	229	
$Ni_{0.52}Pd_{0.48}$	Fm3m	225	
Ni_3Ti	P63/mmc	194	hexagonal
NiTi	Pm3m	221	
Pd_3Ti	Pm3m	221	
Pd_3Ti_2	Amma	63	orthorhombic
$Ti_{1.02}Ni_{0.53}Pd_{0.45}$	Pmmb	51	orthorhombic

Table B.4: Overview of crystal structures identified in the heat-treated Ni-Ti-Pd materials libraries deposited at three different times; the default crystal structure type is cubic unless specified otherwise under prototype.

Appendix C: XRD analysis of Ni-Ti-V thin film materials library

Advantages of adding V with its low melting point and specific gravity [265] to NiTi facilitates large energy absorption during cyclic tensile testing and high critical transformation stress [266]. Change in M_s is due to change in electron concentration of the matrix which occurs due to precipitation [98]. M_s temperature decreases with increasing V concentration up to 6 at.% [51]. No change in M_s due to formation of (Ti,V)Ni + V_9(Ti,Ni) [98, 248]. Higher concentrations of V exhibit broad transformation peaks due to a constrained B19'→B2 transformation of NiTi through presence of more plastically deformed V nanowires [265, 267, 268]. Diameter of V nanowires in $Ni_{38}Ti_{37}V_{25}$ reduces upon cold working [269]. Transformation temperature range is broader for $Ni_{40}Ti_{31}V_{29}$ compared to alloys with lower V content [269]. Increase in grain size due to annealing at higher temperature increased the critical transformation stress [265,270] . Effect of annealing temperature on two-step transformations (B2 ↔R↔B19) for alloys annealed at 450 °C vs 500 °C [265]. V content 1 to 5 at.% in addition to heat treatments at 873, 973, 1073, 1173 K are shown with differential scanning calorimetry and XRD studies to increase electrical resistivity of alloy with increasing V content and heat treatment temperature [271].

ID #	Sample ID	Power [W]			Deposition Time	Annealing		Measured Center Pad Composition
		Ti	Ni	V	[min]	[°C]	[min]	Ni-Ti-V [at. %]
	Ni-Ti-V_47min	100	65	20	47	500	60	58.1 – 36.6 – 5.3

Table C.1: Synthesis conditions for Ni-Ti-V thin film libraries at two deposition times.

Element	Min [at. %]	Max [at. %]	Range [at. %]
Ni-Ti-V_20 min			
Ni	30.7	81.5	50.7
Ti	15.3	65.6	50.3
V	1.8	14.2	12.4

Table C.2: Elemental variation within the Ni-Ti-V thin film library.

C.1 Chemical composition

See section 5.3.4 in chapter 5

C.2 Crystal structure and phase identification

See section 5.3.4 in chapter 5.

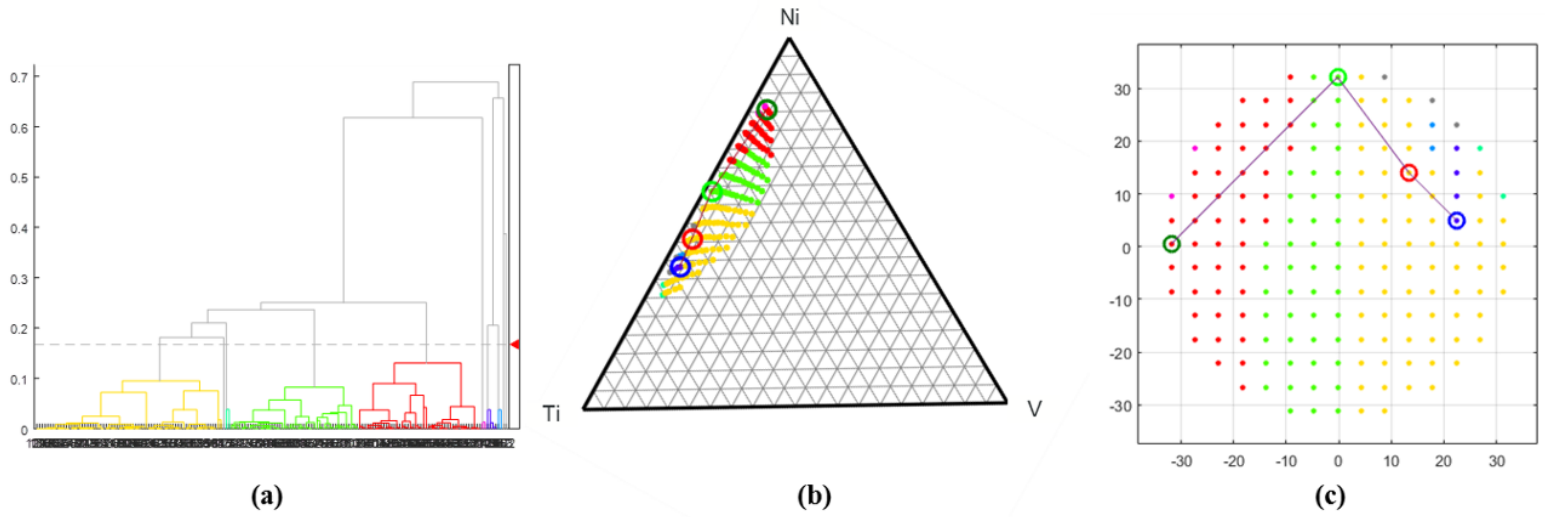

Figure C.1: (a) Dendogram showing hierarchical clustering of XRD patterns for the Ni-Ti-V materials library (b) clustered by compositions and (c) by wafer positions.

Appendix D: XRD analysis of Ni-Ti-Cu-Fe thin film materials library

D.1 Chemical composition

Two films were made under conditions listed in Table D.1 for an elemental range listed in Table D.2.

ID #	Sample ID	Power [W]				Deposition Time	Annealing		Measured Center Pad Composition
	[at. %]	**Ti**	**Ni**	**Cu**	**Fe**	**[min]**	**[°C]**	**[min]**	**Ni-Ti-Cu-Fe [at. %]**
14	$[Ti_{55}–Ni_{33}–Cu_{12}]_{(100x)}Fe_x$	100	27	26	15	30	500	60	33.7 - 55.8 - 6.7 - 3.9
15	$[Ti_{52}–Ni_{36}–Cu_{12}]_{(100x)}Fe_x$	95	27	17	15				36.1 -54.3 - 5.7 - 4.0

Table D.1: Synthesis conditions for Ni-Ti-Cu-Fe thin film materials library.

Element	Min [at. %]	Max [at. %]	Range [at. %]
Ni-Ti-Cu-Fe – 500 °C			
Ni	17.8	58.8	41.0
Ti	31.3	73.0	41.7
Cu	4.9	12.2	7.3
Fe	1.7	9.5	7.8

Table D.2: Elemental variation in the Ni-Ti-Cu-Fe thin film materials library.

D.2 Crystal structure and phase identification

Table D.3 lists the crystal structures present in the two Ni-Ti-Cu-Fe libraries annealed at 500 °C for 1 hr.

Trivial Name	**Space Group**	**Space Group Number**	**Prototype**
$(Cu_{0.03}\ Ni_{0.97})_3$ Ti	P63/mmc	194	hexagonal
$(Fe_{0.5}\ Ni_{0.5})$ Ti	Pm-3m	221	
Cu Ni Ti	I4/mmm	139	tetragonal
Fe	Im-3m	229	
Fe Ni	P	0	
Fe Ti	Pm-3m	221	
Ni Ti	P31m	157	hexagonal
Ni Ti	Pm-3m	221	
Ni Ti	P21/m	11	monoclinic
$Ni_{1.02}\ Ti_{0.98}$	Pm-3m	221	
Ni_3 Ti	P63/mmc	194	hexagonal
	Pm-3m	221	$Ni_{3.04}\ Si_{0.96}$
Ti_2 Cu	Fd-3m	227	

Table D.3: Overview of crystal structures identified in the Ni-Ti-Cu-Fe materials library annealed at 500 °C for 1 hr; the default crystal structure type is cubic unless specified otherwise under prototype.

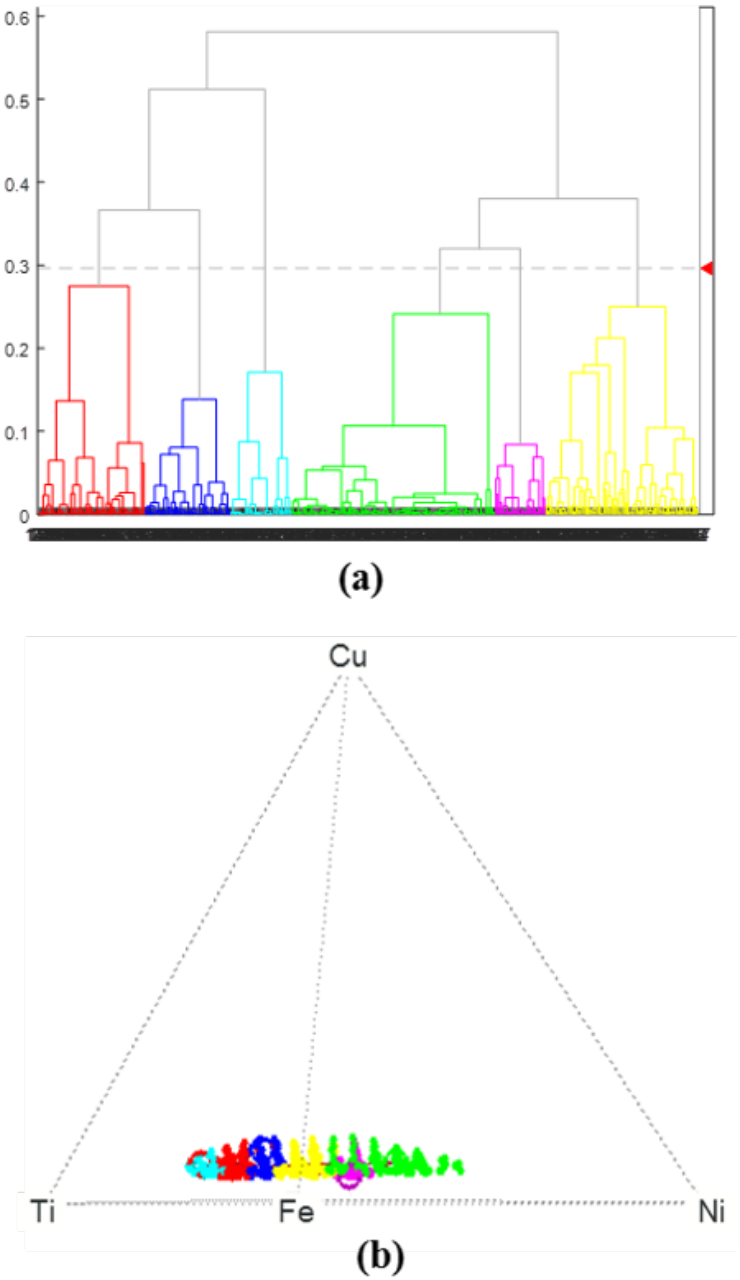

Figure D.1: (a) Dendogram showing hierarchical clustering of XRD patterns for the Ni-Ti-Cu-Fe materials library and (b) 2-dimensional depiction of the corresponding grouping of compositions in the quaternary space.

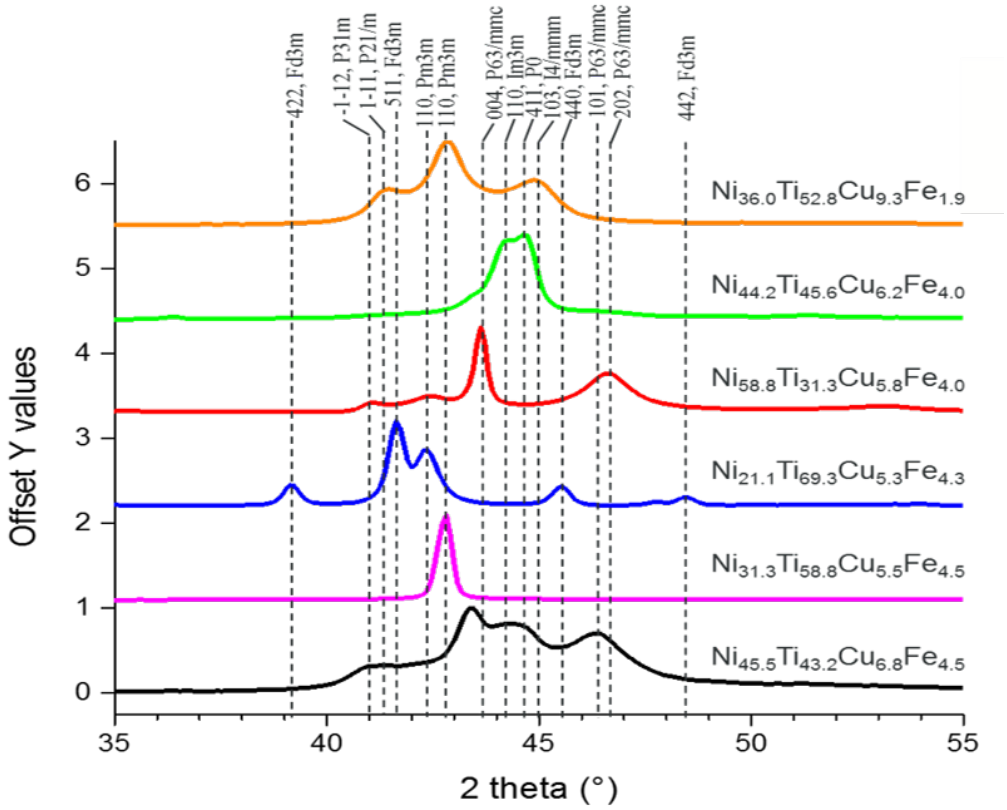

Figure D.2: Selected X-ray diffraction patterns identified from PCC of XRD representing phases present in the Ni-Ti-Cu-Fe materials library annealed at 500 °C for 60 min. Patterns are arranged by ascending Fe content and offset for clarity.

Appendix E: XRD analysis of Ni-Ti-Cu-Co thin film materials library

Impact of gran size in $Ni_{34.2}Ti_{50.8}Cu_{12.5}Co_{2.5}$ thin film samples was recently shown to have a strong asymmetry in stability between thermally and stress induced transformation such that only the fine grain sized film was found to be stable for both. The different grain sizes were prepared via multilayer sputter system and annealed at two different temperatures – 500 °C and 700 °C for 15 min and characterized for their transformation behavior [77] . Compositions of Ni-Ti-Cu-Co have also been shown to have negligible fatigue and an improved material coefficient of performance of 15 [3, 272]. This section explores the effect of two annealing temperatures on Ni-Ti-Cu-Co composition spreads rather than a single composition. Complete sets of high-throughput composition and structure data were used to map structural changes and understand if precipitate hardening to strengthen NiTi thin films can be achieved by annealing them at elevated temperatures. Table E.1 lists the synthesis conditions for the two systems discussed in this section. Aging has been shown to change the martensitic transformation temperatures of NiTi-based alloys [84, 98, 248, 255, 256, 273–287].

E.1 Chemical composition

Automated WDS measurements were carried out on all 354 samples in the two material libraries. Elemental distributions across the wafer and quaternary composition maps are not shown here. However, Table E.1 lists chemical compositions for the center sample pad where the targeted composition is likely to be present. Table E.2 lists the elemental range present in the libraries with little variation between them which simplifies comparison.

ID #	Sample	**Power [W]**				**Deposition Time**	**Annealing**		**Measured Center Pad Composition**
	[at. %]	**Ti**	**Ni**	**Cu**	**Co**	**[min]**	**[°C]**	**[min]**	**Ni-Ti-Cu-Co [at. %]**
8	$[Ti_{52}–Ni_{36}–Cu_{12}]_{(100x)}Co_x$	100	27	26	15	30	500	60	35.7 – 46.7 - 11.9 – 5.7
9							700	15	34.7 – 46.7 - 12.8 – 5.8

Table E.1: Synthesis conditions for Ni-Ti-Cu-Co thin film libraries at two annealing temperatures.

Element	Min [at. %]	Max [at. %]	Range [at. %]
Ni-Ti-Cu-Co – 500 °C			
Ni	19.8	55.7	35.9
Ti	26.8	64.1	37.3
Cu	9.5	19.8	10.3
Co	2.5	13.0	10.5
Ni-Ti-Cu-Co – 700 °C			
Ni	19.3	55.3	36.0
Ti	27.1	63.6	36.5
Cu	9.8	21.0	11.2
Co	2.3	13.4	11.1

Table E.2: Elemental variation within the thin film libraries.

E.2 Crystal structure and phase identification

Like the material libraries before, CombiView was used to perform a Pearson Correlation Coefficient hierarchical cluster analysis of the diffraction patterns. Six and five clusters were determined for the Ni-Ti-Cu-Co libraries at 500 and 700 °C, respectively (Figure E.1 and E.2). Tables E.3, E.4 and E.5 list the crystal structure and space group of all the phases identified in the two libraries, plotted in Figures E.3 and E.4, respectively. The default structure type is a cubic phase unless specified otherwise under prototype. At least five crystal structures are common to both the NiTiCu-V and NiTiCu-Co systems: CuNiTi, NiTi, $Ti(Cu_{0.053}\ Ni_{0.947})_3$, and Ti $Ni_{0.2}Cu_{0.2}$ in orthorhombic and monoclinic arrangements.

Trivial Name	Space Group	Space Group Number	Prototype
($Co_{0.5}$ $Ni_{0.5}$) Ti	Pm-3m	221	
($Co_{0.75}$ $Ni_{0.7}$5) $Ti_{1.5}$	Fd-3m	227	
(Cu Ni) Ti	I4/mmm	139	tetragonal
($Ni_{0.875}$ $Co_{0.125}$) Ti	Pm-3m	221	
$Co_{0.15}$ $Ni_{0.85}$ Ti	Pm-3m	221	
Cu Ni Ti_2	Pm-3m	221	
Ni	P63/mmc	194	hexagonal
Ni Ti	Pm-3m	221	
$Ni_{1.02}$ $Ti_{0.98}$	Pm-3m	221	
Ti Co	Pm-3m	221	
Ti $N_{i0.8}$ $Cu_{0.2}$	Pmam	51	orthorhombic

Table E.3: Overview of crystal structures identified in the Ni-Ti-Cu-Co materials libraries annealed at 500 °C for 1 hr; the default crystal structure type is cubic unless specified otherwise under prototype.

Trivial Name	Space Group	Space Group Number	Prototype
$(Cu_{19}$ Ni$)_{0.2}$	Fm-3m	225	
Co Ti2	Fd-3m	227	
$Co_{0.52}$ $Cu_{0.48}$	Fm-3m	225	
	P63/mmc	194	$Cu_{0.5}$ Ge_2 $Ni_{2.5}$
$Cu_{0.81}$ $Ni_{0.19}$	Fm-3m	225	
	Pm-3n	223	Mo_3 $Ni_{0.24}$ $Si_{0.76}$
Ni	Fm-3m	225	
Ni Ti	Pm-3m	221	
Ni Ti_2	Fd-3m	227	
$Ni_{0.5}$ $Cu_{0.5}$	Im-3m	229	
Ni3 Ti	P63/mmc	194	hexagonal
Ti ($Co_{1.5}$ $Ni_{1.5}$)	P63/mmc	194	hexagonal
Ti $(Cu_{0.053}$ $Ni_{0.947})_3$	P63/mmc	194	hexagonal
Ti $Ni_{0.8}$ $Cu_{0.2}$	Pmam	51	orthorhombic
Ti $Ni_{0.8}$ $Cu_{0.2}$	P21/m	11	monoclinic

Table E.4: Overview of crystal structures identified in the Ni-Ti-Cu-Co materials libraries annealed at 700 °C for 15 min; the default crystal structure type is cubic unless specified otherwise under prototype.

Formula	Space Group	Space Group Number	Prototype
$(Co_{0.5}\ Ni_{0.5})\ Ti$	Pm-3m	221	
$(Co_{0.75}\ Ni_{0.75})\ Ti_{1.5}$	Fd-3m	227	
Cu Ni Ti	I4/mmm	139	tetragonal
$(Cu_{19}\ Ni)_{0.2}$	Fm-3m	225	
$(Ni_{0.875}\ Co_{0.125})\ Ti$	Pm-3m	221	
$Co\ Ti_2$	Fd-3m	227	
$Co_{0.15}\ Ni_{0.85}\ Ti$	Pm-3m	221	
$Co_{0.52}\ Cu_{0.48}$	Fm-3m	225	
$Cu\ Ni\ Ti_2$	Pm-3m	221	
$Cu_{0.81}\ Ni_{0.19}$	Fm-3m	225	
	Pm-3n	223	$Mo_3\ Ni_{0.24}\ Si_{0.76}$
Ni	Fm-3m	225	
Ni	P63/mm	194	$Cu_{0.5}\ Ge_2\ Ni_{2.5}$
Ni Ti	Pm-3m	221	
$Ni\ Ti_2$	Fd-3m	227	
$Ni_{0.5}\ Cu_{0.5}$	Im-3m	229	
$Ni_{1.02}\ Ti_{0.98}$	Pm-3m	221	
$Ni_3\ Ti$	P63/mmc	194	hexagonal
$Ti\ (Co_{1.5}\ Ni_{1.5})$	P63/mmc	194	hexagonal
$Ti\ (Cu_{0.053}\ Ni_{0.947})_3$	P63/mmc	194	hexagonal
Ti Co	Pm-3m	221	
$Ti\ Ni_{0.8}\ Cu_{0.2}$	P21/m	11	monoclinic
$Ti\ Ni_{0.8}\ Cu_{0.2}$	Pmam	51	orthorhombic

Table E.5: Overview of all crystal structures identified in the Ni-Ti-Cu-Co materials libraries; the default crystal structure type is cubic unless specified otherwise under prototype.

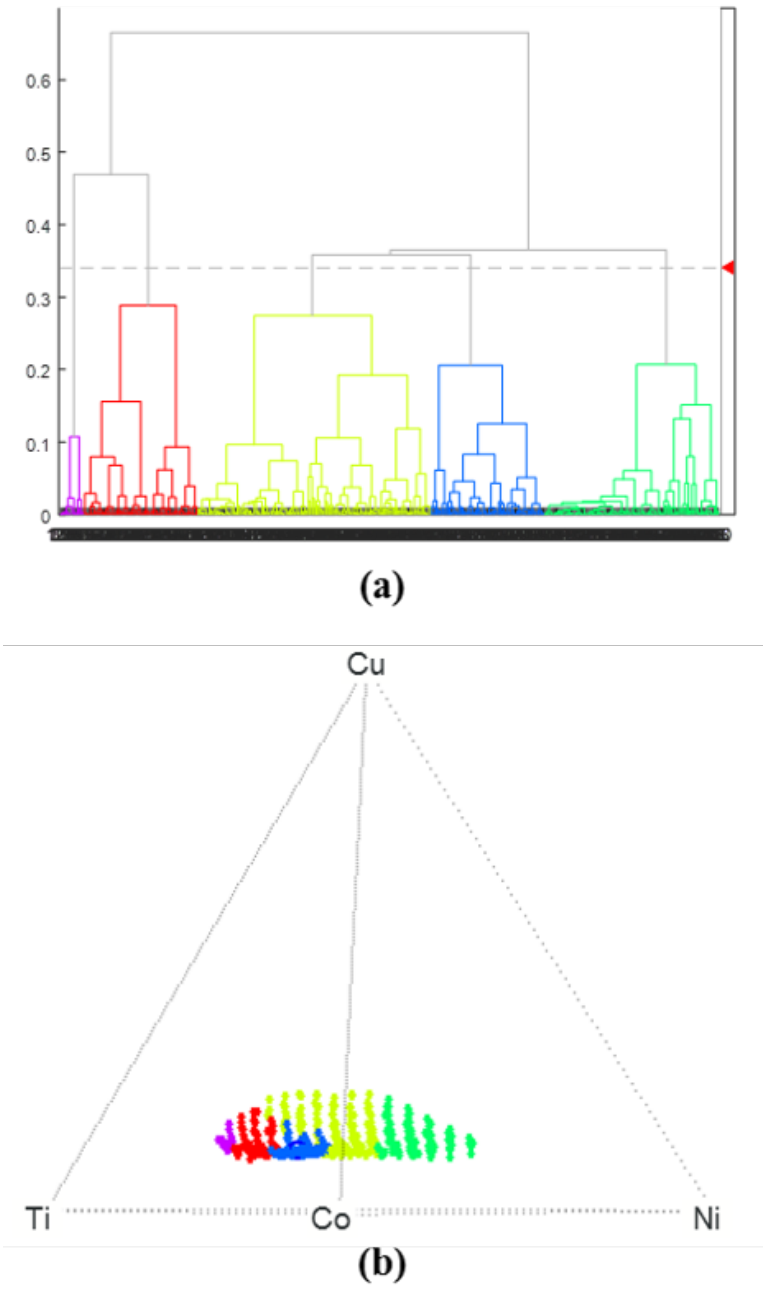

Figure E.1: (a) Dendogram showing hierarchical clustering of XRD patterns for the Ni-Ti-Cu-Co materials library annealed at 500 °C for 1 hr and (b) 2-dimensional depiction of the corresponding grouping of compositions in the quaternary space.

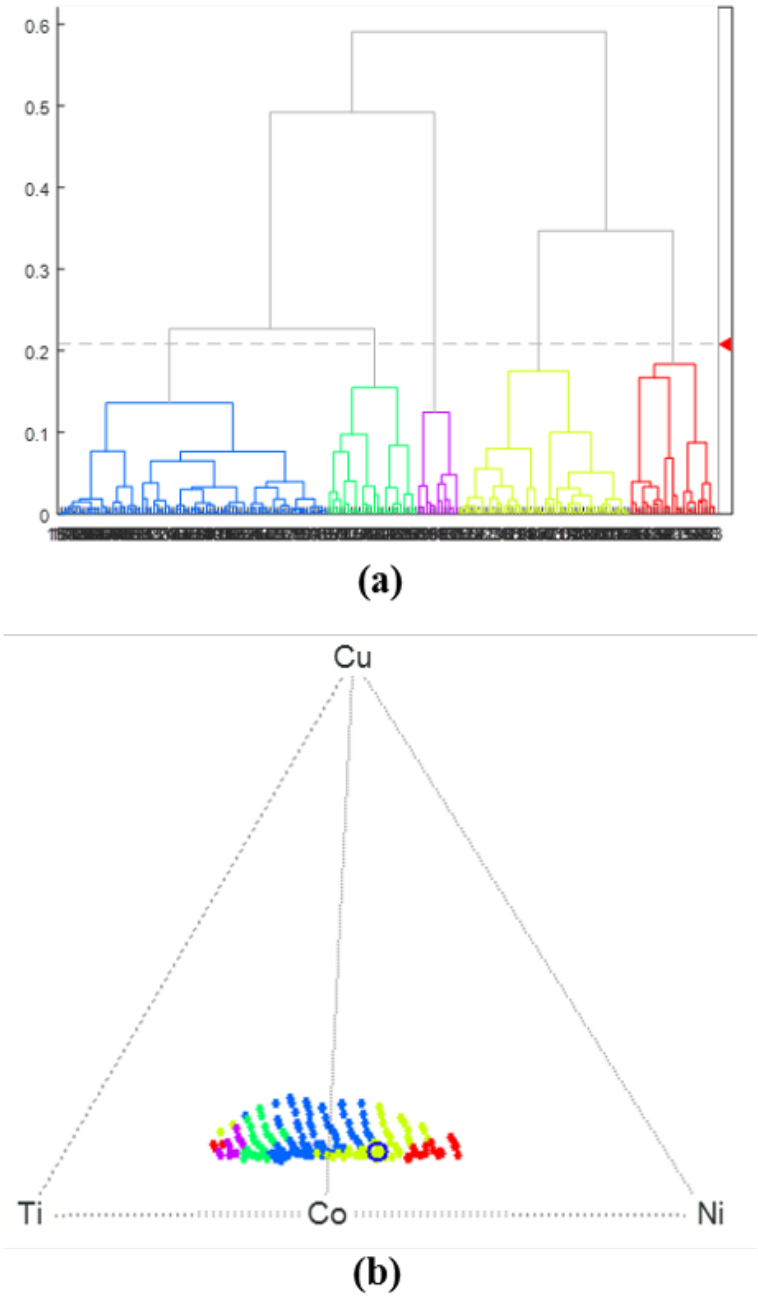

Figure E.2: (a) Dendogram showing hierarchical clustering of XRD patterns for the Ni-Ti-Cu-Co materials library annealed at 700 °C for 15 min and (b) 2-dimensional depiction of the corresponding grouping of compositions in the quaternary space.

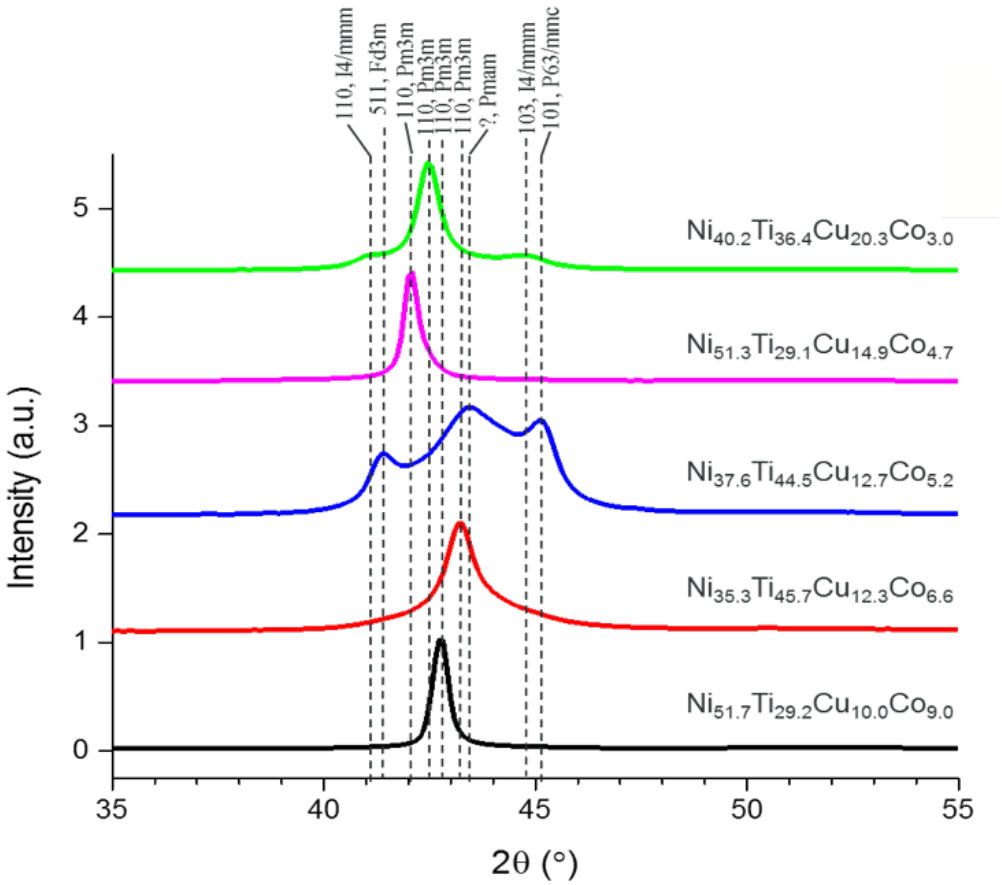

Figure E.3: Selected X-ray diffraction patterns identified from PCC representing phases present in the Ni-Ti-Cu-Co materials library annealed at 500 °C for 60 min. Patterns are arranged by ascending Co content and offset for clarity.

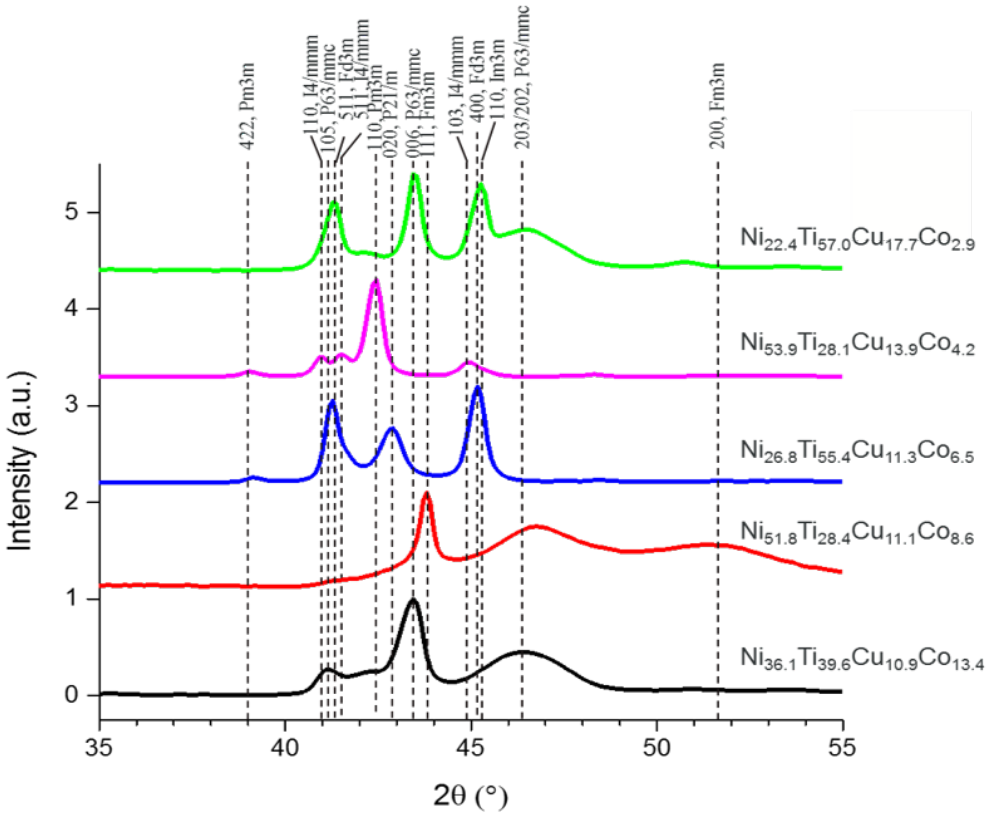

Figure E.4: Selected X-ray diffraction patterns (wafer positions 164, 126, 78, 26, and 3) identified from PCC representing phases present in the Ni-Ti-Cu-Co materials library annealed at 700 °C for 15 min. Patterns are arranged by ascending Co content and offset for clarity.

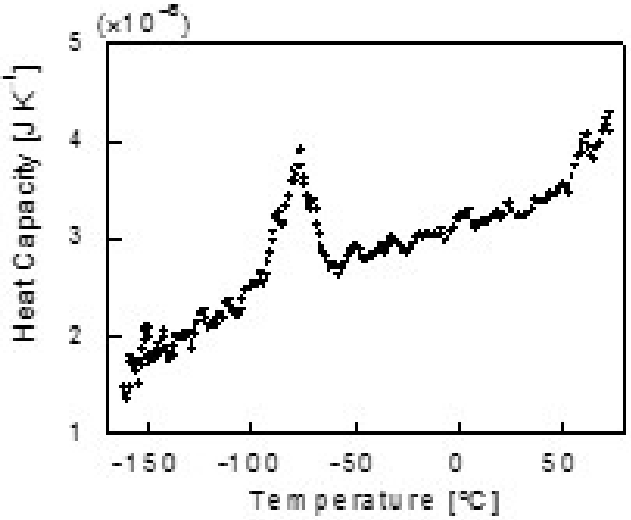

Figure E.5: Plot of measured heat capacity as a function of temperature in $Ni_{36.3}Ti_{46.1}Cu_{11.9}Co_{5.7}$ at.% thin film. The peak indicates occurrence of phase transformation.

Appendix F: XRD analysis of Ni-Ti-Cu-Pd thin film materials library

F.1 Chemical composition

Automated WDS measurements were carried out on all the samples in the two materials libraries. Elemental distributions across the wafer and quaternary composition maps are not shown here. Nonetheless, Table F.1 lists chemical compositions for the center sample pad where the targeted composition is likely to be present. Table F.2 lists the elemental range present in the libraries with little variation between them which simplifies comparison.

ID #	Sample	Power [W]				Deposition Time	Annealing		Measured Center Pad Composition
	[at. %]	**Ti**	**Ni**	**Cu**	**Pd**	**[min]**	**[°C]**	**[min]**	**Ni-Ti-Cu-Pd [at. %]**
10	$[Ti_{55}–Ni_{33}–Cu_{12}]_{(100x)}$ Pdx	100	24	26	6	30	500	60	34.7 – 48.7 – 12.5 – 4.1
12	$[Ti_{52}–Ni_{36}–Cu_{12}]_{(100x)}$ Pd_x	100	22	26	6				31.6 – 49.7 – 14.2 – 4.5
13							700	15	32.5 – 49.2 – 13.7 – 4.6

Table F.1: Synthesis conditions for Ni-Ti-Cu-Pd thin film libraries at two annealing temperatures.

Element	Min [at. %]	Max [at. %]	Range [at. %]
Ni-Ti-Cu-Pd – 500 °C			
Ni	16.7	54.7	38.0
Ti	27.8	66.2	38.4
Cu	9.2	23.5	14.3
Pd	2.0	9.8	7.8
Ni-Ti-Cu-Pd – 700 °C			
Ni	17.2	51.6	34.4
Ti	29.2	64.3	35.1
Cu	11.3	23.2	11.9
Pd	2.1	10.5	8.4

Table F.2: Elemental variation within the Ni-Ti-Cu-Pd thin film libraries.

F.2 Crystal structure and phase identification

Tables F.3 and F.4 list the crystal structures present in the two Ni-Ti-Cu-Pd libraries annealed at differed temperatures.

Trivial Name	Space Group	Space Group Number	Prototype
$(Cu_{0.03}\ Ni_{0.97})_3$ Ti	P63/mmc	194	hexagonal
$Cu_{0.923}\ Ti_{0.077}$	Fm3m	225	
(Cu Ni) Ti	I4/mmm	139	tetragonal
$(Cu\ Ni\ Pd)_{0.333}$	Fm3m	225	Cu Pd, Ni Pd
$Cu_3\ Ti_2$	P4/nmm	129	tetragonal
$Cu_4\ Ti_3$	I4/mmm	139	tetragonal
Cu Ni Ti	I4/mmm	139	tetragonal
$Ni_{0.52}\ Pd_{0.48}$	Fm3m	225	
$Ni_{1.02}\ Ti_{0.98}$	Pm3m	221	
Ni_3 Ti	P63/mmc	194	hexagonal
Ni Ti_2	Fd3m	227	
Pd_3 Ti	Pm3m	221	

Table F.3: Overview of crystal structures identified in the Ni-Ti-Cu-Pd libraries annealed at 500 °C for 1 hr. Default structure is cubic unless specified otherwise.

Trivial Name	Space Group	Space Group Number	Prototype
$(Cu_{0.03}Ni_{0.97})_3$ Ti	P63/mmc	194	hexagonal
(Cu Ni) Ti	I4/mmm	139	tetragonal
$Cu_{0.035}Ni_{0.565}Ti_{0.40}$	P4/nmm	129	tetragonal
$Cu_{0.6}\ P_{0.4}$	Pm3m	221	
Cu Ni Ti	I4/mmm	139	tetragonal
Cu Ni Ti_2	Pm3m	221	
Cu Pd	Fm3m	225	
$Ni_{0.25}\ Cu_{0.75}$	Im3m	229	
$Ni_{1.02}\ Ti_{0.98}$	Pm3m	221	
Ni Ti_2	Fd3m	227	
Pd Cu	Pm3m	221	

Table F.4: Overview of crystal structures identified in the Ni-Ti-Cu-Pd library annealed at 700 °C for 15 min. Default structure is cubic unless specified otherwise.

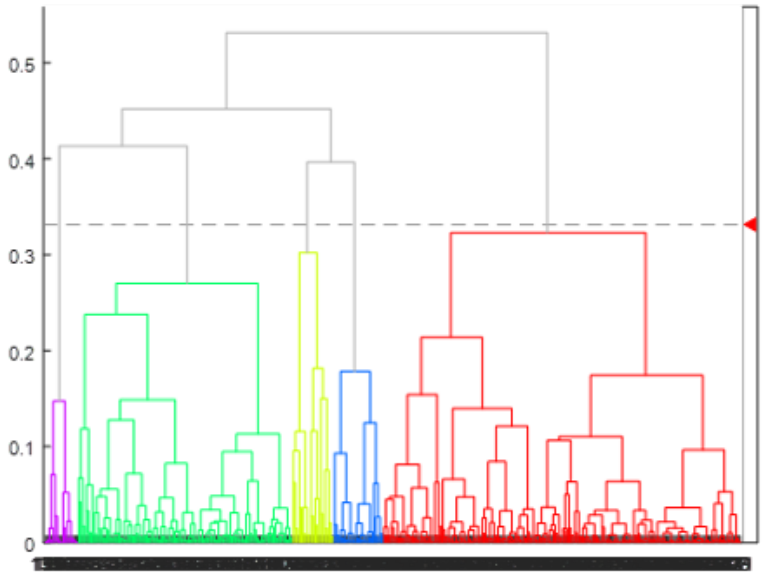

(a)

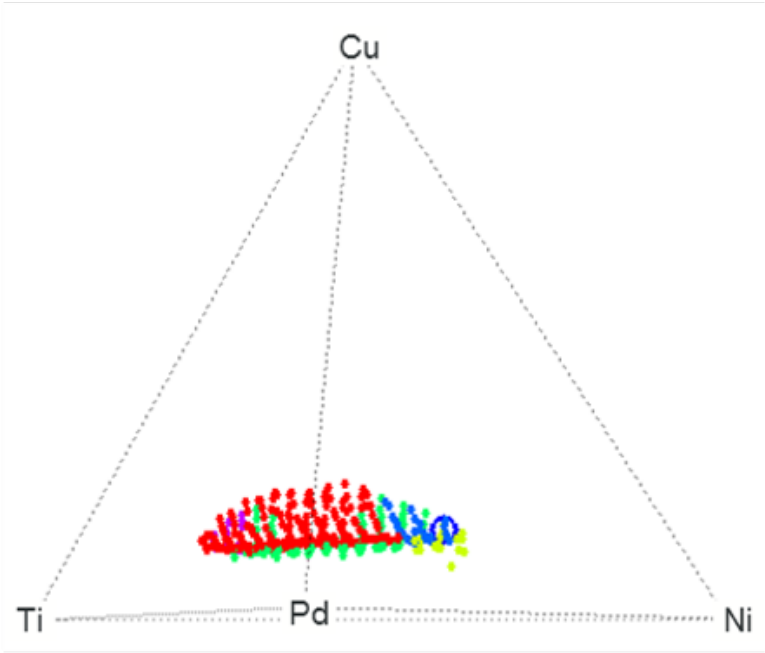

(b)

Figure F.1: (a) Dendogram showing hierarchical clustering of XRD patterns for the Ni-Ti-Cu-Pd materials library annealed at 500 °C for 1 hr and (b) 2-dimensional depiction of the corresponding grouping of compositions in the quaternary space.

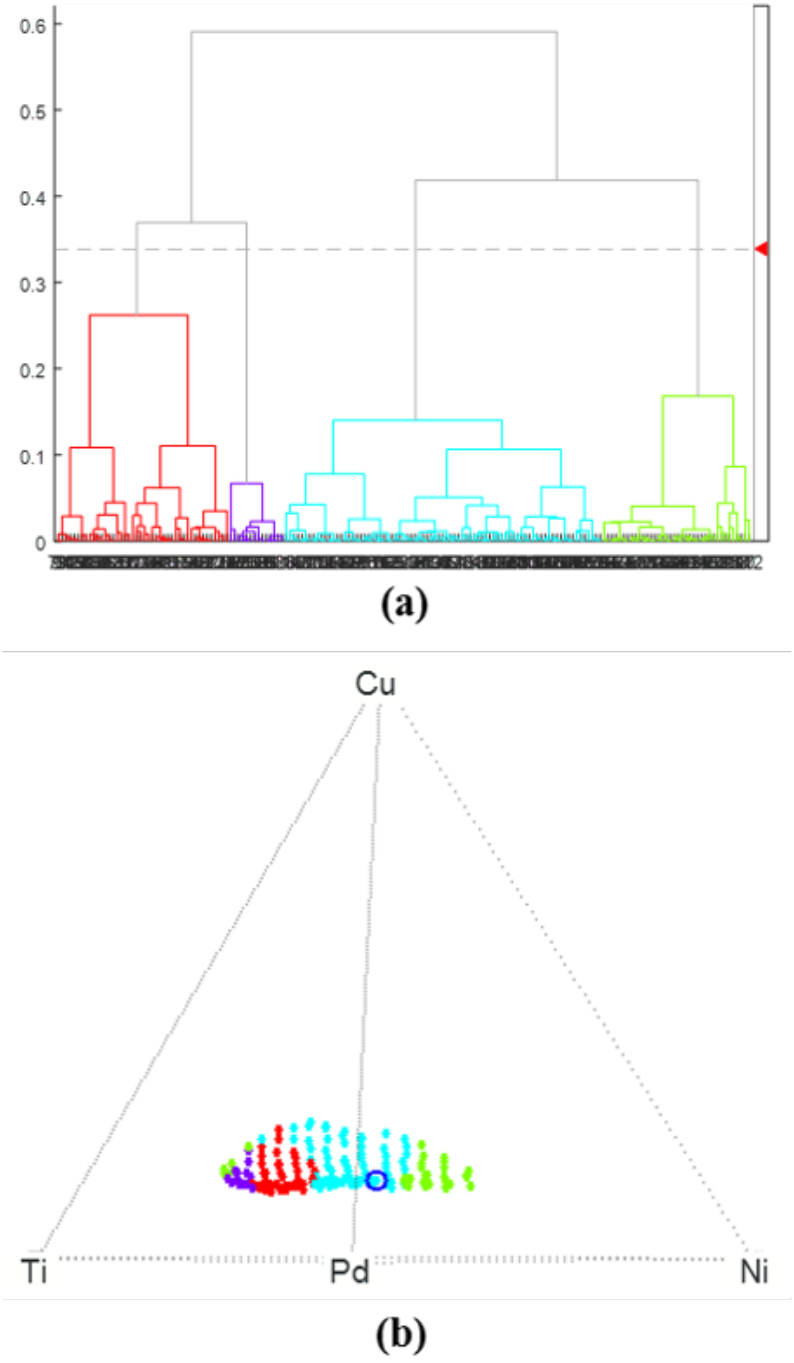

Figure F.2: (a) Dendogram showing hierarchical clustering of XRD patterns for the Ni-Ti-Cu-Pd materials library annealed at 700 °C for 15 min and (b) 2-dimensional depiction of the corresponding grouping of compositions in the quaternary space.

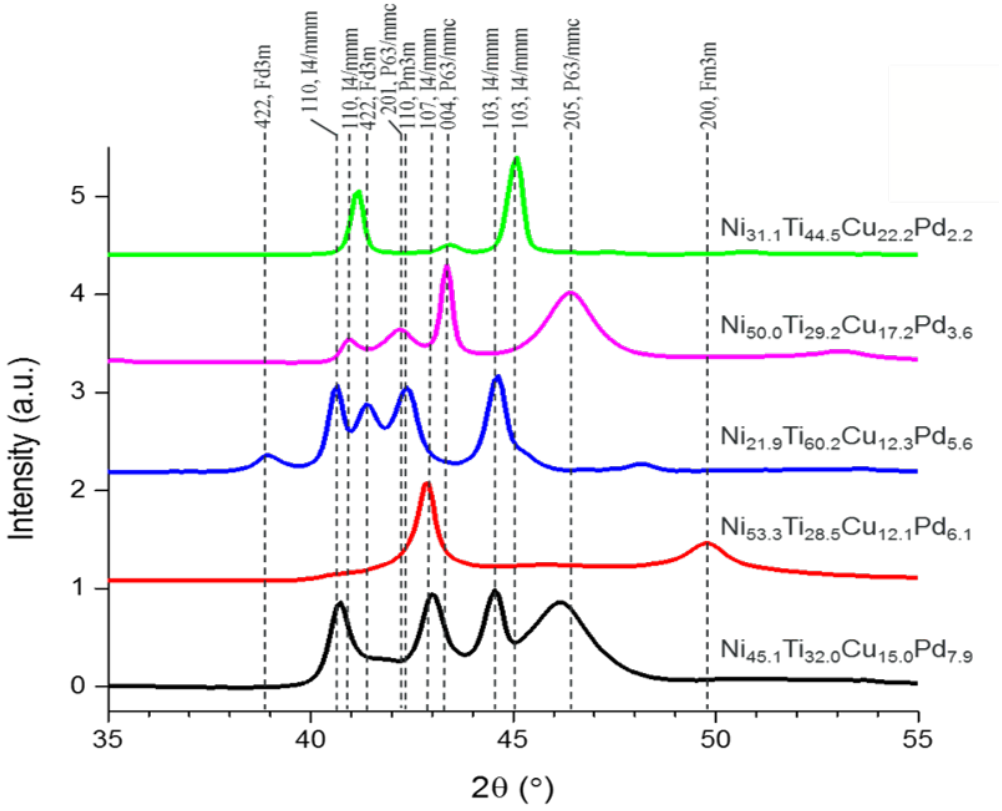

Figure F.3: Selected X-ray diffraction patterns identified from PCC representing phases present in the Ni-Ti-Cu-Pd materials library annealed at 500 °C for 60 min. Patterns are arranged by ascending Pd content and offset for clarity.

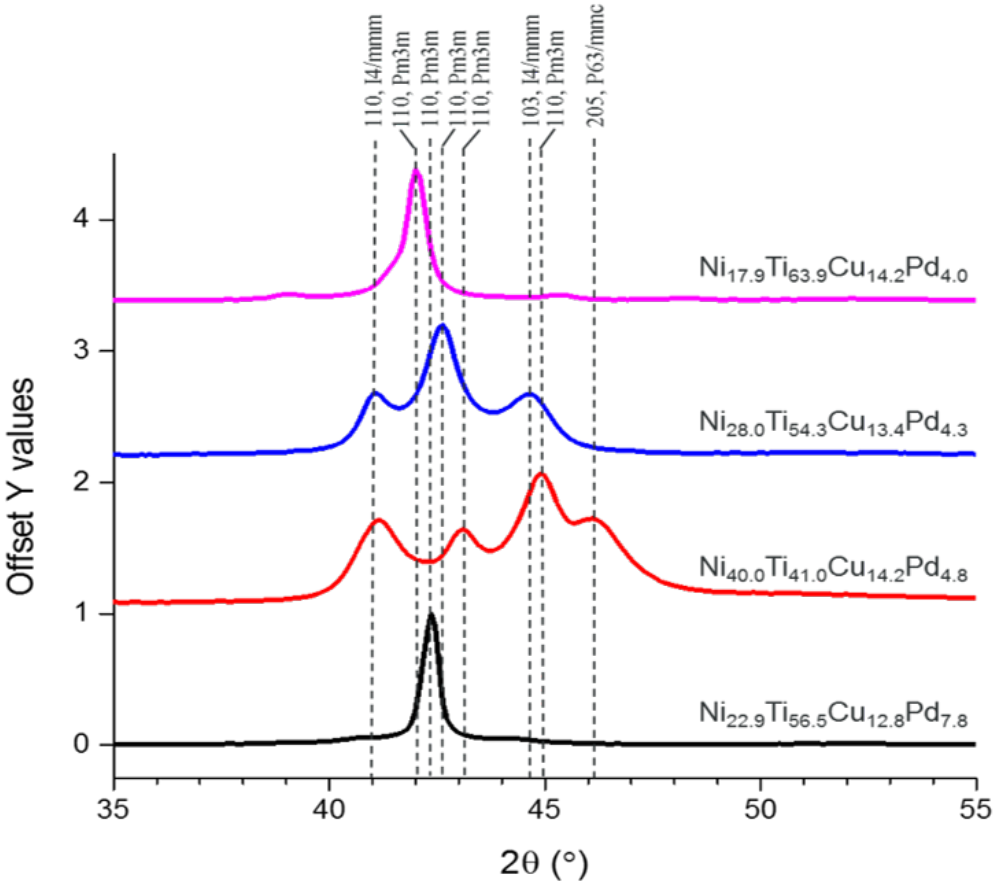

Figure F.4: Selected X-ray diffraction patterns identified from PCC (wafer positions 96, 91, 86 and 25) representing phases present in the Ni-Ti-Cu-Pd materials library annealed at 700 °C for 15 min. Patterns are arranged by ascending Pd content and offset for clarity.

Appendix G: Chemical bonding in Ni-Ti-Co from XPS

These results were recently published in *Journal of Vacuum Science and Technology A* [288].

High resolution spectra were acquired across the materials library for the main 2p elemental lines for the principle metals. A spectral stack of the Ti 2p lines is shown in Figure G.1(a). Differences in spectral form were observed between positions on the wafer indicating differences in the chemical environment and composition of Ti – Figure G.1(b) and G.1(c) show the stark difference between points 153 and 152, respectively. Chemical-state peak fitting indicates the presence of Ti in at least four different chemical states: +4, typically bound to oxygen in the form of titania; +3 a reduced oxide TiO_{2-x}; Ti carbide and metallic Ti [289, 290] . Distribution of Ti^{4+} follows the phase boundary found in XRD and the non-linear decreasing slope *R(T)* curves. The starkest chemical state difference between the two locations is the carbide content which is significantly more abundant at position 152. Figures G.1(g-j) show the distribution of chemical states across the 3-inch wafer indicating a maximum concentration of carbide in the upper right wafer region (Figure G.1(j)).

To confirm presence of carbide, high resolution C 1s spectra were acquired for all analysis positions (Figure G.1(d)). Peak fitting protocols were applied across all spectra (Figure G.1(e-f)). The most intense chemical state of carbon present on the surface is adsorbed adventitious carbon at 285 eV with green peak components which is typical of air-exposed samples. For some regions, however, a distinct peak could be seen at lower binding energy 281.8 eV, indicating carbide formation. A distribution plot of the peak fitted carbide is shown in Figure G.1(k). The C 1s carbide peak distribution matches the Ti 2p peak fitting, indicating a link between the two spectral sets. This correlation suggests that the carbide is titanium carbide and not a carbide of a different metal. Depth profiling using impinging Ar^+ ions was performed to determine the distribution of surface materials (Figure G.2). After etching the surface for several etch cycles, the contribution of carbon on the surface had decreased as the adventitious carbon was removed and the atomic concentration had become steady state for the main elements present indicating the analysis is representative of the bulk composition. Significantly, the carbide composition is constant around 2 at.% with depth, indicating it is not a surface artefact but propagates deeper into the sub-surface and bulk material, similar to observations by Greczynski et al. [291]. By comparison with the Ti 2p peak fitting procedure, which showed the same distribution trend across the wafer, the carbide was slightly underestimated ($\sim$1.72 % compared to 2 %). This error may be due to s/n statistics, or more probably, inaccurate background subtraction. This complication of background subtraction is particularly well documented for 2p transition metal orbitals. Nevertheless, the error is within that expected for the technique. For this reason,

further carbide studies are advised for both peaks – metal and C 1s – to ensure correct chemical state assignment but for quantification to be derived from the C 1s peak due to its simpler line shape, which is less prone to incorrect fitting and peak assignment. XRD patterns for positions 97 and 139, within the vicinity of 153 and 152, respectively, confirm presence of TiC as well (Figure G.3). Further studies are needed to understand why carbide was observed in a specific region over others and to determine the implications of its presence [292].

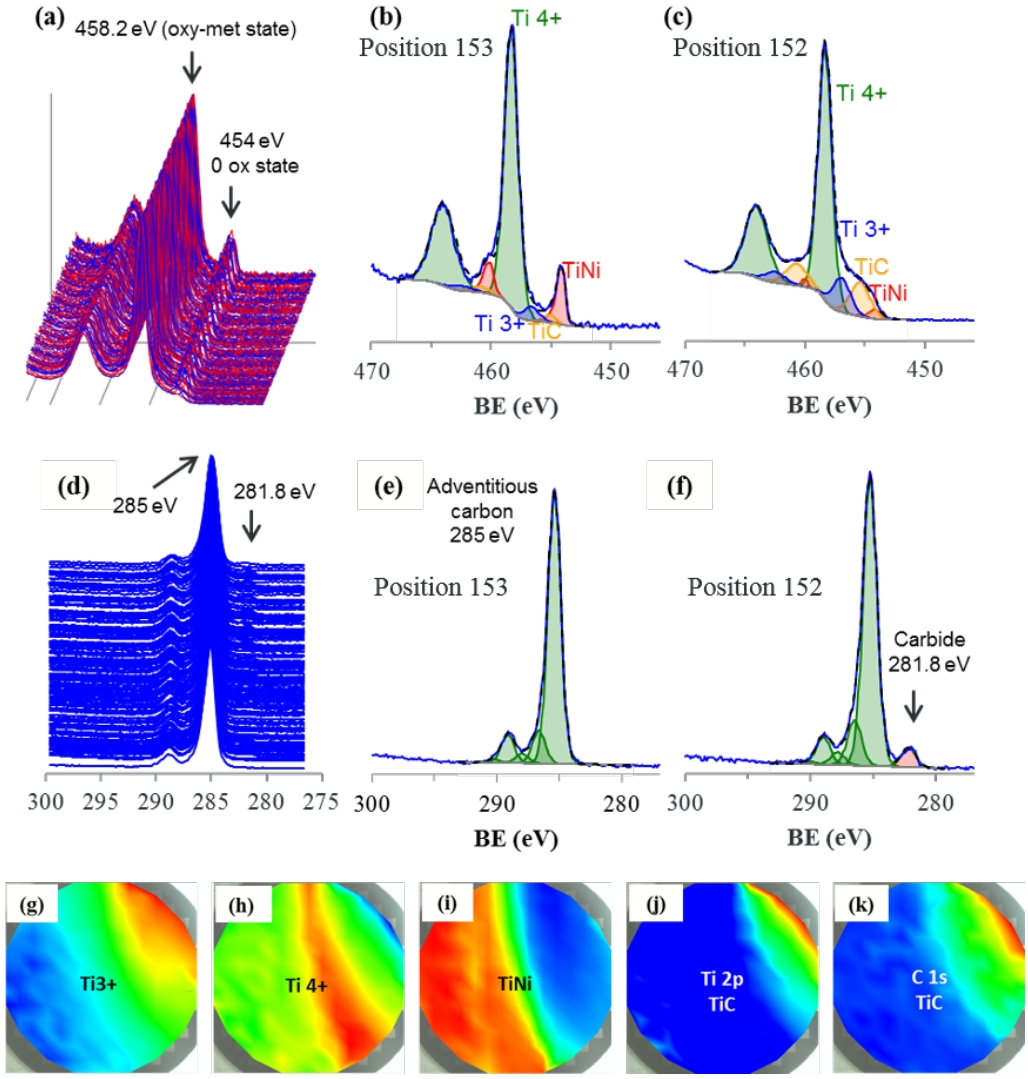

Figure G.1: (a) High resolution datasets of Ti 2p peak acquired across wafer allowed identification of significant carbide presence. (b) XPS spectra from two different regions on the wafer between 470 eV and 445 eV showing peak evolution as evidence of different chemical bonding. Curve fitting for the two Ti 2p spectra from wafer positions 153 and 152 show Ti-rich region forming Ti^{4+} and TiNi bonds and (c) presence of Ti^{3+} and TiC, respectively. (d) High resolution datasets of C 1s indicating carbide presence as determined from curve fitting showing (e) adventitious carbon peak at 285 eV and (f) carbide peak at 281.8 eV for the same positions. Peak fitted distribution of (g) Ti^{3+}, (h) Ti^{4+}, (i) TiNi, (j) TiC and (k) C 1s across the wafer. High to low distributions are indicated by variation in color from red to blue, respectively; wafer oriented with long flat edge on bottom.

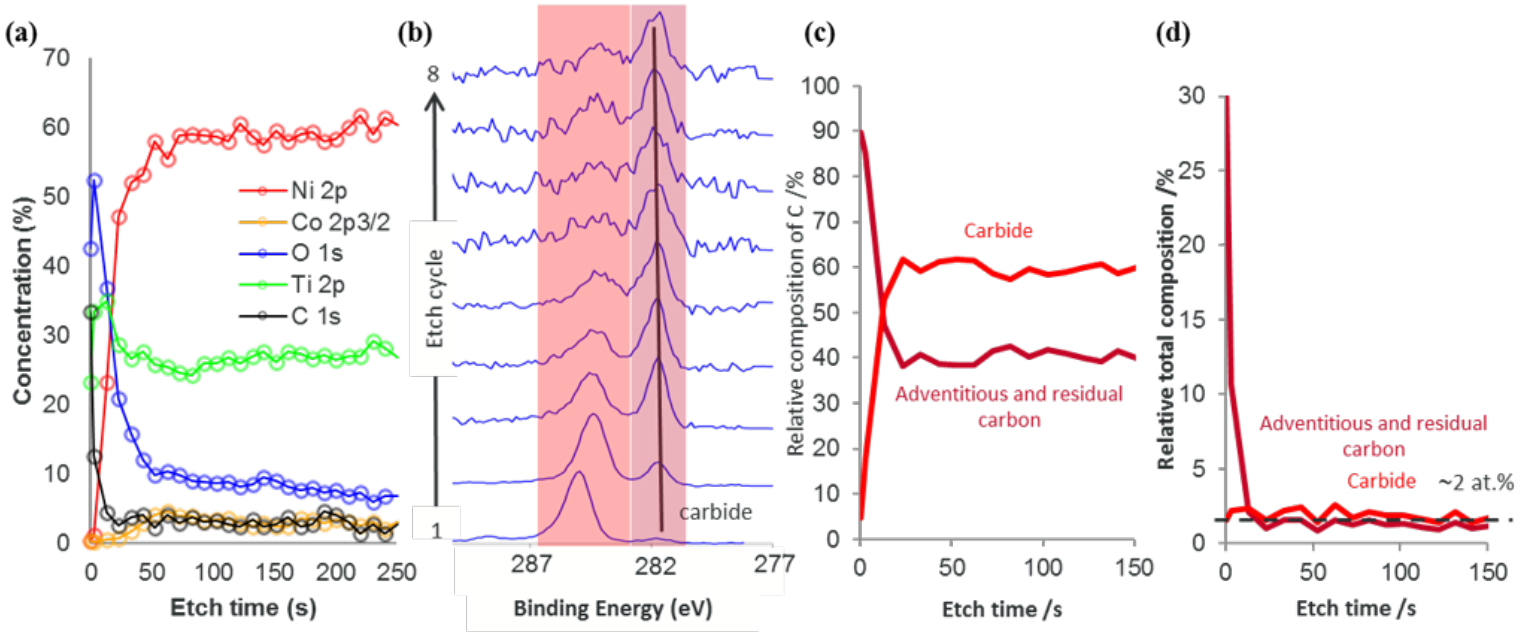

Figure G.2: (a) Depth profile obtained using 2 keV Ar^+ ions for position 152, (b) C 1s spectra for selected etch times, (c) evolution of carbide and adventitious carbon concentrations relative to each other and (d) the overall composition.

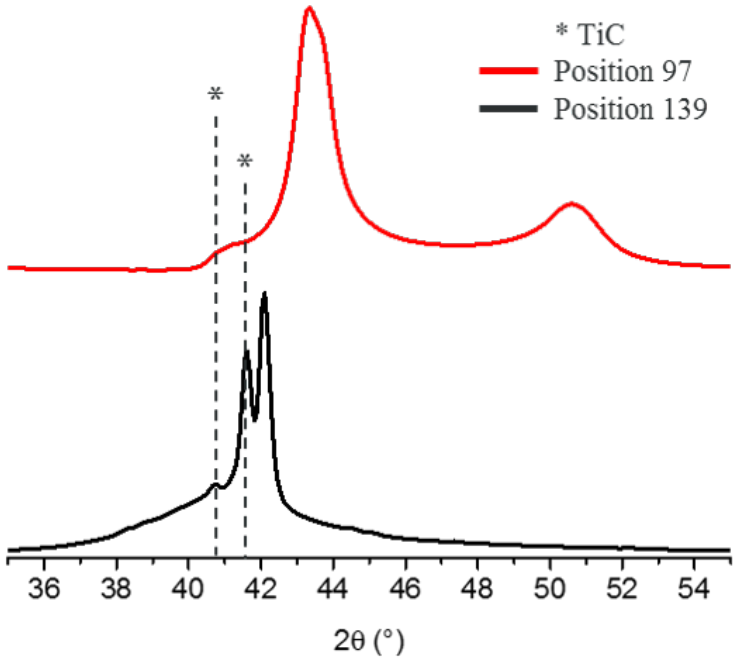

Figure G.3: XRD patterns for positions 97 and 139 marking titanium carbide peaks.

Appendix H: NMF analysis of XPS spectra

The analysis presented in the previous subsection demonstrates the enormous utility XPS methods bring to high-throughput studies. However, the absence of established methods for automated analysis of large datasets collected with this technique can hamper its spread. In this section, I show that many of the analysis tools used in the high-throughput community can be successfully adapted for this purpose.

Non-negative Matrix Factorization (NMF) is a well-known unsupervised machine learning method used for decomposition of mixtures formed by various types of non-negative signals [125]. The non-negativity constraint in NMF is often sufficient to guarantee that the extracted signals are sparse and easy to interpret, unlike the components obtained by methods such as principal component analysis (PCA) [293]. An additional advantage of NMF is that it can work with data in which the signals are not independent but partially correlated. It has been used extensively to quickly analyze large XRD datasets generated by measuring combinatorial libraries [114, 126, 127].

One of the complications of the classical NMF algorithm is that it requires *a priori* estimate of the number of end members. A modification of NMF addressing this limitation has been developed. It complements the conventional NMF with a custom semi-supervised clustering and Silhouette statistics, which allows simultaneous identification of the optimal number and shapes of the unknown basis components. The modified NMF protocol was used to successfully decompose the largest available dataset of human cancer [294] genomes, and has been very recently applied to several XRD datasets [126]. A resolution to peak shifting not caught by hierarchical cluster analysis is NMF which does not always give physically relevant solutions; a way around both is dynamic time warping (DTW) [115].

The collected XPS data was analyzed using the general NMF framework presented in experimental section 2.7. The design matrix X is formed by stacking the XPS spectra on top of each other. The resultant X has dimensions 177×1356 (number of points in the composition library × number of binding energies in each XPS spectrum). Two versions of the XPS spectra are considered: raw unprocessed and background subtracted spectra.

Initially, the background subtracted spectra–containing less information, and thus easier to analyze–were considered. The expanded NMF method estimated five to be the optimal number of basis spectra (Figure H.2). Their abundancies distributed over the wafer are shown in Figure H.1(f – j) in the text. A close match is observed in the results upon comparison of the distinct regions extracted by NMF with those by a human expert shown in Figure H.1(a – e). The pattern of the main

peaks of the basis spectra confirms the correspondence, and allows an easy labeling of the predominantly Ni, Ti, Co, and C regions. While this does not by itself produce new information, the fact that NMF easily reproduces the results obtained by a human expert demonstrates that XPS analysis can be at least partially automated.

Analyzing the raw data further reinforces previous results (Figure H.1(k – o)). The optimal number of NMF components is again five (Figure H.3). The outlines of the regions extracted from the abundancies of the new basis spectra are consistent with the NMF results on the background subtracted XPS data. The basis spectra themselves provide detailed information about the chemical composition of the film. The analysis of the entire dataset is significantly simplified by the decomposition, which allows researchers to focus on the most salient features of the data.

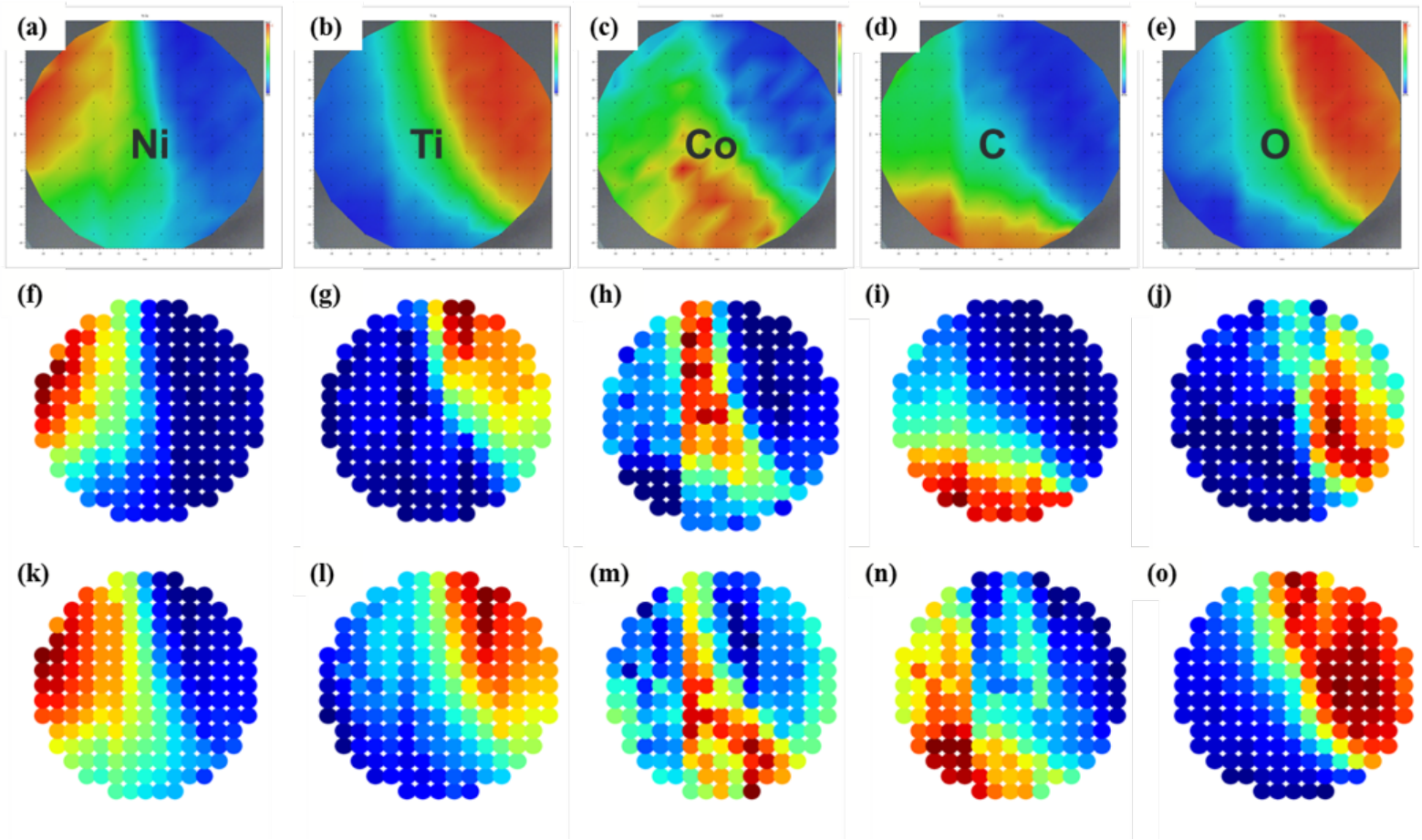

Figure H.1: (a – e) Elemental distributions calculated from XPS survey scans, (f – j) Results of NMF performed on background subtracted XPS, and (k – o) NMF performed on raw XPS data. NMF distributions are ordered left to right based on component solution number. High to low distributions are indicated by variation in color from red to blue, respectively.

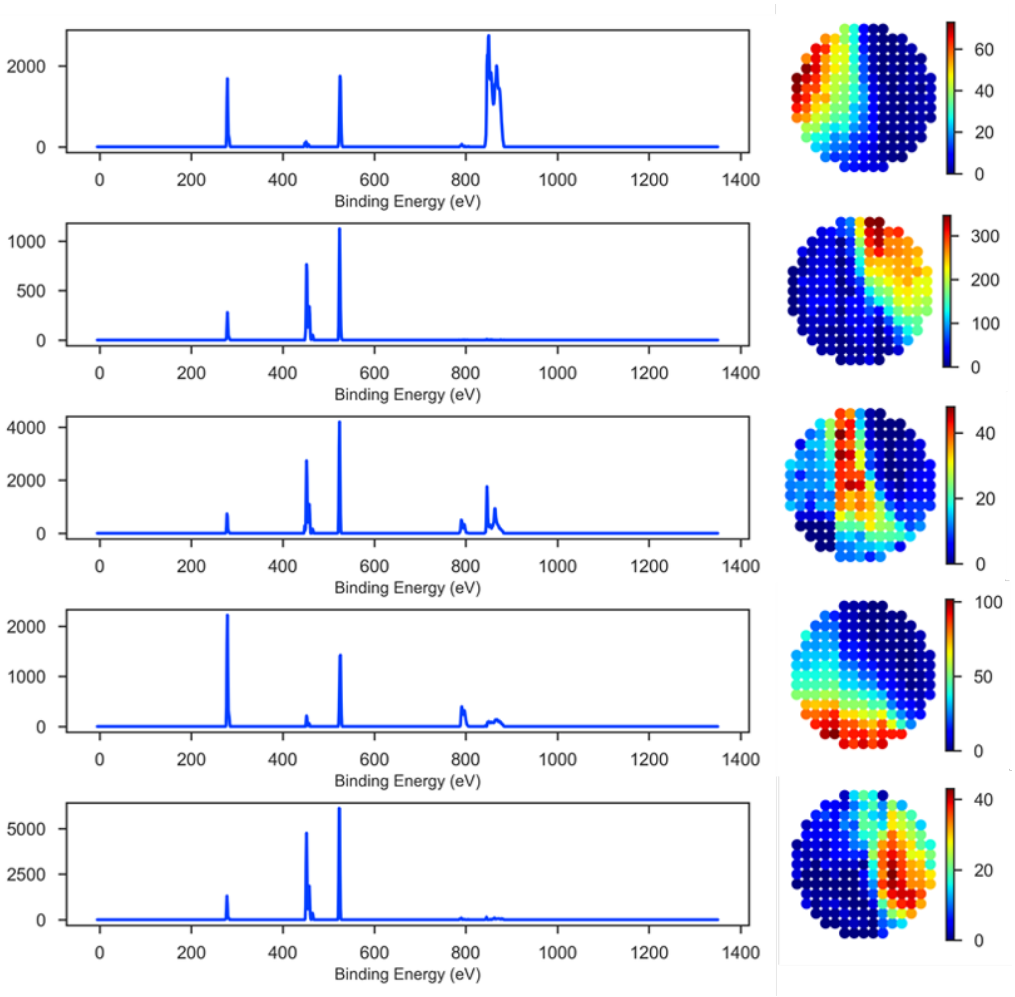

Figure H.2: Basis spectra determined from expanded NMF method for background subtracted XPS data and their corresponding distribution across the wafer. Listed in descending order by solution number.

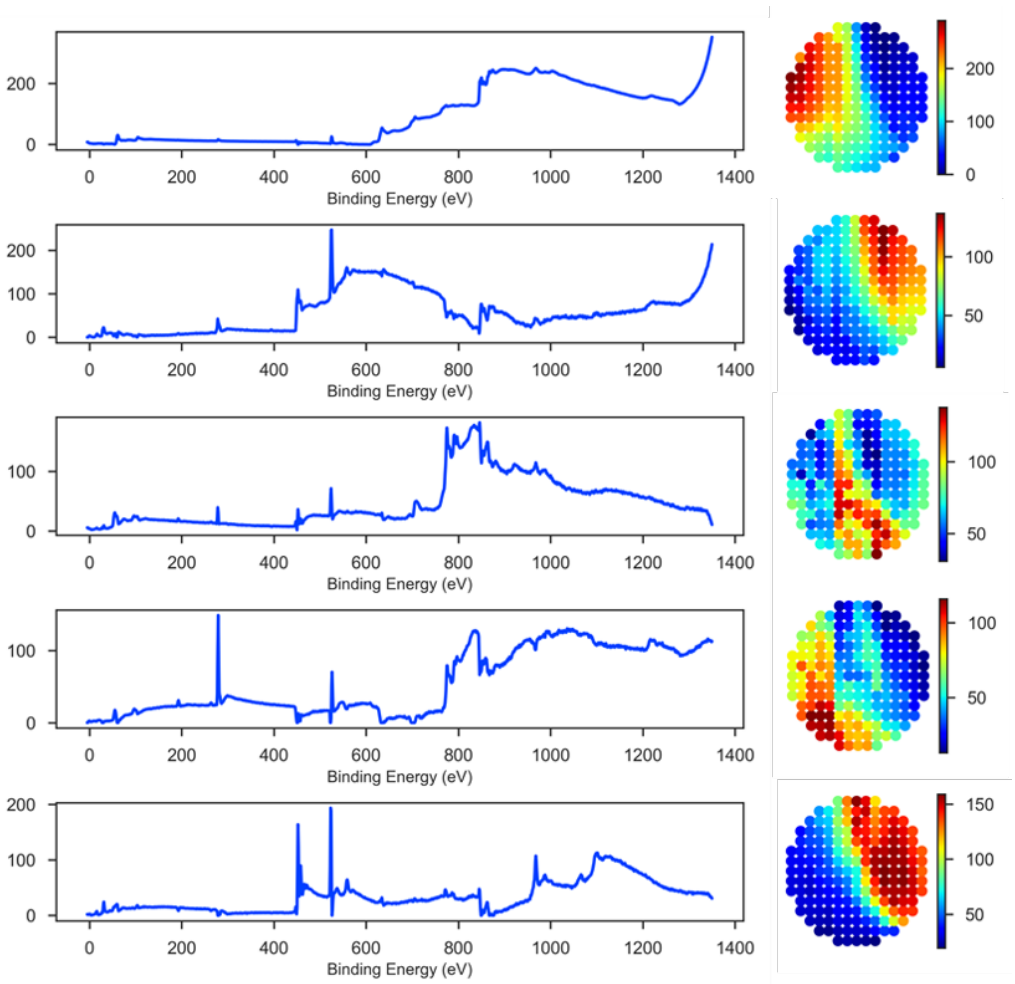

Figure H.3: Basis spectra determined from expanded NMF method for unprocessed raw XPS data and their corresponding distribution across the wafer. Listed in descending order by solution number.

Appendix I: Process to convert CombiView file into python-ready file in MATLAB

1. Import file into Matlab as numeric matrix

   >> a=NiTiCuFeSampleID2BGsubXRD;

   >> b=a.';

2. Select *b* → "Save as" in folder location of choice → load in origin as *.mat* life → C:—Users—Naila—Downloads →

3. Convert CombiView type file into Python ready *.mat* file using MATLAB for NMF analysis in Python

   (a) Import file into Matlab as numeric matrix

   (b) For XRD files, create a new variable file from first line of file and delete line in imported file

   (c) CMP = FileNameComposition

   (d) TTH = FileNameBGsubXRD_TTH

   (e) XRD = FileNameBGsubXRD

(f) Save NewFileName CMP TTH XRD

(g) Load NewFileName

Example:

Save NiTiCuCoAllPython.mat CMP TTH XRD

Load ('NiTiCuCoallPython.mat')

4. Files save in C:—Users—Naila—Documents—MATLAB

→ copy file to C:—Users—Naila—Downloads

(a) NiTiCuVAllPython.mat

(b) NiTiCuFeAllPython.mat

(c) NiTiCuPdSID13Python.mat

(d) NiTiCuPdSID4Python.mat

(e) NiTiCuCoAllPython.mat

(f) NiTiCuCoSID2.mat

(g) NiTiCuCoSID3.mat

To use the above *.mat* files for analysis in Python:

Jupyter files located in → C:—Users—Naila—Downloads →

1. NMF_NiTiCuCoSID2.ipynb

2. NMF_NiTiCuCoSID3.ipynb

3. NMF_NiTiCuV.ipynb

4. NMFpractice_run_NiTiCuCo.ipynb

5. NMF_NiTiCuFe.ipynb

6. NMF_NiTiCuPd.ipynb

7. NMF_NiTiCuPd_SID4.ipynb

NMFpractice_run_Bootcamp_LatentVariableAnalysis.ipynb

Appendix J: Process to convert *.mat* file into *.txt* format using MATLAB

Starting file = MATLAB generated *.mat* file from Appendix C

- Load file into MATLAB (shows as variables - b)
- Use syntax:

  >>a = b [name of file listed under workspace as 781x178 double]

  >>csvwrite('NiTiCuCo_SID3.txt',a)

- Check "Current Folder" for pathway to location where file is saved

Example:

Location: C:—Users—Naila—Dropbox—20180531 - Dell—ThermoelasticCooling

_ITakeuchi_NMA—2.Characterization—NiTiCu-X—

NiTiCu-X transposed XRD matlab files

Convert *NiTiCuCoSampleID3BGsubXRD2019T.mat*

To *NiTiCuCoSampleID3BGsubXRD2019T.txt*

1. Open MATLAB
2. Load NiTiCuCoSampleID3BGsubXRD2019T.mat
3. Shows as Variables – b; Workspace file listed as 781x178 double
4. >>a = b
5. >>csvwrite('NiTiCuCoSampleID3BGsubXRD2019T.txt',a)
6. Check for .txt file in location "C:—Users—Naila—Documents—MATLAB" from Current Folder File Pathway
7. Transfer file to final resting location

Appendix K: Process to transpose CombiView format XRD data in MATLAB

Objective 1: Convert CombiView format text files into matrix such that sample number are in columns instead of rows by using transposing function

- Starting file = CombiView ready format *.txt* file
- CombiView format has row 0 = 2theta values, column 0 + row 2 = signal intensity for materials library sample 1 of 177

To transpose 2theta and intensity organized by row to organized by column in MATLAB:

1. Import "NameOfFileUploaded.txt" file with data into MATLAB as numeric matrix – shows file as 178x781 table
2. Use syntax

   a=NameOfFileUploaded

b=a.'

3. Select *b* in "workspace" tab and save as "NameOfFileUploaded_transpose.mat" in appropriate folder

4. To save as *.txt* file, use syntax

   csvwrite('NameOfFileUploaded_transpose.txt',b)

5. Check current folder for file path where file is saved or Check for *.txt* file in location "C:—Users—Naila—Documents—MATLAB)" from Current Folder File Pathway

6. Transfer file to final resting location

Appendix L: Process to transpose and normalize XRD data in MATLAB

L.1 Objective 1: Convert CombiView format text files into matrix such that sample number are in columns instead of rows

- Starting file = CombiView ready format *.txt* file processed into a transposed *.txt* file → see previous appendix
- Transposed file has row 0 + column 2 = signal intensity for materials library sample 1 of 177; column 0 = 2theta values
- CombiView format has row 0 = 2theta values, column 0 + row 2 = signal intensity for materials library sample 1 of 177

Procedure:

1. Import "NameOfFileUploaded.txt" file with data into MATLAB as numeric matrix – shows file as 178x781 table

2. Use syntax:

   a=NameOfFileUploaded

   b=a.'

3. Select *b* in "workspace" tab and save as "NameOfFileUploaded_transpose.mat" in appropriate folder

4. To save as *.txt* file, use syntax

   csvwrite('NameOfFileUploaded_transpose.txt',b)

L.2 Objective 2: Normalize all intensity values against largest intensities

Procedure:

- Import *.txt* file with data into MATLAB as numeric matrix

- Use syntax T=NameOfFile T(:, 2:end) = normc(T(:, 2:end)) *%normalise everything but 1st column*

- To save as *.txt* file, use syntax csvwrite('NameOfFile_normalized.txt',T)

L.3 Example: Processing NiTiHf20min.txt data file

- Turning NiTiHf file in combiview format

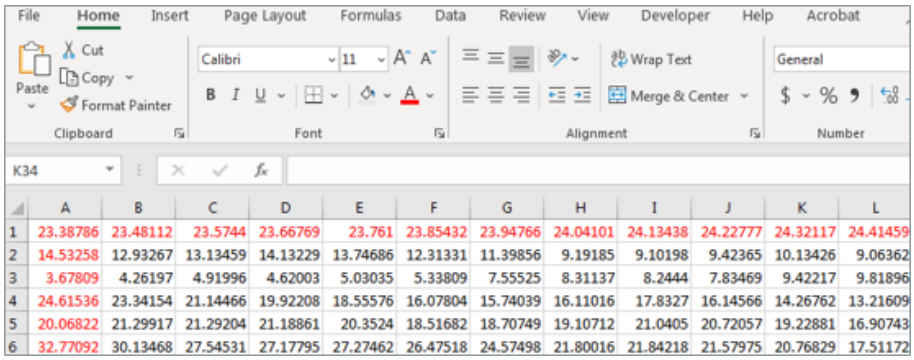

	A	B	C	D	E	F	G	H	I	J	K	L
1	23.38786	23.48112	23.5744	23.66769	23.761	23.85432	23.94766	24.04101	24.13438	24.22777	24.32117	24.41459
2	14.53258	12.93267	13.13459	14.13229	13.74686	12.31331	11.39856	9.19185	9.10198	9.42365	10.13426	9.06362
3	3.67809	4.26197	4.91996	4.62003	5.03035	5.33809	7.55525	8.31137	8.2444	7.83469	9.42217	9.81896
4	24.61536	23.34154	21.14466	19.92208	18.55576	16.07804	15.74039	16.11016	17.8327	16.14566	14.26762	13.21609
5	20.06822	21.29917	21.29204	21.18861	20.3524	18.51682	18.70749	19.10712	21.0405	20.72057	19.22881	16.90743
6	32.77092	30.13468	27.54531	27.17795	27.27462	26.47518	24.57498	21.80016	21.84218	21.57975	20.76829	17.51172

  - Import NiTiHf20_shortlisted.txt as numeric matrix with delimiters tab, comma, space
  - a= NiTiHf20shortlisted
  - b=a.'

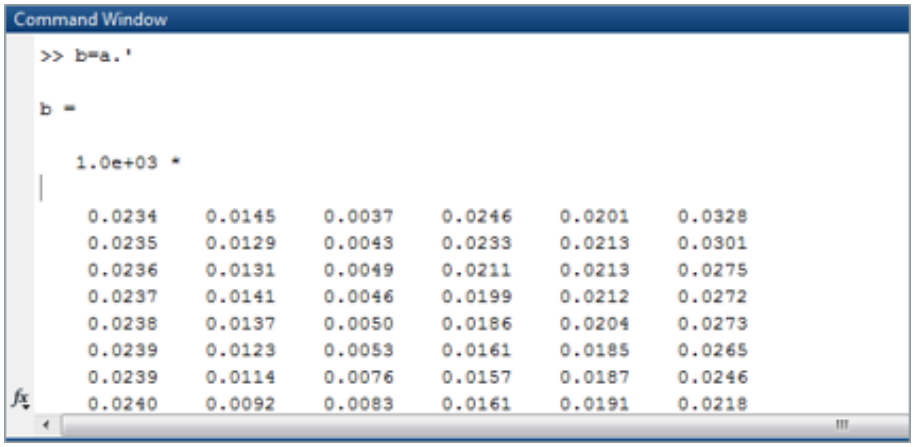

```
>> b=a.'

b =

   1.0e+03 *

    0.0234    0.0145    0.0037    0.0246    0.0201    0.0328
    0.0235    0.0129    0.0043    0.0233    0.0213    0.0301
    0.0236    0.0131    0.0049    0.0211    0.0213    0.0275
    0.0237    0.0141    0.0046    0.0199    0.0212    0.0272
    0.0238    0.0137    0.0050    0.0186    0.0204    0.0273
    0.0239    0.0123    0.0053    0.0161    0.0185    0.0265
    0.0239    0.0114    0.0076    0.0157    0.0187    0.0246
    0.0240    0.0092    0.0083    0.0161    0.0191    0.0218
```

  - csvwrite('NiTiHf20shortlisted_Transposed.txt',b)
  - Re-import NiTiHf20shortlisted_Transposed.txt as numeric matrix with delimiters tab, comma, space

– d=NiTiHf20shortlistedTransposed1

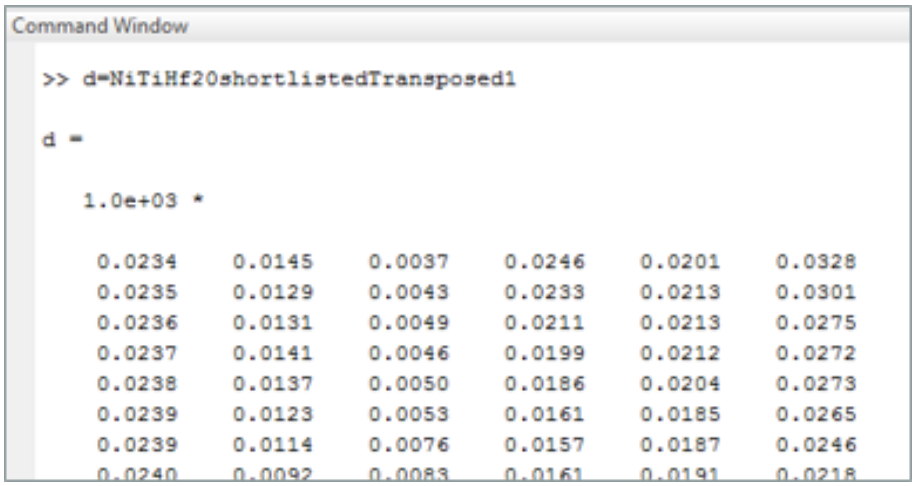

– d(:, 2:end) = normc(d(:, 2:end))

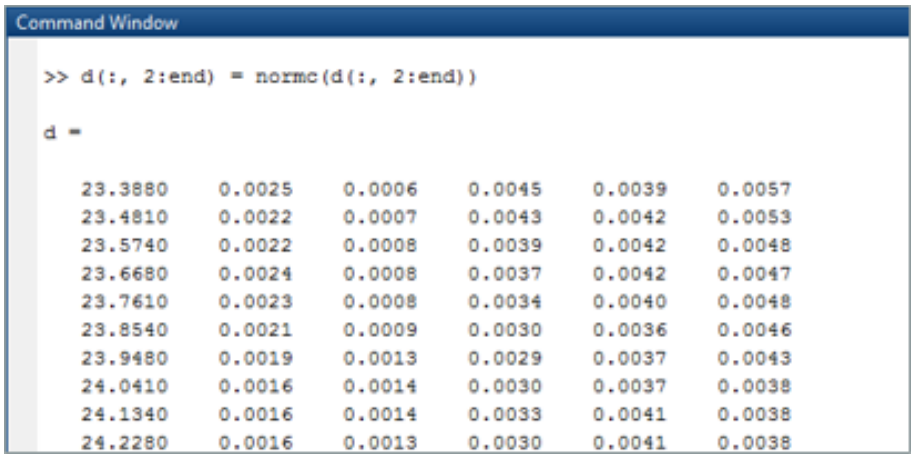

– csvwrite('NiTiHf20shortlisted_Transposed_normalized.txt',d)

Appendix M: Calibrated deposition rate for elements under given powers

Element	**Power**	**Thickness**	**Time**	**Rate**
–	[W]	[nm]	[min]	[nm/min]
Ti	100	233	30	7.75
Ni	26	119		3.96
Cu	17	41		1.37
Co	15	20.5		0.68
Fe	15	20		0.66
Pd	18	76.6		2.55
V	15	16		0.53

Table M.1: Calibrated deposition rate for elements under given powers.

Appendix N: Synthesis parameters for thin films investigated in this thesis

Sample ID	Power [W]			Deposition Time	Annealing	
	Ti	Ni	X	[min]	[°C]	[min]
NiTiCo	100	50	18	51	500	60
NiTiHf_20min deposition	100	31	25	20	500	60
NiTiHf_45min deposition	100	31	25	45	500	60
NiTiPd_15min deposition	100	30	20	15	500	60
NiTiPd_40min deposition	100	30	20	40	500	60
NiTiPd_65min deposition	100	30	20	65	500	60
NiTiPd_30min_NoAnneal	100	30	15	30	-	-
NiTiV	100	65	20	47	500	60

Table N.1: Synthesis parameters for ternary thin film libraries investigated in this thesis.

ID #	Materials	Targeted Center Pad Composition	Power [W]				Deposition Time	Annealing		Measured Center Pad Composition
		[at. %]	Ti	Ni	Cu	X	[min]	[°C]	[min]	[at. %]
1	NiTiCu-Fe	$[Ti_{55}–Ni_{33}–Cu_{12}]_{(100x)}$ Fe_x	100	26	17	15	30	500	60	55.3 - 33.8 - 6.8 - 3.9
2		$[Ti_{52}–Ni_{36}–Cu_{12}]_{(100x)}$ Fe_x	95	27	17	15				54.6 - 35.1 - 6.1 - 4.0
3	NiTiCu-V	$[Ti_{55}–Ni_{33}–Cu_{12}]_{(100x)}$ V_x	95	24	30	15				47.4 - 34.5 - 14.9 - 3.0
4		$[Ti_{52}–Ni_{36}–Cu_{12}]_{(100x)}$ V_x	85	27	30	15				42.6 - 39.4 - 15.2 - 2.6
5	NiTiCu-Co	$[Ti_{55}–Ni_{33}–Cu_{12}]_{(100x)}$ Co_x	100	24	26	15				48.9 - 33.0 - 12.0 - 5.9
6		$[Ti_{52}–Ni_{36}–Cu_{12}]_{(100x)}$ Co_x	100	27	26	15				46.0 - 36.3 - 11.9 - 5.6
7	NiTiCu-Pd	$[Ti_{55}–Ni_{33}–Cu_{12}]_{(100x)}$ Pd_x	100	24	26	6				49.1 - 33.7 - 12.9 - 4.2
8		$[Ti_{52}–Ni_{36}–Cu_{12}]_{(100x)}$ Pd_x	100	22	26	6				50.2 - 31.5 - 13.7 - 4.4

Table N.2: Synthesis parameters and center compositions for quaternary thin film libraries investigated in this thesis.

Materials	Targeted Center Pad Composition	Power [W]				Deposition Time	Annealing		Measured Center Pad Composition
	[at. %]	Ti	Ni	Cu	X	[min]	[°C]	[min]	[at. %]
NiTiCu-Co	$[Ti_{52}–Ni_{36}–Cu_{12}]_{(100x)}$ Co_x	100	27	26	15	30	700	15	47.6 - 34.9 - 11.6 - 5.8
NiTiCu-Pd	$[Ti_{52}–Ni_{36}–Cu_{12}]_{(100x)}$ Pd_x	100	22	26	6				50.6 - 31.4 - 13.1 - 4.8

Table N.3: Synthesis parameters for films evaluated for influence of annealing temperature on film properties.

Materials	Targeted Center Pad Composition	Power [W]				Deposition Time	Annealing	
	[at. %]	Ti	Ni	Cu	X	[min]	[°C]	[min]
NiTiCu-Co	$[Ti_{55}–Ni_{33}–Cu_{12}]_{(100x)}$ Co_x	100	24	26	15	30	500	60
NiTiCu-Pd	$[Ti_{52}–Ni_{36}–Cu_{12}]_{(100x)}$ Pd_x	100	24	26	15			

Table N.4: Selected compositions for nano-calorimetry characterization.

Awards

1. University of Maryland (UMD) Materials ENgineering Teaching Research (MENT&R) Fellowship Award under the U.S. Department of Education's Graduate Assistance in Areas of National Need (GAANN) Fellowship – **January 2020**

2. Silver Graduate Student Award, Materials Research Society Fall Conference, Boston, MA – **December 2019**

3. Dean's Special Commendation Award for Exceptional Service, A. James Clark School of Engineering, UMD – **May 2018**

4. Outstanding Graduate Assistant Award, University of Maryland, College Park, MD – **April 2018**

5. International School for Materials for Energy and Sustainability (ISMES), 2017 Summer School Scholarship, California Institute of Technology, Pasadena, CA – **July 2017**

6. National Science Foundation Graduate Research Fellowship (), awarded **March 2016**

7. Dean's Graduate Scholarship, University of Maryland, College Park – **August 2015**

8. The Chrysler Foundation Scholarship, Society of Women Engineers – **August 2015**

Publications

1. XPS Group Array Analysis of a Combinatorial Ni-Ti-Co Thin Film Library

   Jonathan Counsell, **Naila M. Al Hasan**, Edward Walton, Tieren Gao, Huilong Hou, Ichiro Takeuchi *Journal of Vacuum and Science Technology A*, 38 (6), p. 063407-1 - 063407-8, **2020**

2. Combinatorial Exploration and Mapping of Phase Transformation in a Ni-Ti-Co Thin Film Library

   Naila M. Al Hasan Huilong Hou, Tieren Gao, Jonathan Counsell, Suchismita Sarkar, Sigurd Thienhaus, Edward Walton, Peer Decker, Apurva Mehta, Alfred Ludwig, Ichiro Takeuchi *ACS Combinatorial Science*, 22 (11), p. 641 - 648, **2020**

3. Combinatorial Synthesis and High-Throughput Characterization of Microstructure and Phase Transformation in Ni-Ti-Cu-V Quaternary Thin-Film Library

   Naila M. Al Hasan, Huilong Hou, Suchismita Sarkar, Sigurd Thienhaus, Apurva Mehta, Alfred Ludwig, Ichiro Takeuchi *Engineering*, 6 (6), p. 637-643, **2020**

4. Fatigue-resistant high-performance elastocaloric materials made by additive manufacturing

   Huilong Hou, Emrah Simsek, Tao Ma, Nathan S. Johnson, Suxin Qian, Cheikh Cissé, Drew Stasak, **Naila M. Al Hasan**, Lin Zhou, Yunho Hwang, Reinhard Radermacher, Valery I. Levitas, Matthew J. Kramer, Mohsen Asle Zaeem, Aaron P. Stebner, Ryan T. Ott, Jun Cui, Ichiro Takeuchi *Science*, 366 (6469), p. 1116-1121, **2019**

5. Elastocaloric Cooling of Additive Manufactured Shape Memory Alloys with Large Latent Heat

   Huilong Hou, Emrah Simsek, Drew Stasak, **Naila M. Al Hasan**, Suxin Qian, Ryan Ott, Jun Cui, Ichiro Takeuchi *Journal of Physics D: Applied Physics*, 50 (40), 404001, **2017**

6. Database of Structural Phases in Ternary and Quaternary NiTi-Based Thin Film Alloy Libraries

   Naila M. Al Hasan, Huilong Hou, Suchismita Sarkar, Apurva Mehta, Ichiro Takeuchi *in preparation*, December 2020

Presentations

1. Invited presentation, "Combinatorial Exploration of Phase Transformation in NiTi-Based Alloys", Technische Universitat Dresden Summer School MATERIALS 4.0 Conference, **August 2020**

2. Oral presentation, "Combinatorial Exploration of Phase Transformation in Ni-Ti-Cu-V Shape Memory Library for Elastocaloric Cooling Applications", Materials Research Society Fall Meeting, Boston MA, **December 2019** – *Silver Graduate Student Award*.

3. "Thermoelastic Compression of NiTi in a 400 W Prototype for Solid State Cooling System", presented at the Sixth International School for Materials for Energy and Sustainability (ISMES VI), California Institute of Technology, Pasadena CA, **July 2017**

4. "Compressive thermoelastic cooling prototype", demonstration presented at the Annual Advanced Research Projects Agency – Energy (ARPA-E) Summit, Washington DC, **January 2017**

5. "Compression of NiTi in a 400 W Thermoelastic Prototype for Solid State Cooling Applications", presented at the MRS Fall Meeting, Boston MA, **November 2016**

#DefundThePolice
#BlackLivesMatter

ACS Combinatorial Science

pubs.acs.org/acscombsci

Research Article

Combinatorial Exploration and Mapping of Phase Transformation in a Ni−Ti−Co Thin Film Library

Naila M. Al Hasan, Huilong Hou, Tieren Gao, Jonathan Counsell, Suchismita Sarker, Sigurd Thienhaus, Edward Walton, Peer Decker, Apurva Mehta, Alfred Ludwig, and Ichiro Takeuchi*

Cite This: *ACS Comb. Sci.* 2020, 22, 641−648

Read Online

ACCESS | Metrics & More | Article Recommendations | Supporting Information

ABSTRACT: Combinatorial synthesis and high-throughput characterization of a Ni−Ti−Co thin film materials library are reported for exploration of reversible martensitic transformation. The library was prepared by magnetron co-sputtering, annealed in vacuum at 500 °C without atmospheric exposure, and evaluated for shape memory behavior as an indicator of transformation. Composition, structure, and transformation behavior of the 177 pads in the library were characterized using high-throughput wavelength dispersive spectroscopy (WDS), X-ray photoelectron spectroscopy (XPS), X-ray diffraction (XRD), and four-point probe temperature-dependent resistance ($R(T)$) measurements. A new, expanded composition space having phase transformation with low thermal hysteresis and Co > 10 at. % is found. Unsupervised machine learning methods of hierarchical clustering were employed to streamline data processing of the large XRD and XPS data sets. Through cluster analysis of XRD data, we identified and mapped the constituent structural phases. Composition−structure−property maps for the ternary system are made to correlate the functional properties to the local microstructure and composition of the Ni−Ti−Co thin film library.

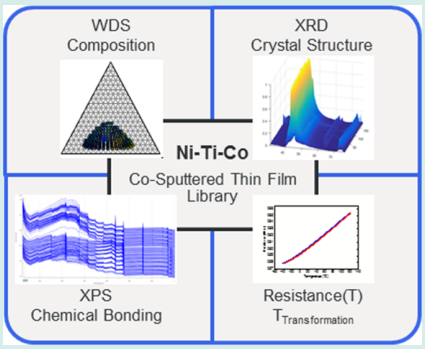

KEYWORDS: *Ni−Ti−Co, shape memory alloys, elastocaloric cooling, property mapping, machine learning, cluster analysis*

INTRODUCTION

Shape memory effect (SME) is a property that allows shape memory alloys (SMAs) to regain their shape when deformed through application of stress or temperature. The underlying mechanism is a reversible, diffusion-less, first-order martensitic transformation between two crystallographic phases.[1] The high temperature, high symmetry cubic phase is called austenite. The low temperature, low symmetry phase is called martensite, which can be present as twinned, detwinned, or a mixture of both in monoclinic and orthorhombic variants.[1] The temperatures at which transformation from martensite to austenite begins and ends are called A_s and A_f whereas the temperatures for the reverse pathway are marked by M_s and M_f. A cosputtered Ni−Ti−Co thin film library is investigated for SME through the evaluation of the phase transformation. First reported in 1975,[2] the Ni−Ti−Co alloy has since found wide applications: as a component of permanent magnets,[3−5] high-entropy alloys,[6,7] shape memory alloys,[8] and superalloys[9,10] along with substantive use in biomedical applications.[11−21] The addition of Co to NiTi has been shown to reduce the M_s and A_s temperatures in combination with the Ni content; it has also been shown to increase yield strength.[22,23] These improvements are sought out in elastocaloric cooling technology where ambient transition temperatures and small thermal hysteresis are desired.[24] Until now, investigations on the structural phases, mechanical properties, elastic properties, and phase transformation behavior that have been reported for Ni−Ti−Co involved one-by-one bulk preparation that covered a limited composition space, with addition of Co investigated only up to 10 at. %.[25,21,26−34] A more comprehensive study of the ternary system by Zhou et al., to determine the liquidus surface projection at 1373 K also involved one-by-one bulk preparation of 35 alloys. They evaluated the microstructure and different crystallographic phases present but did not report on the mechanical or transformation properties of Ni−Ti−Co.[35] To the best of the authors' knowledge, no systematic investigations of phase transformation in Ni−Ti−Co alloys, both in bulk and in the thin-film form that probes a greater composition space, have been reported thus far. Hence, this study aims to fill this information gap in identifying composition regions having martensitic phase transformation, with a focus on small thermal hysteresis.

We employ combinatorial materials science to facilitate a rapid investigation for the discovery, design, and development of new materials. It involves the correlation between physical

Received: May 21, 2020
Revised: July 22, 2020
Published: August 4, 2020

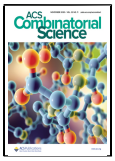

https://dx.doi.org/10.1021/acscombsci.0c00097
ACS Comb. Sci. 2020, 22, 641−648

properties and composition through concurrent sample synthesis and high-throughput experimentation (HTE).[36] Combinatorial thin film synthesis allows access to a greater number of compositions than previously explored.[37] When combined with high-throughput characterization techniques, a systematic evaluation of parameters of interest can be carried out to fine-tune the functionalities of materials. Promising compositions can then be scaled up for bulk studies.

To quickly identify the compositions that transform in the ambient temperature range, a Ni−Ti−Co composition spread was synthesized using magnetron co-sputtering, and its composition−structure−property was mapped with high-throughput characterization. Unsupervised machine learning methods were used to both manage the large data sets acquired and analyze them efficiently.[38,39] The composition was determined using wavelength dispersive spectroscopy (WDS). We also evaluated the use of X-ray photoelectron spectroscopy (XPS) as a high-throughput chemical characterization technique; an automated, typical WDS measurement of a 177-sample library takes about 6 h whereas total acquisition time for XPS survey scans for the same sample library requires only half the time. Although surface effects and corrosion behavior of NiTi-based bulk as well as thin-film systems have been previously studied with XPS,[11,40−43] we report on systematic high-throughput XPS characterization and an indexed spectral database for Ni−Ti−Co. Using synchrotron X-ray diffraction (XRD) and high-throughput four-point probe temperature-dependent resistance $R(T)$ measurements, we report on the microstructure, phase diagram, and martensitic transformation behavior of Ni−Ti−Co alloys. We also report on phase transformation in compositions beyond $Ni_{50-x}Ti_{50}Co_x$ (x = 0 to 10 at. %). Furthermore, we identified a composition space with small thermal hysteresis (ΔT) that is promising for higher transformation efficiency and long-term stability.

RESULTS AND DISCUSSION

Figure 1 shows a ternary elemental plot of the compositional range covered in this study. With an x-y scanning table and characterization tools, the library was spatially analyzed, which offers another way to visualize data. Images of the materials library and corresponding labeled wafer positions are shown in the Supporting Information, Figure S1, parts a and b, respectively. Throughout the paper, we will use both methods to facilitate understanding of the different insights; experimental details are provided at the end.

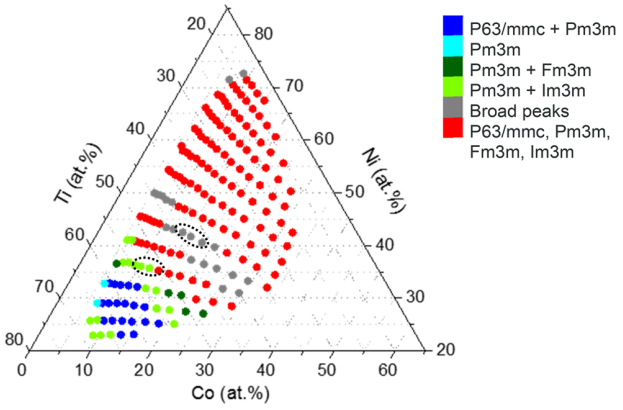

Figure 1. Ternary plot of Ni, Ti, and Co determined from high-throughput WDS. Compositions are grouped by color based on results for crystallographic phases from the Pearson correlation coefficient (PCC) hierarchical clustering model. Compositions grouped inside gray ellipses were determined to transform through an intermediate structure.

Characterization of Chemical Composition. Chemical composition determined from WDS shows elemental concentrations of 22.8 at. % < C_{Ni} < 72.8 at. %, 17.6 at. % < C_{Ti} < 68.2 at. %, and 5.4 at. % < C_{Co} < 33.2 at. %. Distribution of the elements by wafer position is shown in Figure S2a−c; these match the physical configuration of the targets inside the deposition chamber. The center of this library on the wafer has a composition of $Ni_{46.2}Ti_{40.1}Co_{13.7}$. Compositions with the highest and lowest Ni content are $Ni_{72.6}Ti_{18.6}Co_{8.8}$ and $Ni_{23}Ti_{68}Co_9$, highest and lowest Ti are $Ni_{23}Ti_{68}Co_9$ and $Ni_{67.5}Ti_{17.7}Co_{14.8}$, and highest and lowest Co are $Ni_{34.4}Ti_{32.5}Co_{33.1}$ and $Ni_{45.5}Ti_{49}Co_{5.5}$, respectively. Additionally, we obtained crystallographic evidence for carbide and oxide phases of Ti. Chemical composition data from WDS and XPS agree qualitatively for Ni and Ti distributions shown in Figure S2a,b and Figure S2d,e. Slight difference observed in the spatial distribution of Co (Figure S2, parts c and f) may be associated with a surface energy effect as XPS captures chemical activity present in the top 10 nm. In addition to differences in sampling depths, the variation in Co distribution may also be due to local surface aggregation of Co for a particular alloy blend. Despite the reduction in measurement time from XPS, we use WDS compositions going forward due to its higher accuracy and precision in quantifying elemental content. We do, however, use oxidation state mapping from XPS to understand crystallographic trends in the following sections.

Transformation Temperature Determination with Four-Point Probe Measurements. Compositions in the library were screened for phase transformation using a custom high-throughput four-point probe measurement system as measurable electrical changes accompany crystal structural changes during phase transformation.[44,45] We successfully identified compositions with phase transformation and narrow ΔT in the ambient temperature range. Film sheet resistance as a function of temperature, $R(T)$, was measured between −40 and +120 °C. Austenitic start (A_s), austenitic finish (A_f), martensitic start (M_s), and martensitic finish (M_f) temperatures were determined by applying the tangent method to the $R(T)$ curves, as demonstrated in the inset of Figure 2a. The first-order martensitic transformation is associated with a thermal hysteresis (ΔT) that reduces the reversibility of the transformation. This hysteresis is a result of energy dissipation due to frictional work and plastic accommodation during lattice distortions.[46−49] The hysteresis width determines the energy loss and inefficiency of the transformation such that a narrow width favors sustained reversibility.[50] Thermal hysteresis is determined by the difference between austenitic finish (A_f) and martensitic start (M_s) temperatures.

The $R(T)$ curves obtained can be divided into three categories—(1) linear, non-transforming curves with increasing slopes, (2) nonlinear, transforming curves (Figure 2a), and (3) linear, non-transforming curves with decreasing slopes (examples are highlighted with a black box in Figure S3). Linear $R(T)$ curves with increasing slopes showing no transformation were obtained for most of the library. Of the 177 compositions measured, 31 were observed to have reversible transformation behavior and hence, shape memory effect; these are listed by ascending Ni content in Table 1.

https://dx.doi.org/10.1021/acscombsci.0c00097
ACS Comb. Sci. 2020, 22, 641−648

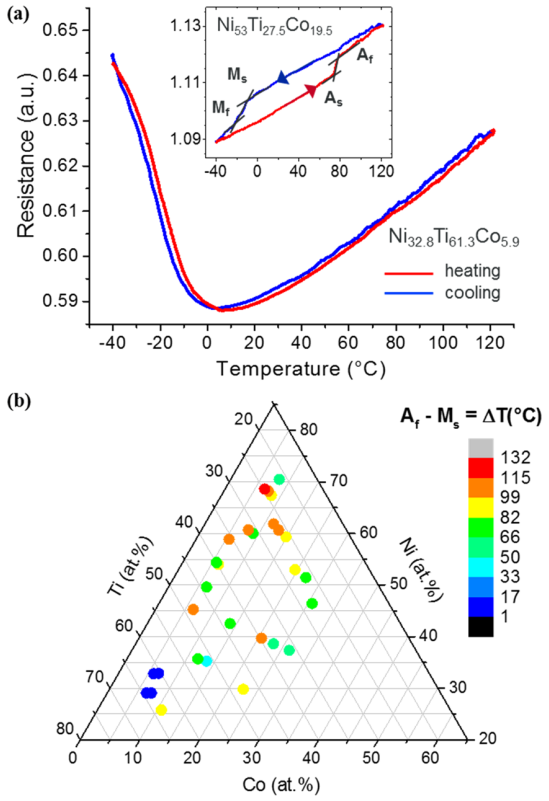

Figure 2. (a) $R(T)$ curve for $Ni_{32.8}Ti_{61.3}Co_{5.9}$ showing near-zero thermal hysteresis. Inset shows the tangent method to determine phase transformation temperatures A_s, A_f, M_s, and M_f from $R(T)$ curve for $Ni_{53}Ti_{27.5}Co_{19.5}$ alloy showing reversible phase transformation with large thermal hysteresis. (b) Distribution of thermal hysteresis $\Delta T = A_f - M_s$ in °C as a function of composition. Color scale bar from blue to red indicates small to large temperature widths.

Composition regions with SME at Co content greater than 10 at. % were identified for the first time. SME was observed in an elemental range for Ni from 25.8 to 70.5 at. %, Ti from 21.4 to 64.3 at. %, and Co from 5.5 to 26.4 at. %, respectively. Temperature ranges observed for martensite start, austenite finish and thermal hysteresis were $-25.2\ °C < M_s < 106.5\ °C$, $-23.2\ °C < A_f < 140.4\ °C$, and $0.7\ °C < \Delta T < 131.2\ °C$, respectively. Distribution of thermal hysteresis is shown in Figure 2b. Four compositions with $5.9\ \text{at. \%} < C_{Co} < 18.3\ \text{at. \%}$ were observed to have ΔT between 0.5 and 2.1 °C with the higher Co composition transforming at higher temperatures (M_s = 106.5 °C, A_f = 107.9 °C). Average A_f and M_s temperatures are around 79.6 and 14.4 °C, respectively, which are essential for SMA use in ambient temperatures. Some transformation pathways were incomplete in the evaluated range as seen from the missing M_s values in Table 1. These results are important as SME has been reported in bulk compositions of $Ti_{50}Ni_{50-x}Co_x$ (x = 2, 4, 6, and 8) but not observed for $Ti_{50}Ni_{40}Co_{10}$ measured at liquid nitrogen temperature.[14,29] Addition of Co preferentially substitutes Ni up to 14 at. % which has been shown to reduce the M_s. Although only a slight reduction in M_s is observed, our observations are overall in agreement with previous reports demonstrating addition of Co to reduce A_s and M_s through substitution of Ni.[23] Seven compositions were determined to have phase transformation through an intermediate structure (dotted gray ellipses, Figure 1a). These are not listed in the table as additional nanocharacterization measurements and temperature-dependent XRD are needed to verify these observations. Nonetheless, a two-step transformation has been previously reported for bulk Ni−Ti−Co and is also well-known to occur in NiTi as well as ternary systems such as TiNiCu, TiNiFe, and TiNiMo.[25,51−55]

Table 1. Composition, Martensitic Start (M_s), Austenitic Finish (A_f), and Thermal Hysteresis (ΔT) Determined from $R(T)$ for Ternary Ni−Ti−Co SMA Library by Ascending Ni Content

at. %			°C		
Ni	Ti	Co	M_s	A_f	$A_f - M_s = \Delta T$
25.8	63.5	10.7	−10.3	73.1	83.5
29.1	64.3	6.6	−25.2	−23.2	2.0
29.1	63.5	7.4	–	−8.3	8.3
29.8	47.7	22.5	–	83.9	83.9
32.8	61.3	5.9	−4.9	−2.8	2.1
32.9	60.4	6.7	−15.0	−14.3	0.7
35.2	51.2	13.6	58.0	95.8	37.9
35.7	52.4	11.9	–	79.6	79.6
37.3	36.3	26.4	0.8	61.1	60.3
38.6	38.3	23.1	15.5	79.4	64.0
39.7	39.7	20.6	10.6	109.9	99.3
42.5	43.6	13.9	–	72.9	72.9
45.3	48.4	6.3	−8.8	95.9	104.7
46.4	27.9	25.7	2.0	81.9	79.9
49.6	44.0	6.4	40.4	116.8	76.4
51.4	26.4	22.2	1.3	78.6	77.2
53.0	27.5	19.5	−12.8	78.5	91.3
54.0	39.8	6.2	22.8	109.7	86.9
54.4	40.0	5.7	24.8	94.2	69.4
58.9	35.6	5.5	29.7	140.4	110.6
59.3	25.8	14.9	0.7	95.8	95.0
59.5	22.2	18.3	106.5	107.9	1.5
60.0	31.0	9.0	19.3	99.0	79.7
60.7	26.4	13.0	−2.4	104.8	107.2
60.7	31.4	7.9	3.3	105.3	102.0
61.8	26.6	11.5	−6.3	104.3	110.6
65.3	27.9	6.8	73.5	111.0	37.5
67.4	24.2	8.4	16.1	104.0	87.8
68.2	24.3	7.5	5.2	107.7	102.6
68.6	24.7	6.6	−24.9	106.2	131.2
70.5	21.4	8.2	19.6	69.5	49.9

Crystal Structure and Phase Determination. We employed an unsupervised machine learning algorithm to determine a phase map for the Ni−Ti−Co library. Hierarchical cluster analysis using the Pearson correlation coefficient (PCC) was performed on high-throughput synchrotron XRD patterns (Figure S5a), collected at room temperature for the 177 annealed compositions, which delineates and separates compositions based on differences or similarities in their diffraction patterns. This also allows us to rapidly determine composition-structure relationships in the Ni−Ti−Co materials library.

The MATLAB-based data visualization platform Combi-View allows linking of sample composition with its XRD and XPS spectral patterns (Figure S4) and was used to perform the hierarchical cluster analysis on the XRD data (Figure S5).[56] An initial cluster analysis resulted in 32 groups. Upon refining and combining cluster groups based on number of low intensity peaks, six groups were determined consisting of 16 phases (see

https://dx.doi.org/10.1021/acscombsci.0c00097
ACS Comb. Sci. 2020, 22, 641−648

space group in Table 2). Representative XRD patterns were analyzed using EVA4 XRD software from Bruker and matched

Table 2. Crystal Structures Identified in the Ni−Ti−Co Thin Film Materials Library[a]

formula	space group	space group number	prototype
$(CoNi_2)Ti$	*P*63/*mmc*	194	hexagonal
$(Co_{0.15}Ni_{0.85})Ti$	*Pm*3*m*	221	
$(Co_{0.5}Ni_{0.5})Ti$	*Pm*3*m*	221	
$(Co_5NiTi_4)_{0.2}$	*Pm*3*m*	221	
$(Ni_{0.875}Co_{0.125})Ti$	*Pm*3*m*	221	
	*I*4/*mmm*	139	tetragonal
			$Al(Cr_{1.818}Ti_{0.182})$
			$Al(Cr_{1.818}Nb_{0.182})$
CoO	*Fm*3*m*	225	
CoTi	*Pm*3*m*	221	
Co_2GeTi	*Fm*3*m*	225	
Co_2NiTi	*Fm*3*m*	225	Co_2NiGa
			FeNi
			$MgNi_2Sn$
Co_2Ti_4O	*Fd*3*m*	227	
Co_3Ti_3O	*Fd*3*m*	227	
	*Iba*2	45	orthorhombic
			$Cr_{0.9585}Ga_2Sb_2$
	*P*1*m*1	6	monoclinic
			FeNi
NiTi	*P*21/*m*	11	monoclinic
NiTi	*P*3	147	hexagonal
NiTi	*Pm*3*m*	221	
$NiTi_2$	*Fd*3*m*	227	
$Ni_{1.02}Ti_{0.98}$	*Pm*3*m*	221	
Ni_2Ti	*R*3*m*	166	rhombo.h.axes
Ni_2Ti_4O	*Fd*3*m*	227	
Ni_4Ti_3	*R*3	148	rhombohedral
	*I*4/*m*	87	Tetragonal
			Ni_4W
$Ti(Co_{1.5}Ni_{1.5})$	*P*63/*mmc*	194	CoMnSn
TiC	*Fm*3*m*	225	TiCoNiSn
TiCo	*Pm*3*m*	221	
$Ti_4Ni_2O_{0.3}$	*Fd*3*m*	227	
	*F*43*m*	216	$(CoNi)Sn_2Ti_2$
			Ti_2NiAl
	*Im*3*m*	229	NiV
			TiV
	Pmam	51	orthorhombic
			$TiNi_{0.8}Cu_{0.2}$
	Pmmn	59	orthorhombic
			$NbNi_3$

[a]The default crystal structure type is cubic unless specified otherwise under prototype.

against the International Centre for Diffraction Data (ICDD) database.[57] Results of the cluster analysis and phase distribution in a ternary composition plot are shown in Figure S5b,c and Figure 1, respectively. Selected diffraction patterns representing phases present in the six groups defined by PCC are shown in Figure 3. Crystal structures identified in this alloy library are listed in Table 2. Depending on where a composition was in the thermal cycle of the transformation, we expected to identify cubic, monoclinic, or orthorhombic structures for compositions exhibiting phase transformation.

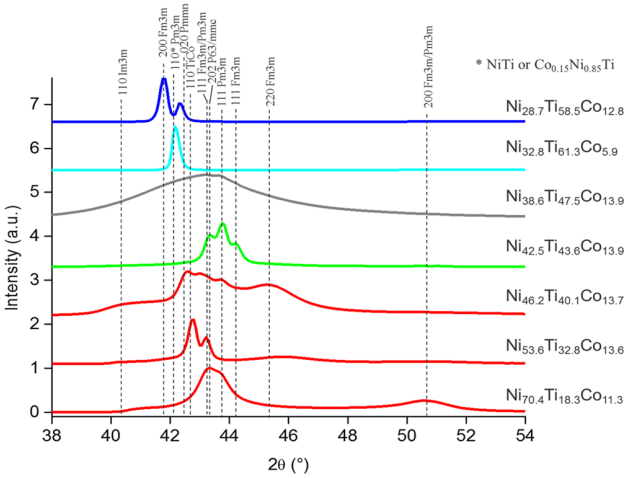

Figure 3. Selected X-ray diffraction patterns (wafer positions 94, 172, 91, 90, 89, 87, and 82 from top to bottom) representing phases present in the six clusters identified by PCC arranged in ascending Ni content. Patterns are offset for clarity.

Most common crystal type present was cubic austenite structure *Pm*3*m* in the form of NiTi or $Co_{0.15}Ni_{0.85}Ti$ crystal types and present in a single phase in only two compositions, $Ni_{29.1}Ti_{64.3}Co_{6.6}$ and $Ni_{32.8}Ti_{61.3}Co_{5.9}$ (positions 163 and 172, light blue cluster in Figure 1)—both of these also had near-zero thermal hysteresis $R(T)$ curves. The *Pm*3*m* phase is present predominantly in a mixture with other cubic phases *Im*3*m* and *Fm*3*m*, shown as dark green, light green, and red groups in Figure 1. These were observed to have linear, non-transforming $R(T)$ curves (Figure S3). For compositions in the Ni-rich region, mixed phases of hexagonal (prototype Ni_4In) and cubic (prototypes TiV, Co_2NiGa, $Co_{0.5}Ni_{0.5}Ti$, and $GaTiCo_2$) crystal structures were present, seen in red in Figure 1. Rhombohedral Ni_2Ti and Ni_4Ti_3 structures were also identified, and it was noted that NiTi is present in cubic, monoclinic, and hexagonal forms. For compositions with SME discussed in the previous section, both single phase and a mixture of cubic with orthorhombic structures were identified as seen from light and dark blue patterns in Figure 3. A mixture of hexagonal NiTi and cubic $(Co_5NiTi_4)_{0.2}$ for $Ni_{32.9}Ti_{60.4}Co_{6.7}$ (wafer position 162) also exhibited transformation with near-zero thermal hysteresis. It is important to note that this is a qualitative, not a quantitative assignment. Similarly, for $Ni_{42.5}Ti_{43.6}Co_{13.9}$(wafer position 90), where a potential two-step transformation was observed, a mixture of hexagonal $Ti(Co_{1.5}Ni_{1.5})$ and cubic *Pm*3*m*, *Im*3*m* structures of the prototypes $Co_{0.807}Ge_{0.123}W_{0.070}$ and $Cr_{0.875}Ti_{0.125}$ were identified. Since our library explores a composition space not yet reported, these and other prototype structures listed in the table provide an understanding of the type of crystal structures that may be present as we could not match every XRD peak with a listing in the ICDD. Finally, the gray cluster in Figure 1 is defined by a non-crystalline phase in which broad peaks were observed in the 2θ range of 40° to 48° (gray pattern in Figure 3) that corresponded with linear, non-transforming $R(T)$ curves characterized by decreasing slopes. This gray cluster forms a phase boundary separating NiTi−$NiTi_2$ double phase for compositions rich in Ti (dark blue in Figure S5c), which follows a distribution of Ti^{4+} peak observed from XPS mapping (Figure S6). Although no clear relationship could be drawn between variation of Ni or Co content with phase trans-

https://dx.doi.org/10.1021/acscombsci.0c00097
ACS Comb. Sci. 2020, 22, 641−648

formation, crystallographic evidence for SME could be established, in agreement with theoretical and experimental observations reported in the literature.[11−13,28,35,54] These results also build on the challenging work associated with determining stable intermediate phases.[33]

DISCUSSION

To understand the relationship between composition, structure, and phase transformation, we can now align the data for material properties of the Ni−Ti−Co library across the chemical composition space. Phase transformation was observed in different parts of the composition plot with very little apparent connection to elemental variation. Of all the cubic space groups, transforming compositions are comprised of the *Pm*3*m* type in single phase or in mixture with *Fm*3*m*. While other compositions have similar crystal structures, they do not undergo transformation; this may be due to the presence of other crystal types such as non-transforming cubic and hexagonal phases. It is also difficult to determine the exact influence of composition on the presence of a particular crystal type since these are not single phases. Furthermore, the presence of additional phases may demand greater energy for the SME phase to transform, thereby increasing the thermal hysteresis width. This is supported by stable $R(T)$ curves having near zero thermal hysteresis for compositions $Ni_{29.1}Ti_{64.3}Co_{6.6}$ and $Ni_{32.8}Ti_{61.3}Co_{5.9}$ at positions 163 and 172 with a single crystal phase of NiTi or $Co_{0.15}Ni_{0.85}Ti$ types. Fabricating a materials library having smaller concentration gradients and centered around the composition space identified to have narrow hysteresis coupled with temperature-dependent XRD measurements may better elucidate the crystal phase composition of the transforming samples. Additionally, while scale-up of these compositions to verify the narrow thermal hysteresis in bulk is needed, thin films of Ni−Ti−Cu and Ni−Ti−Cu−V have been successfully scaled up and tested over many cycles.[58,59] Abrupt changes in $R(T)$ curves are also observed from one measurement area to the next such that they have linear and/or non-linear curves characterized by decreasing slopes from left to right (Figure S3). A cluster of XRD patterns reflects a similar distribution across the wafer and forms a phase boundary separating NiTi−$NiTi_2$ double phase for compositions rich in Ti (Figure S5c). XPS mapping of the Ti^{4+} peak across the wafer further confirms this observation (SI Figure S6). It may be that the annealing time is not long enough to produce large enough crystallites in this area of the materials library. Overall, while it is difficult to draw a definitive relationship between variation of Ni or Co content with phase transformation, we establish crystallographic evidence for SME, in agreement with observations already reported in literature for other Ni−Ti−Co alloys.[11−13,28,35,54] Nonetheless, these results expand on the challenging work of determining stable intermediate phases reported previously.[33]

CONCLUSION

A combinatorial Ni−Ti−Co thin film materials library covering a large composition space was synthesized using magnetron cosputtering and annealed at 500 °C for 1 h in vacuum. Large data sets of composition, transformation temperatures, and crystal structure were obtained from high-throughput WDS and XPS, four-point probe temperature-dependent resistance, and synchrotron XRD measurements that enabled rapid materials characterization and screening. Transformation temperatures were probed in the −40 to +120 °C range to screen for shape memory alloys that could be used in ambient temperature applications. By employing combinatorial synthesis and high-throughput experimentation, we demonstrate the effectiveness of the methodology in systematically mapping phase transformation and drawing composition-structure−property relationships. Cross sample position analysis between and within data sets allowed for greater insights, and the following observations were drawn:

- Chemical composition space bounded between 22.8 at. % < C_{Ni} < 72.8 at. %, 17.6 at. % < C_{Ti} < 68.2 at. %, and 5.4 at. % < C_{Co} < 33.2 at. % was synthesized.
- Phase transformation was observed in compositions beyond the range previously reported as $Ni_{50-x}Ti_{50}Co_x$ (x = 0 to 10 at. %), with Co concentration between 5 and 26 at. %.
- A new compositional region having narrow thermal hysteresis (ΔT between 0.5 and 2 °C) centered around 6 at. % Co in Ti-rich regions was identified.
- Transforming compositions are composed of mixtures of cubic structures from *Pm*3*m* and *Fm*3*m* space groups as well as orthorhombic and hexagonal structures.
- Non-transforming compositions were characterized by crystalline mixtures of multiple cubic *Pm*3*m* phases, *Pm*3*m* with *Fm*3*m* along with *Im*3*m* cubic phases in addition to non-crystalline phases defined by broad XRD peaks around 2θ = 40°.
- Alloys with distinct XRD patterns for a single cubic phase showed near-zero thermal hysteresis.
- Large data sets produced in this work may be used to develop machine learning models for predictive experimentation.

In summary, this study highlights a strategy that can be extended to other alloy systems and properties to discover new materials with enhanced functionalities.

EXPERIMENTAL APPROACH

For ease of data management, all experiments were performed with the long flat edge of the wafer positioned at the bottom. Sample pads were numbered from left to right with 1 to 5 parallel to the long flat edge and continuing to rows above (Figure S1).

Magnetron Sputtering of Thin Films. Ternary thin film composition spread between 150 and 250 nm was deposited on a 3-in. diameter thermally oxidized (2 μm SiO_2) Si wafer (thickness 400 μm, IWS) in an ultrahigh vacuum (base pressure: 5×10^{-7} Torr, 6.6×10^{-5} Pa) magnetron sputtering system at room temperature. A patterned Si mask was placed on the wafer to delineate 177 individual compositions evenly across the wafer at a Δx, Δy of 4.5 mm. High purity Ni (99.995%), Ti (99.995%), and Co (99.97%) targets (1.5 in. diameter, 0.125 in. thick, Lesker) were co-sputtered with ultrahigh purity Argon gas (99.9997%, Airgas) pressure of 5×10^{-3} Torr (0.6 Pa). The thin film library was deposited over a period of 51 min using a DC power source for Ni and Ti sputtered at 50 and 100 W, respectively, and an RF power source of 18 W for Co. The substrate was water cooled to avoid crystallization during sputter deposition and to maintain low temperatures.[60] The resulting film was annealed in a vacuum at 500 °C for 1 h.

https://dx.doi.org/10.1021/acscombsci.0c00097
ACS Comb. Sci. 2020, 22, 641−648

Wavelength Dispersive Spectroscopy (WDS). Chemical composition of the Ni−Ti−Co thin film library was determined by using WDS in an electron probe microanalyzer (EPMA) JXA 8900R Microprobe, with an acceleration voltage of 15 kV. Calibration was done using polished pure metal with an experimental error margin of <0.3 at. %. WDS was selected over energy dispersive spectroscopy (EDS) due to its higher accuracy and precision in quantifying elemental content via better energy resolution from peak/background ratio.[61]

High-Throughput X-ray Diffraction (XRD) Measurements. Structural information was obtained by X-ray diffraction (XRD) measurements conducted at room temperature at SLAC National Accelerator Laboratory beamline 1−5. The 14.99 keV beam of wavelength 0.82657 Å was collimated to ∼0.3 mm × 0.3 mm. An exposure rate of 30 s was used to collect data on a MarCCD detector. A small grazing incidence angle of 1−2° was used to scan the library and minimize influence of diffraction from the silicon substrate.

Geometric parameters of 2D detector such as direct beam position, rotation, tilting, and sample to detector distance was extracted for data analysis using a LaB_6 powder pattern. These parameters were used to transform initial raw images that were acquired as a function of Q and χ in diffraction coordinate into 1D diffraction patterns by integrating and normalizing over the χ angle. Bragg angle (2θ) is related to scattering vector (Q) by the relationship $Q = 4 \times \pi \times \sin(\theta)/\lambda$, with wavelength ($\lambda$) help to generate a more traditional 1D spectrum (intensity vs 2θ). These were then analyzed using EVA4 XRD software (Bruker) and matched against the International Center for Diffraction Data (ICDD) database.[57]

Cluster Analysis of XRD data. An unsupervised machine learning algorithm was used as an exploratory data analysis tool as well as a phase mapping tool. A Pearson correlation coefficient (PCC) clustering model was applied using CombiView, a MATLAB-supported data visualization platform developed by the Takeuchi group. It used the criteria for similarity and dissimilarity between input data such that data grouped into a cluster share similar characteristics than data in other clusters.[62] For two spectra x and y having means $\bar{x}$ and $\bar{y}$, PCC is defined as[38]

$$C_{xy} = \frac{\sum_{i=1}^{n}(x_i - \bar{x})(y_i - \bar{y})}{\left[\sum_{i=1}^{n}(x_i - \bar{x})^2 \sum_{i=1}^{n}(y_i - \bar{y})^2\right]^{1/2}}$$

This clustering model was applied to the diffraction patterns of the 177 points in the library.

High-Throughput X-ray Photoelectron Spectroscopy (XPS). XPS analyses were carried out with a Kratos Axis NOVA spectrometer using a monochromatic Al Kα source (30 mA, 15 kV). XPS can detect all elements except hydrogen and helium, probes the surface of the sample to a depth of 5−7 nm, and has detection limits ranging from 0.001 to 0.5 at. % depending on the element/matrix. The instrument work function was calibrated to give a binding energy (BE) of 83.96 eV for the Au 4f7/2 line for metallic gold and the spectrometer dispersion was adjusted to give a BE of 932.62 eV for the Cu 2p3/2 line of metallic copper. The Kratos charge neutralizer system was used on all specimens. Survey scan analyses were carried out with an analysis area of 300 × 700 μm and a pass energy of 160 eV. High resolution analyses were carried out with an analysis area of 300 × 700 μm and a pass energy of 20 eV. Spectra have been charge-corrected to the main line of the carbon 1s spectrum (adventitious carbon) set to 285.0 eV (Table 3).

Table 3. XPS Species and Associated Binding Energies

photoelectron peak	binding energy (eV)
Ni 2p	853
Co 2p	778
O 1s	530
Ti 2p	455
C 1s	285

For quantification, Shirley background subtraction removed the contribution of inelastically scattered electrons. For chemical state analysis, peaks were fitted with symmetric Gaussian−Lorentzian components using the ESCApe data system and were quantified using modified Wagner relative sensitivity factors. Spatial distribution plots were performed using the ESCApe data system whereby a series of analysis points can be created either freehand or as a grid. The spectra were analyzed as grouped data post quantification. A Delaunay triangulation is fitted onto the acquisition locations.[63] A linearly interpolated color scheme is then applied to each triangle based on the vertex values, each of which represents an acquired atomic concentration value.

Four-Point Probe Resistance−Temperature $R(T)$ Measurements. Transformation temperature parameters of A_s, A_f, M_s, M_f, and $\Delta T(A_f - M_s)$ were determined from resistance as a function of temperature $R(T)$ measurements. A customized automated four-point probe test stand developed at Ruhr Universität Bochum was used to rapidly characterize the entire library. On the basis of a measurement methodology described by van der Pauw, the test stand has a probe head mounted on a z-axis with 5 sets of four-point probes enclosed in a box purged with N_2 gas.[64,44,45] Probe tips are spaced at 500 μm and automated to measure resistance with a 50-mA current source between −40 and +120 °C with a heating/cooling rate of 5 °C/min. The library was subjected to 84 temperature cycles during this experiment.

■ ASSOCIATED CONTENT

Supporting Information

The Supporting Information is available free of charge at https://pubs.acs.org/doi/10.1021/acscombsci.0c00097.

Additional figures including index number map, elemental distribution maps, XRD and XPS patterns, $R(T)$ mapped by wafer position, cluster analysis method, and oxidation state distribution (PDF)

■ AUTHOR INFORMATION

Corresponding Author

Ichiro Takeuchi − *Department of Materials Science and Engineering, University of Maryland, College Park, Maryland 20742, United States;* orcid.org/0000-0003-2625-0553; Email: takeuchi@umd.edu

Authors

Naila M. Al Hasan − *Department of Materials Science and Engineering, University of Maryland, College Park, Maryland 20742, United States;* orcid.org/0000-0001-8339-0187

Huilong Hou − *Department of Materials Science and Engineering, University of Maryland, College Park, Maryland 20742, United States;* orcid.org/0000-0003-0865-1142

https://dx.doi.org/10.1021/acscombsci.0c00097
ACS Comb. Sci. 2020, 22, 641−648

Tieren Gao − *Department of Materials Science and Engineering, University of Maryland, College Park, Maryland 20742, United States*
Jonathan Counsell − *Kratos Analytical Limited, Manchester M17 1 GP, U.K.*
Suchismita Sarker − *Stanford Synchrotron Radiation Lightsource, SLAC National Accelerator Laboratory, Menlo Park, California 94025, United States;* orcid.org/0000-0002-8820-1143
Sigurd Thienhaus − *Materials Discovery and Interfaces, Ruhr-Universität Bochum, 44801 Bochum, Germany*
Edward Walton − *Kratos Analytical Limited, Manchester M17 1 GP, U.K.*
Peer Decker − *Materials Discovery and Interfaces, Ruhr-Universität Bochum, 44801 Bochum, Germany*
Apurva Mehta − *Stanford Synchrotron Radiation Lightsource, SLAC National Accelerator Laboratory, Menlo Park, California 94025, United States;* orcid.org/0000-0003-0870-6932
Alfred Ludwig − *Materials Discovery and Interfaces, Ruhr-Universität Bochum, 44801 Bochum, Germany;* orcid.org/0000-0003-2802-6774

Complete contact information is available at: https://pubs.acs.org/10.1021/acscombsci.0c00097

Author Contributions

T.G. prepared the materials library; the manuscript and the Supporting Information were prepared with contributions from all authors. All authors have given approval to the final version of the manuscript.

Funding

N.M.A.H. acknowledges financial support by the National Science Foundation Graduate Research Fellowship Program under Grant No. DGE 1322106.

Notes

The authors declare no competing financial interest.
The raw data is available for future discussion/analysis upon request to the authors.

■ ACKNOWLEDGMENTS

The authors thank Valentin Stanev, Boian S. Alexandrov, Alan Savan, Christopher Klingshirn, Isabel Lloyd, Lourdes Salamanca-Riba, and Jason Hattrick-Simpers for fruitful discussions.

■ ABBREVIATIONS

WDS, wavelength dispersive spectroscopy; XRD, X-ray diffraction; XPS, X-ray photoelectron spectroscopy; PCC, Pearson correlation coefficient

■ REFERENCES

(1) Miyazaki, S., Fu, Y. Q., Huang, W. M., Eds., *Thin Film Shape Memory Alloys, Fundamentals and Device Applications*, 1st ed.; Cambridge University Press: Cambridge, U.K., 2009.
(2) Kornilov, I. I.; Kachur, E. V.; Belousov, O. K. Investigation of TiNi-TiCo system. *Russ. Metall.* **1975**, *2*, 162−163.
(3) Bozorth, R. M. *Ferromagnetism*; Wiley VCH - IEEE Press: 1993.
(4) Ahmad, Z.; Akbar, S.; Farooque, M.; Ul Haq, A.; Yan, M. Synthesis and magnetic properties of Nb-doped Al−Ni−Co−Ti−Cu−Fe permanent magnets. *Philos. Mag. Lett.* **2011**, *91* (3), 173−181.
(5) Belyaev, I. V.; Bazhenov, V. E.; Moiseev, A. V.; Kireev, A. V. New Fe- Co- Ni- Cu- Al- Ti Alloy for Single-Crystal Permanent Magnets. *Phys. Met. Metallogr.* **2016**, *117* (3), 214−221.
(6) Yeh, A.-C.; Chang, Y.-J.; Tsai, C.-W.; Wang, Y.-C.; Yeh, J.-W.; Kuo, C.-M. On the Solidification and Phase Stability of a Co-Cr-Fe-Ni-Ti High-Entropy Alloy. *Metall. Mater. Trans. A* **2014**, *45* (1), 184−190.
(7) Samal, S.; Rahul, M. R.; Kottada, R. S.; Phanikumar, G. Hot deformation behaviour and processing map of Co-Cu-Fe-Ni-Ti eutectic high entropy alloy. *Mater. Sci. Eng., A* **2016**, *664*, 227−235.
(8) Mohammad Sharifi, E.; Kermanpur, A. Superelastic behavior of nanostructured Ti50Ni48Co2 shape memory alloy with cold rolling processing. *Trans. Nonferrous Met. Soc. China* **2018**, *28* (7), 1351−1359.
(9) Christofidou, K. A.; Jones, N. G.; Pickering, E. J.; Flacau, R.; Hardy, M. C.; Stone, H. J. The microstructure and hardness of Ni-Co-Al-Ti-Cr quinary alloys. *J. Alloys Compd.* **2016**, *688*, 542−552.
(10) Zhong, Z.; Gu, Y.; Yuan, Y.; Yokokawa, T.; Harada, H. On the low cycle fatigue behavior of a Ni-base superalloy containing high Co and Ti contents. *Mater. Sci. Eng., A* **2012**, *552*, 434−443.
(11) Ahmed, R. A. Electrochemical Properties of Ni_{47} Ti_{49} Co_{4} Shape Memory Alloy in Artificial Urine for Urological Implant. *Ind. Eng. Chem. Res.* **2015**, *54* (34), 8397−8404.
(12) El-Bagoury, N. Microstructure and martensitic transformation and mechanical properties of cast Ni rich NiTiCo shape memory alloys. *Mater. Sci. Technol.* **2014**, *30* (14), 1795−1800.
(13) Kök, M.; Ateş, A. The effect of addition of various elements on properties of NiTi-based shape memory alloys for biomedical application. *Eur. Phys. J. Plus* **2017**, *132* (4), 6.
(14) Jing, R.; Liu, F. The Influence of Co Addition on Phase Transformation Behavior and Mechanical Properties of TiNi Alloys. *Chin. J. Aeronaut.* **2007**, *20* (2), 153−156.
(15) Soni, H.; Sannayellappa, N.; Rangarasaiah, R. M. An experimental study of influence of wire electro discharge machining parameters on surface integrity of TiNiCo shape memory alloy. *J. Mater. Res.* **2017**, *32* (16), 3100−3108.
(16) Huang, X.; Norwich, D. W.; Ehrlinspiel, M. Corrosion Behavior of Ti-55Ni-1.2Co High Stiffness Shape Memory Alloys. *J. Mater. Eng. Perform.* **2014**, *23* (7), 2630−2634.
(17) Phukaoluan, A.; Khantachawana, A.; Kaewtatip, P.; Dechkunakorn, S.; Kajornchaiyakul, J. Improvement of mechanical and biological properties of TiNi alloys by addition of Cu and Co to orthodontic archwires. *Int. Orthod.* **2016**, *14* (3), 295−310.
(18) Mohammad Sharifi, E.; Karimzadeh, F.; Kermanpur, A. Nanocrystallization of the Ti50Ni48Co2 Shape Memory Alloy by Thermomechanical Treatment. *J. Mater. Eng. Perform.* **2015**, *24* (1), 445−451.
(19) Isola, L.; La Roca, P.; Sobrero, C.; Fuster, V.; Vermaut, P.; Malarría, J. Martensitic transformation strain and stability of Ni50-x−Ti50−Cox (x = 3, 4) strips obtained by twin-roll casting and standard processing techniques. *Mater. Des.* **2016**, *107*, 511−519.
(20) Hosoda, H.; Fukul, T.; Inoue, K.; Mishima, Y.; Suzuki, T. Change of Ms Temperatures and its Correlation to Atomic Configurations of Offstoichiometric NiTi-Cr and NiTi-Co Alloys. *MRS Proc.* **1996**, *459*, 287.
(21) Civjan, S.; Huget, E. F.; DeSimon, L. B. Potential Applications of Certain Nickel-Titanium (Nitinol) Alloys. *J. Dent. Res.* **1975**, *54* (1), 89−96.
(22) Kishi, Y.; Yajima, Z.; Shimizu, K. Relation between Tensile Deformation Behavior and Microstructure in a Ti-Ni-Co Shape Memory Alloy. *Mater. Trans.* **2002**, *43* (5), 834−839.
(23) Hosoda, H.; Hanada, S.; Inoue, K.; Fukui, T.; Mishima, Y.; Suzuki, T. Martensite transformation temperatures and mechanical properties of ternary NiTi alloys with offstoichiometric compositions. *Intermetallics* **1998**, *6* (4), 291−301.
(24) Bechtold, C.; Chluba, C.; Lima de Miranda, R.; Quandt, E. High cyclic stability of the elastocaloric effect in sputtered TiNiCu shape memory films. *Appl. Phys. Lett.* **2012**, *101* (9), 091903.
(25) Larnicol, M.; Portier, R.; Ochin, P. Influence of Rapid Solidification on Ni50-xTi50Cx Shape Memory Alloys. *J. Phys. IV* **1997**, *07*, C5-191.

(26) Alqarni, N. D.; Wysocka, J.; El-Bagoury, N.; Ryl, J.; Amin, M. A.; Boukherroub, R. Effect of cobalt addition on the corrosion behavior of near equiatomic NiTi shape memory alloy in normal saline solution: electrochemical and XPS studies. *RSC Adv.* **2018**, *8* (34), 19289−19300.
(27) Soni, H.; Narendranath, S.; Ramesh, M. R. Effects of Wire Electro-Discharge Machining Process Parameters on the Machined Surface of Ti 50 Ni 49 Co 1 Shape Memory Alloy. *Silicone* **2018**, *5*, 19166.
(28) Mohammad Sharifi, E.; Kermanpur, A.; Karimzadeh, F. The effect of thermomechanical processing on the microstructure and mechanical properties of the nanocrystalline TiNiCo shape memory alloy. *Mater. Sci. Eng., A* **2014**, *598*, 183−189.
(29) Fasching, A.; Norwich, D.; Geiser, T.; Paul, G. W. An Evaluation of a NiTiCo Alloy and its Suitability for Medical Device Applications. *J. Mater. Eng. Perform.* **2011**, *20* (4−5), 641−645.
(30) Goryczka, T.; Ochin, P.; Lelątko, J. Shape Memory Effect in NiTiCo Strip Produced by Twin Roll Casting Technique. *Mater. Sci. Forum* **2013**, *738−739*, 348−351.
(31) Jordan, L.; Goubaa, K.; Masse, M.; Bouquet, G. Comparitive study of mechanical properties of various Ni-Ti based shape memory alloys in view of dental and medical applications. *J. Phys. IV* **1991**, *01* (C4), C4-139−C4-144.
(32) Martins, R. M. S.; Schell, N.; von Borany, J.; Mahesh, K. K.; Silva, R. J. C.; Braz Fernandes, F. M. Structural evolution of magnetron sputtered shape memory alloy Ni−Ti films. *Vacuum* **2010**, *84* (7), 913−919.
(33) Gupta, K. P. The Co-Ni-Ti System (Cobalt-Nickel-Titanium). *J. Phase Equilib.* **1999**, *20* (1), 65−72.
(34) Santosh, S.; Sampath, V. Effect of Ternary Addition of Cobalt on Shape Memory Characteristics of Ni−Ti Alloys. *Trans. Indian Inst. Met.* **2019**, *72*, 1481−1484.
(35) Zhou, C.; Guo, C.; Li, J.; Li, C.; Du, Z. Experimental investigations of the Co−Ni−Ti system: Liquidus surface projection and isothermal section at 1373 K. *J. Alloys Compd.* **2018**, *754*, 268−282.
(36) Gebhardt, T.; Music, D.; Takahashi, T.; Schneider, J. M. Combinatorial thin film materials science: From alloy discovery and optimization to alloy design. *Thin Solid Films* **2012**, *520* (17), 5491−5499.
(37) Takeuchi, I.; Lauterbach, J.; Fasolka, M. J. Combinatorial materials synthesis. *Mater. Today* **2005**, *8* (10), 18−26.
(38) Hattrick-Simpers, J.; et al. Rapid structural mapping of ternary metallic alloy systems using the combinatorial approach and cluster analysis. *Rev. Sci. Instrum.* **2007**, *78* (7), 072217.
(39) Long, C. J.; Bunker, D.; Li, X.; Karen, V. L.; Takeuchi, I. Rapid identification of structural phases in combinatorial thin-film libraries using x-ray diffraction and non-negative matrix factorization. *Rev. Sci. Instrum.* **2009**, *80* (10), 103902.
(40) Alqarni, N. D.; Wysocka, J.; El-Bagoury, N.; Ryl, J.; Amin, M. A.; Boukherroub, R. Effect of cobalt addition on the corrosion behavior of near equiatomic NiTi shape memory alloy in normal saline solution: electrochemical and XPS studies. *RSC Adv.* **2018**, *8* (34), 19289−19300.
(41) Firstov, G.; Vitchev, R.; Kumar, H.; Blanpain, B.; Van Humbeeck, J. Surface oxidation of NiTi shape memory alloy. *Biomaterials* **2002**, *23* (24), 4863−4871.
(42) Zheng, Y. F.; Wang, B. L.; Wang, J. G.; Li, C.; Zhao, L. C. Corrosion behaviour of Ti−Nb−Sn shape memory alloys in different simulated body solutions. *Mater. Sci. Eng., A* **2006**, *438-440*, 891−895.
(43) König, D.; Naujoks, D.; de los Arcos, T.; Grosse-Kreul, S.; Ludwig, A. X-Ray Photoelectron Spectroscopy Investigations of the Surface Reaction Layer and its Effects on the Transformation Properties of Nanoscale Ti51Ni38Cu11 Shape Memory Thin Films. *Adv. Eng. Mater.* **2015**, *17* (5), 669−673.
(44) Thienhaus, S.; Zamponi, C.; Rumpf, H.; Hattrick-Simpers, J.; Takeuchi, I.; Ludwig, A. High-throughput characterization of shape memory thin films using automated temperature-dependent resistance measurements. *MRS Proc.* **2005**, *894*, LL06-06.
(45) Thienhaus, S.; Hamann, S.; Ludwig, A. Modular high-throughput test stand for versatile screening of thin-film materials libraries. *Sci. Technol. Adv. Mater.* **2011**, *12* (5), 054206.
(46) Wu, Y.; Ertekin, E.; Sehitoglu, H. Elastocaloric cooling capacity of shape memory alloys − Role of deformation temperatures, mechanical cycling, stress hysteresis and inhomogeneity of transformation. *Acta Mater.* **2017**, *135*, 158.
(47) Planes, A.; Flores-Zúñiga, H.; Soto-Parra, D.; Vives, E.; Matutes-Aquino, J. A.; Mañosa, L. Elastocaloric effect in Ti-Ni shape-memory wires associated with the B2 ↔ B19' and B2 ↔ R structural transitions. *Appl. Phys. Lett.* **2016**, *108* (7), 071902.
(48) Gutfleisch, O.; Gottschall, T.; Fries, M.; Benke, D.; Radulov, I.; Skokov, K. P.; Wende, H.; Gruner, M.; Acet, M.; Entel, P.; et al. Mastering hysteresis in magnetocaloric materials. *Philos. Trans. R. Soc., A* **2016**, *374* (2074), 20150308.
(49) Stern-Taulats, E.; Castán, T.; Mañosa, L.; Planes, A.; Mathur, N. D.; Moya, X. Multicaloric materials and effects. *MRS Bull.* **2018**, *43* (4), 295−299.
(50) Cui, J.; et al. Combinatorial search of thermoelastic shape-memory alloys with extremely small hysteresis width. *Nat. Mater.* **2006**, *5* (4), 286−90.
(51) Ingale, B. D.; Wei, W. C.; Chang, P. C.; Kuo, Y. K.; Wu, S. K. Anomalous transport and thermal properties of NiTi and with Cu and Fe-doped shape memory alloys near the martensitic transition. *J. Appl. Phys.* **2011**, *110*, 113721.
(52) Isola, L.; et al. Load-biased martensitic transformation strain of Ti50−Ni47−Co3 strip obtained by a twin-roll casting technique. *Mater. Sci. Eng., A* **2014**, *597*, 245−252.
(53) Naresh, H.; Bharath, H. S.; Prashantha, S. The Influence of Alloying Constituent Fe on Mechanical Properties Of NiTi Based Shape Memory Alloys. *Mater. Today Proc.* **2017**, *4* (10), 11251−11259.
(54) Honma, T. *Types of Mechanical Characteristics of Shape Memory Alloys: TiNi−Based Shape Memory Alloys*; Shape Memory Alloys; Gordon and Breach Science Publishers: New York, 1987.
(55) Liu, F.; Ding, Z.; Li, Y.; Xu, H. Phase transformation behaviors and mechanical properties of TiNiMo shape memory alloys. *Intermetallics* **2005**, *13* (3−4), 357−360.
(56) Long, C. J. *CombiView download*; SourceForge.net: 2015. [Online]. Available: https://sourceforge.net/projects/xrdsuite/. [Accessed: 06-Jan-2020].
(57) *DIFFRAC.SUITE EVA - XRD Software*; Bruker: [Online]. Available: https://www.bruker.com/products/x-ray-diffraction-and-elemental-analysis/x-ray-diffraction/xrd-software/eva.html. [Accessed: 13-Apr-2020].
(58) Zarnetta, R.; et al. Identification of quaternary shape memory alloys with near-zero thermal hysteresis and unprecedented functional stability. *Adv. Funct. Mater.* **2010**, *20* (12), 1917−1923.
(59) Wieczorek, A.; et al. Thermal Stabilization of NiTiCuV Shape Memory Alloys: Observations During Elastocaloric Training. *Shape Mem. Superelasticity* **2015**, *1* (2), 132−141.
(60) Cho, H.; Kim, H. Y.; Miyazaki, S. Fabrication and characterization of Ti−Ni shape memory thin film using Ti/Ni multilayer technique. *Sci. Technol. Adv. Mater.* **2005**, *6* (6), 678−683.
(61) Goldstein, J., Ed., *Scanning electron microscopy and X-ray microanalysis: A text for biologists, materials scientists, and geologists*; Plenum Publishing Corporation: 1992.
(62) Mueller, T.; Kusne, A.; Ramprasad, R. Machine Learning in Materials Science: Recent Progress and Emerging Applications,. *Reviews in Computational Chemistry* **2016**, *29*, 186−273.
(63) Delaunay, B. Sur la sphère vide. A la mémoire de Georges Voronoï. Classe des sciences mathématiques et naturelles. *Bull. Acad. URSS* **1934**, *6*, 793−800.
(64) van der Pauw, L. J. A method of measuring specific resistivity and Hall effect of discs of arbitray shape. *Philips Res. Rep.* **1958**, *13*, 1.

https://dx.doi.org/10.1021/acscombsci.0c00097
ACS Comb. Sci. 2020, 22, 641−648

Engineering 6 (2020) 637–643

Contents lists available at ScienceDirect

Engineering

journal homepage: www.elsevier.com/locate/eng

Research
Materials Genome Engineering—Article

Combinatorial Synthesis and High-Throughput Characterization of Microstructure and Phase Transformation in Ni–Ti–Cu–V Quaternary Thin-Film Library

Naila M. Al Hasan [a], Huilong Hou [a], Suchismita Sarkar [b], Sigurd Thienhaus [c], Apurva Mehta [b], Alfred Ludwig [c], Ichiro Takeuchi [a,*]

[a] Department of Materials Science and Engineering, University of Maryland, College Park, MD 20742, USA
[b] Stanford Synchrotron Radiation Lightsource, SLAC National Accelerator Laboratory, Menlo Park, CA 94025, USA
[c] Werkstoffe der Mikrotechnik, Ruhr-Universität Bochum, Bochum 44801, Germany

ARTICLE INFO

Article history:
Received 3 June 2019
Revised 10 October 2019
Accepted 24 December 2019
Available online 16 May 2020

Keywords:
Ni–Ti–Cu–V alloys
Combinatorial materials science
Quaternary alloys
Shape memory alloys
Thin-film library
Elastocaloric cooling
Thermoelastic cooling
Phase transformation
High-throughput characterization
Property mapping
Machine learning

ABSTRACT

Ni–Ti–based shape memory alloys (SMAs) have found widespread use in the last 70 years, but improving their functional stability remains a key quest for more robust and advanced applications. Named for their ability to retain their processed shape as a result of a reversible martensitic transformation, SMAs are highly sensitive to compositional variations. Alloying with ternary and quaternary elements to fine-tune the lattice parameters and the thermal hysteresis of an SMA, therefore, becomes a challenge in materials exploration. Combinatorial materials science allows streamlining of the synthesis process and data management from multiple characterization techniques. In this study, a composition spread of Ni–Ti–Cu–V thin-film library was synthesized by magnetron co-sputtering on a thermally oxidized Si wafer. Composition-dependent phase transformation temperature and microstructure were investigated and determined using high-throughput wavelength dispersive spectroscopy, synchrotron X-ray diffraction, and temperature-dependent resistance measurements. Of the 177 compositions in the materials library, 32 were observed to have shape memory effect, of which five had zero or near-zero thermal hysteresis. These compositions provide flexibility in the operating temperature regimes that they can be used in. A phase map for the quaternary system and correlations of functional properties are discussed with respect to the local microstructure and composition of the thin-film library.

1. Introduction

Shape memory alloys (SMAs) of nickel-titanium (Ni-Ti) are functional materials with thermal (one-way effect, 1-WE) and mechanical (pseudoelasticity, PE) "memory" [1]. This property, also known as the shape memory effect (SME), is a result of a first-order, diffusionless, and reversible phase transformation between austenite and martensite structures. When cooling from high temperature, phase transformation from austenite to martensite is characterized by the martensite start (M_s) and finish (M_f) temperatures. Similarly, the reverse process is characterized by the austenite start (A_s) and finish (A_f) temperatures. A thermal hysteresis ΔT occurs when there is a difference in the temperature at which 50% of the material is transformed into martensite upon cooling and 50% into austenite upon heating, so that $\Delta T = A_f - M_s$ [2]. Transformation temperatures (A_f) range between 0 and 100 °C for commercial NiTi alloys with a hysteresis width of 25 to 40 °C [3]. Austenitic and martensitic NiTi structures have cubic B2 and monoclinic B19' crystal lattices, respectively [1,4,5]. In addition, intermediate structures such as rhombohedral or trigonal R-phase and B19 facilitate geometric compatibility during transformation. Phases and crystal lattices present in the Ni–Ti system are extensively studied, but undesirable functional and structural properties including the strong dependence of transformation temperatures on composition and, hence, tight control of synthesis parameters present a significant challenge in their adoption into new technology [6–10]. Nonetheless, Ni–Ti SMAs enjoy widespread applications ranging from actuators, stents, orthodontics, and sensors to eco-friendly refrigeration and even fashion [11–17].

* Corresponding author.
E-mail address: takeuchi@umd.edu (I. Takeuchi).

https://doi.org/10.1016/j.eng.2020.05.003

The transformation temperature regime is a critical parameter in determining the application of SMAs along with their functional fatigue. The addition of ternary and quaternary alloying elements enables the modification and fine-tuning of the material transformation temperature for specific applications [4,9,18]. Combinatorial materials science merges the synthesis of thin films with high-throughput characterization, which allows access to many compounds covering a substantial compositional space with different stoichiometries under identical conditions. Hence, it enables the rapid discovery and development of new materials with targeted properties [19].

In this study, we report on a systematic workflow for the rapid determination of composition–structure–property relationships using combinatorial synthesis and high-throughput experimentation. We report on new Ni–Ti–Cu–V quaternary thin-film compositions having near-zero thermal hysteresis, as determined by high-throughput resistance measurements. Compositional and structural characterization was carried out with wavelength dispersive spectroscopy and high-throughput synchrotron X-ray diffraction (HiTp-XRD). A composition-phase map for the quaternary alloy was developed through automated data analysis employing hierarchical clustering techniques. This work validates theoretical predictions and builds on experimental efforts in developing new SMAs [20,21].

2. Experimental approach

Experiments were carried out with the long flat edge of the wafer positioned at the bottom so that the first set of five sample pads, labeled 1–5 from left to right, were parallel to the edge. This eased and streamlined data management.

2.1. Thin-film synthesis with magnetic sputtering

A quaternary thin-film composition spread for Ni–Ti–Cu–V between 150 and 250 nm thick was deposited on a 3 in (76.2 mm) thermally oxidized (2 μm SiO_2) silicon (Si) wafer (thickness 400 μm, IWS; International Wafer Service, Inc., USA), in an ultrahigh-vacuum (5×10^{-7} torr, 1 torr = 133.32237 Pa), magnetron sputtering system at room temperature. High-purity (99.98%) elemental targets with a diameter of 1.5 in (38.1 mm) were sputtered using DC (direct current from Seren IPS Inc., USA) and RF (radio frequency from Advanced Energy Industries, Inc., USA) power sources with an ultrahigh purity argon (Ar) (99.9997%; Airgas, USA) pressure of 5×10^{-3} torr. Each wafer was covered with a patterned Si mask to delineate 177 individual compositions evenly across the wafer at a Δx, Δy of 4.5 mm. The substrate was water cooled to avoid crystallization during sputter deposition and to maintain low temperatures. The resulting film was annealed in a vacuum at 500 °C for 1 h following the process reported in the literature [21]. Deposition rates were determined for each element used in this work under a given power source for a preset time and are listed in Table S1 of the Supplementary data. Thickness was measured using atomic force microscopy (AFM). Based on the calibrated deposition rates and the density of each element, the required power ratio to achieve a desired composition was determined and is listed in Table S2 of the Supplementary data. The total time for the synthesis and annealing of a thin-film library is 2 h before it is ready for characterization.

2.2. Chemical composition determination

Composition variation in the thin-film library was determined using wavelength dispersive X-ray (WDX) analysis in an electron probe microanalyzer (EPMA) JXA 8900R Microprobe (Microprobe, USA), with an acceleration voltage of 15 kV. Standardization of references was carried out with pure metal references and compositions were determined to be within an experimental error of < 0.3 at%.

2.3. Crystal structure analysis

Structural information was obtained at room temperature by collecting two-dimensional (2D) X-ray diffraction (XRD) patterns on the combinatorial library at beamline 1–5 at the Stanford Synchrotron Radiation Lightsource (SSRL). The experiment was performed with 14.99 keV energy collimated to approximately 0.3 mm × 0.3 mm beam size and a wavelength of 0.82657 Å (8.2657×10^{-9} m). MarCCD detector (Rayonix, L.L.C., USA) was used to collect the data at an exposure rate of 30 s. To minimize the influence of diffraction from the silicon substrate, the library was scanned with a small grazing incidence angle of 1°–2°. The grazing incidence geometry resulted in an approximate 3 mm probe footprint on the library. An automated algorithm was used to measure the entire library with a step size of 4.5 mm.

For data analysis, the geometric parameters of the 2D detector, such as the direct beam position, tilting, rotation, and sample-to-detector distance, were extracted from a measuring-standard LaB_6 powder pattern. These parameters were used to transform the initial raw images that were acquired as a function of Q and χ in the diffraction coordinate into one-dimensional (1D) diffraction patterns by integrating and normalizing over the χ angle. The Bragg angle (2θ) is related to the scattering vector (Q) by the relationship $Q = 4\times\pi\times\sin(\theta)/\lambda$, with wavelength ($\lambda$) helping to generate a more traditional 1D spectrum (intensity vs 2θ).

2.4. Characterization of transformation temperature

Film resistance as a function of temperature, $R(T)$, was measured to determine the transformation temperature, as crystal structure changes correspond with measurable electrical and magnetic changes. Resistance was measured using a four-point probe method described by Van der Pauw in a custom-built high-throughput test stand with an automated platform of five sets of four-point probes [22,23]. The spacing between the probe tips was 500 μm and the test stand was enclosed in a box purged with nitrogen (N_2) gas. Measurements were performed between −40 and 120 °C with a heating/cooling rate of 5 °C·min^{-1} and 50 mA source current.

2.5. Cluster analysis of high-throughput data

An unsupervised machine learning algorithm was used as an exploratory data analysis tool as well as a phase mapping tool. Hierarchical cluster analysis was performed using the Pearson correlation coefficient model with criteria for similarity and dissimilarity between input data, such that data grouped into a cluster shared similar characteristics in comparison with data in other clusters [24]. For two spectra x and y having the means $\bar{x}$ and $\bar{y}$ the Pearson correlation coefficient (PCC) clustering model is defined as [25]

$$C_{xy} = \frac{\sum_{i=1}^{n}(x_i - \bar{x})(y_i - \bar{y})}{\left[\sum_{i=1}^{n}(x_i - \bar{x})^2 \sum_{i=1}^{n}(y_i - \bar{y})^2\right]^{\frac{1}{2}}}$$

It was applied to the diffraction patterns using CombiView (Anritsu, Japan), which is a MATLAB-supported data visualization platform developed by the Takeuchi group.

3. Results and discussions

In this work, we investigated the influence of composition on the structure and transformation property of quaternary

$[Ni_{36}–Ti_{52}–Cu_{12}]_{(100-x)}V_x$ alloys in thin-film form. High-throughput characterization of the composition and crystal structure was performed using wavelength dispersive spectroscopy and synchrotron X-ray diffraction, respectively. Transformation behavior was characterized using resistance measurements as a function of temperature. Machine learning using a MATLAB-based visualization platform CombiView developed in-house was used to sort compositions by diffraction patterns, and therefore structures, into clusters in order to rapidly identify constituent phases and determine phase boundaries.

3.1. Chemical composition

Automated WDS measurements were carried out on all 177 samples in the materials library. Fig. 1 shows the composition variation across the wafer, with atomic percent ranges for the four elements as follows: Ni from 21.3 at% to 58.3 at%; Ti from 23.3 at% to 57.5 at%; copper (Cu) from 12.9 at% to 24.9 at%; and vanadium (V) from 2.9 at% to 6.2 at%. The targeted composition $Ti_{41.8}Ni_{37.5}Cu_{16.0}V_{4.6}$ was obtained in the center. Distribution of the elements corresponds with the elemental target gun positions inside the sputtering chamber.

3.2. Transformation temperature determination from temperature-dependent resistance measurements

The property of interest for this library was SME determined from phase transformation curves. These were obtained by carrying out temperature-dependent resistance measurements. Phase transformation temperatures of austenitic finish (A_f), and martensitic start (M_s) were determined using the tangent method [21]. Phase transformation activity for each composition as a function of wafer position in the thin-film library is shown in Fig. 2(a). Regions of transformation indicated by curves shaped as variations of "U" and "2" were observed to be limited to the right side of the wafer. The left-half portion can be divided into two main regions: The first region encompassed many compositions in the center of the wafer with non-transforming, linear behavior; the second region was limited to compositions in the far left showing non-transforming and nonlinear behavior without clear curves. Positions and compositions clustered by SME activity are shown in Figs. 2(b) and (c), respectively, where there are reversible phase transformations with nonlinear $R(T)$ curves (yellow, teal, pink), non-transforming regions with linear curves in blue, and nonlinear curves in green and red. Phase transformation parameters of

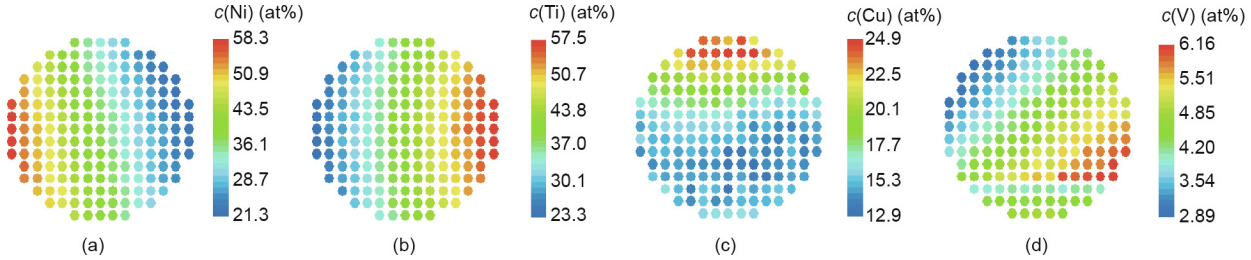

Fig. 1. Elemental distribution of (a) Ni, (b) Ti, (c) Cu, and (d) V on a 3 in Si wafer. The color scale for each element indicates composition in atomic percent from high to low indicated by the progression from red to blue. The wafer was oriented with the long flat edge at the bottom.

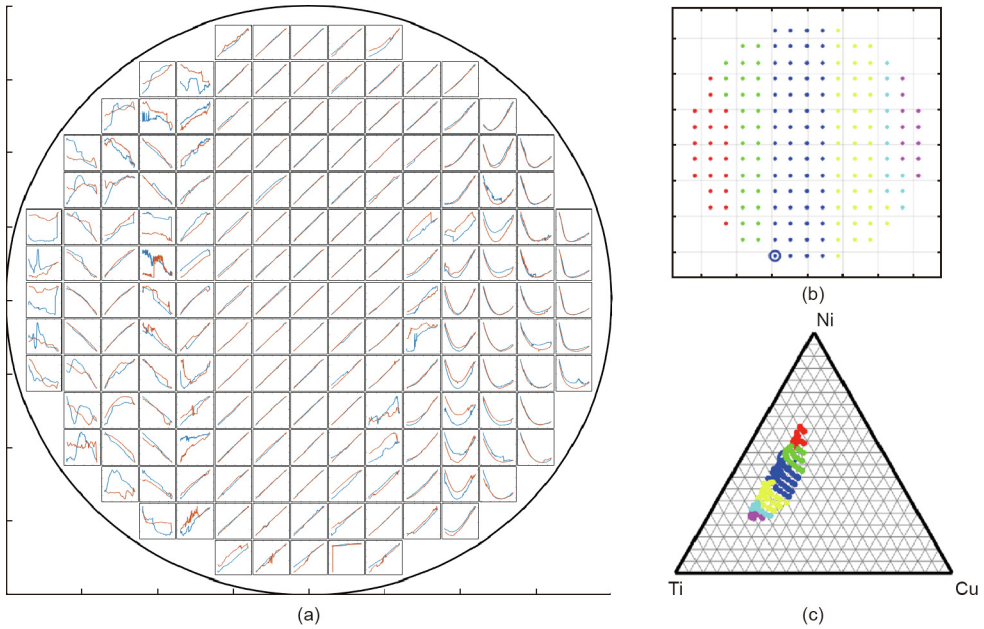

Fig. 2. (a) Temperature-dependent resistance $R(T)$ curves for $[Ni_{36}–Ti_{52}–Cu_{12}]_{(100-x)}V_x$ showing regions of transformation. Reversible transformation is observed on the right portion of the wafer as indicated by broad "U"- and "2"-shaped curves. Heating and cooling curves are indicated by red and blue colors, respectively. (b) Grouping by SME activity of wafer positions and (c) compositions projected on a ternary Cu–Ni–Ti plot, where V is between 2.9 at% and 6.2 at%.

thermal hysteresis ($\Delta T = A_f - M_s$), austenitic finish (A_f), and martensitic start (M_s) temperatures are shown in Fig. 3. All compositions with phase transformation behavior are listed in Table 1. SME was observed in 32 compositions, with five compositions having zero or near-zero thermal hysteresis and one composition having a maximum ΔT of 17.2 °C. The elemental range for compositions having SME was observed as follows: c(Ti) = 49.4 at% to 57.5 at%; c(Ni) = 21.3 at% to 30.9 at%; c(Cu) = 13.8 at% to 21.6 at%; and c(V) = 4.1 at% to 6.2 at%. The boundaries of the temperature regime where transformations to austenite occurred were observed to be centered around 13 °C to 29 °C while the martensitic start temperature was slightly reduced between 10 °C and 20 °C. Thermal hysteresis of ≤ 4 °C was observed in 19 compositions.

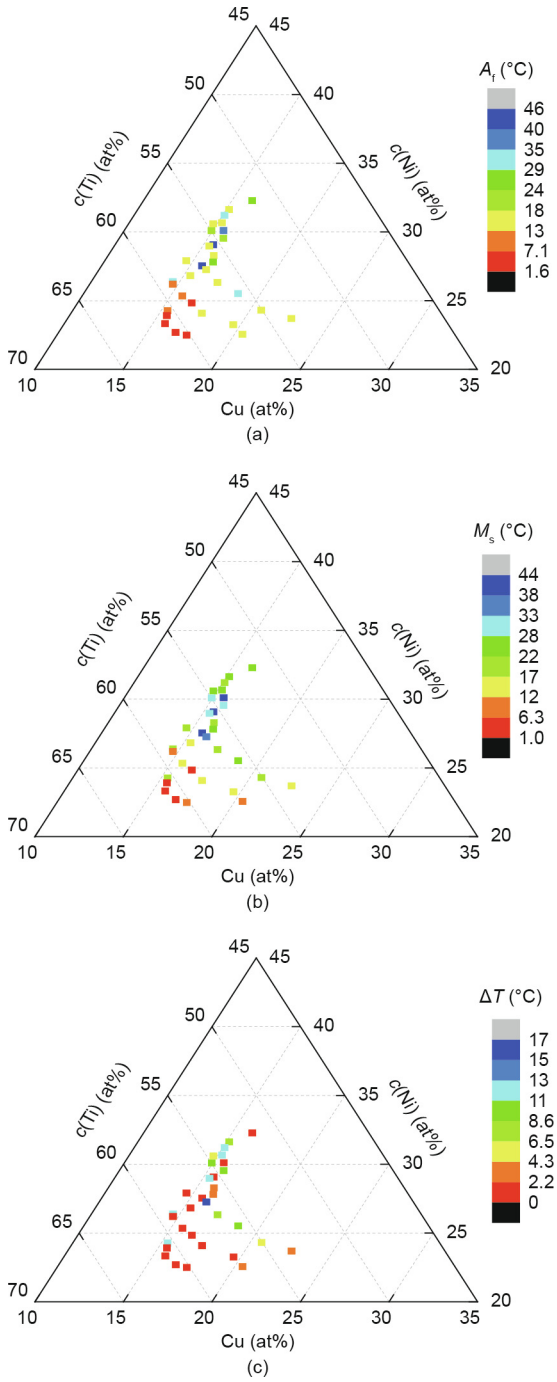

Fig. 3. Ni–Ti–Cu–V compositions having SME projected onto Cu–Ni–Ti ternary plots with the atomic concentration of V held constant between 2.9 at% and 6.2 at%. Phase transformation parameters of (a) austenitic finish (A_f) temperature, (b) martensitic start (M_s) temperature, and (c) thermal hysteresis $\Delta T = A_f - M_s$. Color scale bars from blue to red indicate high to low temperatures.

3.3. Crystal structure and phase identification

The data visualization platform CombiView allows the linking of the sample position on the wafer with its corresponding composition and diffraction pattern. The structural phase diagram was determined through a hierarchical cluster analysis of the diffraction patterns, as shown in Fig. 4. A Pearson correlation coefficient cluster analysis resulted in six clusters for the Ni–Ti–Cu–V materials library. Table 2 lists the crystal structure and space group of the phases found in the library. For non-transforming compositions, both linear and nonlinear $R(T)$ curves were observed, which were attributed to double-phase and low-symmetry crystal structures. The default structure type is a cubic phase, unless specified otherwise under prototype.

3.4. Assessment of the thin-film phase diagram

Results for the transformation properties and phases identified in the present study are listed in Table 1 and Table 2, respectively. Martensitic phase transformation determined from resistance measurement shows that the shape memory effect is limited to the Ti-rich region. SME variation changes with Ni and V content such that SME is observed to be between 21.3 at% and 33.4 at% Ni and between 4.0 at% and 6.2 at% V, respectively. This is in agreement with values reported in bulk by Frenzel et al. [9] and Schmidt et al. [26].

Clustering diffraction patterns using the Pearson correlation coefficient model match the grouping of compositions based on the shape memory behavior. Cubic NiTi with a mixture of cubic

Table 1
Thermal hysteresis, austenitic finish, and martensitic start temperatures for quaternary-Ni-Ti-Cu-V SMAs by ascending Ti content.

c(Ti) (at%)	c(Ni) (at%)	c(Cu) (at%)	c(V) (at%)	A_f (°C)	M_s (°C)	ΔT (°C)
49.4	30.9	15.5	4.2	25.0	24.0	1.0
50.0	29.7	14.3	6.0	22.8	16.0	6.8
50.6	29.4	14.2	5.8	30.0	17.5	12.5
51.0	28.9	14.4	5.7	26.5	15.2	11.3
51.2	22.6	21.6	4.5	14.4	12.0	2.4
51.7	28.9	14.0	5.4	24.0	18.0	6.0
51.7	28.0	15.1	5.2	30.7	20.4	10.3
52.0	27.3	14.6	6.2	45.6	43.5	2.1
52.0	28.5	14.1	5.4	30.6	21.7	8.9
52.1	28.9	15.0	4.1	40.0	38.0	2.0
52.4	23.1	19.7	4.8	21.2	15.2	6.0
52.5	27.3	14.5	5.7	28.8	16.4	12.4
52.5	26.7	15.1	5.8	18.0	14.0	4.0
52.9	26.3	15.3	5.5	26.8	24.0	2.8
53.0	24.2	17.8	5.0	34.4	24.8	9.6
53.3	25.8	14.7	6.1	42.9	41.9	1.0
53.6	25.0	16.3	5.1	21.2	14.4	6.8
53.7	25.8	15.2	5.3	35.2	18.0	17.2
54.2	21.5	19.5	4.9	13.6	10.0	3.6
54.2	22.1	18.6	5.1	14.8	14.0	0.8
54.3	25.2	14.4	6.1	16.0	16.0	0
54.3	26.4	13.8	5.5	19.6	17.6	2.0
55.5	22.8	16.5	5.2	13.2	12.8	0.4
55.5	24.8	13.8	5.9	29.5	17.2	12.3
55.5	23.5	15.6	5.4	5.2	3.6	1.6
55.7	23.9	14.8	5.6	12.0	10.0	2.0
55.8	24.7	13.9	5.7	11.6	9.6	2.0
56.7	22.8	14.4	6.0	21.2	10.4	10.8
57.1	22.5	14.6	5.8	1.6	1.2	0.4
57.1	21.3	16.5	5.1	6.4	4.8	1.6
57.5	22.0	14.8	5.7	6.0	6.0	0
57.5	21.5	15.7	5.3	4.4	2.4	2.0

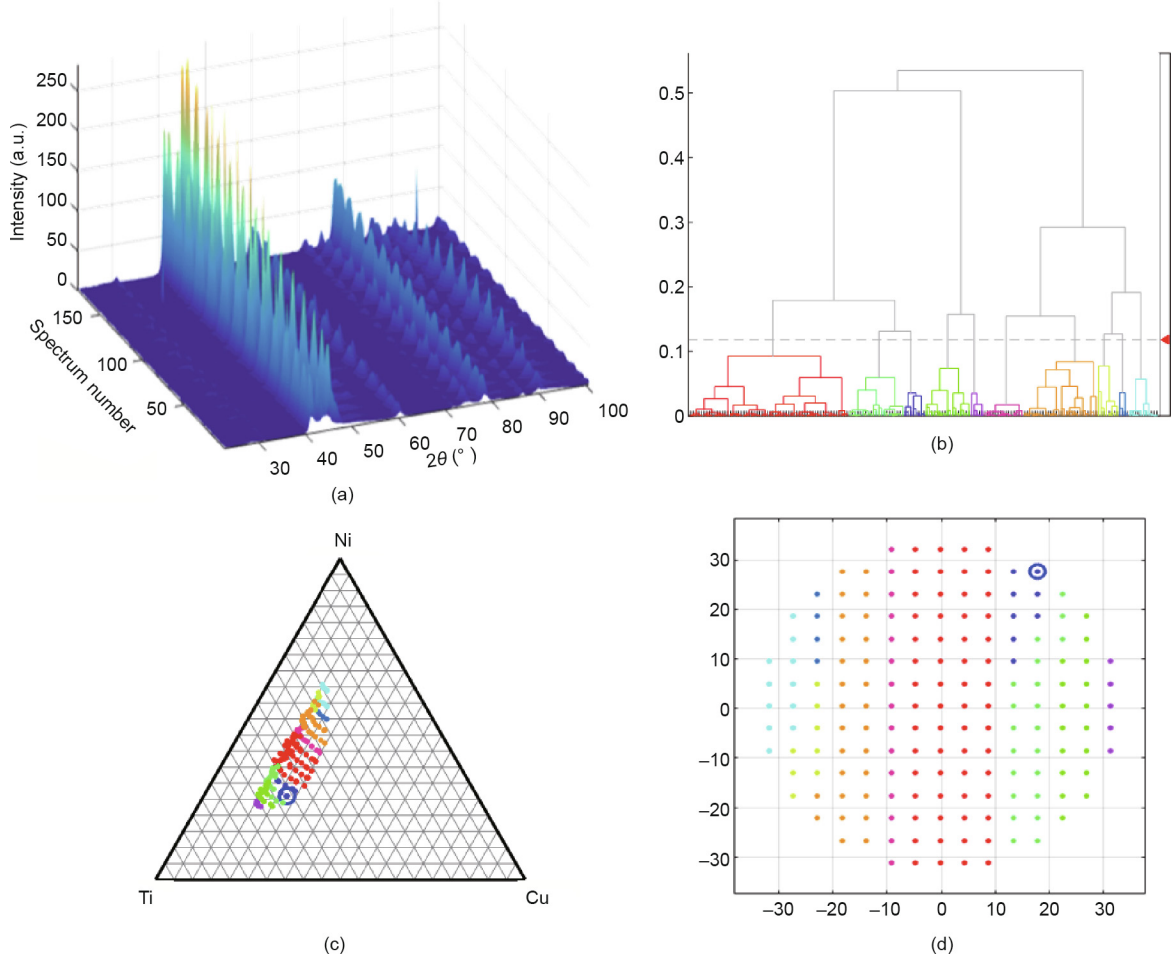

Fig. 4. Hierarchical cluster analysis of diffraction patterns for a quaternary thin-film library covering the range $[Ni_{36}–Ti_{52}–Cu_{12}]_{(100-x)}V_x$. The MATLAB-based data visualization platform CombiView allows linking of the sample position on the wafer with its composition and diffraction pattern, which is used to perform hierarchical cluster analysis to create a structural phase diagram. (a) 177 diffraction patterns with an *x*-axis of 2θ between 22° and 100°; (b) pearson correlation coefficient cluster analysis model showing grouping of XRD patterns based on similarities in peak positions; (c) composition space covered in this study as projected on a ternary plot of Cu–Ni–Ti with constant V identifying structural phase boundaries as delineated from hierarchical clustering shown in (b); (d) grouping by position on wafer (long flat edge at bottom).

Table 2
Overview of crystal structures identified in the Ni–Ti–Cu–V materials library.

Formula	Space group	Space group number	Prototype
NiTi	*Pm*-3*m*	221	$(Ti_{0.64}Zr_{0.36})$ Ni
$TiNi_{0.8}Cu_{0.2}$	$P2_1/m$	11	Monoclinic
CuNi i	*I*4/*mmm*	139	Tetragonal
$Ni_{0.25}Cu_{0.75}$	*Im*3*m*	229	
$Ti_2C_{0.06}$	$P6_3/mmc$	194	Hexagonal
$(Cu_{0.03}Ni_{0.97})_3Ti$	$P6_3/mmc$	194	
$Ti(Ni_{2.79}Cu_{0.21})$	*R*-3*m*	166	Rhombo. H. axes
$TiNi_{0.8}Cu_{0.2}$	*Pmam*	51	Orthorhombic
$Ti(Cu_{0.053}Ni_{0.947})_3$	$P6_3/mmc$	194	
$(Ti_{0.67}V_{0.33})Ni_3$	$P6_3/mmc$	194	
Ti Ni_2 Cu	*Pmmn*	59	

$Ni_{0.25}$ $Cu_{0.75}$ and tetragonal CuNiTi phases were found in Ti-rich regions with the highest V content. The increased replacement of Ni by V was observed to stabilize the transformable cubic and tetragonal martensite variants (Fig. 5). A mix of cubic crystal structure having a prototype formula $(Ti_{0.64}Zr_{0.36})$Ni and hexagonal $Ti(Cu_{0.053}Ni_{0.947})_3$ made up the majority of the composition space covered in this materials library having no transformation. For Ni-rich regions, orthorhombic phases of $TiNi_2Cu$/$TiNi_{0.8}Cu_{0.2}$ mixed with hexagonal $(Ti_{0.67}V_{0.33})Ni_3$ were identified as Ni content was reduced.

The addition of Cu to binary NiTi such that Cu replaces Ni has been shown to decrease the misfit between austenite and martensitic lattices. This translates to a slight decrease in M_s and reduced width of the thermal hysteresis, which, when combined, improves fatigue properties. The influence of the addition of V as a ternary element to NiTi was reported by Frenzel et al. [9], who demonstrated a reduction in M_s. In addition, the mechanical behavior was stabilized so that a small residual strain was maintained, compared with binary NiTi. Ni–Ti–Cu–V has been demonstrated for application as an elastocaloric material that is able to fulfill the potential of using $Ni_{45}Ti_{47.25}Cu_5V_{2.75}$ in ribbon form [26] and $Ni_{50}Ti_{45.3}V_{4.7}$ in a square prismatic form [27]. The identification of new compositions with reduced thermal hysteresis is a starting point for scale-up experiments to determine their long-term robustness through mechanical testing.

3.5. Effect of temperature cycling on film resistance

Thermal stability over many cycles is an important consideration in the optimization of heat transfer and the determination of functional fatigue, specifically, when using SMAs for elastocaloric cooling [28]. Film sheet resistance at room temperature (Fig. 6(a)) was measured prior to cycling the library between −40 and 120 °C for temperature-dependent resistance measurements. The

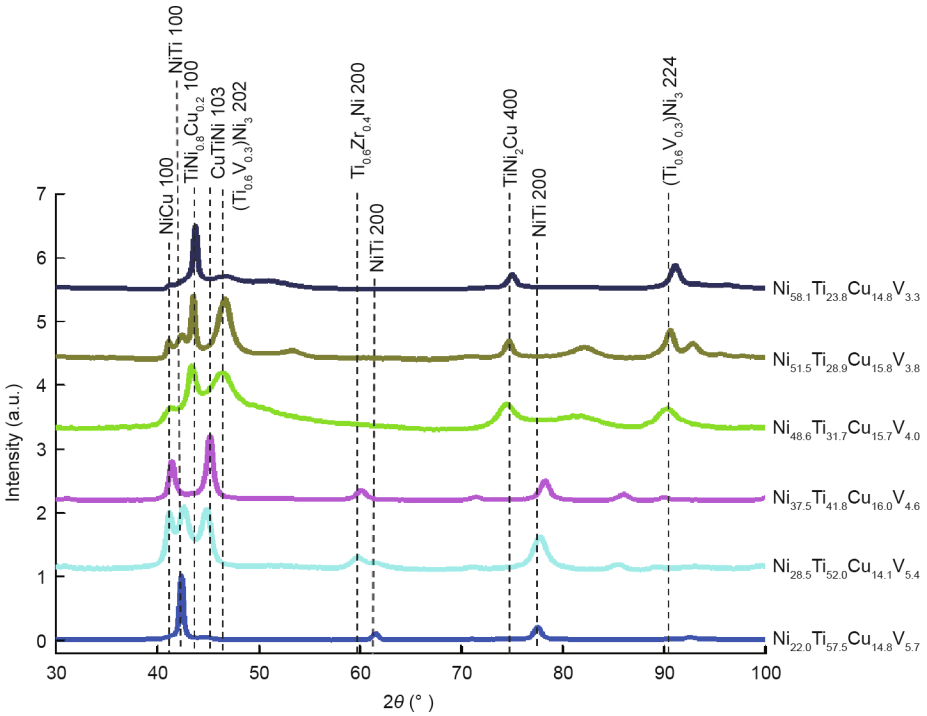

Fig. 5. Selected diffraction patterns representing the six clusters identified by the Pearson correlation coefficient clustering model. Substitution of Ni by V increases with distance from the abscissa, reflecting a shift in the non-transforming orthorhombic and hexagonal phase mixture to transformable cubic and tetragonal crystal structures. Patterns are offset for clarity.

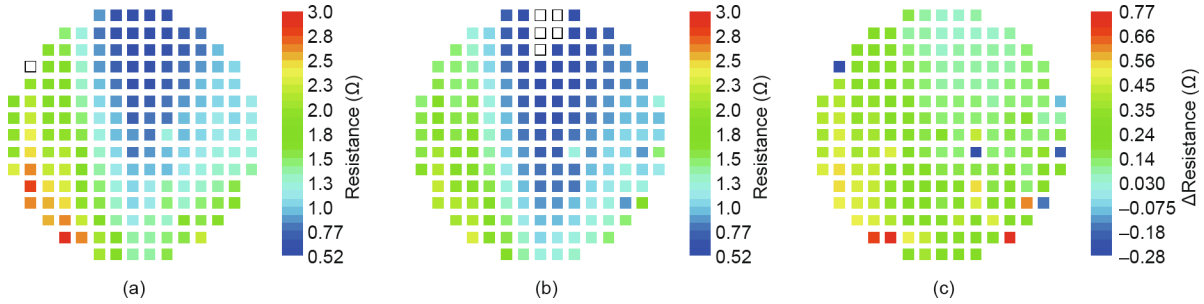

Fig. 6. Thin-film sheet resistance at room temperature (a) before and (b) after 84 temperature cycles between −40 and 120 °C. Post-cycling resistance was mapped using the same scale as pre-cycling; values outside of this range are indicated by colorless boxes. (c) Difference in resistance from (a) and (b). The color scale from red to blue indicates high to low values, respectively. The wafer was oriented with the long flat edge at the bottom.

effect of temperature cycling on film resistance was evaluated since the library was subjected to 84 temperature cycles, and is shown in Fig. 6(b) with the difference mapped in Fig. 6(c). While the SME was stable, as determined from the observation of transformation in Fig. 2, an overall reduction in sheet resistance was observed. XRD measurements collected post-thermal cycling show little to no change in diffraction patterns, thereby suggesting good structural stability (data not shown).

4. Conclusions

In this work, we report on the combinatorial thin-film synthesis and high-throughput characterization of a quaternary alloy. We provide an overview of the dependence of material properties on composition and structure through composition–structure–property maps. The Ni–Ti–Cu–V materials library we synthesized spans a composition region that has shape memory behavior. A strong correlation can be made between the microstructure and phase transformation property and, hence, composition. SMA effect is prominent in the Ti-rich region, with a significant number of compositions having near-zero thermal hysteresis. Increasing addition of V was observed to stabilize the mixture of cubic and tetragonal phases identified in compositions exhibiting SMA behavior. For non-transforming compositions, both linear and nonlinear $R(T)$ curves were observed, which were attributed to double-phase and low-symmetry crystal structures. SME and thermal hysteresis were stable over close to a hundred cycles. This work explored and validated the use of V as a fourth element in fine-tuning the operating temperature of a Ni–Ti–Cu ternary alloy in the ambient temperature regime for elastocaloric cooling applications. Work remains to be undertaken to understand the limits of V addition on the enhancement of efficiency and functional stability of the elastocaloric effect in NiTi alloys.

Acknowledgements

The author thanks Tieren Gao, Peer Decker, Alan Savan, and Manfred Wuttig for fruitful discussions. The authors gratefully

acknowledge funding support by the National Science Foundation Graduate Research Fellowship Program (DGE 1322106).

Compliance with ethics guidelines

Naila M. Al Hasan, Huilong Hou, Suchismita Sarkar, Sigurd Thienhaus, Apurva Mehta, Alfred Ludwig, and Ichiro Takeuchi declare that they have no conflict of interest or financial conflicts to disclose.

Appendix A. Supplementary data

Supplementary data to this article can be found online at https://doi.org/10.1016/j.eng.2020.05.003.

References

[1] Otsuka K, Wayman CM, editors. Shape memory materials. Cambridge: Cambridge University Press; 1998.
[2] Buehler WJ, Wang FE. A summary of recent research on the nitinol alloys and their potential application in ocean engineering. Ocean Eng 1968;1(1):105–20.
[3] Stöckel D. The shape memory effect: phenomenon, alloys, applications. In: Proceedings of the 1995 Shape Memory Alloys for Power Systems EPRI; 1995; Fremont, CA, USA; 1995. p. 1–13.
[4] Otsuka K, Ren X. Physical metallurgy of Ti–Ni-based shape memory alloys. Prog Mater Sci 2005;50(5):511–678.
[5] Lagoudas DC, editor. Shape memory alloys: modeling and engineering applications. Boston: Springer; 2008.
[6] Lobo PS, Almeida J, Guerreiro L. Shape memory alloys behaviour: a review. Procedia Eng 2015;114:776–83.
[7] Mohd Jani J, Leary M, Subic A, Gibson MA. A review of shape memory alloy research, applications and opportunities. Mater Des 2014;56:1078–113.
[8] Zarinejad M, Liu Y. Dependence of transformation temperatures of NiTi-based shape-memory alloys on the number and concentration of valence electrons. Adv Funct Mater 2008;18(18):2789–94.
[9] Frenzel J, Wieczorek A, Opahle I, Maaß B, Drautz R, Eggeler G. On the effect of alloy composition on martensite start temperatures and latent heats in Ni–Ti–based shape memory alloys. Acta Mater 2015;90:213–31.
[10] Otsuka K, Ren XB. Factors affecting the ms temperature and its control in shape-memory alloys. Mater Sci Forum 2002;394–395:177–84.
[11] Morgan N. Medical shape memory alloy applications—the market and its products. Mater Sci Eng A 2004;378(1–2):16–23.
[12] Petrini L, Migliavacca F. Biomedical applications of shape memory alloys. J Metall 2011;2011:1–15.
[13] Otsuka K, Kakeshita T. Science and technology of shape-memory alloys: new developments. MRS Bull 2002;27(2):91–100.
[14] Qian S. Development of thermoelastic cooling systems [dissertation]. Maryland: University of Maryland, College Park; 2015.
[15] Qian S, Geng Y, Wang Y, Pillsbury TE, Hada Y, Yamaguchi Y, et al. Elastocaloric effect in CuAlZn and CuAlMn shape memory alloys under compression. Philos Trans R Soc A Math Phys Eng Sci 2016;374(2074):20150309.
[16] Chluba C, Ge W, Lima de Miranda R, Strobel J, Kienle L, Quandt E, et al. Ultralow-fatigue shape memory alloy films. Science 2015;348(6238):1004–7.
[17] Vasile SI, Grabowska KE, Ciesielska-Wrobel I, Ghitaiga J. Analysis of hybrid woven fabrics with shape memory alloys wires embedded. Fibres Text East Eur 2010;18(1):64–9.
[18] Xue D, Xue D, Yuan R, Zhou Y, Balachandran PV, Ding X, et al. An informatics approach to transformation temperatures of NiTi-based shape memory alloys. Acta Mater 2017;125:532–41.
[19] Xue D, Balachandran PV, Hogden J, Theiler J, Xue D, Lookman T. Accelerated search for materials with targeted properties by adaptive design. Nat Commun 2016;7(1):1–9.
[20] Cui J, Chu YS, Famodu OO, Furuya Y, Hattrick-Simpers J, James RD, et al. Combinatorial search of thermoelastic shape-memory alloys with extremely small hysteresis width. Nat Mater 2006;5(4):286–90.
[21] Zarnetta R, Takahashi R, Young ML, Savan A, Furuya Y, Thienhaus S, et al. Identification of quaternary shape memory alloys with near-zero thermal hysteresis and unprecedented functional stability. Adv Funct Mater 2010;20(12):1917–23.
[22] Van der Pauw LJ. A method of measuring specific resistivity and Hall effect of discs of arbitrary shape. Philips Res Rep 1958;13(1):1–9.
[23] Thienhaus S, Zamponi C, Rumpf H, Hattrick-Simpers J, Takeuchi I, Ludwig A. High-throughput characterization of shape memory thin films using automated temperature-dependent resistance measurements. MRS Proc 2006;894:197.
[24] Mueller T, Kusne A, Ramprasad R. Machine learning in materials science: recent progress and emerging applications. Rev Comput Chem 2016;29:186–273.
[25] Long CJ, Hattrick-Simpers J, Murakami M, Srivastava RC, Takeuchi I, Karen VL, et al. Rapid structural mapping of ternary metallic alloy systems using the combinatorial approach and cluster analysis. Rev Sci Instrum 2007;78(7):072217.
[26] Schmidt M, Ullrich J, Wieczorek A, Frenzel J, Schütze A, Eggeler G, et al. Thermal stabilization of NiTiCuV shape memory alloys: observations during elastocaloric training. Shape Mem Superelasticity 2015;1(2):132–41.
[27] Kim Y, Jo MG, Park JW, Park HK, Han HN. Elastocaloric effect in polycrystalline $Ni_{50}Ti_{45.3}V_{4.7}$ shape memory alloy. Scr Mater 2018;144:48–51.
[28] Bechtold C, Chluba C, Lima de Miranda R, Quandt E. High cyclic stability of the elastocaloric effect in sputtered TiNiCu shape memory films. Appl Phys Lett 2012;101(9):091903.

JVST A
Journal of Vacuum Science & Technology A

ARTICLE

avs.scitation.org/journal/jva

XPS group array analysis of a combinatorial Ni-Ti-Co thin film library

Cite as: J. Vac. Sci. Technol. A 38, 063407 (2020); doi: 10.1116/6.0000333
Submitted: 13 May 2020 · Accepted: 11 September 2020 ·
Published Online: 16 October 2020

Jonathan D. P. Counsell,[1,a)] Naila M. Al Hasan,[2] Edward Walton,[1] Tieren Gao,[2] Huilong Hou,[2] and Ichiro Takeuchi[2]

AFFILIATIONS

[1]Kratos Analytical Limited, Manchester M17 1GP, United Kingdom
[2]Department of Materials Science and Engineering, University of Maryland, College Park, Maryland 20742

[a)]**Electronic mail:** jonathan.counsell@kratos.co.uk

ABSTRACT

The last few decades have seen rapid development in computational and theoretical tools for simulating, fabricating, and characterizing material systems. In this report, the potential of surface characterization by x-ray photoelectron spectroscopy (XPS) to provide rapid elemental and chemical state information is presented. The development of the group analysis array functionality is significant for facilitating processing and display of large datasets in the application of XPS analysis to combinatorial materials discovery. We demonstrate that group array analysis provides a more detailed understanding of the chemical distribution across a Ni-Ti-Co combinatorial thin-film materials library.

I. INTRODUCTION

Surface characterization of film depositions is often performed by analyzing only a limited number of points, with the results assumed to be representative of deposited chemistry. In analyzing data and displaying results, the analyst is often limited to calculating data from the selected points and generating a table with some measure of statistical comparison. Compositional mapping is central to obtaining a comprehensive picture of material systems and mapping active chemical properties such as oxidation state and alloying as a function of composition. This is an integral part of understanding the underlying physical and chemical properties of the material. The development of software to handle large matrices of analysis locations, coupled with group analysis of the results, offers a more comprehensive approach to determine the homogeneity of deposition and identify regions of differing composition and, thus, material properties.

The combinatorial approach involves concurrent synthesis of a large number of samples, called a materials library, that is, rapidly characterized using high-throughput techniques.[1] It has been widely used to discover new material phases for many years now, allowing rapid exploration of compositional and structural properties in complex material systems.[2–9] Examples of some materials include thermally stable perovskite solar cells, room temperature ferromagnetic semiconductors, and fatigue-resistant shape memory alloys. Here, the traditional approach of combinatorial techniques to explore several model systems using x-ray photoelectron spectroscopy (XPS) is coupled with the group analysis array functionality to paint a comprehensive picture of the surface structure of the deposition results. Previous studies have applied XPS with combinatorial methods for polymer array material discoveries.[10,11] These studies look at discrete blends of known polymers, copolymers, and treatments; however, here, we are creating a continuous distribution analysis. The method here could, in fact, be used for any type of material to analyze distributions and interesting chemistries.

NiTiNOL is a well-known and commercialized shape memory effect (SME) material. It undergoes martensitic transformation that lends it two properties—SME and super-elasticity that is the ability to return to its processed shape, thus earning the name shape memory alloy (SMA).[12] The transformation is highly sensitive to composition such that small deviations from the equiatomic configuration yield no SME.[1,2] Nonetheless, efforts have been made to tune properties such as the temperature for onset of transformation, fatigue, and thermal hysteresis by adding a third and fourth element to improve overall efficiency of the material in specific applications.[6, 9,13–15] This quickly becomes a challenge for large

data generation but one that is relatively easily addressed by combinatorial material science in using high-throughput characterization methods. In this report, we investigate the ternary Ni-Ti-Co SMA system where the addition of Co to Ni-Ti is known to reduce the transition start temperature and transformation temperature range that are important parameters for medical and ambient temperature applications.[16,17–25] As such, the aim was to explore an expanded composition region for the system by incorporating up to 30% Co as a ternary element.

II. EXPERIMENT

A Ni-Ti-Co ternary composition spread between 150 and 250 nm thick was deposited on a 3 in. (76.2 mm) Si wafer (thickness 400 μm, IWS) in vacuum (base pressure: 10^{-7} Torr or 6.6×10^{-5} Pa, deposition pressure: 5×10^{-3} Torr or 0.67 Pa) by magnetron co-sputtering of high purity Ni, Ti, and Co targets (99.98%, 38.1 mm diameter; Lesker) at room temperature. The thin film library was deposited over a period of 51 min using a DC power source (Seren IPS) for Ni and Ti sputtered at 50 and 100 W, respectively, and an RF power source (Advance Energy) of 18 W for Co. Substrate was water cooled to avoid crystallization during sputter deposition and to maintain low temperatures. Figure 1(a) shows the geometrical arrangement of the targets inside the sputter chamber relative to the wafer and the setup is shown in Fig. S1.[33] The resulting thin film was annealed in argon (Ar) (99.997%, Airgas) without atmospheric exposure at 500 °C for 1 h, an important step in ensuring crystallization and film homogeneity as recommended by Cho *et al.*[26] Total time for film synthesis and annealing is 2 h before it is ready for characterization. An index number map for the Ni-Ti-Co thin film library is shown in Fig. S2.[33]

XPS analyses were carried out with a Kratos Axis NOVA spectrometer using a monochromatic Al K-alpha source (30 mA, 15 kV). XPS can detect all elements except hydrogen and helium, probes the surface of the sample to a depth of 5–7 nm, and has detection limits ranging from 0.001 to 0.5 at. % depending on the element/matrix. The instrument work function was calibrated to give a binding energy (BE) of 83.96 eV for the Au 4f7/2 line for metallic gold, and the spectrometer dispersion was adjusted to give a BE of 932.62 eV for the Cu 2p3/2 line of metallic copper. The Kratos charge neutralizer system was used on all specimens. Survey scan analyses were carried out with an analysis area of 300×700 mm^2 and a pass energy of 160 eV. High resolution analyses were carried out with an analysis area of 300×700 mm^2 and a pass energy of 20 eV. Spectra have been charge-corrected to the main line of the carbon 1s (adventitious carbon) spectrum set to 285.0 eV (operating conditions: base pressure 4×10^{-10} Torr or 5.3×10^{-8} Pa; operating pressure during depth profiles 2×10^{-8} Torr or 2.6×10^{-6} Pa).

For quantification, Shirley background subtraction removed the contribution of inelastically scattered electrons. For chemical state analysis, peaks were fitted with symmetric Gaussian–Lorentzian components using the ESCApe data system and were quantified using modified Wagner relative sensitivity factors (RSFs). Spatial distribution plots were performed using the ESCApe data system whereby a series of analysis points can be created either freehand or as a grid. The spectra were analyzed as grouped data postquantification. A Delaunay triangulation is fitted onto acquisition locations.[27] A linearly interpolated color scheme is then applied to each triangle based on the vertex values, each of which represents an acquired atomic concentration value.

The surface elemental distribution of the deposited system was initially evaluated with XPS wide energy range, survey scans. Local chemical bonding is investigated using high resolution acquisition to identify regions of interest for additional analyses, including depth profiling of the film to determine the layering nature of the resulting chemical states formed during deposition. Typical acquisition times for survey and high-resolution spectra are 1 min each and 2 h for depth profiles. Chemical composition determination from wavelength dispersive spectroscopy, in contrast, takes 6 h in total.

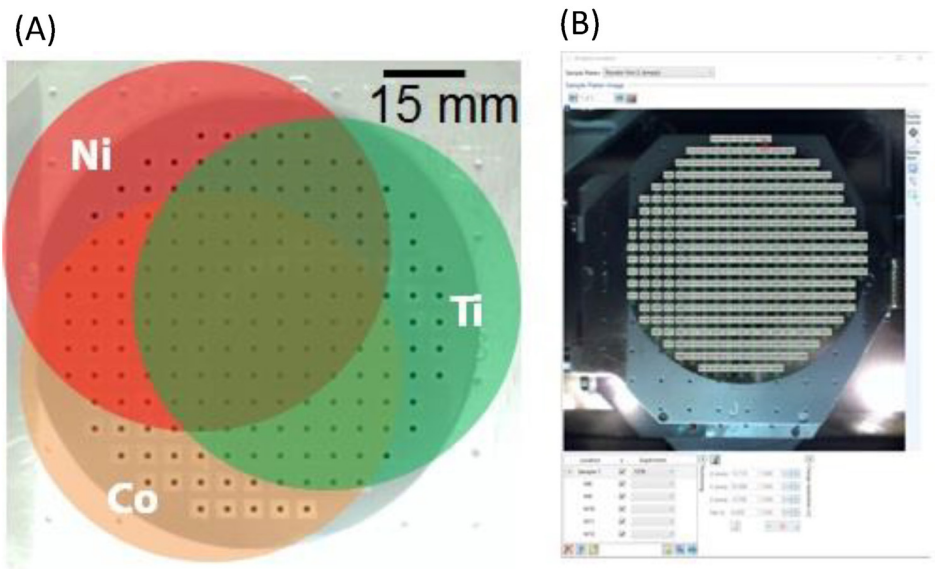

FIG. 1. (a) Geometry of sputter deposition targets relative to the 3-in. wafer substrate. (b) Discrete array analysis positions defined in the ESCApe software. Long flat edge is positioned facing left; sample pads are numbered 1 to 5 [see Fig. S2 (Ref. 33)] from left to right parallel to the flat edge and continue in the same manner in subsequent rows above.

The group array analysis functionality of the ESCApe software allows easy definition of an array of analysis points across the sample. In this library, 177 discrete positions were defined as equally spaced points (Δx, $\Delta y = 4.5$ mm) across the wafer as shown in Fig. 1(b). The positional information of each spectrum was retained so that spectra were linked by Cartesian coordinates, greatly easing subsequent data handling and analysis of elemental distribution. Group analysis is used to generate an overall elemental compositional distribution profile, and similar group analysis is used to explore the different chemical bonding and oxidation states on the surface of the film. A simple model is created for a representative spectrum, whereby the background contribution of inelastically scattered electrons is removed and the peak areas are calculated. This model includes the RSFs for each given element. The model is applied to each spectrum and fitted. A three-point average is applied to the end point of each background to remove noise contributions. The distribution maps are generated from these quantifications per marker locations.

Al Kα excited 60 s survey spectra were acquired at each position such that the entire data collection was achieved in 3 h. To facilitate data processing, the ESCApe software has an automated peak identification capability that can be extended to define a background around the core level transition that results in a quantified survey spectrum. This is propagated across all 177 spectra so that elemental quantification is achieved in a matter of minutes.

Where subsurface alloy composition was required, sputter profiles were performed using 2 keV Ar^+ ions with a 2×2 mm etch crater. For this ion energy and crater size, an etch rate of 10 nm/min is typical on Ta_2O_5. Etch time is shown for the depth profiles. The etch cycles were repeated until a steady-state elemental composition was measured. Depth profiling was performed using an ion gun of 45° from the surface normal; 99.999% purity Argon was used.

III. RESULTS AND DISCUSSION

The elemental concentrations determined from the survey spectra were plotted as a function of position as shown in Fig. 2. We observed the elemental concentration to vary across the surface, with the highest concentrations for each element being adjacent to the sputter target position shown in Fig. 1(a). Several trends are apparent from the distribution maps. The elemental distribution of oxygen (O) content is perfectly coincident with titanium (Ti) which, in its free metallic state, is highly reactive (it is commonly used as a getter pump in UHV systems). Here, a similar effect is presumably occurring whereby free oxygen reacts with Ti to form an oxide TiO_2 during the deposition process. The coverage of carbon (C) is also nonuniform, presumably once again, showing variations in surface free energy and, therefore, adsorption/reactivity. We discuss this more later. Because some changes were introduced to the vacuum chamber prior to this particular deposition, there was reason to believe that there may be the presence of

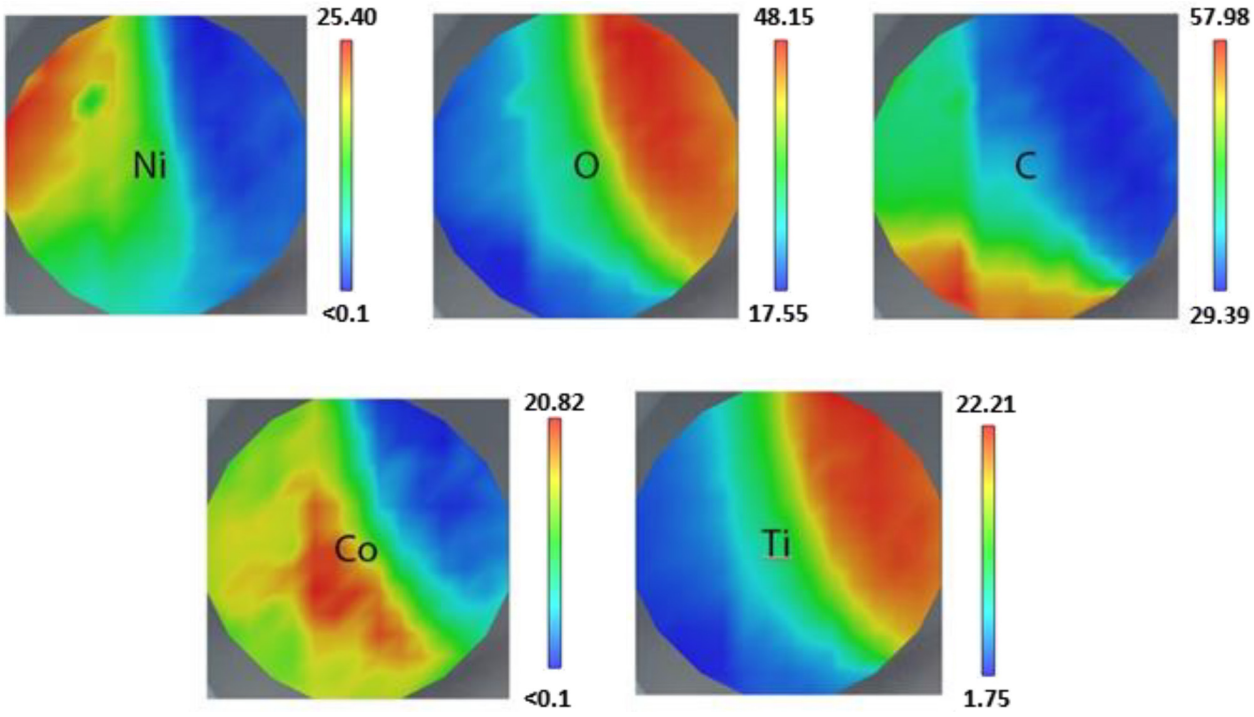

FIG. 2. Elemental concentrations as a function of position where the "hotter" colors indicate higher concentration in at. %.

contaminants. As discussed later in the text, the XPS data proved to be useful in identifying the surface contaminants.

To demonstrate the greater information that can be extracted from the array dataset, the Ni distribution and chemistry was investigated. Figure 3(a) shows the nickel (Ni) $2p_{3/2}$ region summed from all 177 spectra with a model fit. The red component at 850.2 eV binding energy is assigned to Ni in the metallic state alloyed with Co/Ti. The blue components are assigned to Ni^{2+} that is most likely to be nickel hydroxide as evidenced by the distinctive shake-up structure above the photoemission peak at 857.8 eV.[23] The model shown in Fig. 3(a) was propagated across all the spectra, and the relative concentration of each chemical state (Ni^{2+}, Ni) was plotted as a color map across the wafer, shown in Fig. 3(b).

To understand the subsurface alloy composition, two positions were chosen to perform sputter depth profiles. This allowed the determination of the alloy composition after removal of carbon adsorbed on the surface as contamination. The profile was continued until a steady-state elemental composition was reached. Figure 4 shows the depth profiles from two analysis positions, Nos. 76 and 218.

From the depth profiles, it was observed that the surface adsorbed carbon, which is 35–40 relative at. % of the surface composition, is removed after first two or three etch cycles. It is noted that carbon is not completely removed, which prompts further investigation described below. For the Ti rich region associated with position No. 218, there is an increase in the surface concentration of Ti which implies some surface segregation of Ti during the alloying process.

To gain further insight into carbon chemistry, both across the surface of the wafer and within the bulk of the material, a sputter depth profile was performed at a position adjacent to No. 218 (detailed above, where surface segregation of the Ti was observed). During the depth analysis, a high-resolution C 1s spectrum was also acquired allowing determination of chemistry into the bulk of the material. The depth profile for position No. 207 and high-resolution C 1s region are displayed in Fig. 5.

The high-resolution C 1s spectra indicate that the adventitious hydrocarbon envelope, between 285.0 and 287.5 eV, is removed after four etch cycles (data not shown). However, the carbide peak persists into the bulk of the material (Fig. 5). Under typical high vacuum growth conditions used in this work, several sources of C are possible, with two perhaps most obvious choices being residual gas molecules and target contaminants. Dissociation of residual C═O molecules upon contact with the surface can be expected

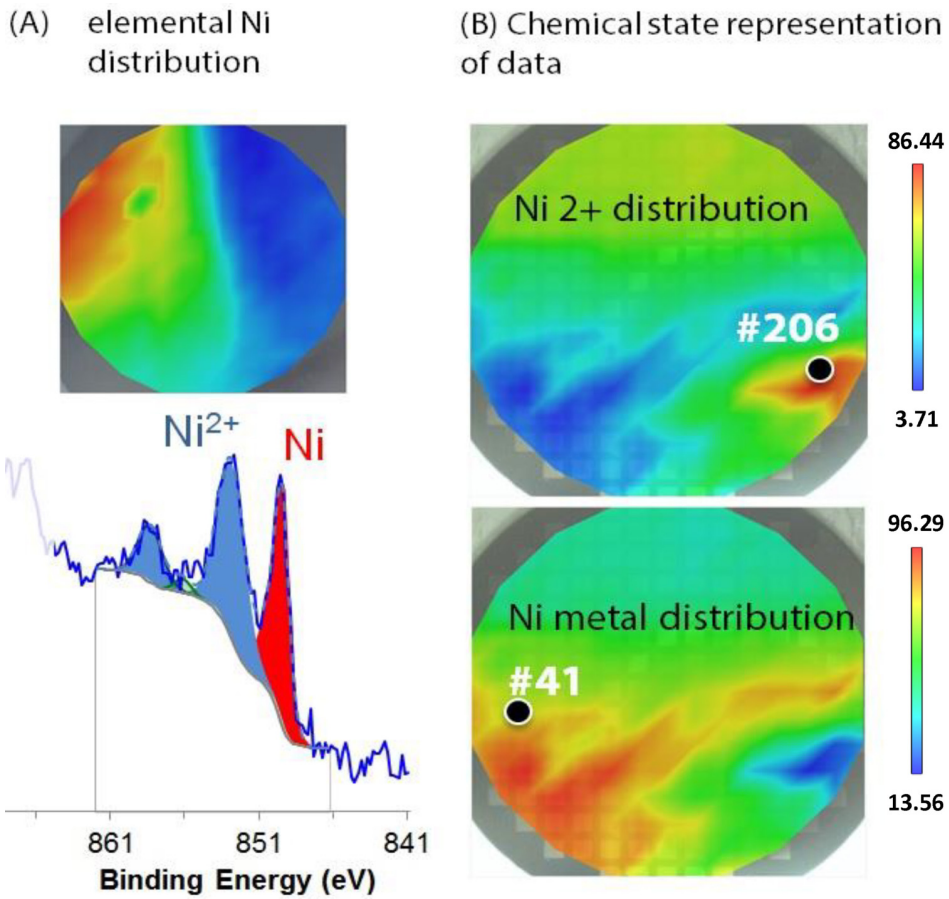

FIG. 3. (a) Elemental distribution of the Ni and summed Ni $2p_{3/2}$ region with model fit for metallic and Ni^{2+} oxidation state. (b) Relative chemical state distributions of the two Ni chemical states.

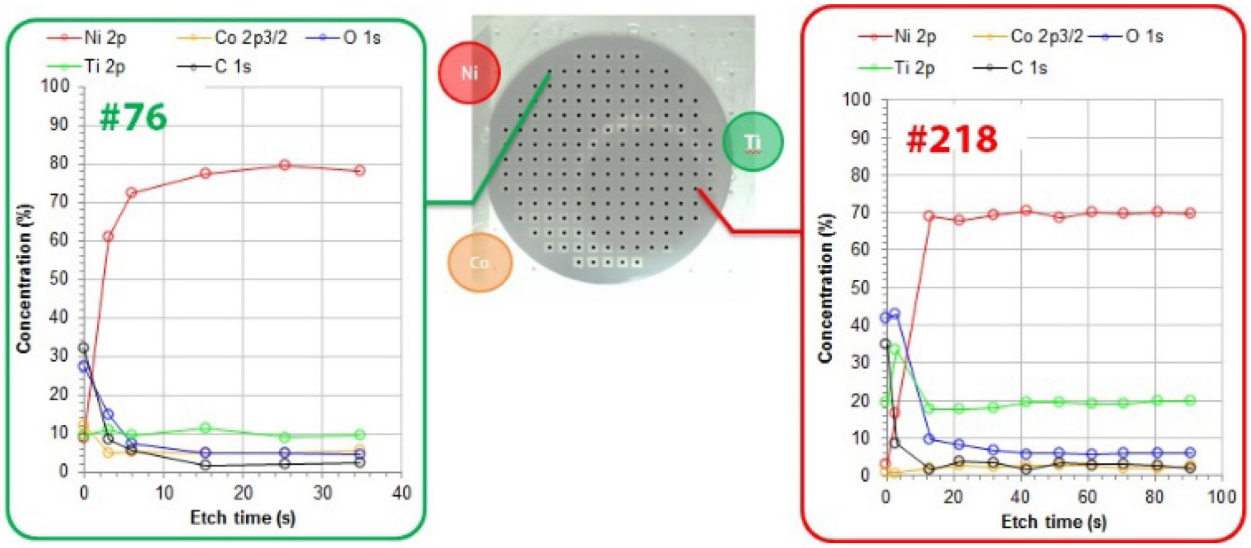

FIG. 4. 2 keV Ar^+ sputter depth profiles into the bulk alloy material at point Nos. 76 and 218.

based on the results of *ab initio* studies performed for the CO_2/TiAlN system.[28] In addition, C=O can dissociate upon electron impact in low pressure discharge (bond dissociation energy is 11.2 eV) constituting an alternative source of free carbon.[29] Moreover, the apparently low level of target contaminants specified by the vendors (here <0.1%) can be misleading as light elements like carbon are preferably sputtered along the target normal, so their content in the film might be significantly higher than in

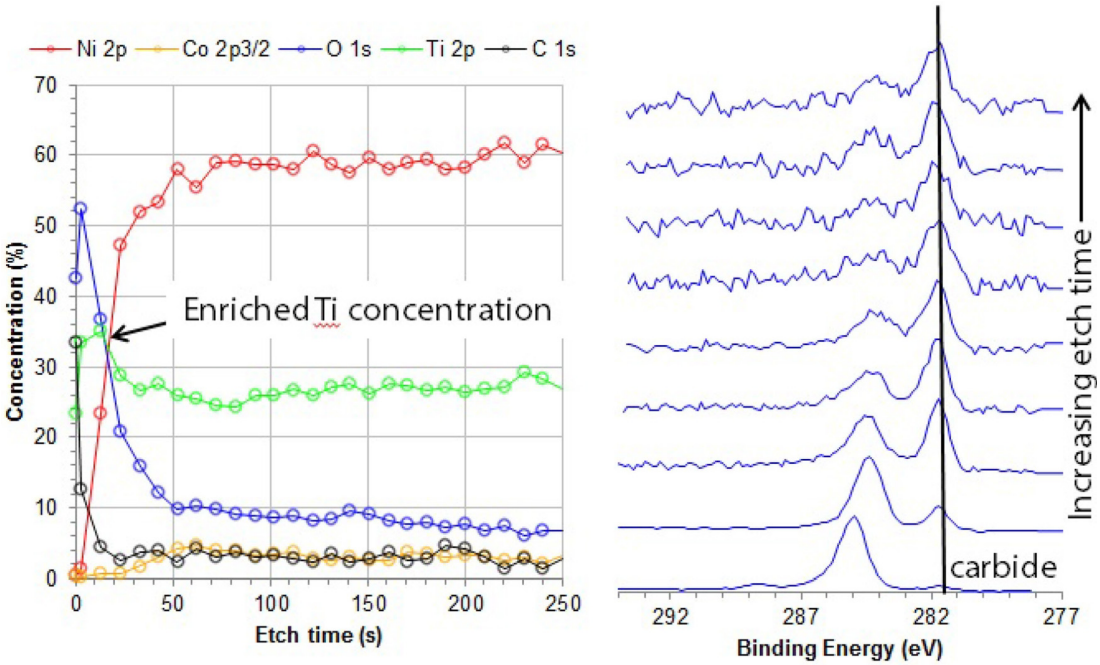

FIG. 5. Sputter depth profile through position No. 207 with the C 1s narrow region spectra acquired during the profile.

the target.[28] Since both the background system pressure and the target purity level used in this work are typical for industrial processing, it is reasonable to assume that the unintentional carbide formation reported here also takes place for other industrially grown functional coatings with an affinity for carbon.[30]

Lateral distribution of the carbon species was determined by fitting a model to the C 1 s envelope for the adventitious hydrocarbon and the carbide species. Representative spectra for these carbon containing species are shown in Fig. 6, along with the lateral distribution of the carbide material across the wafer. It should be noted that the distribution of carbide does not match with that of overall carbon composition. The simple explanation is that they are two different species that arise under different conditions, one during deposition and film formation and the other postatmospheric exposure. The elemental carbon distribution is dominated by adventitious carbon.

Further investigation of thin film chemistry was undertaken by measuring the Ti 2p high resolution spectra using the array acquisition method. In Fig. 7(a), representative Ti 2p spectra from two discrete position Nos. 7 and 207 are shown. A model was created to fit the envelope with components corresponding to Ti-carbide, metallic Ti, Ti^{3+}, and Ti^{4+} (TiO_2). This model was fitted to all 177 spectra, and the distribution of each chemical state was plotted as a function of position, as shown in Fig. 7(b).

It is immediately apparent that distribution of TiC concentration is coincident with carbide functionality identified in the C 1s spectra and plotted as a function of position in Fig. 6. It is noted that the material properties of the thin film depend on the composition, and since the initial search for viable shape memory alloy compositions is screening rapidly through many combinatorial thin films, it is important to know both the precise synthesis conditions

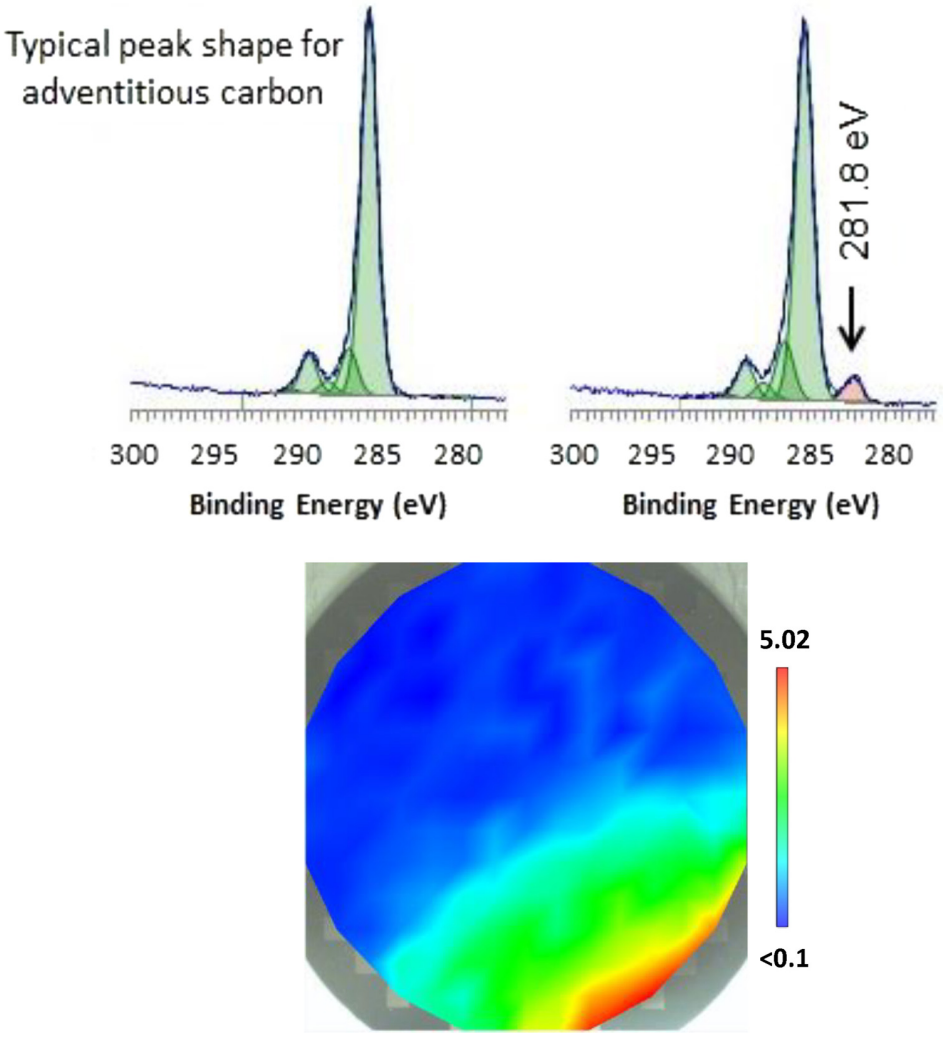

FIG. 6. High resolution C 1s spectra from areas showing only adventitious hydrocarbon and adventitious hydrocarbon with carbide. Also shown is the carbide distribution across the wafer.

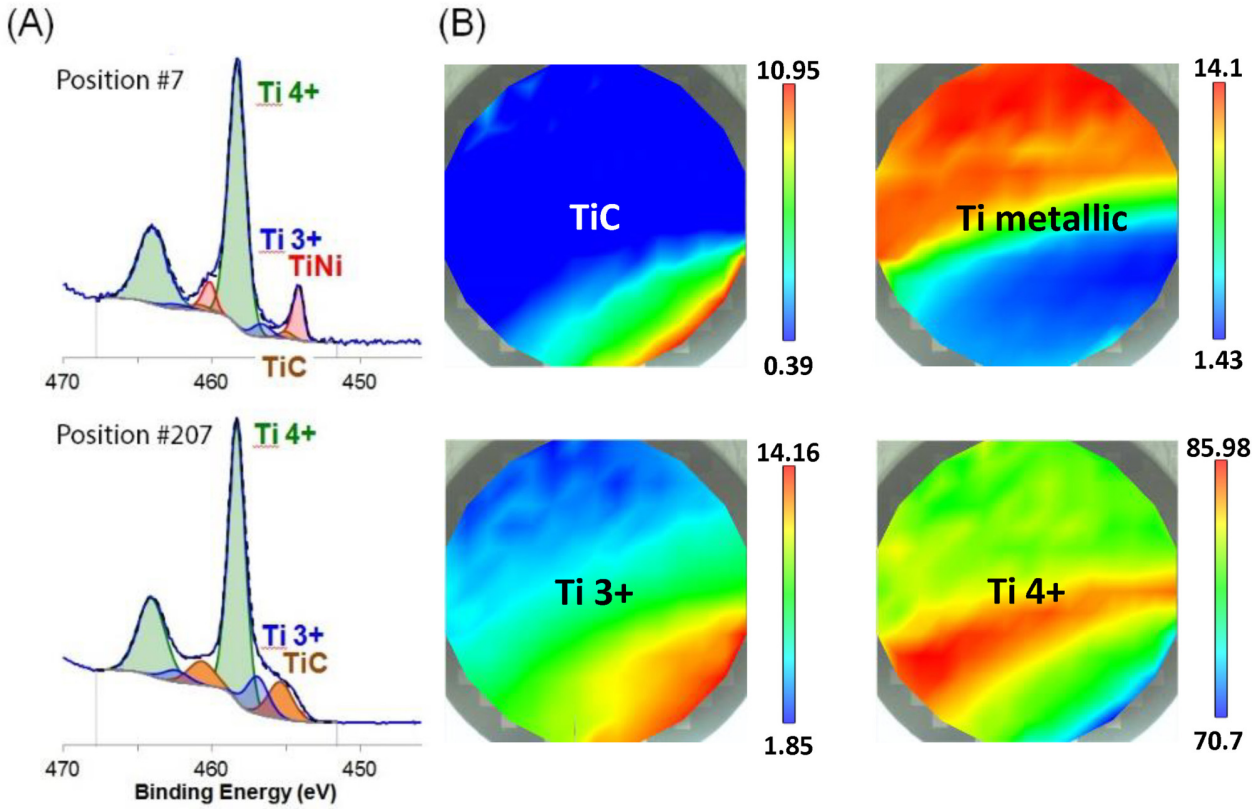

FIG. 7. (a) Representative Ti 2p high resolution spectra taken from position Nos. 7 and 207, respectively, with a model fitted to account for Ti chemical states. (b) Distribution of Ti chemistry identified in (a).

for reproducibility and impact of the synthesis conditions. If the carbide has any influence on the material properties and steps are taken to limit carbon as a contaminant, then it is important to understand how to modify the synthesis procedure accordingly. Further analysis of these locations performed with x-ray diffraction confirms the presence of carbide in the bulk lattice (Fig. S3[33]). Of course, we cannot categorically say there is no other carbide formation (CoC, for instance) but neither was it observed during the spectral analysis. Indeed, it should be noted that even though the carbide was observed before etching, the peak observed during etching could have a contribution from the knock-on effect from ion bombardment.

It should also be noted that during these depth profile experiments, the elemental concentration of O never reached zero at. %. This may have been caused by the presence of oxygen during the deposition process from either minor leaks to the chamber or oil contamination. Having established that this was a potential issue, the chamber was deep cleaned and reconditioned to be leak free. Thus, the XPS results were vital in establishing and mitigating the contaminant problem.

Finally, as mentioned before, the coverage of carbon is non-uniform presputtering. All three metals, and their oxides, are widely used as hetero- and homogeneous catalysts. It is, therefore, expected that the species present reflect the catalytic pathways of the metals, and their states, on the surface. There is clearly less carbon present on the area rich in TiO_2. We assume this is due to the photocatalytic nature of titania which has been shown previously to facilitate the oxidation of hydrocarbons into volatiles (CO_2, H_2O) under both visible and UV radiation.[31] This sample was exposed to atmosphere and ambient light and, therefore, some of the adsorbed carbon may be removed in this manner. The ionizing x-ray radiation may also have contributed to this process; however, H_2O and O_2 would typically need to be present in abundance, which is unlikely under UHV conditions. Ni/NiO_x is also photocatalytically active and has been shown to promote the reductive carboxylation of hydrocarbons.[32] The relative abundance of carbon on the surface and the higher concentration in the cobalt-rich area can, therefore, be assumed to relate to the reactivity of the surface species and, thus, the nature of the reactions taking place—some pathways create volatile CO/CO_2 decreasing the overall content, while others may promote the deposition of Carbon once the hydrocarbon has cracked. These further illustrate the importance of deposition and analysis methods and their use in the field of catalyst discovery.

IV. SUMMARY AND CONCLUSIONS

The development of the group array analysis, acquisition, and processing software provides much more intelligent use of large amounts of data. This, in turn, allows greater insight into the deposited thin film materials library and facilitates the combinatorial approach to material research, discovery, and development. This work demonstrates automation of a workflow for peak identification, background subtraction, and subsequent quantification such that it is no longer considered a rate limiting step in working with large amounts of data. The approach could be applied to all samples, yielding improved statistics and understanding of elemental relationships. Finally, the suitability of XPS as a precise and fast technique for materials' characterization was demonstrated.

ACKNOWLEDGMENTS

Many thanks to Alex Shard of NPL for fruitful discussions. N.M.A. acknowledges financial support from the National Science Foundation Graduate Research Fellowship Program under Grant No. DGE 1322106.

REFERENCES

[1]I. Takeuchi, J. Lauterbach, and M. J. Fasolka, Mater. Today **8**, 18 (2005).
[2]S. H and J. Thampi, Chem. Bus. **10**, 16 (1996).
[3]I. Takeuchi *et al.,* Nat. Mater. **2**, 180 (2003).
[4]A. Ludwig, npj Comput. Mater. **5**, 70 (2019).
[5]B. P. MacLeod *et al.*, Sci. Adv. **6**, eaaz8867 (2019).
[6]T. Gebhardt, D. Music, T. Takahashi, and J. M. Schneider, Thin Solid Films **520**, 5491 (2012).
[7]Q. Wang *et al.,* Appl. Surf. Sci. **189**, 271 (2002).
[8]S. Sun *et al.,* Joule **3**, 1437 (2019).
[9]R. Zarnetta *et al.,* Adv. Funct. Mater. **20**, 1917 (2010).
[10]A. J. Urquhart *et al.,* Adv. Mater. **19**, 2486 (2007).
[11]A. D. Celiz *et al.,* Biomater. Sci. **2**, 1604 (2014).
[12]K. Otsuka and C. M. Wayman, *Shape Memory Materials* (Cambridge University, Cambridge, 1998), ISBN: 9780521663847.
[13]R. Zarnetta *et al.,* Acta Mater. **57**, 4169 (2009).
[14]R. Zarnetta, P. J. S. Buenconsejo, A. Savan, S. Thienhaus, and A. Ludwig, Intermetallics **26**, 98 (2012).
[15]J. Frenzel *et al.*, Acta Mater. **90**, 213 (2015).
[16]K. Otsuka and X. Ren, Prog. Mater. Sci. **50**, 511 (2005).
[17]R. A. Ahmed, Ind. Eng. Chem. Res. **54**, 8397 (2015).
[18]N. El-Bagoury, Mater. Sci. Technol. **30**, 1795 (2014).
[19]M. Kök and A. Ates, Eur. Phys. J. Plus **132**, 6 (2017).
[20]R. Jing and F. Liu, Chin. J. Aeronaut. **20**, 153 (2007).
[21]X. Huang, D. W. Norwich, and M. Ehrlinspiel, J. Mater. Eng. Perform. **23**, 2630 (2014).
[22]A. Phukaoluan, A. Khantachawana, P. Kaewtatip, S. Dechkunakorn, and J. Kajornchaiyakul, Int. Orthod. **14**, 295 (2016).
[23]E. Mohammad Sharifi, F. Karimzadeh, and A. Kermanpur, J. Mater. Eng. Perform. **24**, 445 (2015).
[24]H. Hosoda, T. Fukul, K. Inoue, Y. Mishima, and T. Suzuki, MRS Proc. **459**, 287 (1996).
[25]S. Civjan, E. F. Huget, and L. B. DeSimon, J. Dent. Res. **54**, 89 (1975).
[26]H. Cho, H. Y. Kim, and S. Miyazaki, Sci. Technol. Adv. Mater. **6**, 678 (2005).
[27]B. Delaunay, "Sur La Sphère Vide. A La Mémoire de Georges Voronoï. Classe Des Sciences Mathématiques et Naturelles," Bull. l'Académie l'URSS **6**, 793–800 (1934).
[28]A. P. Grosvenor, M. C. Biesinger, R. S. C. Smart, and N. S. McIntyre, Surf. Sci. **600**, 1771 (2006).
[29]P. C. Cosby, J. Chem. Phys. **98**, 7804 (1993).
[30]G. Greczynski, S. Mráz, L. Hultman, and J. M. Schneider, Appl. Surf. Sci. **385**, 356 (2016).
[31]J. Schneider *et al.,* Chem. Rev. **114**, 9919 (2014).
[32]S. Saini, H. Singh, P. K. Prajapati, A. K. Sinha, and S. L. Jain, ACS Sustain. Chem. Eng. **7**, 11313 (2019).
[33]See supplementary material at https://doi.org/10.1116/6.0000333 for a schematic of the sputtering configuration and index number map for the thin film library.

Bibliography

[1] K. Otsuka and X. Ren, "Physical metallurgy of Ti–Ni-based shape memory alloys," *Progress in Materials Science*, vol. 50, pp. 511–678, 7 2005.

[2] J. Tušek, K. Engelbrecht, L. P. Mikkelsen, and N. Pryds, "Elastocaloric effect of Ni-Ti wire for application in a cooling device," *Journal of Applied Physics*, vol. 117, p. 124901, 3 2015.

[3] J. Frenzel, G. Eggeler, E. Quandt, S. Seelecke, and M. Kohl, "High-performance elastocaloric materials for the engineering of bulk- and micro-cooling devices," *MRS Bulletin*, vol. 43, pp. 280–284, 4 2018.

[4] T. Gebhardt, D. Music, T. Takahashi, and J. M. Schneider, "Combinatorial thin film materials science: From alloy discovery and optimization to alloy design," *Thin Solid Films*, vol. 520, pp. 5491–5499, 6 2012.

[5] R. Löbel, S. Thienhaus, A. Savan, and A. Ludwig, "Combinatorial fabrication and high-throughput characterization of a Ti-Ni-Cu shape memory thin film composition spread," *Materials Science and Engineering A*, vol. 481-482, pp. 151–155, 5 2008.

[6] "Magnetron Sputtering - an overview — ScienceDirect Topics."

[7] S. T. Thornton and A. Rex, *Modern Physics for Scientists and Engineers*. 1993.

[8] "Wavelength-Dispersive X-Ray Spectroscopy (WDS)."

[9] D. Stasak and N. Al Hasan, "JEOL-8900R-Wavelength Dispersive/Energy Dispersive Combined Microanalyzer Standard Operating Procedure," tech. rep., 2017.

[10] S. Fackler, *COMBINATORIAL INVESTIGATION OF RARE-EARTH FREE PERMANENT MAGNETS*. PhD thesis, University of Maryland, College Park, 2015.

[11] C. Long, *NEAR-FIELD MICROWAVE MICROSCOPY AND MULTIVARIATE ANALYSIS OF XRD DATA*. PhD thesis, University of Maryland, College Park, 2011.

[12] R. Zarnetta, R. Takahashi, M. L. Young, A. Savan, Y. Furuya, S. Thienhaus, B. Maaß, M. Rahim, J. Frenzel, H. Brunken, Y. S. Chu, V. Srivastava, R. D. James, I. Takeuchi, G. Eggeler, and A. Ludwig, "Identification of quaternary shape memory alloys with near-zero thermal hysteresis and unprecedented functional stability," *Advanced Functional Materials*, vol. 20, no. 12, pp. 1917–1923, 2010.

[13] A. A. Wilson, M. Muñoz Rojo, B. Abad, J. A. Perez, J. Maiz, J. Schomacker, M. Martín-Gonzalez, D. A. Borca-Tasciuc, and T. Borca-Tasciuc, "Thermal conductivity measurements of high and low thermal conductivity films using a scanning hot probe method in the 3ω mode and novel calibration strategies," *Nanoscale*, vol. 7, pp. 15404–15412, 10 2015.

[14] N. Hirst, "Buildings and Climate Change," in *Design and Management of Sustainable Built Environments*, pp. 23–30, London: Springer London, 2013.

[15] "Air Conditioning — Department of Energy."

[16] "Refrigerant Management — Drawdown."

[17] W. Goetzler, R. Zogg, J. Young, and J. Schmidt, "Energy Savings Potential and Research, Development, & Demonstration Opportunities for Residential Building Heating, Ventilation, and Air Conditioning Systems," tech. rep., Navigant Consulting Inc., prepared for US DoE, 2012.

[18] S. Crossley, N. D. Mathur, X. Moya, N. D. M. S. Crossley, and X. Moya, "New developments in caloric materials for cooling applications," *AIP ADVANCES*, vol. 5, no. 6, p. 067153, 2015.

[19] X. Moya, S. Kar-Narayan, and N. D. Mathur, "Caloric materials near ferroic phase transitions," *Nature Materials*, vol. 13, no. 5, pp. 439–450, 2014.

[20] A. Ölander, "AN ELECTROCHEMICAL INVESTIGATION OF SOLID CADMIUM-GOLD ALLOYS," *Journal of the American Chemical Society*, vol. 54, pp. 3819–3833, 10 1932.

[21] L. Vernon and H. Vernon, "Process of manufacturing articles of thermoplastic synthetic resins," 2 1937.

[22] J. M. Jani, M. Leary, A. A. Subic, and M. A. Gibson, "A review of shape memory alloy research, applications and opportunities," *Materials & Design (1980-2015)*, vol. 56, pp. 1078–1113, 4 2014.

[23] J. Sui, Z. Gao, Y. Li, Z. Zhang, and W. Cai, "A study on NiTiNbCo shape memory alloy," *Materials Science and Engineering: A*, vol. 508, pp. 33–36, 5 2009.

[24] E. MOHAMMAD SHARIFI and A. KERMANPUR, "Superelastic behavior of nanostructured Ti50Ni48Co2 shape memory alloy with cold rolling processing," *Transactions of Nonferrous Metals Society of China*, vol. 28, pp. 1351–1359, 7 2018.

[25] C. Rodriguez and L. C. Brown, "The thermal effect due to stress-induced martensite formation in B-CuAlNi single crystals," *Metallurgical and Materials Transactions A*, vol. 11, pp. 147–150, 1980.

[26] L. C. Brown, "Thermal Effect in Pseudoelastic Single Crystals of beta-CuZnSn.," *Metallurgical transactions. A, Physical metallurgy and materials science*, vol. 12, pp. 1491–1494, 1981.

[27] L. M. E. V. A. P. Erell Bonnot, Ricardo Romero, E. Bonnot, R. Romero, L. Mañosa, E. Vives, and A. Planes, "Elastocaloric Effect Associated with the Martensitic Transition in Shape-Memory Alloys," *Physical Review Letters*, vol. 100, p. 125901, 3 2008.

[28] M. Schmidt, A. Schütze, and S. Seelecke, "Elastocaloric cooling processes: The influence of material strain and strain rate on efficiency and temperature span," *APL Materials*, 2016.

[29] G. B. KAUFFMAN and I. MAYO, "The Story of Nitinol: The Serendipitous Discovery of the Memory Metal and Its Applications," *The Chemical Educator*, vol. 2, pp. 1–21, 6 1997.

[30] W. J. Buehler, J. V. Gilfrich, and R. C. Wiley, "Effect of Low-Temperature Phase Changes on the Mechanical Properties of Alloys near Composition TiNi," *Journal of Applied Physics*, vol. 34, pp. 1475–1477, 5 1963.

[31] L. Mañosa and A. Planes, "Materials with Giant Mechanocaloric Effects: Cooling by Strength," *Advanced Materials*, vol. 29, p. 1603607, 3 2017.

[32] H. Hou, E. Simsek, T. Ma, N. S. Johnson, S. Qian, C. Cissé, D. Stasak, N. Al Hasan, L. Zhou, Y. Hwang, R. Radermacher, V. I. Levitas, M. J. Kramer, M. A. Zaeem, A. P. Stebner, R. T. Ott, J. Cui, and I. Takeuchi, "Fatigue-resistant high-performance elastocaloric materials made by additive manufacturing Downloaded from," tech. rep., 2019.

[33] A. Chauhan, S. Patel, R. Vaish, and C. R. Bowen, "A review and analysis of the elasto-caloric effect for solid-state refrigeration devices: Challenges and opportunities," *MRS Energy & Sustainability*, vol. 2, no. iii, p. E16, 2015.

[34] D. J. Hartl and D. C. Lagoudas, "Aerospace applications of shape memory alloys," *Proceedings of the Institution of Mechanical Engineers, Part G: Journal of Aerospace Engineering*, vol. 221, pp. 535–552, 4 2007.

[35] C. Bil, K. Massey, and E. J. Abdullah, "Wing morphing control with shape memory alloy actuators," *Journal of Intelligent Material Systems and Structures*, vol. 24, pp. 879–898, 5 2013.

[36] F. Butera, A. Coda, and G. Vergani, "Shape memory actuators for automotive applications," *Nanotec IT newsletter.*, pp. 12–16, 2007.

[37] R. A. Ahmed, "Electrochemical Properties of Ni ¡sub¿47¡/sub¿ Ti ¡sub¿49¡/sub¿ Co ¡sub¿4¡/sub¿ Shape Memory Alloy in Artificial Urine for Urological Implant," *Industrial & Engineering Chemistry Research*, vol. 54, pp. 8397–8404, 9 2015.

[38] N. El-Bagoury, "Microstructure and martensitic transformation and mechanical properties of cast Ni rich NiTiCo shape memory alloys," *Materials Science and Technology (United Kingdom)*, vol. 30, pp. 1795–1800, 11 2014.

[39] M. Kök and A. Ate¸s, "The effect of addition of various elements on properties of NiTi-based shape memory alloys for biomedical application," *The European Physical Journal Plus*, vol. 132, no. 185, p. 6, 2017.

[40] R.-r. JING and F.-s. LIU, "The Influence of Co Addition on Phase Transformation Behavior and Mechanical Properties of TiNi Alloys," *Chinese Journal of Aeronautics*, vol. 20, pp. 153–156, 4 2007.

[41] H. Soni, N. Sannayellappa, and R. M. Rangarasaiah, "An experimental study of influence of wire electro discharge machining parameters on surface integrity of TiNiCo shape memory alloy," *Journal of Materials Research*, vol. 32, pp. 3100–3108, 8 2017.

[42] X. Huang, D. W. Norwich, and M. Ehrlinspiel, "Corrosion Behavior of Ti-55Ni-1.2Co High Stiffness Shape Memory Alloys," *Journal of Materials Engineering and Performance*, vol. 23, pp. 2630–2634, 7 2014.

[43] A. Phukaoluan, A. Khantachawana, P. Kaewtatip, S. Dechkunakorn, and J. Kajornchaiyakul, "Improvement of mechanical and biological properties of TiNi alloys by addition of Cu and Co to orthodontic archwires," *International Orthodontics*, vol. 14, pp. 295–310, 9 2016.

[44] E. Mohammad Sharifi, F. Karimzadeh, and A. Kermanpur, "Nanocrystallization of the Ti50Ni48Co2 Shape Memory Alloy by Thermomechanical Treatment," *Journal of Materials Engineering and Performance*, vol. 24, pp. 445–451, 1 2015.

[45] L. Isola, P. La Roca, C. Sobrero, V. Fuster, P. Vermaut, and J. Malarría, "Martensitic transformation strain and stability of Ni50x–Ti50–Cox (x = 3 , 4) strips obtained by twin-roll casting and standard processing techniques," *Materials & Design*, vol. 107, pp. 511–519, 10 2016.

[46] H. Hosoda, T. Fukul, K. Inoue, Y. Mishima, and T. Suzuki, "Change of Ms Temperatures and its Correlation to Atomic Configurations of Offstoichiometric NiTi-Cr and NiTi-Co Alloys," *MRS Proceedings*, vol. 459, p. 287, 1 1996.

[47] S. Civjan, E. F. Huget, and L. B. DeSimon, "Potential Applications of Certain Nickel-Titanium (Nitinol) Alloys," *Journal of Dental Research*, vol. 54, pp. 89–96, 1 1975.

[48] L. Van Langenhove and C. Hertleer, "Smart clothing: a new life," *International Journal of Clothing Science and Technology*, vol. 16, pp. 63–72, 2 2004.

[49] A. N. Bucsek, G. A. Hudish, G. S. Bigelow, R. D. Noebe, and A. P. Stebner, "Composition, Compatibility, and the Functional Performances of Ternary NiTiX High-Temperature Shape Memory Alloys," *Shape Memory and Superelasticity*, vol. 2, no. 1, pp. 62–79, 2016.

[50] C. Aksu Canbay, S. Ozkul, and H. Mustafa Ahmed, "The ternary and quaternary systems in Cu-based shape memory alloys," *AIP Conference Proceedings*, vol. 2178, no. November, 2019.

[51] J. Frenzel, A. Wieczorek, I. Opahle, B. Maaß, R. Drautz, and G. Eggeler, "On the effect of alloy composition on martensite start temperatures and latent heats in Ni-Ti-based shape memory alloys," *Acta Materialia*, vol. 90, pp. 213–231, 5 2015.

[52] C. Chluba, W. Ge, R. Lima de Miranda, J. Strobel, L. Kienle, E. Quandt, and M. Wuttig, "Ultralow-fatigue shape memory alloy films," *Science*, vol. 348, pp. 1004–7, 5 2015.

[53] L. Sun and W. M. Huang, "Nature of the multistage transformation in shape memory alloys upon heating," *Metal Science and Heat Treatment*, vol. 51, pp. 573–578, 11 2009.

[54] A. Planes, H. Flores-Zúñiga, D. Soto-Parra, E. Vives, J. A. Matutes-Aquino, L. Mañosa, J. A. Matutes-Aquino, H. Flores-Zúñiga, and A. Planes, "Elastocaloric effect in Ti-Ni shape-memory wires associated with the B2 B19' and B2 R structural transitions," *Applied Physics Letters*, vol. 108, p. 071902, 2 2016.

[55] S. K. Wu, H. C. Lin, and T. S. Chou, "A study of electrical resistivity, internal friction and shear modulus on an aged Ti49Ni51 alloy," *Acta Metallurgica Et Materialia*, vol. 38, pp. 95–102, 1 1990.

[56] W. D. J. Callister and D. Rethwisch, *Fundamentals of Materials Science and Engineering*. John Wiley & Sons, Inc., 4th ed., 2012.

[57] P. Wollants, M. D. Bonte, J. R. Z. f. metallkunde, and u. 1979, "Thermodynamic analysis of the stress-induced martensitic-transformation in a single-crystal," *lirias.kuleuven.be*, vol. 70, no. 2, pp. 113–117, 1979.

[58] K. Otsuka and C. M. Wayman, *Shape Memory Materials*. Cambridge: Cambridge University Press, 1998.

[59] P. Wollants, J. Roos, and L. Delaey, "Thermally- and stress-induced thermoelastic martensitic transformations in the reference frame of equilibrium thermodynamics," *Progress in Materials Science*, vol. 37, pp. 227–288, 1 1993.

[60] S. Miyazaki, Y. Qing Fu, and W. Min Huang, eds., *Thin Film Shape Memory Alloys, Fundamentals and Device Applications*. Cambridge: Cambridge University Press, 1 ed., 2009.

[61] B. D. Ingale, W. C. Wei, P. C. Chang, Y. K. Kuo, and S. K. Wu, "Anomalous transport and thermal properties of NiTi and with Cu and Fe-doped shape memory alloys near the martensitic transition," *Journal of Applied Physics*, vol. 110, no. 11, 2011.

[62] J. Cui, Y. S. Chu, O. O. Famodu, Y. Furuya, J. Hattrick-Simpers, R. D. James, A. Ludwig, S. Thienhaus, M. Wuttig, Z. Zhang, and I. Takeuchi, "Combinatorial search of thermoelastic shape-memory alloys with extremely small hysteresis width.," *Nature materials*, vol. 5, pp. 286–90, 4 2006.

[63] K. Otsuka and X. Ren, "Recent developments in the research of shape memory alloys," *Intermetallics*, vol. 7, no. 5, pp. 511–528, 1999.

[64] R. Kainuma, S. Takahashi, and K. Ishida, "Thermoelastic Martensite and Shape Memory Effect in Ductile Cu-AI-Mn Alloys," *Metallurgical and materials transactions A*, vol. 27, no. 8, pp. 2187–2195, 1996.

[65] H. E. Karaca, S. M. Saghaian, G. Ded, H. Tobe, B. Basaran, H. J. Maier, R. D. Noebe, and Y. I. Chumlyakov, "Effects of nanoprecipitation on the shape memory and material properties of an Ni-rich NiTiHf high temperature shape memory alloy," *Acta Materialia*, vol. 61, no. 19, pp. 7422–7431, 2013.

[66] Y. Liu, "Some factors affecting the transformation hysteresis in shape memory alloys," in *Shape memory alloys: manufacture, properties and applications* (Chen HR, ed.), ch. 13, pp. 361–369, Nova Science Publishers, 2010.

[67] E. Stern-Taulats, T. Castán, L. Mañosa, A. Planes, N. D. Mathur, and X. Moya, "Multicaloric materials and effects," *MRS Bulletin*, vol. 43, pp. 295–299, 4 2018.

[68] O. Gutfleisch, T. Gottschall, M. Fries, D. Benke, I. Radulov, K. P. Skokov, H. Wende, M. Gruner, M. Acet, P. Entel, and M. Farle, "Mastering hysteresis in magnetocaloric materials," *Philosophical Transactions of the Royal Society A: Mathematical, Physical and Engineering Sciences*, vol. 374, p. 20150308, 8 2016.

[69] E. Hornbogen, "The effect of variables on martensitic transformation temperatures," *Acta Metallurgica*, vol. 33, pp. 595–601, 4 1985.

[70] R. Hamilton, H. Sehitoglu, Y. Chumlyakov, and H. Maier, "Stress dependence of the hysteresis in single crystal NiTi alloys," *Acta Materialia*, vol. 52, pp. 3383–3402, 6 2004.

[71] Z. Zhang, R. D. James, and S. Müller, "Energy barriers and hysteresis in martensitic phase transformations," *Acta Materialia*, vol. 57, pp. 4332–4352, 9 2009.

[72] S. M. Song and B. J. Cho, "Contact resistance in graphene channel transistors," *Carbon letters*, vol. 14, no. 3, pp. 162–170, 2013.

[73] J. M. Ball and R. D. James, "Proposed experimental tests of a theory of fine microstructure and the two-well problem," *Philosophical Transactions of the Royal Society A: Mathematical, Physical and Engineering Sciences*, vol. 338, no. 1650, 1992.

[74] R. D. James and Z. Zhang, *A Way to Search for Multiferroic Materials with "Unlikely" Combinations of Physical Properties*. Berlin: Springer, 1 ed., 2005.

[75] R. D. James and K. F. Hane, "Martensitic transformations and shape-memory materials," *Acta Materialia*, vol. 48, no. 1, pp. 197–222, 2000.

[76] K. Bhattacharya, S. Conti, G. Zanzotto, and J. Zimmer, "Crystal symmetry and the reversibility of martensitic transformations," *Nature*, vol. 428, pp. 55–59, 3 2004.

[77] C. Chluba, W. Ge, T. Dankwort, C. Bechtold, R. L. de Miranda, L. Kienle, M. Wuttig, and E. Quandt, "Effect of crystallographic compatibility and grain size on the functional fatigue of sputtered TiNiCuCo thin films," *Philosophical Transactions of the Royal Society A: Mathematical, Physical and Engineering Sciences*, vol. 374, p. 20150311, 8 2016.

[78] S. Hamann, M. E. Gruner, S. Irsen, J. Buschbeck, C. Bechtold, I. Kock, S. G. Mayr, A. Savan, S. Thienhaus, E. Quandt, S. Fähler, P. Entel, and A. Ludwig, "The ferromagnetic shape memory system Fe-Pd-Cu," *Acta Materialia*, vol. 58, pp. 5949–5961, 10 2010.

[79] S. Jaeger, B. Maaß, J. Frenzel, M. Schmidt, J. Ullrich, S. Seelecke, A. Schütze, O. Kastner, and G. Eggeler, "On the widths of the hysteresis of mechanically

and thermally induced martensitic transformations in Ni-Ti-based shape memory alloys," *International Journal of Materials Research*, vol. 106, pp. 1029–1039, 10 2015.

[80] A. Planes, L. Mañosa, D. Ríos-Jara, and J. Ortín, "Martensitic transformation of Cu-based shape-memory alloys: Elastic anisotropy and entropy change," *Physical Review B*, vol. 45, pp. 7633–7639, 4 1992.

[81] L. Mañosa, M. Jurado, A. Planes, J. Zarestky, T. Lograsso, and C. Stassis, "Elastic constants of bcc Cu-Al-Ni alloys," *Physical Review B*, vol. 49, pp. 9969–9972, 4 1994.

[82] X. Ren, N. Miura, J. Zhang, K. Otsuka, K. Tanaka, M. Koiwa, T. Suzuki, Y. I. Chumlyakov, and M. Asai, "A comparative study of elastic constants of Ti-Ni based alloys prior to martensitic transformation," *Materials Science and Engineering A*, vol. 312, pp. 196–206, 8 2001.

[83] J. Tušek, K. Engelbrecht, L. Mañosa, E. Vives, and N. Pryds, "Understanding the Thermodynamic Properties of the Elastocaloric Effect Through Experimentation and Modelling," *Shape Memory and Superelasticity*, vol. 2, pp. 317–329, 12 2016.

[84] S. F. Hsieh and S. K. Wu, "A Study on Ternary Ti-rich TiNiZr Shape Memory Alloys," *Materials Characterization*, vol. 41, pp. 151–162, 10 1998.

[85] T. Biggs, M. B. Cortie, M. J. Witcomb, and L. A. Cornish, "Platinum Alloys for Shape Memory Applications," *Platinum Metals Review*, vol. 47, no. 1, pp. 142–156, 2003.

[86] R. Noebe, S. Draper, D. Gaydosh, A. Garga, B. Lerch, N. Penney, G. Begelow, I. Padula, Santo, and J. Brown, "Effect of Thermomechanical Processing on the Microstructure, Properties, and Work Behavior of a Ti50.5 Ni29.5 Pt20 High-Temperature Shape Memory Alloy," in *International Conference on Shape Memory and Superelastic Technologies*, 5 2006.

[87] N. Singh, A. Talapatra, A. Junkaew, T. Duong, S. Gibbons, S. Li, H. Thawabi, E. Olivos, and R. Arróyave, "Effect of ternary additions to structural properties of NiTi alloys," *Computational Materials Science*, vol. 112, pp. 347–355, 2 2016.

[88] T. Umale, D. Salas, B. Tomes, R. Arroyave, and I. Karaman, "The effects of wide range of compositional changes on the martensitic transformation characteristics of NiTiHf shape memory alloys," *Scripta Materialia*, vol. 161, pp. 78–83, 3 2019.

[89] D. Xue, D. Xue, R. Yuan, Y. Zhou, P. Balachandran, X. Ding, J. Sun, and T. Lookman, "An informatics approach to transformation temperatures of NiTibased shape memory alloys," *Acta Materialia*, no. 125, pp. 532–541, 2017.

[90] G. Bozzolo, R. D. Noebe, and H. O. Mosca, "Site preference of ternary alloying additions to NiTi: Fe, Pt, Pd, Au, Al, Cu, Zr and Hf," *Journal of Alloys and Compounds*, vol. 389, pp. 80–94, 3 2005.

[91] A. Evirgen, I. Karaman, R. Santamarta, J. Pons, C. Hayrettin, and R. Noebe, "Relationship between crystallographic compatibility and thermal hysteresis in Ni-rich NiTiHf and NiTiZr high temperature shape memory alloys," *Acta Materialia*, vol. 121, pp. 374–383, 12 2016.

[92] C. Bechtold, C. Chluba, R. Lima de Miranda, and E. Quandt, "High cyclic stability of the elastocaloric effect in sputtered TiNiCu shape memory films," *Applied Physics Letters*, vol. 101, p. 091903, 8 2012.

[93] W. Tang, R. Sandström, Z. G. Wei, and S. Miyazaki, "Experimental investigation and thermodynamic calculation of the Ti-Ni-Cu shape memory alloys," *Metallurgical and Materials Transactions A*, vol. 31, pp. 2423–2430, 10 2000.

[94] H. Du and Y. Fu, "Deposition and characterization of Ti1x(Ni,Cu)x shape memory alloy thin films," *Surface and Coatings Technology*, vol. 176, pp. 182–187, 1 2004.

[95] O. Mercier and K. Melton, "The Substitution of Cu for Ni in NiTi Shape Memory Alloys," *Metallurgical transactions A*, vol. 10 A, pp. 387–389, 1979.

[96] S. Miyazaki and A. Ishida, "Martensitic transformation and shape memory behavior in sputter-deposited TiNi-base thin films," *Materials Science and Engineering: A*, vol. 273-275, pp. 106–133, 12 1999.

[97] R. Zarnetta, D. König, C. Zamponi, A. Aghajani, J. Frenzel, G. Eggeler, and A. Ludwig, "R-phase formation in Ti39Ni45Cu16 shape memory thin films and bulk alloys discovered by combinatorial methods," *Acta Materialia*, vol. 57, no. 14, pp. 4169–4177, 2009.

[98] M. Zarinejad, Y. Liu, and Y. Tong, "Transformation temperature changes due to second phase precipitation in NiTi-based shape memory alloys," *Intermetallics*, vol. 17, pp. 914–919, 11 2009.

[99] Y. Liang, S. Jiang, Y. Zhang, and J. Yu, "Microstructure, Mechanical Property, and Phase Transformation of Quaternary NiTiFeNb and NiTiFeTa Shape Memory Alloys," *Metals*, vol. 7, no. 8, p. 309, 2017.

[100] Y. Sutou, T. Omori, R. Kainuma, K. Ishida, and N. Ono, "Enhancement of superelasticity in Cu-Al-Mn-Ni shape-memory alloys by texture control," *Metallurgical and Materials Transactions A*, vol. 33, pp. 2817–2824, 9 2002.

[101] D. Zhang, J. Lin, W. Jiang, M. Ma, and Z. Peng, "Shape memory and superelastic behavior of Ti–7.5Nb–4Mo–1Sn alloy," *Materials & Design*, vol. 32, pp. 4614–4617, 9 2011.

[102] M. A. Amin, N. El-Bagoury, M. H. H. Mahmoud, M. M. Hessien, S. S. Abd El-Rehim, J. Wysocka, and J. Ryl, "Catalytic impact of alloyed Al on the corrosion behavior of Co50Ni23Ga26Al1.0 magnetic shape memory alloy and catalysis applications for efficient electrochemical H2 generation," *RSC Advances*, vol. 7, pp. 3635–3649, 1 2017.

[103] P. Decker, J. Fortmann, S. Salomon, P. Krooß, T. Niendorf, and A. Ludwig, "Influence of Cr Alloying (1.5 to 5 at.%) on Martensitic Phase Transformation Temperatures in Co-Ni-Ga-Cr Thin Films," *Shape Memory and Superelasticity*, vol. 5, pp. 106–112, 3 2019.

[104] X. Chen, F. Zhang, M. Chi, S. Yang, C. Wang, X. Liu, and S. Zheng, "Microstructure, superelasticity and shape memory effect by stress-induced martensite stabilization in Cu–Al–Mn–Ti shape memory alloys," *Materials Science and Engineering: B*, vol. 236-237, pp. 10–17, 10 2018.

[105] A. Wieczorek, J. Frenzel, M. Schmidt, B. Maaß, S. Seelecke, A. Schütze, and G. Eggeler, "Optimizing Ni-Ti-based shape memory alloys for ferroic cooling," *Functional Materials Letters*, vol. 10, no. 1, p. 1740001, 2017.

[106] A. Wieczorek, S. Seelecke, J. Ullrich, M. Schmidt, G. Eggeler, A. Schütze, and J. Frenzel, "Thermal Stabilization of NiTiCuV Shape Memory Alloys: Observations During Elastocaloric Training," *Shape Memory and Superelasticity*, vol. 1, pp. 132–141, 6 2015.

[107] M. Schmidt, S. M. Kirsch, S. Seelecke, and A. Schütze, "Elastocaloric cooling: From fundamental thermodynamics to solid state air conditioning," *Science and Technology for the Built Environment*, vol. 22, no. 5, pp. 475–488, 2016.

[108] V. Chevrier and J. R. Dahn, "Production and visualization of quaternary combinatorial thin films," *Measurement Science and Technology*, vol. 17, pp. 1399–1404, 6 2006.

[109] D. J. Sharar, B. F. Donovan, R. J. Warzoha, A. A. Wilson, A. C. Leff, and B. M. Hanrahan, "Solid-state thermal energy storage using reversible martensitic transformations," *Applied Physics Letters*, vol. 114, p. 143902, 4 2019.

[110] T. J. Lu, "Thermal management of high power electronics with phase change cooling," *International Journal of Heat and Mass Transfer*, vol. 43, pp. 2245–2256, 7 2000.

[111] I. Takeuchi, J. Lauterbach, and M. J. Fasolka, "Combinatorial materials synthesis," *Materials Today*, vol. 8, no. 10, pp. 18–26, 2005.

[112] D. Xue, P. V. Balachandran, J. Hogden, J. Theiler, D. Xue, and T. Lookman, "Accelerated search for materials with targeted properties by adaptive design," *Nature Communications*, vol. 7, p. 11241, 12 2016.

[113] J. Hattrick-Simpers, V. L. Karen, I. Takeuchi, M. Murakami, X. Li, R. C. Srivastava, and C. J. Long, "Rapid structural mapping of ternary metallic alloy systems using the combinatorial approach and cluster analysis," *Review of Scientific Instruments*, vol. 78, no. 7, p. 072217, 2007.

[114] C. J. Long, D. Bunker, X. Li, V. L. Karen, and I. Takeuchi, "Rapid identification of structural phases in combinatorial thin-film libraries using x-ray diffraction and non-negative matrix factorization," *Review of Scientific Instruments*, vol. 80, p. 103902, 10 2009.

[115] A. Gilad Kusne, T. Gao, A. Mehta, L. Ke, M. Cuong Nguyen, K.-M. Ho, V. Antropov, C.-Z. Wang, M. J. Kramer, C. Long, and I. Takeuchi, "On-the-fly machine-learning for high-throughput experiments: search for rare-earth-free permanent magnets," *Scientific Reports*, vol. 4, no. 6367, 2014.

[116] H. Cho, H. Kim, and S. Miyazaki, "Fabrication and characterization of Ti–Ni shape memory thin film using Ti/Ni multilayer technique," *Science and Technology of Advanced Materials*, vol. 6, pp. 678–683, 1 2005.

[117] J. Goldstein, ed., *Scanning electron microscopy and X-ray microanalysis: A text for biologists, materials scientists, and geologists.* Plenum Publishing Corporation, 1992.

[118] "Bragg's Law."

[119] R. Lee, *Scanning electron microscopy and X-ray microanalysis.* 1993.

[120] T. Mueller, A. Kusne, and R. Ramprasad, "Machine Learning in Materials Science: Recent Progress and Emerging Applications," in *Reviews in Computational Chemistry* (A. L. Parrill and K. B. Lipkowitz, eds.), vol. 29, John Wiley & Sons, Inc., 1 ed., 2016.

[121] C. J. Long, "CombiView download — SourceForge.net," 2015.

[122] "DIFFRAC.SUITE EVA - XRD Software — Bruker."

[123] "PDF-2 ICDD — XRD Database — 2020 Now Available."

[124] Delaunay B., "Sur la sphère vide. A la mémoire de Georges Voronoï. Classe des sciences mathématiques et naturelles.," *Bulletin de l'Académie de l'URSS*, vol. 6, pp. 793–800, 1934.

[125] A. Cichocki, R. Zdunek, A. H. Phan, and S.-I. Amari, *Nonnegative Matrix and Tensor Factorizations Applications to Exploratory Multi-way Data Analysis and Blind Source Separation.* John Wiley & Sons, 2009.

[126] V. Stanev, V. V. Vesselinov, A. G. Kusne, G. Antoszewski, I. Takeuchi, and B. S. Alexandrov, "Unsupervised phase mapping of X-ray diffraction data by nonnegative matrix factorization integrated with custom clustering," *npj Computational Materials*, vol. 4, p. 43, 12 2018.

[127] S. Ermon, R. L. Bras, S. K. Suram, J. M. Gregoire, C. P. Gomes, B. Selman, and R. B. v. Dover, "Pattern Decomposition with Complex Combinatorial Constraints: Application to Materials Discovery," *Twenty-Ninth AAAI Conference on Artificial Intelligence*, 2 2015.

[128] L. J. van der Pauw, "A method of measuring specific resistivity and Hall effect of discs of arbitray shape," *Philips Research Report*, vol. 13, no. 1, 1958.

[129] S. Thienhaus, C. Zamponi, H. Rumpf, J. Hattrick-Simpers, I. Takeuchi, and A. Ludwig, "High-throughput characterization of shape memory thin films using automated temperature-dependent resistance measurements," *MRS Proceedings*, vol. 894, pp. 06–06, 1 2006.

[130] I. Friedrich, V. Weidenhof, W. Njoroge, P. Franz, and M. Wuttig, "Structural transformations of Ge2Sb2Te5 films studied by electrical resistance measurements," *Journal of Applied Physics*, vol. 87, no. 9, pp. 4130–4134, 2000.

[131] A. Majumdar, "Scanning thermal microscopy," *Annual Review of Materials Science*, vol. 29, pp. 505–585, 8 1999.

[132] A. A. Wilson, *Analysis of non-contact and contact probe-to-sample thermal exchange for quantitative measurements of thin film and nanostructure thermal conductivity by the scanning hot probe method*. PhD thesis, 2017.

[133] A. A. Wilson and T. Borca-Tasciuc, "Quantifying non-contact tip-sample thermal exchange parameters for accurate scanning thermal microscopy with heated microprobes," *Review of Scientific Instruments*, vol. 88, no. 7, p. 074903, 2017.

[134] "AFM Probes — Kelvin Nanotechnology."

[135] A. Kaźmierczak-Bałata, J. Bodzenta, M. Krzywiecki, J. Juszczyk, J. Szmidt, and P. Firek, "Application of scanning microscopy to study correlation between thermal properties and morphology of BaTiO3 thin films," *Thin Solid Films*, vol. 545, pp. 217–221, 2013.

[136] N. M. Al Hasan, H. Hou, T. Gao, J. Counsell, S. Sarker, S. Thienhaus, E. Walton, P. Decker, A. Mehta, A. Ludwig, and I. Takeuchi, "Combinatorial Exploration and Mapping of Phase Transformation in a Ni–Ti–Co Thin Film Library," *ACS Combinatorial Science*, vol. 22, no. 11, pp. 641–648, 2020.

[137] I. I. Kornilov, E. V. Kachur, and O. K. Belousov, "Investigation of TiNi-TiCo system," *Russian Metallurgy*, vol. 2, pp. 162–163, 1975.

[138] R. M. Bozorth, *Ferromagnetism*. Wiley VCH - IEEE Press, 1993.

[139] Z. Ahmad, S. Akbar, M. Farooque, A. ul Haq, and M. Yan, "Synthesis and magnetic properties of Nb-doped Al–Ni–Co–Ti–Cu–Fe permanent magnets," *Philosophical Magazine Letters*, vol. 91, pp. 173–181, 3 2011.

[140] I. Belyaev, V. Bazhenov, A. Moiseev, and A. V. Kireev, "New Fe Co Ni Cu Al Ti Alloy for Single-Crystal Permanent Magnets," *The physics of metals and metallography*, vol. 117, no. 3, pp. 214–221, 2016.

[141] A.-C. Yeh, Y.-J. Chang, C.-W. Tsai, Y.-C. Wang, J.-W. Yeh, and C.-M. Kuo, "On the Solidification and Phase Stability of a Co-Cr-Fe-Ni-Ti High-Entropy Alloy," *Metallurgical and Materials Transactions A*, vol. 45, pp. 184–190, 1 2014.

[142] S. Samal, M. Rahul, R. S. Kottada, and G. Phanikumar, "Hot deformation behaviour and processing map of Co-Cu-Fe-Ni-Ti eutectic high entropy alloy," *Materials Science and Engineering: A*, vol. 664, pp. 227–235, 5 2016.

[143] K. Christofidou, N. Jones, E. Pickering, R. Flacau, M. Hardy, and H. Stone, "The microstructure and hardness of Ni-Co-Al-Ti-Cr quinary alloys," *Journal of Alloys and Compounds*, vol. 688, pp. 542–552, 12 2016.

[144] Z. Zhong, Y. Gu, Y. Yuan, T. Yokokawa, and H. Harada, "On the low cycle fatigue behavior of a Ni-base superalloy containing high Co and Ti contents," *Materials Science and Engineering: A*, vol. 552, pp. 434–443, 8 2012.

[145] Y. Kishi, Z. Yajima, and K. Shimizu, "Relation between Tensile Deformation Behavior and Microstructure in a Ti-Ni-Co Shape Memory Alloy," *MATERIALS TRANSACTIONS*, vol. 43, no. 5, pp. 834–839, 2002.

[146] H. Hosoda, S. Hanada, K. Inoue, T. Fukui, Y. Mishima, and T. Suzuki, "Martensite transformation temperatures and mechanical properties of ternary NiTi alloys with offstoichiometric compositions," *Intermetallics*, vol. 6, no. 4, pp. 291–301, 1998.

[147] M. Larnicol, R. Portier, and P. Ochin, "Influence of Rapid Solidification on Ni50-xTi50Cx Shape Memory Alloys," *J; PHYS. IVNFRANCE*, vol. 7, no. C5, pp. 5–191, 1997.

[148] N. D. Alqarni, J. Wysocka, N. El-Bagoury, J. Ryl, M. A. Amin, and R. Boukherroub, "Effect of cobalt addition on the corrosion behavior of near equiatomic NiTi shape memory alloy in normal saline solution: electrochemical and XPS studies," *RSC Advances*, vol. 8, pp. 19289–19300, 5 2018.

[149] H. Soni, S. Narendranath, M. R. Ramesh, N. S., and R. M. R., "Effects of Wire Electro-Discharge Machining Process Parameters on the Machined Surface of Ti50Ni49Co1 Shape Memory Alloy," *Silicon*, pp. 1–7, 3 2018.

[150] E. Mohammad Sharifi, A. Kermanpur, and F. Karimzadeh, "The effect of thermomechanical processing on the microstructure and mechanical properties of the nanocrystalline TiNiCo shape memory alloy," *Materials Science and Engineering: A*, vol. 598, pp. 183–189, 3 2014.

[151] A. Fasching, D. Norwich, T. Geiser, and G. W. Paul, "An Evaluation of a NiTiCo Alloy and its Suitability for Medical Device Applications," *Journal of materials engineering and performance*, vol. 20, no. 4-5, pp. 641–645, 2011.

[152] T. Goryczka, P. Ochin, and J. Lelątko, "Shape Memory Effect in NiTiCo Strip Produced by Twin Roll Casting Technique," *Materials Science Forum*, vol. 738-739, pp. 348–351, 1 2013.

[153] L. Jordan, K. Goubaa, M. Masse, and G. Bouquet, "Comparitive study of mechanical properties of various Ni-Ti based shape memory alloys in view of dental and medical applications," *Journal de Physique IV Colloque*, vol. 111, no. 01, pp. 139–144, 1991.

[154] R. Martins, N. Schell, J. von Borany, K. Mahesh, R. Silva, and F. Braz Fernandes, "Structural evolution of magnetron sputtered shape memory alloy Ni–Ti films," *Vacuum*, vol. 84, pp. 913–919, 3 2010.

[155] K. P. Gupta, "The Co-Ni-Ti System (Cobalt-Nickel-Titanium)," *Journal of phase equilibria*, vol. 20, no. 1, pp. 65–72, 1999.

[156] S. Santosh and V. Sampath, "Effect of Ternary Addition of Cobalt on Shape Memory Characteristics of Ni–Ti Alloys," *Transactions of the Indian Institute of Metals*, pp. 1–4, 2 2019.

[157] C. Zhou, C. Guo, J. Li, C. Li, and Z. Du, "Experimental investigations of the Co–Ni–Ti system: Liquidus surface projection and isothermal section at 1373K," *Journal of Alloys and Compounds*, vol. 754, pp. 268–282, 7 2018.

[158] G. Firstov, R. Vitchev, H. Kumar, B. Blanpain, and J. Van Humbeeck, "Surface oxidation of NiTi shape memory alloy," *Biomaterials*, vol. 23, pp. 4863–4871, 12 2002.

[159] Y. Zheng, B. Wang, J. Wang, and C. Li, "Corrosion behaviour of Ti–Nb–Sn shape memory alloys in different simulated body solutions," *Materials Science and Engineering: A*, vol. 438-440, pp. 891–895, 11 2006.

[160] D. König, D. Naujoks, T. de los Arcos, S. Grosse-Kreul, and A. Ludwig, "X-Ray Photoelectron Spectroscopy Investigations of the Surface Reaction Layer and its Effects on the Transformation Properties of Nanoscale Ti51Ni38Cu11 Shape Memory Thin Films," *Advanced Engineering Materials*, vol. 17, pp. 669–673, 5 2015.

[161] S. Thienhaus, S. Hamann, and A. Ludwig, "Modular high-throughput test stand for versatile screening of thin-film materials libraries," *Science and Technology of Advanced Materials*, vol. 12, p. 054206, 10 2011.

[162] Y. Wu, E. Ertekin, and H. Sehitoglu, "Elastocaloric cooling capacity of shape memory alloys – Role of deformation temperatures, mechanical cycling, stress

hysteresis and inhomogeneity of transformation," *Acta Materialia*, vol. 135, pp. 158–176, 8 2017.

[163] L. Isola, P. La Roca, A. Roatta, P. Vermaut, L. Jordan, P. Ochin, and J. Malarría, "Load-biased martensitic transformation strain of Ti50–Ni47–Co3 strip obtained by a twin-roll casting technique," *Materials Science and Engineering: A*, vol. 597, pp. 245–252, 3 2014.

[164] H. Naresh, H. S.Bharath, and S. Prashantha, "The Influence of Alloying Constituent Fe on Mechanical Properties Of NiTi Based Shape Memory Alloys," *Materials Today: Proceedings*, vol. 4, pp. 11251–11259, 1 2017.

[165] T. Honma, *Types of Mechanical Characteristics of Shape Memory Alloys: TiNi–Based Shape Memory Alloys*. New York: Shape Memory Alloys, Gordon and Breach Science Publishers, 1987.

[166] F. Liu, Z. Ding, Y. Li, and H. Xu, "Phase transformation behaviors and mechanical properties of TiNiMo shape memory alloys," *Intermetallics*, vol. 13, pp. 357–360, 3 2005.

[167] W. J. Buehler and F. E. Wang, "A summary of recent research on the nitinol alloys and their potential application in ocean engineering," *Ocean Engineering*, vol. 1, pp. 105–120, 7 1968.

[168] D. Stockel, "The shape memory effect: phenomenon, alloys, applications," in *Shape memory alloys for power systems (EPRI)*, pp. 1–13, 1995.

[169] D. C. Lagoudas, ed., *Shape Memory Alloys: Modeling and Engineering Applications*. Springer Science & Business Media, 2008.

[170] "Shape Memory Alloys Behaviour: A Review," *Procedia Engineering*, vol. 114, pp. 776–783, 1 2015.

[171] M. Zarinejad and Y. Liu, "Dependence of Transformation Temperatures of NiTi-based Shape-Memory Alloys on the Number and Concentration of Valence Electrons," *Advanced Functional Materials*, vol. 18, pp. 2789–2794, 9 2008.

[172] K. Otsuka and X. B. Ren, "Factors Affecting the Ms Temperature and its Control in Shape-Memory Alloys," *Materials Science Forum*, vol. 394-395, pp. 177–184, 5 2002.

[173] N. Morgan, "Medical shape memory alloy applications—the market and its products," *Materials Science and Engineering: A*, vol. 378, pp. 16–23, 7 2004.

[174] L. Petrini and F. Migliavacca, "Biomedical Applications of Shape Memory Alloys," *Journal of Metallurgy*, vol. 2011, pp. 1–15, 5 2011.

[175] K. Otsuka and T. Kakeshita, "Science and Technology of Shape-Memory Alloys: New Developments," *MRS Bulletin*, vol. 27, pp. 91–100, 2 2002.

[176] S. Qian, *Development Of Thermoelastic Cooling Systems*. PhD thesis, University of Maryland, College Park, 2015.

[177] S. Qian, Y. Geng, Y. Wang, T. E. Pillsbury, Y. Hada, Y. Yamaguchi, K. Fujimoto, Y. Hwang, R. Radermacher, J. Cui, Y. Yuki, K. Toyotake, I. Takeuchi, Y. Hada, I. Takeuchi, S. Qian, T. E. Pillsbury, J. Cui, Y. Wang, Y. Geng, Y. Yamaguchi, Y. Hwang, K. Toyotake, and R. Radermacher, "Elastocaloric effect in CuAlZn and CuAlMn shape memory alloys under compression," *Philosophical Transactions of the Royal Society A: Mathematical, Physical and Engineering Sciences*, vol. 374, p. 20150309, 8 2016.

[178] Simona-Ileana, K. E. Grabowska, I. Ciesielska-Wrobel, and J. Ghitaiga, "Analysis of hybrid woven fabrics with shape memory alloys wires embedded," *FIBRES & TEXTILES IN EASTERN EUROPE*, vol. 18, no. 1, pp. 64–69, 2010.

[179] D. Xue, R. Yuan, Y. Zhou, D. Xue, T. Lookman, G. Zhang, X. Ding, and J. Sun, "Design of High Temperature Ti-Pd-Cr Shape Memory Alloys with Small Thermal Hysteresis," *Scientific Reports*, vol. 6, pp. 1–7, 2016.

[180] Y. Kim, M.-G. Jo, J.-W. Park, H.-K. Park, and H. N. Han, "Elastocaloric effect in polycrystalline Ni50Ti45.3V4.7 shape memory alloy," *Scripta Materialia*, vol. 144, pp. 48–51, 2 2018.

[181] U.S. Energy Information Administration, "International Energy Outlook," 2016.

[182] H. Nazir, M. Batool, F. J. Bolivar Osorio, M. Isaza-Ruiz, X. Xu, K. Vignarooban, P. Phelan, Inamuddin, and A. M. Kannan, "Recent developments in phase change materials for energy storage applications: A review," *International Journal of Heat and Mass Transfer*, vol. 129, pp. 491–523, 2 2019.

[183] B. Pause, "Phase change materials and their application in coatings and laminates for textiles," in *Smart Textile Coatings and Laminates: A volume in Woodhead Publishing Series in Textiles*, pp. 236–250, Elsevier Ltd, 1 2010.

[184] B. c. Zhao, M. s. Cheng, C. Liu, and Z. m. Dai, "Cyclic thermal characterization of a molten-salt packed-bed thermal energy storage for concentrating solar power," *Applied Energy*, vol. 195, pp. 761–773, 6 2017.

[185] Z. Yang and S. V. Garimella, "Cyclic operation of molten-salt thermal energy storage in thermoclines for solar power plants," *Applied Energy*, vol. 103, pp. 256–265, 3 2013.

[186] N. R. Jankowski and F. P. McCluskey, "A review of phase change materials for vehicle component thermal buffering," *Applied Energy*, vol. 113, pp. 1525–1561, 1 2014.

[187] A. Fallahi, G. Guldentops, M. Tao, S. Granados-Focil, and S. Van Dessel, "Review on solid-solid phase change materials for thermal energy storage: Molecular structure and thermal properties," *Applied Thermal Engineering*, vol. 127, pp. 1427–1441, 12 2017.

[188] M. M. Farid, A. M. Khudhair, S. A. K. Razack, and S. Al-Hallaj, "A review on phase change energy storage: Materials and applications," *Energy Conversion and Management*, vol. 45, pp. 1597–1615, 6 2004.

[189] P. Krulevitch, A. P. Lee, P. B. Ramsey, J. C. Trevino, J. Hamilton, and M. A. Northrup, "Thin film shape memory alloy microactuators," *Journal of Microelectromechanical Systems*, vol. 5, pp. 270–282, 12 1996.

[190] W. P. Eaton and J. H. Smith, "Micromachined pressure sensors: review and recent developments," *Smart Materials and Structures*, vol. 6, no. 5, p. 530, 1997.

[191] A. Kumar, D. Singh, R. N. Goyal, and D. Kaur, "Fabrication and nanoindentation properties of TiN/NiTi thin films and their applications in electrochemical sensing," *Talanta*, vol. 78, pp. 964–969, 5 2009.

[192] G. Sberveglieri, W. Hellmich, and G. Müller, "Silicon hotplates for metal oxide gas sensor elements," *Microsystem Technologies*, vol. 3, no. 4, pp. 183–190, 1997.

[193] W. L. Benard, H. Kahn, A. H. Heuer, and M. A. Huff, "Thin-film shape-memory alloy actuated micropumps," *Journal of Microelectromechanical Systems*, vol. 7, pp. 245–251, 6 1998.

[194] J. F. Goff, "Thermal conductivity, thermoelectric power, and the electrical resistivity of stoichiometric TiNi in the 3° to 300°K temperature range," *Journal of Applied Physics*, vol. 35, pp. 2919–2927, 10 1964.

[195] Y. Terada, K. Ohkubo, K. Nakagawa, T. Mohri, and T. Suzuki, "Thermal conductivity of B2-type aluminides and titanides," *Intermetallics*, vol. 3, pp. 347–355, 1 1995.

[196] M. G. Faulkner, J. J. Amalraj, and A. Bhattacharyya, "Experimental determination of thermal and electrical properties of Ni-Ti shape memory wires," *Smart Materials and Structures*, vol. 9, no. 5, pp. 632–639, 2000.

[197] A. Jain and K. E. Goodson, "Measurement of the thermal conductivity and heat capacity of freestanding shape memory thin films using the 3ω method," *Journal of Heat Transfer*, vol. 130, 10 2008.

[198] N. T. Vu, D. J. Sharar, A. N. Smith, R. J. Warzoha, A. C. Leff, B. F. Donovan, and A. A. Wilson, "Effect of grain size on the thermal properties of nickel-titanium shape memory alloys across the martensite-austenite phase

transition," in *InterSociety Conference on Thermal and Thermomechanical Phenomena in Electronic Systems, ITHERM*, vol. 2019-May, pp. 851–856, IEEE Computer Society, 5 2019.

[199] D. D. Shin, K. P. Mohanchandra, and G. P. Carman, "High frequency actuation of thin film NiTi," *Sensors and Actuators, A: Physical*, vol. 111, pp. 166–171, 3 2004.

[200] C. Zanotti, P. Giuliani, P. Bassani, Z. Zhang, and A. Chrysanthou, "Comparison between the thermal properties of fully dense and porous NiTi SMAs," *Intermetallics*, vol. 18, pp. 14–21, 1 2010.

[201] M. Chirtoc, J. Gibkes, R. Wernhardt, J. Pelzl, and A. Wieck, "Temperature-dependent quantitative 3ω scanning thermal microscopy: Local thermal conductivity changes in NiTi microstructures induced by martensite-austenite phase transition," *Review of Scientific Instruments*, vol. 79, p. 093703, 9 2008.

[202] Y. Terada, K. Ohkubo, S. Miura, and T. Mohri, "Thermophysical Properties of Rh3X for Ultra-High Temperature Applications," *Platinum Metals Review*, vol. 50, no. 2, pp. 69–76, 2006.

[203] C. Zanotti, P. Giuliani, and A. Chrysanthou, "Martensitic-Austenitic phase transformation of Ni-Ti SMAs: Thermal properties," *Intermetallics*, vol. 24, pp. 106–114, 5 2012.

[204] B. Ramachandran, R. C. Tang, P. C. Chang, Y. K. Kuo, C. Chien, and S. K. Wu, "Cu-substitution effect on thermoelectric properties of the TiNi-based shape memory alloys," *Journal of Applied Physics*, vol. 113, p. 203702, 5 2013.

[205] D. G. Cahill, K. Goodson, and A. Majumdar, "Thermometry and thermal transport in micro/nanoscale solid-state devices and structures," *Journal of Heat Transfer*, vol. 124, no. 2, pp. 223–241, 2002.

[206] K. E. Goodson and Y. S. Ju, "Heat conduction in novel electronic films," *Annual Review of Materials Science*, vol. 29, pp. 261–293, 11 1999.

[207] C. A. Paddock and G. L. Eesley, "Transient thermoreflectance from thin metal films," *Journal of Applied Physics*, vol. 60, pp. 285–290, 7 1986.

[208] D. Chu, M. Touzelbaev, K. E. Goodson, S. Babin, and R. F. Pease, "Thermal conductivity measurements of thin-film resist," *Journal of Vacuum Science and Technology B: Microelectronics and Nanometer Structures*, vol. 19, pp. 2874–2877, 11 2001.

[209] S. Govorkov, W. Ruderman, M. W. Horn, R. B. Goodman, and M. Rothschild, "A new method for measuring thermal conductivity of thin films," *Review of Scientific Instruments*, vol. 68, pp. 3828–3834, 10 1997.

[210] M. A. Jothi Rajan, T. S. Vivekanandam, S. K. Ramakrishnan, K. Ramachandran, and S. Umapathy, "Heat transfer in poly(methyl acrylate) by photoacoustic measurements," *Journal of Applied Polymer Science*, vol. 93, pp. 1071–1076, 8 2004.

[211] A. J. Schmidt, R. Cheaito, and M. Chiesa, "A frequency-domain thermoreflectance method for the characterization of thermal properties," *Review of Scientific Instruments*, vol. 80, p. 094901, 9 2009.

[212] K. T. Regner, S. Majumdar, and J. A. Malen, "Instrumentation of broadband frequency domain thermoreflectance for measuring thermal conductivity accumulation functions," *Review of Scientific Instruments*, vol. 84, p. 064901, 6 2013.

[213] J. P. Feser and D. G. Cahill, "Probing anisotropic heat transport using time-domain thermoreflectance with offset laser spots," *Review of Scientific Instruments*, vol. 83, p. 104901, 10 2012.

[214] D. G. Cahill, "Thermal conductivity measurement from 30 to 750 K: The 3ω method," *Review of Scientific Instruments*, vol. 61, pp. 802–808, 6 1990.

[215] "Frequency Domain Thermoreflectance."

[216] D. Rodin and S. K. Yee, "Simultaneous measurement of in-plane and through-plane thermal conductivity using beam-offset frequency domain thermoreflectance," *Review of Scientific Instruments*, vol. 88, p. 014902, 1 2017.

[217] S. M. Lee, D. G. Cahill, and T. H. Allen, "Thermal conductivity of sputtered oxide films," *Physical Review B*, vol. 52, pp. 253–257, 7 1995.

[218] W. Liu and A. A. Balandin, "Thermal conduction in AlxGa1-xN alloys and thin films," *Journal of Applied Physics*, vol. 97, p. 073710, 4 2005.

[219] D. G. Cahill, M. Katiyar, and J. R. Abelson, "Thermal conductivity of a-Si:H thin films," *Physical Review B*, vol. 50, pp. 6077–6081, 9 1994.

[220] Y. Zhang, W. Zhu, F. Hui, M. Lanza, T. Borca-Tasciuc, and M. Muñoz Rojo, "A Review on Principles and Applications of Scanning Thermal Microscopy (SThM)," *Advanced Functional Materials*, vol. 30, p. 1900892, 5 2020.

[221] S. Gomès, A. Assy, and P.-O. O. Chapuis, "Scanning thermal microscopy: A review," *physica status solidi (a)*, vol. 212, pp. 477–494, 3 2015.

[222] J. Juszczyk, A. Kaźmierczak-Bałata, P. Firek, and J. Bodzenta, "Measuring thermal conductivity of thin films by Scanning Thermal Microscopy combined with thermal spreading resistance analysis," *Ultramicroscopy*, vol. 175, pp. 81–86, 4 2017.

[223] K. Kim, W. Jeong, W. Lee, S. Sadat, D. Thompson, E. Meyhofer, and P. Reddy, "Quantification of thermal and contact resistances of scanning thermal probes," *Applied Physics Letters*, 2014.

[224] J. Chung, K. Kim, G. Hwang, O. Kwon, S. Jung, J. Lee, J. W. Lee, and G. T. Kim, "Quantitative temperature measurement of an electrically heated carbon nanotube using the null-point method," *Review of Scientific Instruments*, vol. 81, no. 11, p. 114901, 2010.

[225] A. A. Wilson, "Scanning thermal probe calibration for accurate measurement of thermal conductivity of ultrathin films," *MRS Communications*, vol. 9, no. 2, pp. 650–656, 2019.

[226] A. A. Wilson and D. J. Sharar, "Temperature-Dependent Adhesion Mechanisms of Metal and Insulator Probe-Sample Contact Pairs," in *Proceedings of the 17th InterSociety Conference on Thermal and Thermomechanical Phenomena in Electronic Systems, ITherm 2018*, 2018.

[227] K. Kim, W. Jeong, W. Lee, and P. Reddy, "Ultra-high vacuum scanning thermal microscopy for nanometer resolution quantitative thermometry," *ACS Nano*, vol. 6, no. 5, pp. 4248–4257, 2012.

[228] K. Kim, J. Chung, G. Hwang, O. Kwon, and J. S. Lee, "Quantitative measurement with scanning thermal microscope by preventing the distortion due to the heat transfer through the air," *ACS Nano*, vol. 5, no. 11, pp. 8700–8709, 2011.

[229] K. Kim, J. Chung, J. Won, O. Kwon, J. S. Lee, S. H. Park, and Y. K. Choi, "Quantitative scanning thermal microscopy using double scan technique," *Applied Physics Letters*, vol. 93, no. 20, p. 203115, 2008.

[230] E. Guen, D. Renahy, M. Massoud, J. M. Bluet, P. O. Chapuis, and S. Gomes, "Calibration methodologies for scanning thermal microscopy," in *THERMINIC 2016 - 22nd International Workshop on Thermal Investigations of ICs and Systems*, pp. 110–114, 2016.

[231] Y. Zhang, E. E. Castillo, R. J. Mehta, G. Ramanath, and T. Borca-Tasciuc, "A noncontact thermal microprobe for local thermal conductivity measurement," *Review of Scientific Instruments*, vol. 82, no. 2, p. 024902, 2011.

[232] S. Lefèvre, S. Volz, J.-B. B. Saulnier, C. Fuentes, and N. Trannoy, "Thermal conductivity calibration for hot wire based dc scanning thermal microscopy," *Review of Scientific Instruments*, vol. 74, p. 2418, 4 2003.

[233] S. Lefèvre, J. B. Saulnier, C. Fuentes, and S. Volz, "Probe calibration of the scanning thermal microscope in the AC mode," *Superlattices and Microstructures*, vol. 35, pp. 283–288, 3 2004.

[234] C. Metzke, W. Frammelsberger, J. Weber, F. Kühnel, K. Zhu, M. Lanza, and G. Benstetter, "On the limits of scanning thermal microscopy of ultrathin films," *Materials*, vol. 13, no. 3, p. 518, 2020.

[235] Y. Ge, Y. Zhang, J. M. Weaver, and P. S. Dobson, "Dimension- and shape-dependent thermal transport in nano-patterned thin films investigated by scanning thermal microscopy," *Nanotechnology*, vol. 28, no. 48, p. 485706, 2017.

[236] H. Chae, G. Hwang, and O. Kwon, "Fabrication of scanning thermal microscope probe with ultra-thin oxide tip and demonstration of its enhanced performance," *Ultramicroscopy*, vol. 171, pp. 195–203, 2016.

[237] A. A. Wilson, T. Borca-Tasciuc, H. Wang, and C. Yu, "Thermal conductivity of double-wall carbon nanotube-polyanaline composites measured by a non-contact scanning hot probe technique," in *Proceedings of the 16th InterSociety Conference on Thermal and Thermomechanical Phenomena in Electronic Systems, ITherm 2017*, pp. 1–8, 2017.

[238] J. Maiz, M. Muñoz Rojo, B. Abad, A. A. Wilson, A. Nogales, D. A. Borca-Tasciuc, T. Borca-Tasciuc, and M. Martín-González, "Enhancement of thermoelectric efficiency of doped PCDTBT polymer films," *RSC Advances*, vol. 5, no. 82, pp. 66687–66694, 2015.

[239] D. I. Florescu, L. G. Mourokh, F. H. Pollak, D. C. Look, G. Cantwell, and X. Li, "High spatial resolution thermal conductivity of bulk ZnO (0001)," *Journal of Applied Physics*, vol. 91, no. 2, p. 890, 2002.

[240] T. L. Li and S. L. C. Hsu, "Enhanced thermal conductivity of polyimide films via a hybrid of micro- and nano-sized boron nitride," *Journal of Physical Chemistry B*, vol. 114, no. 20, pp. 6825–6829, 2010.

[241] I. Williams and R. Shawyer, "Certification report for a pyrex glass reference material for thermal conductivity between-75 C and 195 C," tech. rep., 1991.

[242] M. E. DeCoster, K. E. Meyer, B. D. Piercy, J. T. Gaskins, B. F. Donovan, A. Giri, N. A. Strnad, D. M. Potrepka, A. A. Wilson, M. D. Losego, and P. E. Hopkins, "Density and size effects on the thermal conductivity of atomic layer deposited TiO2 and Al2O3 thin films," *Thin Solid Films*, vol. 650, pp. 71–77, 2018.

[243] R. J. Warzoha, N. T. Vu, B. F. Donovan, E. Cimpoiasu, D. J. Sharar, A. C. Leff, A. A. Wilson, and A. N. Smith, "Grain growth-induced thermal property enhancement of NiTi shape memory alloys for elastocaloric refrigeration and thermal energy storage systems," *International Journal of Heat and Mass Transfer*, vol. 154, p. 119760, 2020.

[244] C. J. Glassbrenner and G. A. Slack, "Thermal conductivity of silicon and germanium from 3°K to the melting point," *Physical Review*, vol. 134, no. 4A, p. A1058, 1964.

[245] R. B. Rounds, "The Influence of Point Defects on the Thermal Conductivity of AlN and GaN," 2018.

[246] D. Cucinotta and M. Vanelli, "WHO declares COVID-19 a pandemic," *Acta Biomedica*, vol. 91, no. 1, pp. 157–160, 2020.

[247] Z. Wang, J. E. Alaniz, W. Jang, J. E. Garay, and C. Dames, "Thermal Conductivity of Nanocrystalline Silicon: Importance of Grain Size and Frequency-Dependent Mean Free Paths," *Nano Lett*, vol. 11, no. 6, pp. 2206–2213, 2011.

[248] H. C. Lin, C. H. Yang, M. C. Lin, C. S. Lin, K. M. Lin, and L. S. Chang, "Aging effect on a Ti47.25Ni48.75V4 shape memory alloy," *Journal of Alloys and Compounds*, vol. 449, pp. 119–124, 1 2008.

[249] B. Ramachandran, C. H. Chen, P. C. Chang, Y. K. Kuo, C. Chien, and S. K. Wu, "Thermal and transport properties of as-grown Ni-rich TiNi shape memory alloys," *Intermetallics*, vol. 60, pp. 79–85, 2015.

[250] G. Jóźwiak, G. Wielgoszewski, T. Gotszalk, and L. Kepiński, "Thermal mapping of a scanning thermal microscopy tip," *Ultramicroscopy*, vol. 133, pp. 80–87, 10 2013.

[251] S. I. Sadaq, B. Y. Kumar, S. S. Banu, T. Assistant, and A. Pradesh, "Thermostructural Analysis of Nitinol Tube," *Scholars Journal of Engineering and Technology*, vol. 2, no. 6B, pp. 890–894, 2014.

[252] "Patent Database Search Results: "shape memory alloy" in US Patent Collection."

[253] S. B. Maisel, W. S. Ko, J. L. Zhang, B. Grabowski, and J. Neugebauer, "Thermomechanical response of NiTi shape-memory nanoprecipitates in TiV alloys," *Physical Review Materials*, vol. 1, p. 033610, 2017.

[254] B. Grabowski and C. C. Tasan, "Self-healing metals," in *Self healing materials* (M. D. Hager, S. v. d. Zwaag, and U. S. Schubert, eds.), pp. 387–408, Springer New York LLC, 2 2016.

[255] X. L. Meng, W. Cai, Y. D. Fu, Q. F. Li, J. X. Zhang, and L. C. Zhao, "Shape-memory behaviors in an aged Ni-rich TiNiHf high temperature shape-memory alloy," *Intermetallics*, vol. 16, pp. 698–705, 5 2008.

[256] X. L. Meng, Y. F. Zheng, Z. Wang, and L. C. Zhao, "Effect of aging on the phase transformation and mechanical behavior of Ti36Ni49Hf15 high temperature shape memory alloy," *Scripta Materiala*, vol. 42, no. 4, pp. 341–348, 2000.

[257] H. E. Karaca, E. Acar, H. Tobe, and S. M. Saghaian, "NiTiHf-based shape memory alloys," *Materials Science and Technology (United Kingdom)*, vol. 30, no. 13, pp. 1530–1544, 2014.

[258] S. Besseghini, E. Villa, and A. Tuissi, "Ni-Ti-Hf shape memory alloy: Effect of aging and thermal cycling," *Materials Science and Engineering A*, vol. 273-275, pp. 390–394, 12 1999.

[259] P. T. D.R. Angst and M. Kao, "The Effect of Hafnium Content on the Transformation Temperatures of Ni49Ti51-xHfx. Shape Memory Alloys — Journal de Physique IV," *J. Phys. IV France*, vol. 5, no. 8, pp. 8–747, 1995.

[260] G. S. Firstov, J. Van Humbeeck, and Y. N. Koval, "High Temperature Shape Memory Alloys Problems and Prospects," *Journal of Intelligent Material Systems and Structures*, vol. 17, pp. 1041–1047, 12 2006.

[261] J. Van Humbeeck, "High temperature shape memory alloys," *Journal of Engineering Materials and Technology, Transactions of the ASME*, vol. 121, pp. 98–101, 1 1999.

[262] B. Kockar, I. Karaman, J. I. Kim, and Y. Chumlyakov, "A method to enhance cyclic reversibility of NiTiHf high temperature shape memory alloys," *Scripta Materialia*, vol. 54, pp. 2203–2208, 6 2006.

[263] J. Ma, I. Karaman, and R. D. Noebe, "High temperature shape memory alloys," *International Materials Reviews*, vol. 55, no. 5, pp. 257–315, 2010.

[264] D. R. Coughlin, L. Casalena, F. Yang, R. D. Noebe, and M. J. Mills, "Microstructure–property relationships in a high-strength 51Ni–29Ti–20Hf shape memory alloy," *Journal of Materials Science*, vol. 51, no. 2, pp. 766–778, 2016.

[265] X. Shi, H. Yang, H. Mao, Y. Li, J. Zhang, and X. Yin, "Effect of plastic deformation of V nanowires on the transformation characteristics of NiTiV alloys," *Materials Science and Engineering A*, vol. 735, pp. 162–165, 2018.

[266] H. Mao, H. Yang, X. Shi, Y. Li, J. Zhang, and J. Jiang, "Transformation and superelastic characteristics of large hysteresis TiNi matrix shape memory alloys reinforced by V nanowires," *Materials Letters*, vol. 228, pp. 391–394, 2018.

[267] Y. Zheng, J. Schrooten, L. Cui, and J. Van Humbeeck, "Constrained thermoelastic martensitic transformation studied by modulated DSC," *Acta Materialia*, vol. 51, no. 18, pp. 5467–5475, 2003.

[268] Y. Zheng and L. Cui, "Martensite fraction-temperature diagram of TiNi wires embedded in an aluminum matrix," *Intermetallics*, vol. 12, no. 12, pp. 1305–1309, 2004.

[269] H. Yang, J. Chen, Y. Wu, X. Shi, Y. Li, and J. Jiang, "The transformation characteristics of the NiTi–V composite with dual-scale bcc-V fibers," *Intermetallics*, vol. 116, p. 106650, 1 2020.

[270] X. B. Shi, F. M. Guo, J. S. Zhang, H. L. Ding, and L. S. Cui, "Grain size effect on stress hysteresis of nanocrystalline NiTi alloys," *Journal of Alloys and Compounds*, vol. 688, pp. 62–68, 2016.

[271] M. Kök, A. O. A. Al-Jaf, Z. D. Çirak, I. N. Qader, and E. Özen, "Effects of heat treatment temperatures on phase transformation, thermodynamical parameters, crystal microstructure, and electrical resistivity of NiTiV shape memory alloy," *Journal of Thermal Analysis and Calorimetry*, vol. 139, pp. 3405–3413, 3 2020.

[272] H. Ossmer, C. Chluba, M. Gueltig, E. Quandt, and M. Kohl, "Local Evolution of the Elastocaloric Effect in TiNi-Based Films," *Shape Memory and Superelasticity*, vol. 1, pp. 142–152, 2015.

[273] O. Rios, R. Noebe, T. Biles, A. Garg, A. Palczer, D. Scheiman, H. J. Seifert, and M. Kaufman, "Characterization of ternary NiTiPt high-temperature shape memory alloys," in *Smart Structures and Materials 2005: Active Materials: Behavior and Mechanics* (W. D. Armstrong, ed.), vol. 5761, p. 376, SPIE, 5 2005.

[274] Y. Tong, Y. Liu, Z. Xie, and M. Zarinejad, "Effect of precipitation on the shape memory effect of Ti50Ni25Cu25 melt-spun ribbon," *Acta Materialia*, vol. 56, pp. 1721–1732, 5 2008.

[275] S. K. Wu and S. F. Hsieh, "Martensitic transformation of a Ti-rich Ti40.5Ni49.5Zr10 shape memory alloy," *Journal of Alloys and Compounds*, vol. 297, pp. 294–302, 2 2000.

[276] H. RÖSNER, P. SCHLOSSMACHER, A. V. SHELYAKOV, and A. M. GLEZER, "Formation of TiCu plate-like precipitates in Ti50Ni25Cu25 shape memory alloys," *Scripta Materialia*, vol. 43, no. 10, pp. 871–876, 2000.

[277] H. C. Lin, S. K. Wu, and J. C. Lin, "The martensitic transformation in Ti-rich TiNi shape memory alloys," *Materials Chemistry and Physics*, vol. 37, pp. 184–190, 3 1994.

[278] J. Khalil-Allafi, G. Eggeler, W. W. Schmahl, and D. Sheptyakov, "Quantitative phase analysis in microstructures which display multiple step martensitic transformations in Ni-rich NiTi shape memory alloys," *Materials Science and Engineering A*, vol. 438-440, pp. 593–596, 11 2006.

[279] G. Fan, W. Chen, S. Yang, J. Zhu, X. Ren, and K. Otsuka, "Origin of abnormal multi-stage martensitic transformation behavior in aged Ni-rich Ti-Ni shape memory alloys," *Acta Materialia*, vol. 52, pp. 4351–4362, 8 2004.

[280] V. Y. Abramov, N. M. Aleksandrova, D. V. Borovkov, I. Y. Khmelevskaya, A. V. Korotitskiy, S. Y. Makushev, N. A. Polyakova, N. N. Popov, and S. D. Prokoshkin, "Martensitic transformations and functional properties of thermally and thermomechanically treated Ti-Ni-Nb-based alloys," *Materials Science and Engineering A*, vol. 438-440, pp. 553–557, 11 2006.

[281] M. Peltonen, T. Lindroos, and M. Kallio, "Effect of ageing on transformation kinetics and internal friction of Ni-rich Ni-Ti alloys," *Journal of Alloys and Compounds*, vol. 460, pp. 237–245, 7 2008.

[282] K. Gall, H. Sehitoglu, Y. I. Chumlyakov, I. V. Kireeva, and H. J. Maier, "The influence of aging on critical transformation stress levels and martensite start temperatures in NiTi: Part I- Aged microstructure and micro-mechanical modeling," *Journal of Engineering Materials and Technology, Transactions of the ASME*, vol. 121, pp. 19–27, 1 1999.

[283] H. Rösner, P. Schloßmacher, A. V. Shelyakov, and A. M. Glezer, "The Influence of Coherent and Semi-Coherent TiCu Precipitates on the Martensitic Transformation of Melt-Spun Ti50Ni25Cu25 Shape Memory Ribbons," *MATERIALS TRANSACTIONS*, vol. 42, no. 8, pp. 1758–1762, 2001.

[284] X. D. Han, R. Wang, Z. Zhang, and D. Z. Yang, "A new precipitate phase in a TiNiHf high temperature shape memory alloy," *Acta Materialia*, vol. 46, pp. 273–281, 12 1998.

[285] X. D. Han, W. H. Zou, R. Wang, Z. Zhang, and Yang, "Structure and substructure of martensite in a Ti36.5Ni48.5Hf15 high temperature shape memory alloy," *Acta Materialia*, vol. 44, pp. 3711–3721, 9 1996.

[286] S. Shimizu, Y. Xu, E. Okunishi, S. Tanaka, K. Otsuka, and K. Mitose, "Improvement of shape memory characteristics by precipitation-hardening of Ti-Pd-Ni alloys," *Materials Letters*, vol. 34, pp. 23–29, 2 1998.

[287] T. Sawaguchi, M. Sato, and A. Ishida, "Microstructure and shape memory behavior of Ti51.2(Pd27.0Ni21.8) and Ti49.5(Pd28.5Ni22.0) thin films," *Materials Science and Engineering A*, vol. 332, pp. 47–55, 7 2002.

[288] J. D. P. Counsell, N. M. Al Hasan, E. Walton, T. Gao, H. Hou, and I. Takeuchi, "XPS group array analysis of a combinatorial Ni-Ti-Co thin film library," *Journal of Vacuum Science and Technology A*, vol. 38, no. 6, pp. 063407–1, 2020.

[289] Y. Gong, R. Tu, and T. Goto, "High-speed deposition of titanium carbide coatings by laser-assisted metal–organic CVD," *Materials Research Bulletin*, vol. 48, pp. 2766–2770, 8 2013.

[290] D. Xie, F. Wen, W. Yang, X. Li, Y. Leng, G. Wan, H. Sun, and N. Huang, "Carbon-Doped Titanium Oxide Films by DC Reactive Magnetron Sputtering Using CO2 and O2 as Reactive Gas," *Acta Metallurgica Sinica (English Letters)*, vol. 27, pp. 239–244, 4 2014.

[291] G. Greczynski, S. Mráz, L. Hultman, and J. Schneider, "Unintentional carbide formation evidenced during high-vacuum magnetron sputtering of transition metal nitride thin films," *Applied Surface Science*, vol. 385, pp. 356–359, 11 2016.

[292] J. Frenzel, E. P. George, A. Dlouhy, C. Somsen, M. F. Wagner, and G. Eggeler, "Influence of Ni on martensitic phase transformations in NiTi shape memory alloys," *Acta Materialia*, vol. 58, no. 9, pp. 3444–3458, 2010.

[293] D. D. Lee and H. S. Seung, "Learning the parts of objects by non-negative matrix factorization," *Nature*, vol. 401, pp. 788–791, 10 1999.

[294] L. B. Alexandrov, S. Nik-Zainal, D. C. Wedge, S. A. J. R. Aparicio, S. Behjati, A. V. Biankin, G. R. Bignell, N. Bolli, A. Borg, A.-L. Børresen-Dale, S. Boyault, B. Burkhardt, A. P. Butler, C. Caldas, H. R. Davies, C. Desmedt, R. Eils, J. E. Eyfjörd, J. A. Foekens, M. Greaves, F. Hosoda, B. Hutter, T. Ilicic, S. Imbeaud, M. Imielinski, N. Jäger, D. T. W. Jones, D. Jones, S. Knappskog, M. Kool, S. R. Lakhani, C. López-Otín, S. Martin, N. C. Munshi, H. Nakamura, P. A. Northcott, M. Pajic, E. Papaemmanuil, A. Paradiso, J. V. Pearson, X. S. Puente, K. Raine, M. Ramakrishna, A. L. Richardson, J. Richter, P. Rosenstiel, M. Schlesner, T. N. Schumacher, P. N. Span, J. W. Teague, Y. Totoki, A. N. J. Tutt, R. Valdés-Mas, M. M. van Buuren, L. van 't Veer, A. Vincent-Salomon, N. Waddell, L. R. Yates, J. Zucman-Rossi, P. Andrew Futreal, U. McDermott, P. Lichter, M. Meyerson, S. M. Grimmond, R. Siebert, E. Campo, T. Shibata, S. M. Pfister, P. J. Campbell, M. R. Stratton, T. Shibata, S. M. Pfister, P. J. Campbell, and M. R. Stratton, "Signatures of mutational processes in human cancer," *Nature*, vol. 500, pp. 415–421, 8 2013.